1. Report No.	2. Government Accession No.	3. Recipient's Catalog No.
FHWA/TX-07/0-4826-1		

4. Title and Subtitle	5. Report Date
BEST PRACTICES FOR THE USE OF SILICEOUS RIVER GRAVEL IN CONCRETE PAVING	December 2006 Published: February 2009
	6. Performing Organization Code
7. Author(s) Juanyu Liu, Anal K. Mukhopadhyay, Manuel Celaya, Soheil Nazarian, and Dan G. Zollinger	8. Performing Organization Report No. Report 0-4826-1
9. Performing Organization Name and Address Texas Transportation Institute The Texas A&M University System College Station, Texas 77843-3135	10. Work Unit No. (TRAIS)
	11. Contract or Grant No. Project 0-4826
12. Sponsoring Agency Name and Address Texas Department of Transportation Research and Technology Implementation Office P. O. Box 5080 Austin, Texas 78763-5080	13. Type of Report and Period Covered Technical Report: September 2003-August 2006
	14. Sponsoring Agency Code

15. Supplementary Notes

Project performed in cooperation with the Texas Department of Transportation and the Federal Highway Administration.

Project Title: Use of Crushed Gravel in Concrete Paving

URL: http://tti.tamu.edu/documents/0-4826-1.pdf

16. Abstract

Fracture toughness (K_{IC}) value at early ages of concrete was used to represent the interfacial bond between aggregate and mortar of a variety of coarse aggregates types and concrete mixtures. A fractional factorial design based on Taguchi's orthogonal array using four factors (i.e., aggregate type, w/cm, replacement of ultra-fine fly ash, and curing method) was selected to conduct the detailed laboratory study. The statistical analysis indicated the following decreasing rank order with respect to the relative importance of each factor to K_{IC}: aggregate type, curing method, w/cm, and ultra-fine fly ash content. A comprehensive investigation of aggregate properties relative to physical, geometric, and chemical characteristics was conducted. The research findings indicated that the aggregate-mortar interfacial bond for a given cement paste was found not to be a simple function of any one of the aggregate properties, but a function of all three properties aggregated together. The application of utility theory to the evaluation of overall contribution of aggregate properties to the bonding performance of concrete, and feasibility of design combinations enables agencies to select the best aggregate type, modify aggregates by blending different aggregates, and optimize the design combinations for concrete paving construction, to relieve delamination and further spalling distresses.

The interfacial fracture energy can be predicted once a design combination is known based on the linear relation with both concrete and mortar fracture energy. A fracture mechanics based approach was proposed with the facilitation of numerical analysis to predict the occurrence of delamination. The criterion for predicting early age delamination occurrence is that delamination occurs when $K_I > K_{IC}$. Through examples of practical design and construction methods, this approach is able to assess the probability of delamination occurrence, which will facilitate selection and evaluation of the effectiveness of pavement design methods to prevent delamination and spalling problems in concrete paving.

Test sections of both winter and summer were established based on the research finding from laboratory investigations, theoretical modeling, and numerical analysis. Future performance of these sections will determine if the measures taken to arrest delamination were successful or not.

17. Key Words	18. Distribution Statement
Siliceous River Gravel, Concrete, Delamination, Spalling, Fracture Toughness, Bond Strength, Interfacial Transition Zones, Design of Experiment, Delamination Prediction and Detection	No restrictions. This document is available to the public through NTIS: National Technical Information Service Springfield, Virginia 22161 http://www.ntis.gov

19. Security Classif. (of this report)	20. Security Classif. (of this page)	21. No. of Pages	22. Price
Unclassified	Unclassified	298	

BEST PRACTICES FOR THE USE OF SILICEOUS RIVER GRAVEL IN CONCRETE PAVING

by

Juanyu Liu
Graduate Assistant Researcher
Texas Transportation Institute

Anal K. Mukhopadhyay
Associate Research Scientist
Texas Transportation Institute

Manuel Celaya
Research Specialist
Center for Transportation Infrastructure Systems
The University of Texas at El Paso

Soheil Nazarian
Professor of Civil Engineering
Director
Center for Transportation Infrastructure Systems
The University of Texas at El Paso

and

Dan G. Zollinger
Associate Research Engineer
Texas Transportation Institute

Report 0-4826-1
Project 0-4826
Project Title: Use of Crushed Gravel in Concrete Paving

Performed in cooperation with the
Texas Department of Transportation
and the
Federal Highway Administration

December 2006
Published: February 2009

TEXAS TRANSPORTATION INSTITUTE
The Texas A&M University System
College Station, Texas 77843-3135

DISCLAIMER

The contents of this report reflect the views of the authors, who are responsible for the facts and the accuracy of the data presented herein. The contents do not necessarily reflect the official view or policies of the Texas Department of Transportation (TxDOT) and/or the Federal Highway Administration (FHWA). This report does not constitute a standard, specification, or regulation. The engineer in charge of the project was Dan G. Zollinger, Texas P.E. #67129.

ACKNOWLEDGMENTS

The authors wish to express their appreciation to the Texas Department of Transportation personnel for their support throughout this project, as well as the Federal Highway Administration. We would also like to thank the project directors Elizabeth (Lisa) Lukefahr, and the members of the project monitoring committee, Charles Gaskin, German Claros, and Quincy Allen for their valuable technical comments during this project.

TABLE OF CONTENTS

Page

TABLE OF CONTENTS (Continued)

Page

LIST OF FIGURES

Figure **Page**

LIST OF FIGURES (Continued)

Figure **Page**

LIST OF FIGURES (Continued)

Figure **Page**

LIST OF FIGURES (Continued)

Figure **Page**

LIST OF FIGURES (Continued)

Figure **Page**

LIST OF FIGURES (Continued)

Figure **Page**

LIST OF TABLES

CHAPTER I
PROJECT BACKGROUND

INTRODUCTION

Spalling is a very common distress type in siliceous river gravel (SRG) continuously reinforced concrete (CRC) pavements along transverse cracks. It refers to the dislodging of concrete segments (>½" in depth) along a joint or crack in a concrete slab within 0.6 m (2 ft) of a joint or crack (SHRP 1993). Due to the depth of the distress, spalling does affect the quality of the pavement smoothness and ride quality, and has been very expensive to maintain and repair. Early age delamination, a necessary precursor of spall damage, is typically oriented parallel to and at a shallow depth (½" or greater) below the surface of the pavement, developing often within days after paving (Zollinger et al. 2004). This failure plane, horizontally oriented near the pavement surface and in the vicinity of transverse cracks or joints, can lead to spalling by fatigue primarily due to repetitive traffic loads passing over the delaminated area. Spalling distress should be distinguished from 'flaking' or 'chipping' along the edges of a crack. Although chipping may be categorized as spalling it represents, at best, a very low severity level that rarely becomes a matter for repair or maintenance.

In Texas, gravel aggregates have been extensively used particularly in the Houston District for CRC pavement construction for many years; however, some of these pavements in many instances have been subjected to debonding, early age delamination, and eventual spalling damages.

A series of studies funded by TxDOT since the early 1990s had been conducted to gain a better understanding of mechanisms, material properties, and construction practices, and to provide guidelines and recommendations for minimizing early age delamination in concrete pavements made with gravel aggregates. Several questions related to early age delamination and eventual spalling failure in gravel concrete pavements still remained unresolved. Can gravel aggregates continue to be used? How does one evaluate an aggregate source for spall performance? Accordingly, how would

one formulate a mixture design? Occurrences of delamination need to be investigated through microstructural characterization of interfacial transition zones (ITZ) in paving concretes. Is it possible to use this evaluation and predict the conditions and measures to prevent delamination occurrence? Accordingly, this project focuses on answering these questions and providing guidelines and recommendations for using gravel aggregates in concrete paving.

PROJECT RESEARCH OBJECTIVES

The objective of this project is to develop a mechanistic understanding of the delamination process and provide recommendations to minimize early age delamination for using gravel aggregates in concrete paving, which will address:

- development of a test protocol to measure the bond strength between aggregates and cement mortar,
- evaluation of the effectiveness of corrective measures to minimize the potential for delamination and optimization of material design,
- investigation of the effects of aggregate characteristics on the bonding performance of concrete,
- development of early age delamination detection in the field, and
- approach development for predicting delamination occurrence

PROJECT WORK PLAN

To meet the objective of this project, the research team conducted the following major tasks.

Task 1: Literature Review

A comprehensive literature review was conducted to gather relevant key information pertaining to ITZ, current representations and measurements of interfacial bond between aggregates and mortar, the effects of concrete mixture proportions (i.e.,

various aggregate and non-aggregate factors), method of construction and method of curing on bonding strength of concrete, and previous efforts to improve bond strength. The bonding mechanism and details of delamination and spalling modeling were reviewed. Findings from the literature review under this task are presented in Chapter II.

Task 2: Experimental Design and Laboratory Testing

Based on a previous study (Zollinger et al. 1993), fracture toughness of concrete is used to represent the bond strength between aggregate and mortar. A test method developed by the Texas Transportation Institute (TTI) using a modified split tensile specimen based on size effect law (SEL) (Tang et al. 1999) is used to determine fracture toughness and process zone length.

Various possible corrective measures (related to construction practice as well as mix design) to improve the interfacial bonding between aggregate and mortar were investigated in the laboratory, to identify the most effective corrective measures including application of different aggregate types, lowering of the water-cement ratio, improvement of curing, and application of ultra-fine fly ash among others.

An orthogonal-array based fractional factorial design (Taguchi et al. 1993) involving the possible corrective measures was used to evaluate the effects of various factors on the bonding strength. Compressive strength and fracture toughness testing at different ages were conducted for each test run corresponding to the fractional factorial design. The test data were analyzed by MINITAB statistical software (Mathews 2004) to evaluate the significances of each factor to achieve better fracture toughness performance. The optimum combination was subsequently chosen and validated in further laboratory testing. The detailed work under this task is presented in Chapter III.

Task 3: Aggregate Properties Characterization and Application of Utility Theory

The aggregate properties investigated under this task include physical, geometric, and chemical properties. Physical properties investigated include aggregate gradation, oven-dry bulk specific gravity (BSG-od) and dry rodded unit weight (DRUW), and

absorption capacity (AC). The aggregate shape and texture characteristics were analyzed using the Aggregate Imaging System (AIMS) available at TTI and are considered as geometric properties. The effects of aggregate physical and geometric properties on mechanical interlocking in bonding were investigated in details.

The mineralogy in conjunction with surface free energy is considered as aggregate chemical properties. The Universal Sorption Device (USD) was used to determine the surface energy of aggregates. This method utilizes a vacuum gravimetric static sorption technique that identifies gas adsorption characteristics of selected solvents with known surface free energy components to indirectly determine the surface energies of the aggregate (Cheng 2002).

Utility theory (Ledbetter et al. 1977) facilitates a way to compare dissimilar things based on their values and utilities, and can be used to synthesize and account for a variety of factors that play a role to varying degrees in engineering processes. A rating system based on utility theory was applied to evaluate the overall contribution of aggregate properties on concrete bonding. Chapter III provides the detailed description and results of this task.

Task 4: Approach for Predicting the Delamination Occurrence through Stress Analysis Approach

Stress intensity and fracture toughness are key fracture mechanics parameters that can be used by materials engineers and designers in design analysis (Boresi et al. 1993; Irwin 1958; Irwin 1957; Hertzberg 1976). Within the scope of linear elastic fracture mechanics, the stress field at the crack tip is determined by the stress intensity factors (K_I). Therefore, by comparing K_I and fracture toughness (K_{IC}) (a measure of bond strength), one can then determine the crack stability of the material under given loading conditions. The K_{IC} value at early ages of concrete has been used to represent the nature of the interfacial bond between aggregate and mortar relative to the delamination. Therefore, it appears to be feasible to predict the occurrence of delamination by comparing the development of K_I and K_{IC}. In this manner, it can also

be used for evaluating the effectiveness of pavement design methods to prevent delamination and spalling problems.

Until now, many methods have been adopted to compute K_I, such as finite element method, boundary element method, and finite difference method, etc. Among these, finite element method is the most popular tool. In this project, finite element software packages—Temperature and Moisture Analysis of Curing Concrete ($TMAC^2$) (Jeong 2003) and ABAQUS (ABAQUS 2003) were applied to predict the development of K_I. Though temperature variation is also a factor in the delamination development, this project specifically focuses on early age concrete behavior associated with volumetric contraction due to moisture induced shrinkage. Therefore, a coupled hygro-mechanical stress analysis is numerically carried out using typical concrete pavement examples. The K_I at an early age is investigated by incorporating distribution and history of moisture relative to the material-related moisture transport property in the analysis. The correlation to the development of delamination was then evaluated by comparing the K_I against K_{IC} developed under lab investigation through examples with different design factors. The work in this task is presented in Chapter IV.

Task 5: Development of Non-destructive Delamination Detection Protocol

Under this task, it was planned to develop a delamination detection protocol using Echo impact (lamb-wave scanning) and ground penetrating radar (GPR) technologies to monitor delamination in the field Portland Cement Concrete (PCC) slabs through a two-phase investigation. The first phase involves optimizing the operating and measuring parameters for both echo impact and GPR to detect delamination, and the second phase involves field application of the developed detection protocol where delamination/spalling is a prominent distress feature. The main purpose behind developing a detection protocol through the above two-phase investigation was non-destructive monitoring of delamination in a new test section. The detailed work under this task is presented in Chapter V.

Task 6: Test Sections Validation and Guideline Framework Development

The laboratory work and numerical analysis conducted in the previous tasks reveal important information on curing and climatic conditions, mixture design, aggregate combinations, time of placement, and method of early age crack (relative to delamination) control to provide sufficient guidance to establish test sections. A total of 20 gravel test sections were constructed in the Houston District in order to validate the laboratory findings. Because weather conditions during placement is one of the most significant factors affecting early age CRC performance, 10 test sections on SH 288 (approximately 3 miles south of Beltway 8) were constructed in fall (November 2005) and the other 10 test sections on SH 35 in West Columbia were constructed in spring (late April 2006).

Field data have been collected through various techniques available at TTI, TxDOT, University of Texas at El Paso (UTEP), and the Center of Transportation Research (CTR). Weather data, concrete temperature and relative humidity profiles, and drying shrinkage development in the above test sections were monitored for the first 5 to 6 days, whereas pavement crack surveys were conducted to monitor the crack development pattern for more than a month. Bonding strength corresponding to each test section under field conditions was measured by fracture toughness testing. Monitoring of delamination development (if any) through Nondestructive Testing (NDT) technique was conducted periodically. The probability of delamination was predicted based on the relationship between calculated stress and measured strength. The delamination prediction was validated by both NDT techniques and visual observation of concrete cores taken from the test sections.

Upon completion of experimental data analysis, numerical simulation and modeling, and field testing and validation, the results were synthesized. A step-by-step process of selecting both construction practices and mix design parameters through the inclusion of aggregate rating, delamination probability, and recommendations relative to method of construction for using gravel aggregates in concrete paving is provided. Chapter VI describes the detailed results under this task.

A step by step procedure with example for the guidelines development is presented in Chapter VII. The conclusions and recommendations are presented in Chapter VIII.

CHAPTER II
LITERATURE REVIEW

A comprehensive literature review was conducted to gather relevant key information pertaining to:

- interfacial transition zone;
- measurements of interfacial bond between aggregates and mortar;
- the effects of concrete mixture proportions (i.e., various aggregate and non-aggregate factors), method of construction, and method of curing on bonding strength of concrete; and
- bonding mechanism and details of delamination and spalling modeling. Findings from the literature review are described as follows.

DELAMINATION MECHANISM

As shown in Figure 2.1 (a) (Soares and Zollinger 1998), spalling refers to the breakdown or dislodging of concrete segments along a joint or crack in a concrete slab within 0.6 m (2 ft) of a joint or crack (SHRP 1993, Senadheera and Zollinger 1996) that can affect the structural slab integrity. A significant contributor to spalling is the existence of shallow, horizontal delaminations that are oriented parallel to and at a shallow depth below the surface of the pavement (Figure 2.1 [b]). As shown in Figure 2.2, water starts to evaporate from inside concrete to the air during and after placement of paving concrete. The rate of evaporation is much faster at the top part (1 to 2 inch) of the pavement than that at the inner part and leading to a non-uniform distribution of relative humidity (i.e., a moisture gradient). The development of an evaporation induced moisture gradient is a function of the ambient weather and curing conditions during and after placement of the concrete. If the moisture gradient is very prominent due to high evaporation, it can create a horizontal shear stress differential due to differential drying shrinkage, which can lead to the development of shallow level delamination (a horizontal failure plane near the surface). Presence of delamination in

the vicinity of transverse cracks or joints can eventually lead to the development of spall damage due to repeated traffic loading or any number of mechanisms causing in-plane compressive stress in the delaminated segments.

(a) Spalling damage (b) Delamination

Figure 2.1. Spalling and Delamination.

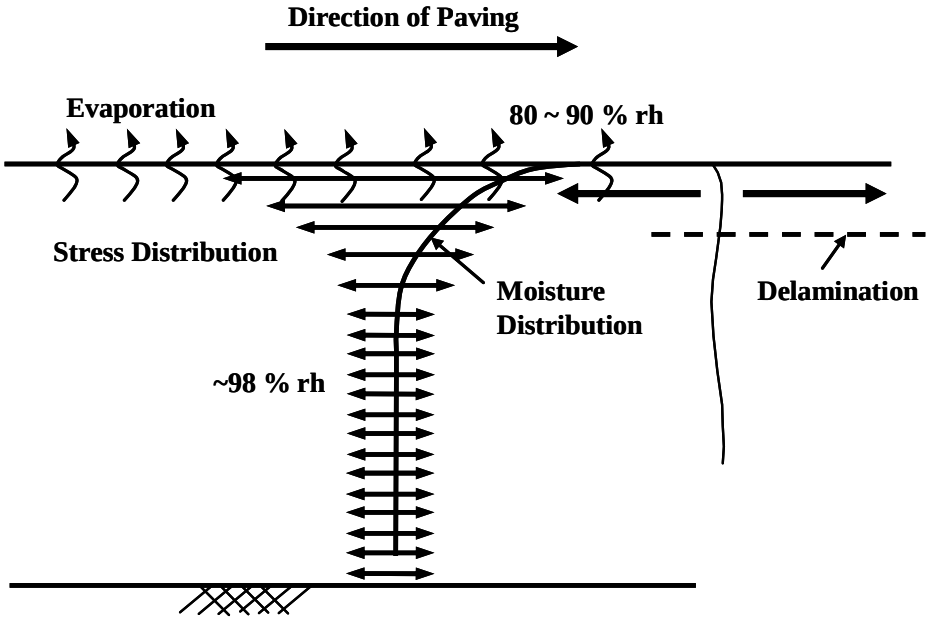

Figure 2.2. Formation of Horizontal Delamination.

Early age delamination occurs when shear stresses caused by the moisture variation surpass the concrete shear strength. A design framework for delamination formation and subsequent spalling development was introduced by Soares and Zollinger (1998), where they considered stresses due to moisture variation within the scope of the formation of delamination fracture, and determined shear stress relative to delamination from stress functions derived from median-thick plate theory in a fashion similar to that shown by Westergaard (1927) and Tang et al. (1993).

Conditions necessary for formation of delamination include low interfacial strength between the aggregate and mortar and sufficient evaporation of pore water from the hydrating concrete, resulting in differential drying shrinkage near the pavement surface (Wang and Zollinger 2000). In concrete mixtures made with siliceous river gravel coarse aggregates, a greater tendency exists to cause early age delamination and eventual spalling. A better understanding of the role of aggregate types, aggregate-mortar bond characteristics, and the tendency of concrete to allow water to evaporate during curing in developing delamination is the key to having better control over spall distress.

INTERFACIAL BOND BETWEEN AGGREGATE AND MORTAR

The interfacial transition zone in concrete refers to the region surrounding a reinforcing phase as exists in concrete as "*aureole de transition,*" derived originally from optical microscope observations made by Farran (Grandet and Ollivier 1980) many years ago. Scrivener and Pratt (1986) reported that "the relative movement of the sand and cement grains during mixing, and possibly settling of the aggregates before the cement paste sets, may lead to regions of low paste density around grains and to areas of localized bleeding at the aggregate-cement interface in which large calcium hydroxide ($Ca(OH)_2$) crystals precipitate." The interface regions are, in general, much different from the bulk cement paste in terms of morphology and orientation of the hydrating phases, and porosity. At least in part due to bleeding referred to earlier, the interface

region between aggregate and cement paste is more porous than bulk paste, leading to lower densities (Figure 2.3).

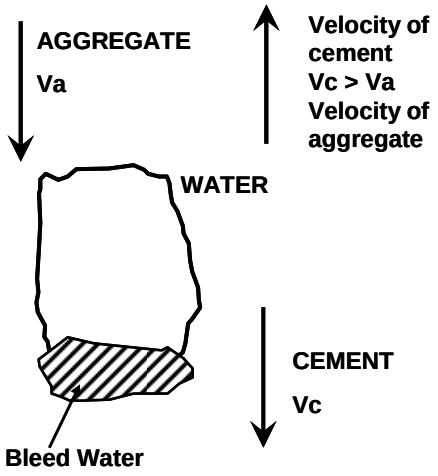

(a) Accumulation of Bleed Water

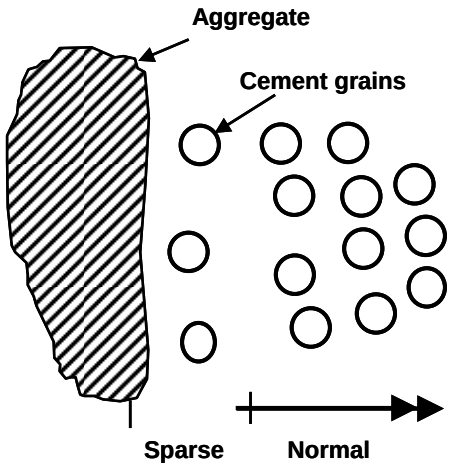

(b) Wall Effect

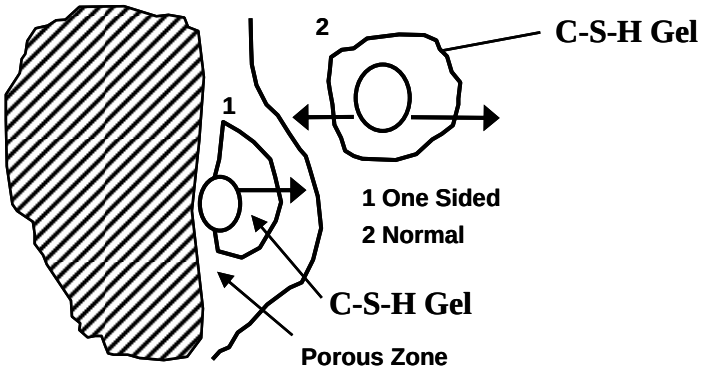

(c) One Sided Growth of C-S-H Gel

Figure 2.3. Factors Leading to Porous Aggregate-Hydrated Cement Paste (HCP) Interface (Subramanian 1999).

The major ITZ models in the literature come from Grandet and Ollivier (1980), Monteiro et al. (1985), and Zimbelmann (1985), as shown in Figure 2.4. These models differ primarily in the presence of a C-S-H film, preferential orientation of the $Ca(OH)_2$ crystals at the interface (either horizontal or vertical), epitaxial development of $Ca(OH)_2$ crystals within the transition zone, and the presence of ettringite in direct contact with the aggregate. The fracture path often runs along the cleavage planes of oriented $Ca(OH)_2$ crystals. Mehta and Monteiro (1988) stated that "in mature pastes, the fracture surface generally contains unusually large areas of calcium hydroxide crystals." Due to the large crystal size and, therefore, a small surface area, the inter-particle bonding forces between calcium hydroxide crystals or between other particles and calcium hydroxide crystals in the cement paste are weak.

Extensive studies have been done on the microstructure of cement paste/aggregate interfacial zone by using scanning electron microscopy (SEM), x-ray diffraction (XRD), and mercury intrusion porosimetry (MIP) techniques (Scrivener and Gartner 1988, Nehdi and Mindess 1997, Zhang et al. 1996, Winslow et al. 1994). Many studies (Scrivener and Pratt 1986, Monteiro et al. 1985, Scrivener and Gartner 1988, Larbi and Bijen 1990, Monteiro and Ostertag 1989) reported that the thickness of the interfacial region is approximately 40 to 50 μm, with the major difference in characteristics from the bulk paste occurring within the first 20 μm from the physical interface. The weakest part of the interface of this interfacial zone lies not right at the physical interface, but 5 to 10 μm away from it within the paste fraction. Microscopic examination of polished concrete surfaces revealed that the mean spacing between the aggregate particles is only about 75 to 100 μm. Even though the variability of this spacing is large, it suggests that with an interfacial zone thickness of approximately 50 μm, most of the HCP lies within the interfacial zone and only a small volume of bulk HCP exists. This indicates that the representation of the actual concrete in the models is far from satisfactory.

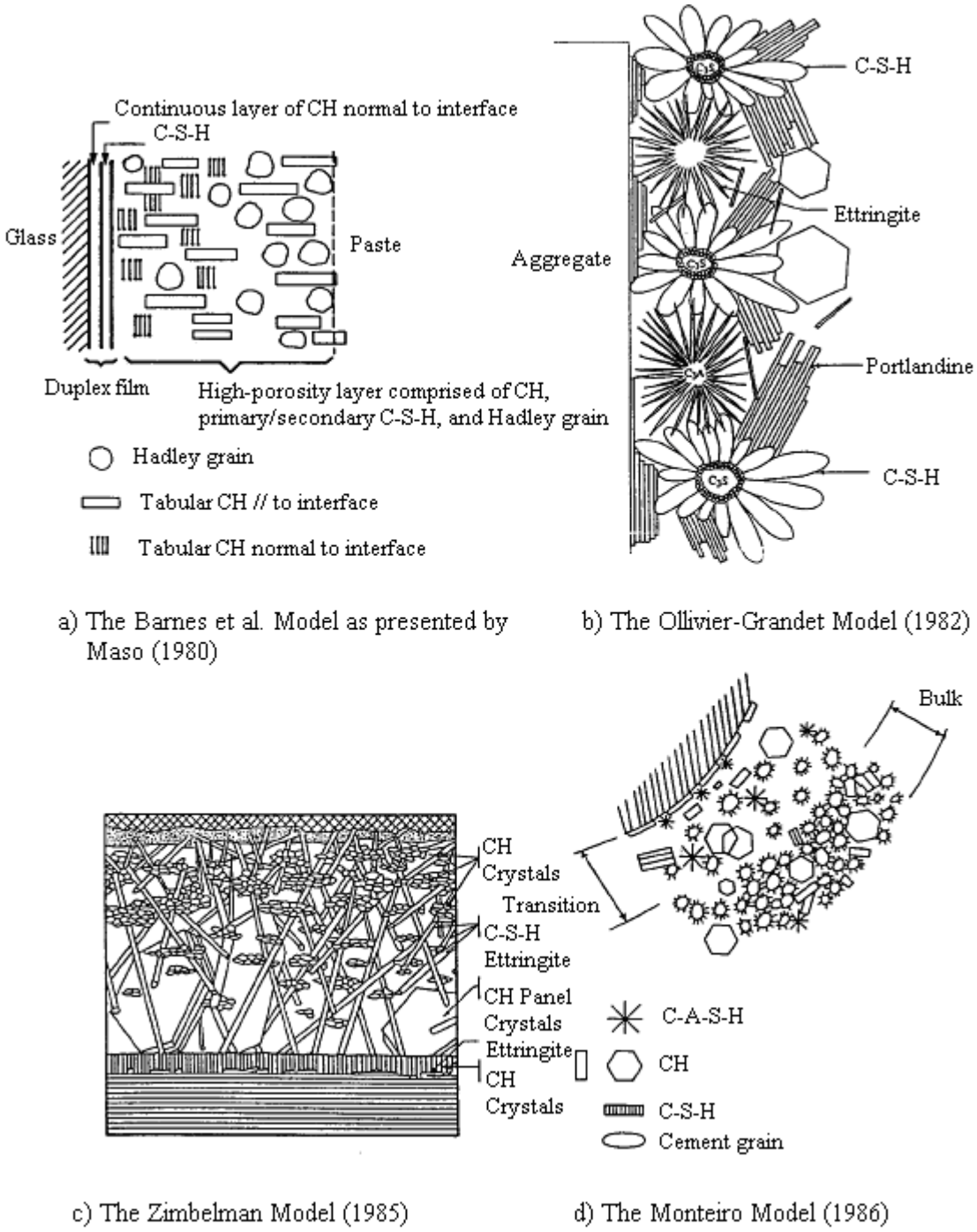

Figure 2.4. Various Models of ITZ.

Interfacial Bond Strength Testing

There are no standard test methods to measure or quantify strength of the interfacial zone. Some of the indirect methods of measuring bond are:

- "push-out" test, in which cement mortar is cast against an aggregate prism and the interface is tested in shear;
- modified indirect tensile test, in which a predetermined notch is cast, the specimen is tested in the indirect mode, and the fracture face is analyzed; and
- volumetric surface texture analysis (VST), through this test process the micro- and macro-texture of the fracture face can be analyzed and also the crack path can be determined.

As shown in Figure 2.5, 11 of the techniques that have been used for measuring aggregate-mortar bond strength were summarized by Alexander et al. (1965), such as mid-point and one-third-point transverse tests; cantilever methods; conventional, centrifugal, and indirect tensile tests; and axial compression tests on shear bond specimens.

Akçaoğlu et al. (2002) investigated the influence of surface, rigidity, and size of aggregates and w/cm of the matrix on bond strength at the ITZ. They have also investigated the bond-matrix failure process through testing of mortar cube specimens inserted with a single spherical steel aggregate into the center of the specimens under uniaxial compression where tensile strength loss after the application of 40 percent, 60 percent, and 80 percent of compressive strength were used to represent the interfacial bond strength.

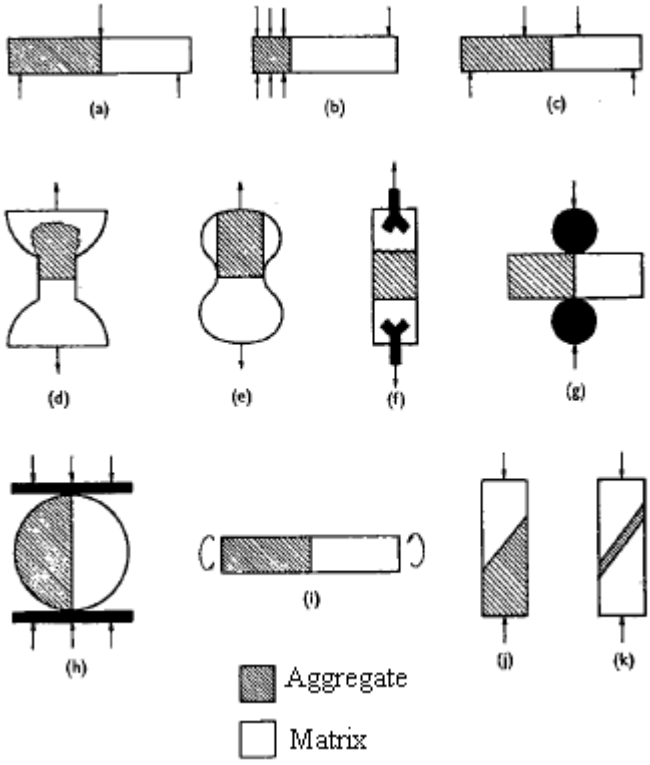

Figure 2.5. Techniques Used for Measuring Aggregate-Cement Bond Strength.

No current strength theory has been applied directly to the interface between aggregate and cement paste due to the complexity of the microstructure. As a first approximation, Ping and Beaudoin (1992) built a relationship between interfacial bond strength and electrical conductivity of the transition zone, considering interfacial bond strength is directly proportional to the total area fraction of solid phases associated with fracture surface in the transition zone. The interfacial bond strength is linearly related to the electrical conductivity of the transition zone. Bond strength for the non-porous aggregate-portland cement paste system is proportional to the negative thickness ratio of the water layer and transition zone and inversely proportional to the w/cm ratio.

The emerging technology with fractal analysis may pose as a considerable advance toward the development of new methods for aggregate-mortar bond, which will be better than techniques such as AASHTO T 177 Flexural Strength of Concrete (Using

Simple Beam with Center Point Loading) and AASHTO T 97 Flexural Strength of Concrete (Using Simple Beam with Third Point Loading), which have been used among others, to determine bond strength (Fowler et al. 1996).

Interfacial Microhardness

As a nondestructive method, microhardness measurement is a measure of strength of metals and nonporous materials. The test method employs the Vicker's pyramid indentor placed in a conditioned box. Hardness is calculated by the following formula (Ramachandran 1995):

$$H_v\left(Kg\ mm^{-2}\right) = \frac{1854.4 \times P}{d^2} \qquad (2.1)$$

where P = load (g), d = mean value of the indentation diagonals, and H_v = microhardness. Microhardness can be useful as a measure of strength development in cements and cement minerals hydrated for different lengths of time.

As a measure of specific surface energy, the hardness of materials has very close relation with mechanical properties of materials. Microhardness testing provides a tool for quantifying microstructural gradients across the ITZ. Microhardness measurements can contribute to characterization of the properties of the ITZ relative to the bulk cement paste matrix and also provide one means of estimating the width of the ITZ. Where the ITZ microstructure is weaker than the bulk region, a depression in the microhardness profile is expected within the zone of influence of the aggregate, the profile at the aggregate surface also being influenced by the strength of the paste-aggregate bond (Asbridge 2002).

The relation between the fracture behavior and microhardness makes it possible to predict the fracture parameters from microhardness measurements (Beaudoin 1982). Tamimi (1994) applied both minimum and maximum microhardness of cement paste-aggregate interface to represent the interfacial bond.

Fracture Parameters

Through microstructural studies, Prokopski (1991) stated that it is the transition zone, and specifically, the aggregate-cement paste interface, where the greatest number of defects occur, and that the concrete failure process commences at the transition zone. Therefore, it is reasonable to utilize the methods of fracture mechanics to relate the fracture parameters to the structural defects (primary cracks). Fracture toughness (or critical stress intensity factor) was commonly used to represent the interfacial bond, because it can be used as a criterion to evaluate concrete quality (Prokopski and Langier 2000), and it can describe the sensitivity of coarse aggregate characteristics to the aggregate-mortar interfacial bond (Senadheera and Zollinger 1996).

A number of studies on the interface fracture mechanics of biomaterial systems have been made (Rice 1988; Hutchinson 1990). Fracture of a biomaterial interface can be expressed in terms of two parameters, an energy release rate, G, and a phase angle, ψ. Interface cracking occurs when G reaches a critical value, defined as the interface fracture energy, Γ_i (Büyüköztürk and Lee 1993). A micromechanical model (Mohamed and Hansen 1999) was developed based on the numerical simulation to investigate the crack-aggregate interaction in concrete materials, and the results showed that the tensile strength ratio, fracture energy ratio, and the moduli ratio between the aggregate and the matrix play the dominant role in determining the crack penetration condition.

Pye and Beaudoin (1992) proposed an energy approach to bond strength determination in cement systems, and they stated that interface fracture energy is a more appropriate descriptor of the quality of the cement paste-substrate bond due to the progressive failure of the bond. In the study conducted by Tan et al. (1995), Tschegg's wedge splitting test (Tschegg et al. 1995), already used for testing of concrete and asphalt, had been slightly modified for testing the fracture behavior of sandstone-matrix and limestone-matrix interfaces. Their results showed that the specific fracture energies of sandstone-mortar and limestone-mortar interfaces were much lower than for bulk mortar. Wong et al. (1999) investigated the mortar-aggregate interfaces from both the three-point bending test of notched beams with mortar-aggregate interface above the

notch and splitting tensile test on mortar-aggregate interface cubes. The parameters studied included:

- interfacial flexural strength,
- interfacial fracture energy,
- interfacial fracture toughness, and
- interfacial splitting tensile strength.

The interfacial fracture toughness (K^{if}) was determined based on the theory of interface fracture mechanics for bi-materials, which has the complex form of $K^{if} = K_1^{if} + K_2^{if}$, where the two components $K_1{}^{if}$ and $K_2{}^{if}$ denote the normal stress intensity and the shear stress intensity, respectively. The magnitude of the shear stress intensity is much smaller than that of the normal stress intensity, which indicates that the fracture of the interface between the cement mortars and the aggregates can be approximately considered as the Mode I fracture (tension mode of fracture), and thus, the values of $K_1{}^{if}$ are comparable with the toughness of mortar (K_{IC}^{m}). The values of $K_1{}^{if}$ were about one-third of the values of K_{IC}^{m}, which is correlated with results of Saito and Kawamura's (1986). The interfacial fracture energy (G_F^{if}) was only about 10 percent of the corresponding mortar fracture energy (G_F^m). This is consistent with the results obtained from the aggregate push-out test (Mitsui et al. 1994) and the wedge splitting test (Tschegg et al. 1995). The ratio G_F^{if} / G_F^m was much smaller than the ratio $K_1{}^{if} / K_{IC}^{m}$, indicating the fact that fracture energy and fracture toughness reflect different aspects of the interfacial failure.

Factors Affecting Aggregate-Mortar Interfacial Bond

The influencing factors of aggregate-paste interfacial bond can be broadly subdivided into two categories, i.e., aggregate and non-aggregate factors, which are discussed below.

Aggregate-related Factors

The bond between the concrete mortar and aggregate results from some combination of mechanical interlocking between cement hydration products and the aggregate surface, and a chemical bonding resulting from a reaction between aggregate and cement paste (Struble et al.1980). The nature of the interfacial zone depends on the microstructure characteristics of the aggregate, in which any of the three mechanisms, physical interaction, physical-chemical interaction, and mechanical interlock, may be dominant (Zhang and Gjorv 1990). All three physical, geometric, and chemical properties of coarse aggregate are influential interfacial bond-related aggregate factors and vary significantly with aggregate types (Senadheera and Zollinger 1996, Zimbelmann 1985, Perry and Gillot 1977, Prokopsi and Halbiniak 2000).

The effects of aggregate type and size are important parameters in the formation of ITZ structure and subsequently in the failure process of concrete. Porous aggregates provide an excellent bond because their high absorption characteristics minimize the water accumulation at the interfaces and also improve the contact area between the paste and the aggregate. The failure surfaces of the concrete made with larger size coarse aggregate show significant traces of pulling out of the aggregate from the matrix. Liu et al. (2006) summarized the reasons why larger aggregate size can have a detrimental effect on the interfacial bonding:

- For a given volume of coarse aggregate, a larger maximum size reduces the specific surface area of aggregate.
- An increased stress concentration and microcracks in the vicinity of the aggregate are expected with decreased surface area.

- Larger aggregate particles tend to accumulate more bleed water around it, which could lead to a higher local w/cm and, subsequently, a higher porosity in the ITZ than the ITZ around the smaller aggregates (Elsharief et al. 2003).
- The effect of aggregate size on the weakness of ITZ and the failure process of concrete with low w/cm ratio is of paramount importance (Akçaoğlu et al. 2002). With larger aggregates, low w/cm ratio matrices result in more critical ITZs with a more condensed microcrack cloud in a narrower region (higher tensile stress distribution). Increasing aggregate size leads to lowering bond strength.

Indirect evidence of the bonding mechanisms due to mechanical interlocking aided by the aggregate surface texture has been established (Alexander et al. 1965, Hsu and Slate 1963) by comparing the bond strength of fractured rock surfaces with that of polished rock surfaces. Aggregate shape characteristics affect the proportioning of portland cement concrete mixtures, the rheological properties of the mixtures, aggregate-mortar bond, and the interlocking strength of the concrete joint/crack (Al-Rousan 2004). Previous studies (Mindness et al. 2002, Kosmatka et al. 2002, Will 2000, Fowler et al. 1996) indicated that the bond strength between the cement paste and a given coarse aggregate generally increases as particles change from smooth and rounded to rough and angular. Rough, textured surfaces will improve the mechanical component of the bond by increasing the amount of surface area available for bonding with the paste for a given aggregate content. The surface roughness of the aggregate shows significant influence on the fracture toughness of the interface and the bond strength of the interface (Alexander 1993, Rao and Prasad 2002). A study conducted by Trende and Büyüköztürk (1998) showed that for a given type of loading conditions the critical interface fracture energy release rate, G_i, increases with rougher aggregate surfaces for both Mode I and mixed-mode tractions. The interlocking of angular particles results in a strong aggregate skeleton under applied loads, whereas round particles tend to slide by or roll over each other, resulting in an unsuitable and weaker structure. Using a high percentage of flat and elongated particles might cause problems

when placing the concrete, which will result in voids and incomplete consolidation of the mix, and thus contribute to spalling. In addition, it may cause a high internal stress concentration that leads to easier bond failure (Meininger 1998).

Alexander et al. (1965) reported that bond strength varied widely according to the rock type and surface roughness of the aggregate, with the strengths varying by a factor of as much as 2 between different aggregates. Variation in bond strength could alternatively be explained by different roughness factors of different aggregates. However, regardless of whether the bond is primarily due to either mechanical interlocking or chemical reaction, the true surface area of the aggregate available for bonding is an important aspect of bonding. The true surface area entails the size, shape, and surface texture of aggregate particles.

Chemical bonds form as a result of chemical interaction between the hydrated cement compounds and the constituent minerals of the aggregate. Farran (1956) first concluded that the bond strength was due to a combination of chemical reactions between aggregate and cement paste, and epitaxial growth of $Ca(OH)_2$ on the aggregate surface. Langton and Roy (1980) explored the difference in morphology of the transition zone present near reactive and nonreactive aggregates. Mehta and Monteiro (1988) concluded that the transition zone around limestone aggregate is strengthened while the transition zone around quartz aggregate does not show signs of strength increase. Senadheera and Zollinger (1996) also stated that carbonate aggregates produce higher bond strengths than silicate aggregates. These studies were mainly based on strength data of $\geq$ 28 days. However, a reduction in bond strength between aggregate made of veins of recrystallized calcite with poorly crystalline silica and paste at early ages (1 to 3 days) was observed in the study conducted by Tasong et al. (1999). It was explained that formation of porous ITZ as a result of chemical reaction between pore solution and aggregate was responsible for bond strength reduction at early ages. However, at later ages ($\geq$ 28 days), filling of this porosity with later reaction products resulted in an increase in bond strength.

Non-aggregate Factors

Non-aggregate factors discussed here include w/cm, mineral and chemical admixtures, and processing methods.

Water/Cementitious Ratio (w/cm). Numerous studies (Simeonov and Ahmad 1995, Zimbelmann 1985) have indicated that the w/cm is a predominant influencing factor of aggregate-mortar interfacial bond. The porosity of the transition zone, its thickness and properties, and the quality of the matrix are all closely related to w/cm. An increased porosity has been found to occur in the area of the aggregate-cement paste interface caused by the higher w/cm in this region with a simultaneous decrease in w/cm in the bulk of the matrix (Brandt 1995), while reducing w/cm from 0.55 to 0.40 resulted in an ITZ with characteristics that were not distinguishable from those of the bulk paste as demonstrated by backscattered electron (BSE) images (Elsharief et al. 2003). Yuan and Gud (1998) reported that the local increase in w/cm in the area of the aggregate-cement paste interface is proportional to the amount of free unbound water, and any action increasing the contents of the solid phase reduces the effect of the transition zone on the strength properties of concrete. Simenov and Ahmad (1995) also pointed out that reduction in w/cm ratio makes this critical ITZ region narrower. However, according to Bentz et al.'s research (1992), w/cm has little effect on the transition zone thickness, while substantially influencing its porosity.

Prokopski and Langier (2000) conducted the fracture toughness investigations for concretes made from natural gravel aggregate, with various w/cms, without silica fume and with silica fume addition. The largest values of the critical stress intensity factor were shown by concretes with the lowest w/cm (both with and without silica fume addition). This was caused by considerably lower porosity of the aggregate-cement paste transition zone as observed in microstructural examinations, which had in this case a compact structure with a small number of structural defects. As the w/cm increased, an increase in the structural porosity of the aggregate-cement paste transition zone occurred, which caused a promoted propagation of cracks and resulted in lower values of

stress intensity factor. For concretes with the lowest w/cm, the forces of adhesion of the aggregate to the cement paste were high (higher than the strength of gravel grains), which resulted in the propagation of cracks through the coarse aggregates and the formation of flat-fracture surface. In the case of concretes with a large w/cm, the aggregate-cement paste transition zone was highly porous and weak, which resulted in the development of a crack in this zone; the so-called overgrain fractures, highly irregular and rough. The microstructural examinations (Prokopski et al. 1997) showed that the aggregate-cement paste transition zone in concrete from gravel aggregate with a low w/cm (concrete without silica fume addition) and both with a low w/cm and a silica fume addition was uniform and dense, with only a small number of structural discontinuities. A transgranular character of fracture was observed in this case, with its cracks going through the aggregate particles, which caused the formation of a flat-fracture surface. The strength of the aggregate-cement paste interface was in this case higher than the strength of gravel aggregates, which resulted in the highest values of fracture toughness.

Mineral and Chemical Admixtures. Extensive studies have also been done on use of mineral admixtures in concrete and their effects on the microstructure of ITZ (Goldman and Bentur 1992, Bentur and Cohen 1987, Charles-Gibergues et al. 1982). Mineral admixtures influence the development of the microstructure in the interfacial zone because of two main factors:

- a densification due to pore filling mechanism by the mineral admixture particles if the size of the additions is much finer than the size of the cement grains; and
- a modification of the hydration process-consumption of calcium hydroxide and contribution of additional C-A-S-H.

Silica fume affects the pattern of crystallization and degree of orientation of $Ca(OH)_2$ crystals at the aggregate surface, resulting in a very thin interface during the

first few days of hydration (Cheng-yi and Feldman 1985, Larbi and Bijen 1990, Toutanji et al. 1999, Wong et al. 1999). It has been identified to be able to strengthen the interfaces when used in concrete (Pope and Jennings 1992, Goldman and Bentur 1989, Rao and Prasad 2002). The interfacial bond improvement effect of such materials is due to their small particle size and pozzolanic reactivity, leading to the elimination of water film on aggregate surfaces in noncoated aggregate-cement systems, denser microstructures, and stronger interfacial bond.

Fly ash is another type of pozzolanic material widely being used as a cement replacement to produce high-performance concrete and high-volume fly ash concrete (Langley et al. 1989, Carette et al. 1993). Many researchers indicated that low-calcium fly ash (ASTM Class F) also improves the interfacial zone microstructures, although it is generally coarser and less reactive than silica fume. Mehta and Monteiro (1988) indicated that fly ash is effective in reducing the thickness of the interfacial zone and porosity in the interfacial zone after prolonged curing. Saito and Kawamura (1989) demonstrated that fly ash significantly reduced the degree of orientation of $Ca(OH)_2$ crystals and suppressed the precipitation of $Ca(OH)_2$ crystals and formation of ettringite in the interfacial zone. The research conducted by Bijen and Selst (1992) indicated that fly ash reduced not only the preferential orientation but also the quantity of $Ca(OH)_2$. Besides, Bentz and Garboczi (1991) predicted through computer simulation studies that replacing 20 percent of cement with fly ash with smaller particle size resulted in higher interfacial strength than that of the control portland cement paste. Wong et al. (1999) investigated the properties of fly ash-modified cement mortar-aggregate interface, and the results showed that a 15 percent fly ash replacement increases the interfacial bond strength and interfacial fracture toughness at the ages of 28 and 90 days. Fly ash replacements at all the levels studied result in higher interfacial fracture energy at the age of 90 days due to the pozzolanic action of fly ash. Researchers also showed the interest in the effects of chemical admixtures on the contribution of ITZ (Xu et al. 2000).

Aggregate Processing and Charging Sequence. Buch and Early (1999) stated that the use of crushed aggregates, sand-blasted aggregates, and aggregates coated with calcium hydroxide can enhance the bond strength. There is a marginal improvement in the indirect tensile strength of sand-blasted limestone concrete mixtures. The softer limestone is subjected to "roughening" under the sand blasting process and thereby improving the mortar-aggregate bond.

Sand Enveloped with Cement Concrete (SEC) was developed by Hayakawa and Itoh (1982). The procedure was basically the same as for mixing of conventional concrete, except that the water was divided into two portions and added into the mixer at two separate times. The amount of the first water addition was controlled to be 25 percent by weight of the cement to be used, including any surface moisture of the sand and gravel. The effectiveness of this two-stage mixing method in reducing the bleeding capacity and improving the interfacial bond was also evaluated by Tamimi (1994).

Methods of Improving Interfacial Bond

Based on the foregoing discussion on the factors influencing aggregate-mortar interfacial bond, the methods to improve the interfacial bond are listed below.

Reducing Water at the Interfaces

One can expect to get improved properties of the interface, simply by reducing the w/cm ratio, which is also confirmed by experimental results by Mitsui et al. (1993). When the w/cm ratio was reduced from 0.65 to 0.35, the push-out load (a measure of bond strength) was increased from 1200 N to 1600 N, and the porosity at a distance of 50 μm was reduced from 24 percent to 18 percent. A further reduction in water content near the interface can be achieved by using aggregates having slightly porous surfaces. The excess water is drawn into these pores and cement particles are also pulled toward the surface, which is known as the filter effect (Bentz et al. 1987). Another suggestion is to reduce the surface tension of water through the use of a water reducing agent or

surfactant, which ultimately reduces the thickness of the water film on the aggregate. Ping and Beaudoin (1992) indicated that the thickness of the water layer on the aggregate surface during mixing is also a principal factor affecting bond strength at the interface between nonporous aggregate and portland cement paste. As discussed earlier, SEC concrete (Hayakawa and Itoh 1982, Tamimi 1994) was developed as a concrete made by adding water at two separate times. Compared with the conventional concrete, the concrete with two-stage water addition exhibits lower bleeding and higher micro-hardness of the cement paste-aggregate interface as a result of lowering the w/cm ratio at the interface due to the "SEC" method. Therefore, modified charging sequence could be an efficient way (especially for concrete with high w/cm) other than reducing the w/c ratio alone to minimize water availability at the interfaces.

Improving Mortar Strength

Scholer (1967) suggested that the stress level for initiation of micro-level cracks in concrete is primarily a function of the mortar strength. Hence, one way to improve interfacial bond strength would be to improve the strength of the cement mortar (Buch and Early 1999). However, the measures to increase mortar strength should not affect other properties of the resulting concrete. For example, if higher cement content is used to increase mortar strength in concrete, the shrinkage strains in concrete may also increase, thereby reducing any benefit that may have been gained from increasing mortar strength.

Addition of Fine Mineral Admixtures

Addition of fine mineral admixtures (e.g., ultra-fine fly ash and silica fume) can improve the ITZ by simply a pore filling mechanism. Average size of cement particles is around 30 to 40 μm. The small particles (around 5 μm average diameter) from fine mineral admixtures will fill up the pores and densify the interface and, hence, improve the bond. Research conducted by Mitsui et al. (1993) showed that normal concrete with w/cm = 0.35 had a push-out load of 1600 N and a porosity of 18 percent. The addition

of 10 percent micro silica (w/cm = 0.35) dramatically improved the porosity characteristics to 3 percent and the push-out load to 2600 N. Rao and Prasad (2002) also presented similar results that the bond strength of concrete increases due to the pozzolanic reaction of silica fume, which improves the physical interaction at the interface.

Coating the Aggregate Faces with a Reactive Layer

Zimbelmann (1987) suggested that the bond strength of the transition zone might be improved by inducing a chemical reaction or physical interaction between the aggregate and the hydrated cement paste. By precoating the aggregate particles with cement/silica fume slurry, the push-out load was increased from 2600 N to 4200 N and the porosity at the interface transition zone was practically eliminated (Mitsui et al. 1994). In their investigation on the effect of the bond between the matrix and the aggregates on the cracking mechanism and fracture parameters of concrete, Guinea et al. (2002) demonstrated that surface treatment of bitumen and paraffin coatings makes the bond weak, whereas epoxy resin coating treatment makes the bond strong.

CHAPTER III
LABORATORY INVESTIGATION

GENERAL

As described in Chapter II, extensive research has been done previously to improve the interfacial bonding between aggregate and mortar, although most of the studies dealt with later age concrete (28 days or over) strength. Since in our project, the interfacial bonding at early age is more critical than that at later ages, various possible corrective measures to improve the early age interfacial bonding were investigated in the laboratory, and the results are presented in this chapter. A fractional factorial design (Taguchi method) based on an "orthogonal array," which allows the user to analyze many factors with a few combinations (Mason et al. 1989), was used to evaluate the effects of various key factors on the bonding strength. The experimental design and associated laboratory testing are described in this chapter. The analysis results of the Taguchi design by statistical software such as MINITAB are presented. The optimum combination is subsequently chosen and validated in further laboratory tests. An aggregate rating system created by combining all categories of aggregate properties (e.g., physical, geometrical, and mineralogical/chemical) into a single rating index through utility theory has been introduced. For all tests conducted in the laboratory, at least two samples were prepared for each setup for each K_{IC} measurement. For all tests, three replicates were conducted.

FRACTURE TOUGHNESS TO REPRESENT AGGREGATE-MORTAR INTERFACIAL BOND

As described in Chapter II, fracture parameters have been used to represent aggregate-mortar interfacial bond. Investigation of the fracture toughness of concrete has remained a major research topic for decades because of the recognition that structural behavior is controlled not only by compressive strength of concrete, but also by the independent material parameter related to fracture toughness (K_{IC}). It is indicated

from previous research that K_{IC} at early ages of concrete can be used as criteria to evaluate concrete quality, and it can describe the sensitivity of coarse aggregate characteristics relative to the aggregate-mortar bond (Zollinger et al. 1993). Therefore, in this project, K_{IC} was used to represent the interfacial bond between aggregate and mortar of a variety of coarse aggregates types and concrete mixtures.

The SEL and its generalized theory summarizes the observed size effect on the nominal strength of concrete structures. It presents a fracture model of concrete in which K_{IC} and another associated fracture parameter, process zone length (c_f), are objectives. It can be synthesized as (Tang et al. 1999):

$$\sigma_N = c_n \frac{K_{IC}}{\sqrt{g'(\alpha_0)c_f + g(\alpha_0)d}} \tag{3.1}$$

where,

σ_N = nominal strength of specimen (or structure),

c_n = arbitrarily defined constant, usually taken so as to make σ_N the maximum tensile stress in the specimen of the same type with no crack,

d = specimen size,

$g(\alpha_0)$ = $\pi c_n^2 \alpha F^2(\alpha)$,

α = geometry factor,

$F(\alpha)$ = geometry function, obtained with finite element analysis,

$g'(\alpha_0)$ = derivative of $g(\alpha)$, and

α_0 = ratio of the initial crack length ($2a_0$) to the specimen dimension d.

For specimens of a given geometry, Equation 3.1 can be converted to a linear regression:

$$Y = AX + C \tag{3.2}$$

where,

$$Y = \frac{c_n^2}{g'(\alpha_0)\sigma_N^2}$$

$$X = \frac{g(\alpha_0)}{g'(\alpha_0)} d$$

$$A = \frac{1}{K_{IC}^2} \text{ and}$$

$$C = \frac{c_f}{K_{IC}^2}$$

It is obvious that after linear regression, K_{IC} can be calculated from the regression coefficients and values of $g(\alpha_0)$ and $g'(\alpha_0)$.

The variable-notch, one-size, split-tensile test method (Tang et al. 1996) developed at TTI was based upon the above equations. This method allows for the use of specimens of the same size and shape but with different notch lengths, which provides for a great amount of convenience in specimen preparation. The various configurations illustrated in Figure 3.1 were utilized in order to enhance the accuracy of the test method relative to specimen geometry effects. For these split tensile specimens:

$$\sigma_N = \frac{P}{\pi b R} \tag{3.3}$$

where,

b = length of the cylinder,

R = radius of the cylinder = d/2, and

P = the total compressive load.

Equation 3.3 also implies that $c_n = 1/\pi$ in Equation 3.1. For the three different geometric shapes of the specimens in Figure 3.1, different $F(\alpha)$ and associated $g(\alpha)$ and

g′(α) were obtained based on finite element analysis (Tang et al. 1996). For the regular split cylinder (a and b in Figure 3.1),

$$F(\alpha) = 0.964 - 0.026\alpha + 1.472\alpha^2 - 0.256\alpha^3 \qquad (3.4)$$

and for the holed cylinder (c in Figure 3.1),

$$F(\alpha) = 2.849 - 10.451\alpha + 22.938\alpha^2 - 14.940\alpha^3 \qquad (3.5)$$

The cylindrical specimens are 6-inch in diameter (i.e., d in Equation 3.1), and 12-inch in length (i.e., b in Equation 3.3). The first specimen is notchless ($2a_0 = 0$); the second specimen contains a small notch of $2a_0 = 1$ inch; and the third specimen contains a 1-inch diameter hole with a 1.5-inch notch extending on each side of the hole, in such a way that $2a_0$ is 4 inch.

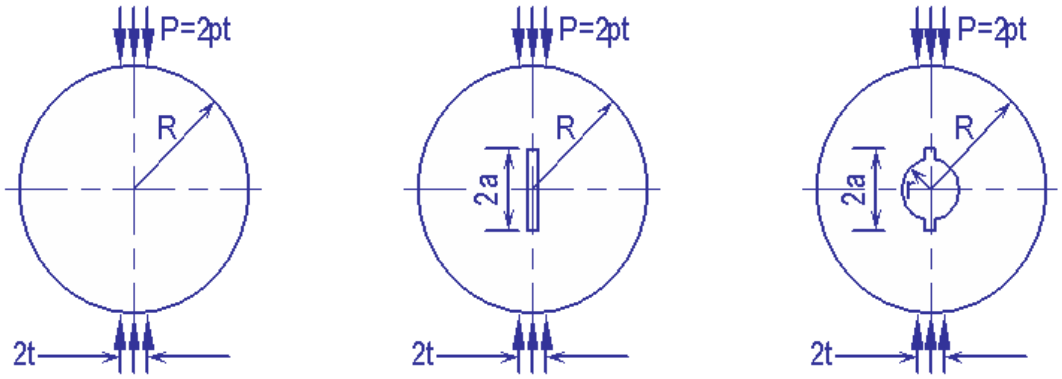

(a) Notchless (b) Notched (c) Notched with a hole

Figure 3.1. Specimen Geometries.

A spreadsheet was programmed to facilitate the above procedures. The only input necessary for the calculations is the maximum applied load for each of the three different specimens. By filling the measured maximum loads of specimens in the spreadsheet, K_{IC} is computed instantly.

Previous experience suggests that coarse aggregate type has a significant influence on concrete bond performance (Senadheera and Zollinger 1996, Shelby and McCullough 1960). Two different aggregates were chosen to conduct the preliminary tests:

- a natural gravel (Riverside Campus, College Station, Texas), and
- a limestone (Caldwell, Texas).

Table 3.1 and Figure 3.2 present physical properties and gradation of two aggregates, respectively. It can be seen that these two aggregates have similar maximum aggregate size, specific gravity, and dry-rodded unit weight but different absorption capacity (limestone is higher than natural gravel). Experiments were conducted using a common mixture proportion (6 sacks/cubic yard of cement factor, 0.75 of coarse aggregate factor, and 0.43 of water/cement ratio) and a normal indoor curing at room temperature.

Table 3.1. Physical Properties of Different Aggregates.

Aggregate Type	Gsb-od	%AC	DRUW (lb/ft^3)
Natural gravel	2.58	0.70%	101.4
Limestone	2.58	1.87%	97.5

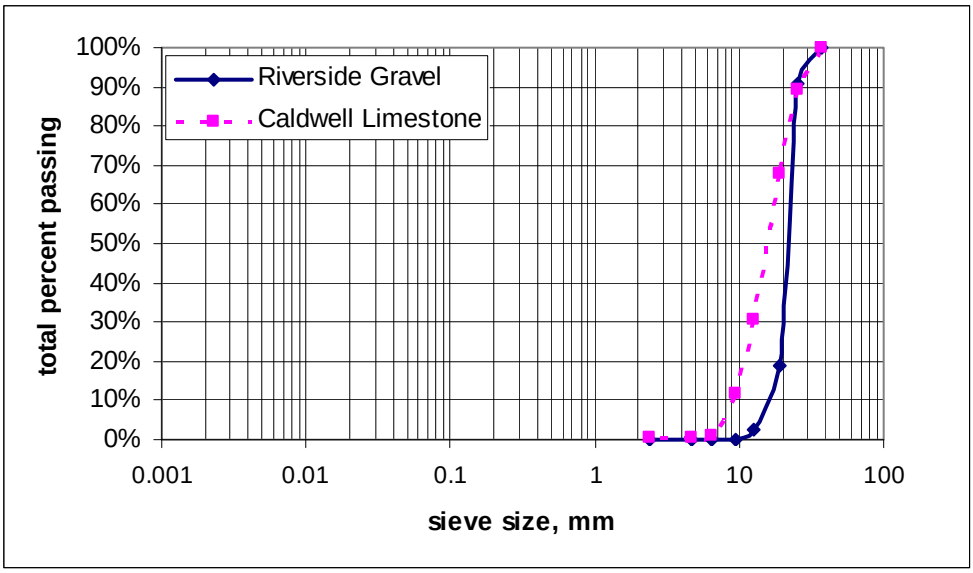

Figure 3.2. Gradation Curves for Two Aggregate Types.

Figure 3.3 shows the fracture toughness results of concretes with these two aggregates at two different ages (12 hours and 1 day). Concrete with gravel aggregate showed lower fracture toughness values than that with limestone aggregate irrespective of curing ages, which is in accordance with data that were obtained through previous research work (Gutierriz de Velasco and McCullough 1981). It is indicated that selecting the right aggregate type can benefit bonding performance of concrete. In the next chapter, a comprehensive investigation of aggregate properties will explain why different aggregate types can have different contribution to the concrete bonding capability. Therefore, the present fracture toughness test can be considered as a reasonable representation of aggregate-paste bond strength and selected as a performance evaluation test for the laboratory testing program under the present project.

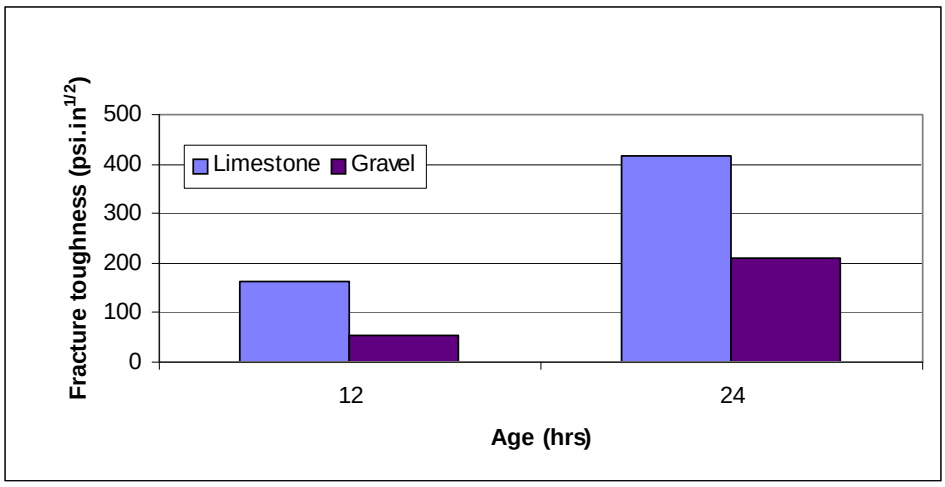

Figure 3.3. Fracture Toughness of Concretes at Different Ages.

MEASURES TO IMPROVE EARLY AGE AGGREGATE-MORTAR INTERFACIAL BOND

As mentioned in Chapter II, the bond of the aggregate-mortar interface at an early age is one of the most significant factors affecting the development of delamination, which is affected by both aggregate and non-aggregate factors. The aggregate factors believed to be pertinent to the aggregate-mortar interfacial bond include physical, chemical, and geometric properties varying significantly with aggregate type (e.g., Senadheera and Zollinger 1996, Alexander 1993, Rao and Prasad 2002, Monteiro and Mehta 1986, Tasong et al. 1998). The non-aggregate factors such as w/cm, mineral admixtures (e.g., ultra-fine fly ash), and curing method have predominant effects on aggregate-mortar bond (Senadheera and Zollinger 1996, Alexander 1993, Rao and Prasad 2002, Monteiro and Mehta 1986, Tasong et al. 1998, Goldman and Bentur 1992, Bentur and Cohen 1987, Charles-Gibergues et al. 1982, Wu et al. 1999, Wainwright and Cabrera 1990, Zollinger et al. 1994). A better understanding of those factors to the bonding performance of concrete is of great importance in order to prevent delamination and spalling distresses. Therefore, aggregate type, w/cm, ultra-fine fly ash content, and curing method were chosen as the control factors in the laboratory investigation. Crushing was considered originally as a

remedial measure to control delamination; however, the following discussion based on some selective experiments precludes that possibility. The two other factors, i.e., dense aggregate gradation and modified charging sequence, are also considered as measures to improve early age bond and are discussed in the field test sections in Chapter VI. The effect of construction-related factors (e.g., curing) can only be better studied under field conditions. Therefore, the research team has conducted a field test section program to validate the laboratory findings, which are described in the next chapter.

Crushing Treatment of Aggregates

To identify the effect of aggregate crushing in the bond strength of concrete, bond strengths of concrete with crushed and natural siliceous river gravel from Victoria, Texas, were determined and compared. The physical properties and gradation for each aggregate are shown in Table 3.2 and Figure 3.4, respectively. It is observed that the crushed gravel and the natural gravel have very similar size distribution. However, the latter has much higher absorption capacity than the former, whereas other properties are more or less similar. The mixture proportion remains the same as in the previous section under aggregate types.

In the fracture toughness test (described earlier), the lower the fracture toughness, the lower the bond strength. In Figure 3.5, the coefficient of variation (COV) for 1-day data was 2.8 percent and 3.4 percent for concrete made with natural and crushed aggregates, respectively, and that for 3-day data was 8.3 percent and 8.0 percent, respectively. In Figure 3.6, the COV for 1-day data was 3.0 percent and 2.1 percent for concrete made with natural and crushed aggregates, respectively, and that for 3-day data was 4.6 percent and 4.3 percent, respectively. Within the allowable variation of the data and based on the strength data for up to 3 days for these two test runs (shown in Figures 3.5 and 3.6), concrete with natural gravel showed higher compressive strength and fracture toughness than that with crushed gravel, which means that crushing aggregates does not help to improve concrete bonding performance. Figures 3.7 and 3.8 provide the surface appearance with respect to texture of both crushed and natural gravel particles. The crushed gravel particles in Figure 3.7 show smooth crushed faces

(smoother than natural gravel particles) but with high angularity. Those particles are mostly amorphous or crypto-crystalline silica particles (e.g., chert), which predominate in that gravel. On the contrary, natural gravel particles (as received without any crushing) in Figure 3.8 show surfaces with high roundness (low angularity) but with higher surface roughness than crushed gravel. This is correlated with lower early age fracture toughness in crushed gravel concrete than that of natural gravel. Further investigation and findings of the contribution of aggregate properties to bond strength of concrete will be described in Chapter IV.

Table 3.2. Physical Properties of Two Gravel Aggregates.

Aggregate Type	Gsb-od	Percent AC	DRUM (lb/ft^3)	%Solid
Natural gravel	2.56	1.42	103.3	64.63
Crushed gravel	2.58	0.72	97	60.22

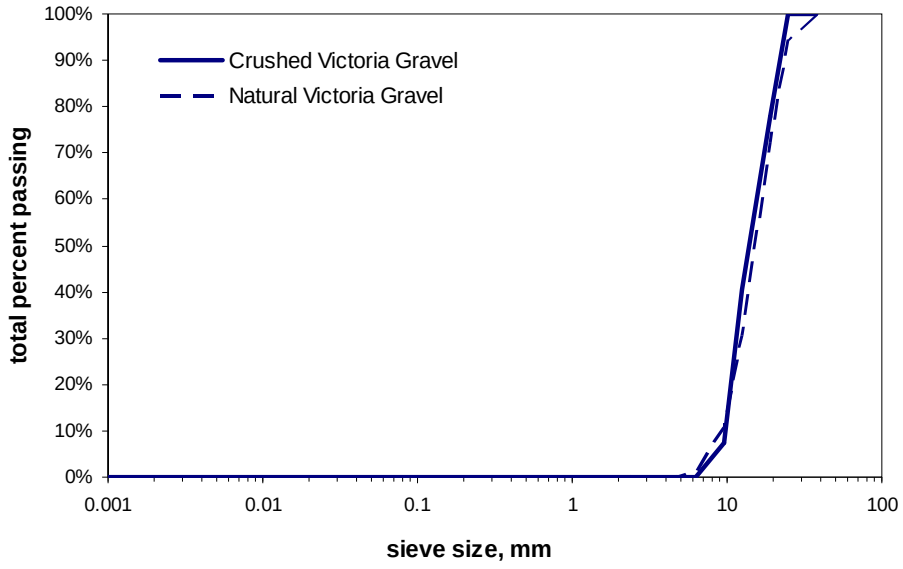

Figure 3.4. Gradation Curves for Coarse Aggregates.

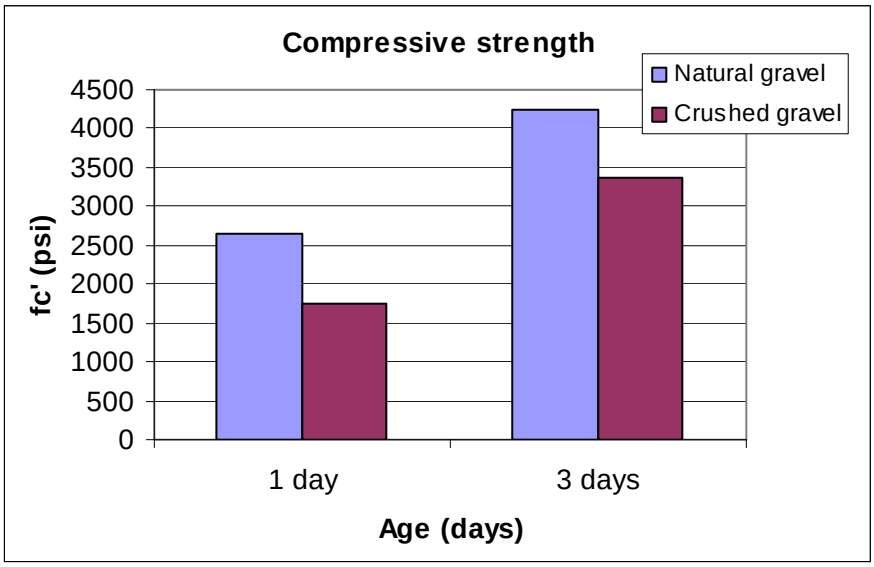

Figure 3.5. Compressive Strength of Concretes at Different Ages.

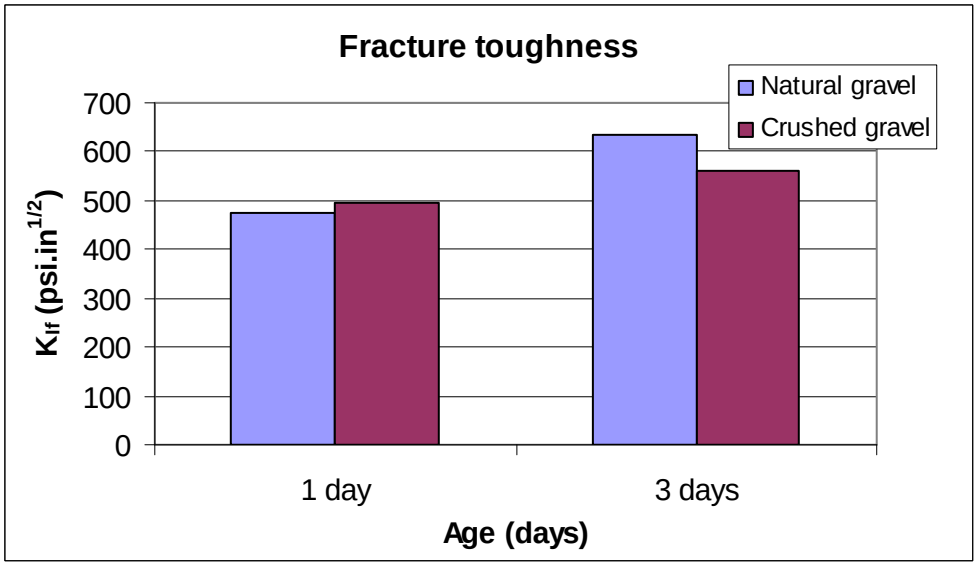

Figure 3.6. Fracture Toughness of Concretes at Different Ages.

Figure 3.7. Crushed Gravel Particles.

Figure 3.8. Natural Gravel Particles.

EXPERIMENTAL DESIGN ANALYSIS

Widely used as screening designs, fractional factorial experiments such as the Taguchi method allow the user to analyze many factors with a few runs (Mason et al. 1989). In addition, orthogonal arrays used in the Taguchi designs are balanced; that is, all factors are weighted equally in the experiment, thus allowing factors to be analyzed independently of each other (Mathews 2004). Therefore, it is desirable to apply the Taguchi method in this project when our purpose is to identify how important an effect each key design factor has on the aggregate-mortar interfacial bond, and which level can provide the best performance.

Before a Taguchi orthogonal array is chosen, all pre-experimental planning needs to be completed, including identifying the number of control factors that are of interest and the number of levels for each factor, and determining the number of runs that can be performed and the impact of other considerations on the design selection.

The step-by-step procedure that has been undertaken to develop a fractional factorial experimental lab design based on Taguchi's Design of Experiment (DOE) is listed below:

- Select the control factors.
- Select the number of levels of each factor.
- Select an appropriate orthogonal array for the experiment.
- Decide how to measure the quality characteristic of interest.
- Conduct the experiment and identify the factors that most strongly affect the chosen target.
- Predict and verify the optimum design combination.

The description for each item in relevance with the present laboratory investigation (formulation, conducting experiments, data collection, data analysis, etc.) is discussed below.

Selecting the Control Factors

Aggregate type, w/cm, fly ash content (both ultra-fine fly ash and normal class F ash), and curing method were chosen as the control factors in this project.

Selecting the Number of Levels of Each Factor

For each factor, three different levels were selected. Two gravels and one limestone (as a reference) aggregate were selected for the aggregate type factor, and Victoria gravel (VG), Garwood gravel (GG), and Georgetown limestone (GL) were designated gravel from Victoria, Texas; gravel from Garwood, Texas; and limestone from Georgetown, Texas, respectively. The ultra-fine (Micro^3) fly ash was provided by Boral Industries Inc, San Antonio, Texas, at three levels of 8 percent, 15 percent, and 20 percent replacement of cementitious materials, respectively. Typical Type I portland cement was used, and the three levels for the w/cm ratio were 0.40, 0.42, and 0.45. The three levels for the curing methods included:

- wet mat curing (WMC)—sealing concrete specimens using plastic sheets after casting,
- normal curing with curing compound (NCC)—spraying curing compound (1240-White series provided by W. R. Meadows, Inc.) on concrete after surface is dry, and
- no curing (WOC)—keeping specimens in normal conditions without any treatment.

.

Selecting an Appropriate Orthogonal Array for the Experiment

Assuming there is no interaction between each factor, an orthogonal array L_9 (3^4) was selected for the experimental design, where the array L_9 requires only nine runs out of 81 full factorial combinations of four factors with three levels each. This array is orthogonal in the fact that all factor levels are weighted equally across the entire design. Table 3.3 lists the nine test runs according to the L_9 orthogonal array, and Table 3.4 lists

associated mix proportions. For each test run, six cylindrical (6 by 12 in.) specimens (with three different geometric shapes as shown in Figure 3.1) were cast for fracture toughness testing, and three cylindrical (6 by 12 in) specimens for compressive strength testing.

Table 3.3. Nine Test Runs According to Orthogonal Array.

Tests	Aggregate Type	Ultra-fine Fly Ash	w/cm	Curing
1	VG	8%	0.40	WMC
2	VG	15%	0.42	NCC
3	VG	20%	0.45	WOC
4	GG	8%	0.42	WOC
5	GG	15%	0.45	WMC
6	GG	20%	0.40	NCC
7	GL	8%	0.45	NCC
8	GL	15%	0.40	WOC
9	GL	20%	0.42	WMC

Table 3.4. Associated Mix Proportions for Nine Test Runs.

Tests	Batch Proportion Weights (lbs/ft^3)				
	Cement	CA*	Sand	Water	Fly Ash
1	19.22	77.47	42.86	10.19	1.67
2	17.75	77.47	41.37	10.59	3.13
3	16.71	77.47	39.49	11.18	4.18
4	19.22	77.05	42.16	10.31	1.67
5	17.75	77.05	40.15	10.9	3.13
6	16.71	77.05	42.47	9.89	4.18
7	19.22	70.63	45.13	13.56	1.67
8	17.75	70.63	47.33	12.55	3.13
9	16.71	70.63	45.97	12.95	4.18

* *CA — coarse aggregates*

Deciding How to Measure the Quality Characteristic of Interest

Fracture toughness along with compressive strength were considered to represent performance evaluation properties for all nine test runs.

Conducting the Experiment and Identifying the Factors that Most Strongly Affect the Chosen Target

For the fracture toughness test, two types of steel inserts were used in the cylindrical molds when the concrete was cast, and then pulled out by a slide hammer 3 or 4 hours after the concrete was cast. The specimens were demolded 1 day after casting and cured until the test date. During testing, two plywood strips were used for load bearing for each test (ASTM 1995). The specimen was placed for the notch to be vertical to the platen of the testing machine, that is, in the direction of the compressive load. Maximum load for each specimen was then recorded after all of the specimens were broken. The measured maximum loads of specimens were filled in a programmed spreadsheet, and linear regression was performed to compute the K_{IC}.

Figures 3.9 and 3.10 illustrate compressive strength and fracture toughness results for the nine test runs. Each test run showed different development with time. However, an increase in both compressive strength and K_{IC} with concrete age was observed. Figures 3.11, 3.12, and 3.13 illustrate examples of ITZ microstructure of concrete. It can be seen that for mixes of tests 3 and 5, there was $Ca(OH)_2$ along the aggregates. However, for the mix of test 6, the amount of $Ca(OH)_2$ within the ITZ was reduced greatly, or practically there was no $Ca(OH)_2$ in the ITZ. Those observations matched the fracture toughness results very well, which indicated that the less $Ca(OH)_2$ within the ITZ and the denser the ITZ structure, the stronger the interfacial bonding.

Previous field experience has shown that a few days after paving is the most critical time for delaminations to form in concrete paving. On this basis, the 1-day K_{IC} value was selected as the output response in the experimental design. Both signal-to-noise ratios (S/N ratios, which provide a measure of robustness) and means (for static

design) were used to evaluate the significances of factors. The option of *larger is better* was chosen for S/N ratio, because our goal is to maximize the value of K_{IC}.

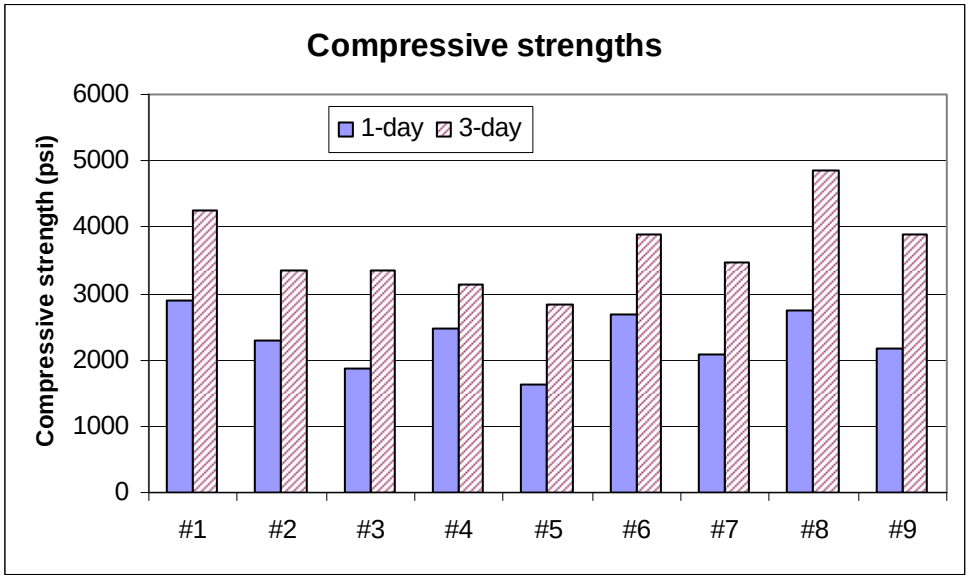

Figure 3.9. Compressive Strength Results.

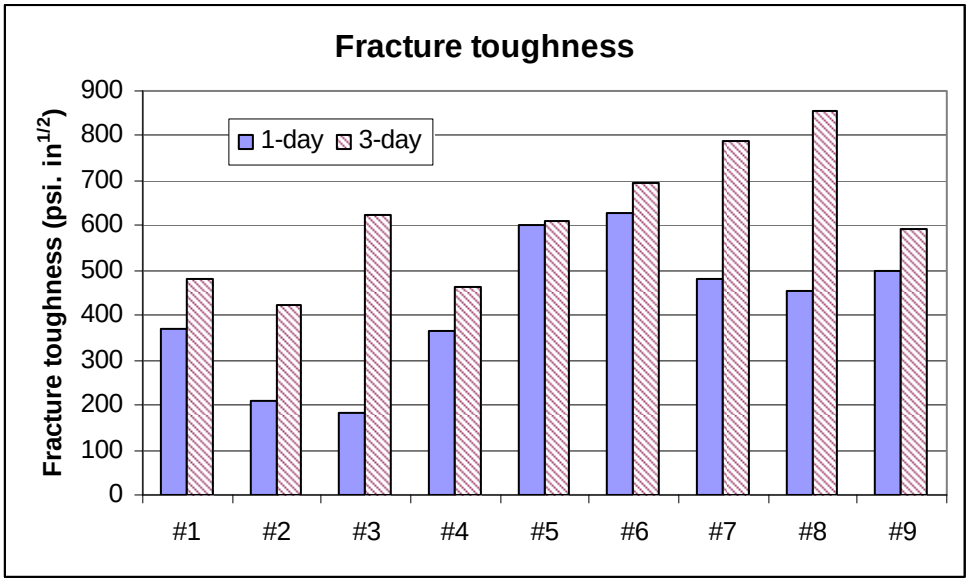

Figure 3.10. Fracture Toughness Results.

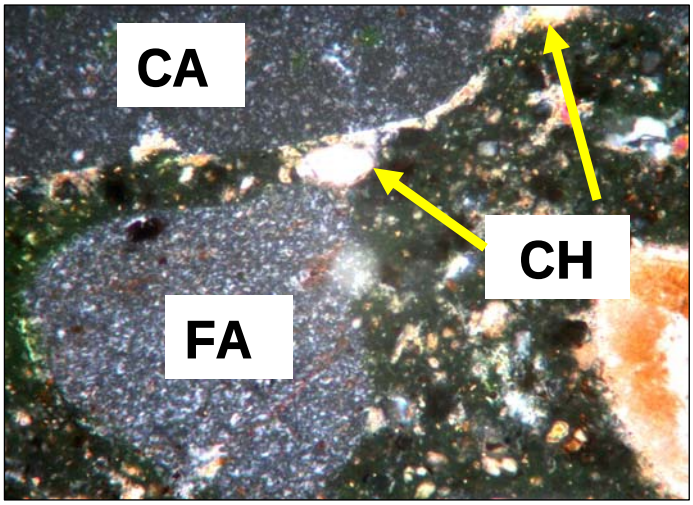

Figure 3.11. One-day ITZ Microstructure of Test 3 Mix (CA – Coarse aggregate, FA – Fine Aggregate, CH – Calcium Hydroxide).

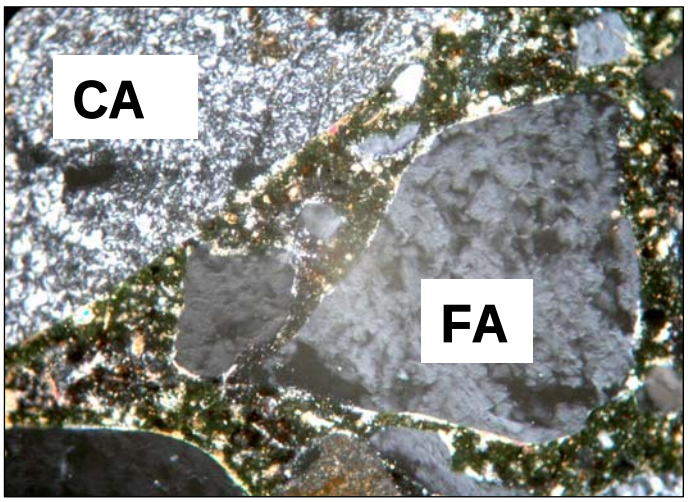

Figure 3.12. One-day ITZ Microstructure of Test 5 Mix.

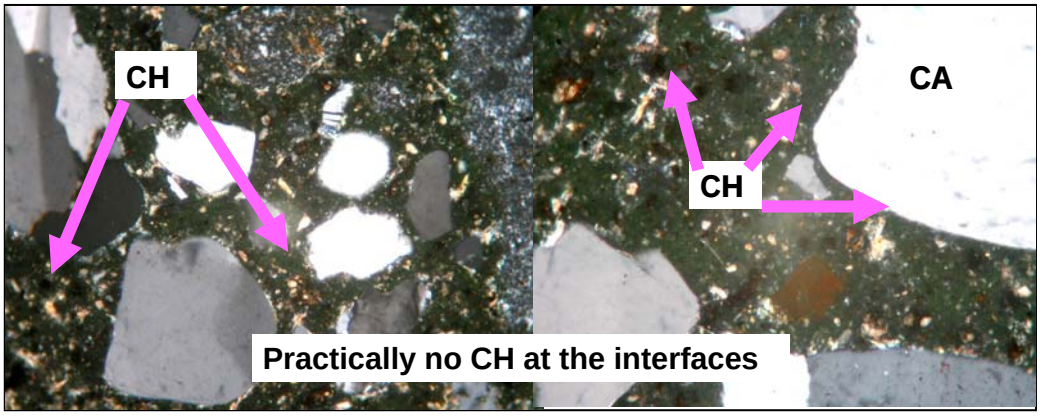

Figure 3.13. One-day ITZ Microstructure of Test 6 Mix.

The experimental design was analyzed by a statistical software named MINITAB (Mathews 2004) based on the K_{IC} values of all test runs. The MINITAB software is able to calculate response tables for both S/N ratios and means versus the control factors. These tables can then be used to determine whether the factors are significantly related to the K_{IC} performance and each factor's relative importance in the model. The response tables for means and S/N shown in Tables 3.5 and 3.6 summarize the average of each response characteristic (i.e., means and S/N ratios) for each level of each factor from MINITAB software. The tables also include ranks of factors based on Delta statistics (Mathews 2004), which compare the relative magnitude of the effects of the respective factors. MINITAB assigns ranks based on Delta values; rank 1 to the highest Delta value, rank 2 to the second highest, and so on. The highest Delta value (or the rank) indicates the greatest impact of the factor on the target value of output. In terms of the Delta values, both response tables indicate the following decreasing rank order with respect to the relative importance of each factor to K_{IC}: aggregate type, curing method, w/cm, and ultra-fine fly ash content. Aggregate type was identified as the factor that most strongly affects the bond between aggregate and the mortar.

Table 3.5. Response Table of Experimental Design with Respect to Means.

Level	Aggregate Type	Ultra-fine Fly Ash	w/cm	Curing Method
1	253.238	406.637	483.753	489.749
2	530.763	420.425	357.871	439.160
3	478.422	435.361	420.799	333.515
Delta	277.525	28.724	125.882	156.234
Rank	1	4	3	2

Table 3.6. Response Table of Experimental Design with Respect to S/N Ratios.

Level	Aggregate Type	Ultra-fine Fly Ash	w/cm	Curing Method
1	47.629	52.112	53.487	53.634
2	54.257	51.687	50.538	51.995
3	53.590	51.677	51.451	49.848
Delta	6.628	0.4352	2.950	3.786
Rank	1	4	3	2

In addition, the level averages in the response tables can determine which level of each factor provides the best result. For each factor, a higher level average indicates the better level of this factor in terms of the bonding performance. It can be also observed from the main effects plots (i.e., Figures 3.14 and 3.15), which display graphs of the averages in the response tables. A horizontal line is drawn at the grand mean of all factors. The effect at each level can be identified from the difference between the means and the reference line. For example, for aggregate type factor, both main effects plots for means and S/N ratios indicate that level 2 provided the highest value, which means that GG provided the best performance. The result is different from findings of previous field practice, which normally showed the better performance of limestone.

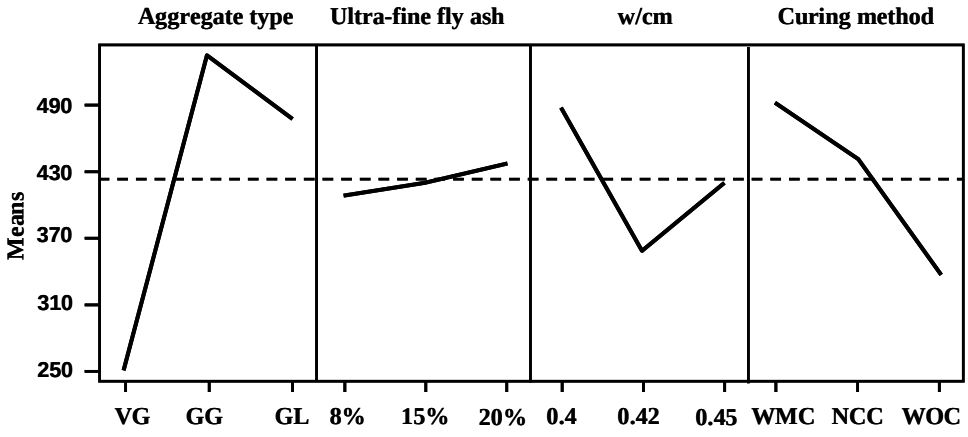

Figure 3.14. Main Effects Plot of Means.

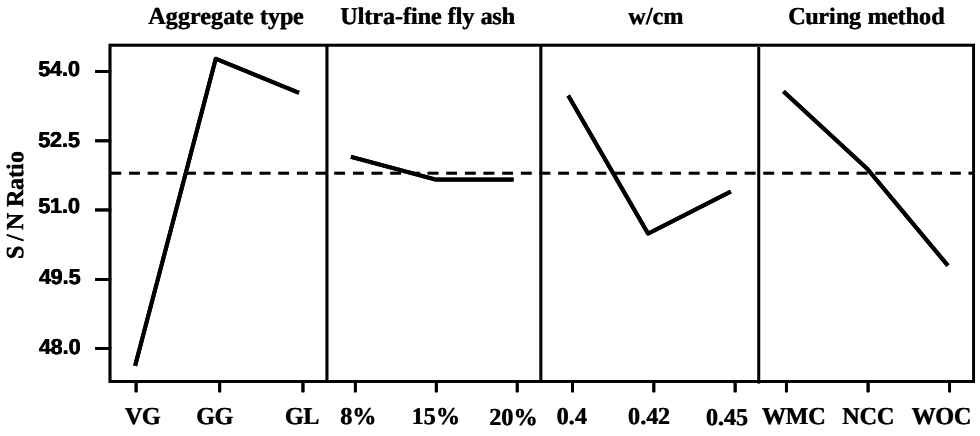

Figure 3.15. Main Effects Plot of S/N Ratios.

For w/cm, the results show that level 1 (i.e., 0.4 of w/cm) was the best, and for curing method, level 1 (i.e., WMC) was the desired one. As for the ultra-fine fly ash factor, Figure 3.14 shows that level 3 (i.e., 20 percent of ultra-fine fly ash) was the best, while Figure 3.15 shows level 1 (i.e., 8 percent of ultra-fine fly ash). If looking at response tables for means and S/N ratios (Tables 3.5 and 3.6), the factor of ultra-fine fly ash ranked the lowest, which means ultra-fine fly ash plays the least important role in the

bonding performance of concrete at early age. In addition, three levels of ultra-fine fly ash have very close values of average for both means and S/N ratios, which also implied that this factor is not significantly related to the K_{IC}. Therefore, there will not be a significant difference on the bonding performance for varying content of ultra-fine fly ash. It may be because, at a very early age of concrete, ultra-fine fly ash mainly plays a role as a filler for densification of the packing of the particles instead of its pozzolanic reactivity.

Predicting and Verifying the Optimum Design Combination

Hence, considering all the above reasons, the optimum design combination was chosen as: GG (gravel from Garwood, TX) + 8 percent ultrafine fly ash + 0.4 of w/cm + WMC. The predicted results of S/N ratio and mean from the MINITAB software were 58.014, and 648.478, respectively, which were both higher than any value in the associated response tables (Tables 3.5 and 3.6). Figure 3.16 illustrates the K_{IC} results of this optimum combination. The K_{IC} at 1-day reached up to 722.34 psi·in$^{1/2}$, which was obviously higher than that of any test run. It can be seen from Figure 3.17 that there was no coarse $Ca(OH)_2$ but ultra-fine fly ash at the interfaces for the optimum mix, which indicated its dense ITZ structure and strong interfacial bonding. Therefore, the prediction of optimum design based on experimental design analysis was validated. These results confirm that, with appropriate design, use of gravel aggregate in concrete paving can still provide better and more desirable bonding performance for concrete.

AGGREGATE PROPERTIES

In the previous section, among the four key construction design factors considered, aggregate type has the greatest effect on the bonding performance between aggregate and mortar. In addition, the GG's exhibition of best contribution on bonding performance among the three aggregate types considered in this project is different from previous research findings. Hence, a comprehensive investigation on aggregate characteristics including physical, geometric, and chemical properties of aggregate types

was conducted. A rating system using utility theory was developed to evaluate the overall contribution of aggregate properties to the bonding performance of concrete and the feasibility of design combinations.

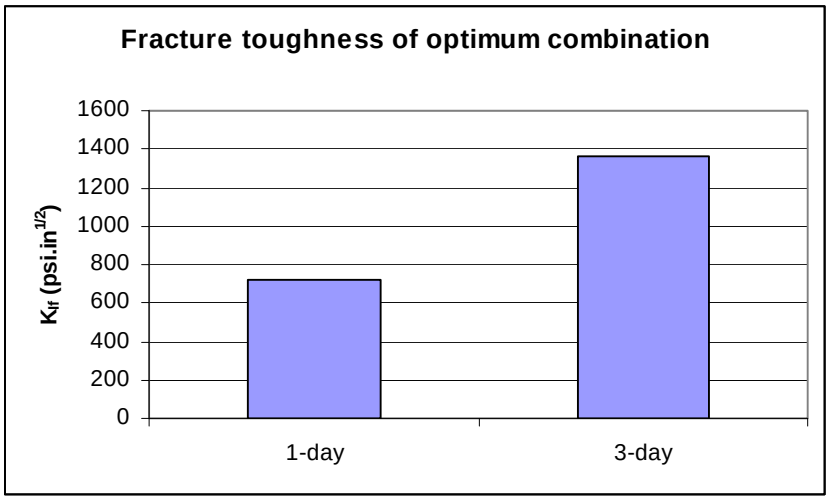

Figure 3.16. Fracture Toughness of Optimum Combination.

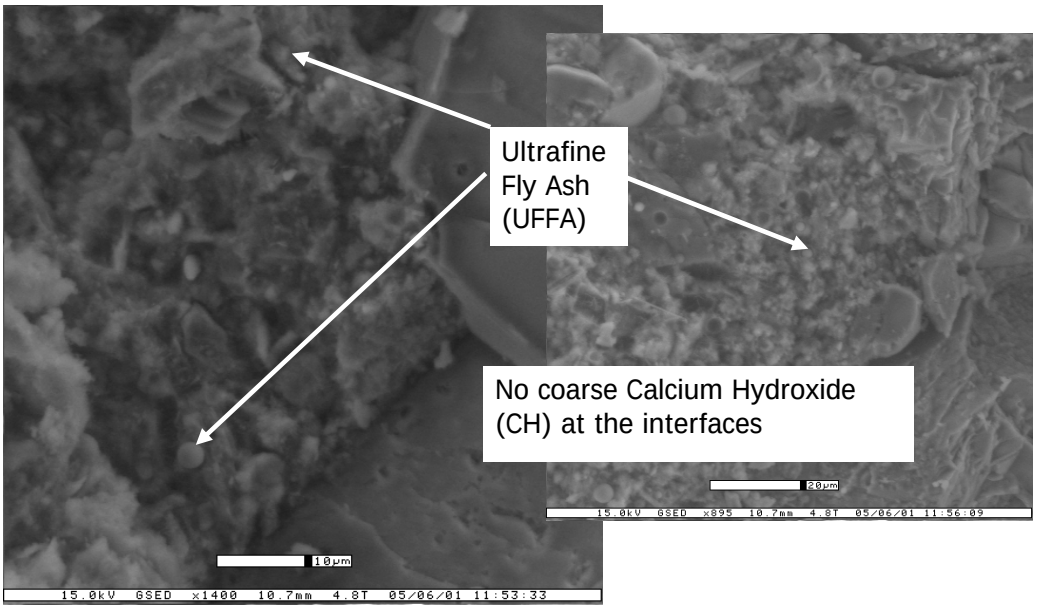

Figure 3.17. ITZ Microstructure of One-day Optimum Mix.

Aggregate Surface Free Energy Measurement

By definition, surface free energy of a solid is the energy needed to create or heal a unit surface area of material. The concept of surface energy can be explained from a molecular, mathematical, and thermodynamics point (Cheng 2002). The surface free energy of aggregate is primarily composed of a nonpolar component—the Lifshitz-van der Waals component; and an acid-base component (Fowkes 1962, Good 1992). Equation 3.6 is used to describe the total surface free energy and its components:

$$\Gamma = \Gamma^{LW} + \Gamma^{AB} \tag{3.6}$$

where,

Γ = surface free energy of aggregate,

Γ^{LW} = Lifshitz-van der Waals component of the surface free energy, and

Γ^{AB} = acid-base component of the surface free energy.

The Lifshitz-van der Waals force contains at least three components: London dispersion force, Debye induction force, and Keesom orientation force. The London dispersion force is the attraction between neighboring electronic shells. It is an induced dipole to induced dipole interaction. The Debye induction force is produced by a dipole inducing a dipole in a neighboring molecule. The Keesom orientation force is the interaction of two dipoles orienting themselves in relation to each other (Hefer 2004).

The acid-base interaction includes all interactions of electron donor (proton acceptor)—electron acceptor (proton donor) type bonds including hydrogen bonding. To quantitatively predict and treat the acid-base interaction, Good (1992) postulated a resolution of the acid-base term, Γ^{AB}, into a Lewis acidic surface parameter and a Lewis basic surface parameter. The relationship among the Γ^{AB} and its components is shown in Equation 3.7:

$$\Gamma^{AB} = 2\sqrt{\Gamma^{+}\Gamma^{-}} \tag{3.7}$$

where,

Γ^+ = Lewis acid component of surface interaction, and

Γ^- = Lewis base component of surface interaction.

Surface Free Energy Measurement of Aggregate

The measurement of the surface free energy of solids is not straightforward because it cannot be measured directly. There are several direct and indirect methods to measure surface energy of aggregate, including inverse gas chromatography (IGC) (Ahsan and Taylor 1999), atomic force microscopy (AFM) (Beach et al. 2002), microcalorimetry (Yildirim 2001), and universal sorption device (USD) (Cheng 2002).

Gas chromatography is a simple technique for the separation based on the fact that each solute has a different interaction with the stationary phase, which results in different travel times for different solutes carried by an inert gas through a column with known characteristics. Therefore, the IGC at infinite dilution can be used to determine surface energy and its components by measuring the retention volumes of different probe gases through a column of small aggregate particles. These experiments are relatively fast and commercial devices are now available that make the process fully automated. However, there is only one commercial instrument that supplies software for surface energy analysis.

The AFM is a direct method to measure the intrinsic surface forces that take part in fundamental adhesion at an interface. It would be possible to obtain all the surface energy components by using cantilevers with chemically functionalized tips. The operation of this device requires some experience since careful positioning of the tip near the surface is required. Practicality limitations associated with aggregate measurements result from the heterogeneity and topographical features on aggregate surfaces, not being compatible with the scale at which these instruments are designed to operate.

The microcalorimetry method is attractive in that the measurement of sorption heats is relatively simple and could be used to obtain surface energy and its components. The conversion from enthalpy to free energies can be accomplished in two ways:

- by measuring contact angles at different temperatures, or
- by performing gas sorption experiments.

However, a procedure that would require the measurement of contact angles of aggregates at different temperatures would be neither practical nor efficient.

The USD method is a vacuum gravimetric static sorption technique that identifies gas sorption characteristics of selected solvents to indirectly determine the surface energies of aggregate. Sorption methods are particularly suitable due to their ability to accommodate the peculiarity of sample size, irregular shape, mineralogy, and surface texture associated with aggregates. Therefore, it was applied in this project for the surface energy measurements of aggregates.

The USD is comprised of a Rubotherm magnetic suspension balance system, a computer system (with Messpro software), a temperature control unit, a high quality vacuum unit, a vacuum regulator, pressure transducers, a solvent container, and a vacuum dissector. A schematic of the main components of the USD setup is illustrated in Figure 3.18.

The Rubotherm magnetic suspension balance has the ability to measure a sample mass of up to 200 g to an accuracy of 10^{-5} g, which is sufficient for precise measurement of mass increase due to gas adsorbed onto the aggregate surface. The whole USD system is fully automated with predetermined pressure set-points that automatically trigger when the captured balance readings reach equilibrium. Aggregate samples between the No.4 and No.8 sieve size were thoroughly cleaned with distilled water and oven-dried for measurement.

During the USD test process, once the chamber is vacuumed, a solvent vapor is injected into the aggregate system. A highly sensitive magnetic suspension balance is

used to measure the amount of solvent adsorbed on the surface of the aggregate. The vapor pressure at the aggregate surface is measured at the same time. The surface energy of the aggregate is calculated after measuring the adsorption of three different solvents (i.e., distilled water, *n*-hexane, and methyl propyl ketone [MPK]) with known specific surface free energy components, as listed in Table 3.7. Data (vapor pressure, adsorbed gas mass, and test time) are measured and captured electronically via the Messpro software.

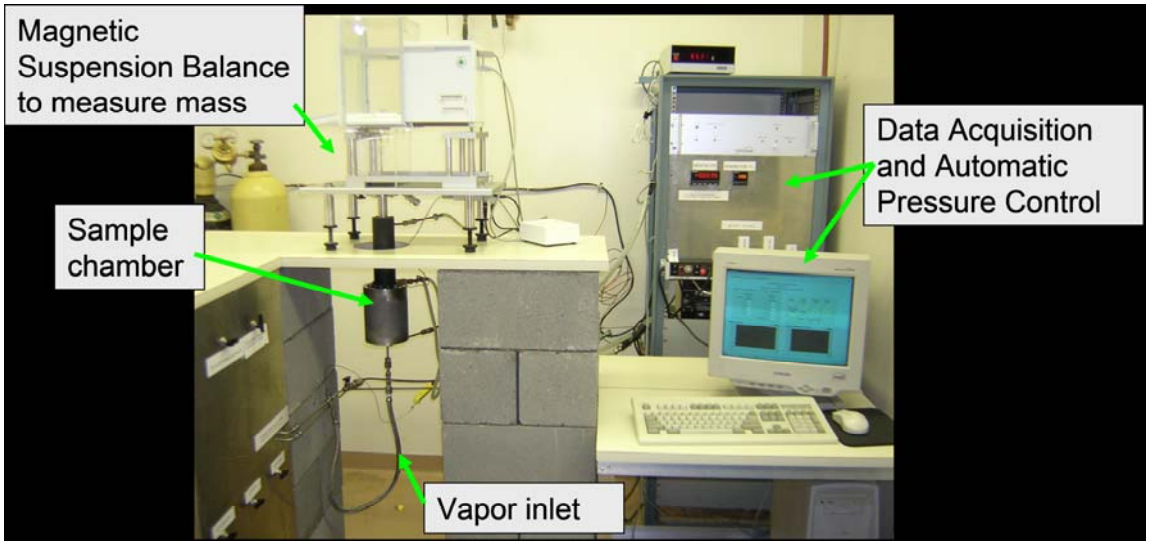

Figure 3.18. USD Setup.

Table 3.7. Surface Energy Components of Water, n-hexane, and MPK @ 25°C.

Solvent	Surface Free Energy Components (ergs/cm^2)				
	Γ_{Li}	Γ_{Li}^{LW}	Γ_{Li}^{+}	Γ_{Li}^{-}	Γ_{Li}^{AB}
Distilled water	72.60	21.60	25.50	25.50	51.00
n-hexane	18.40	18.40	0.00	19.60	0.00
MPK	24.70	24.70	0.00	0.00	0.00

Once the adsorbed solvent mass and vapor pressure on the aggregate surface have been measured and the adsorption data corrected for solvent vapor buoyancy using the generalized Pitzer correlation model, the specific surface area of the aggregate is then calculated using the BET (Brunauer, Emmett, and Teller) model shown by Equation 3.8:

$$\frac{P}{n(P_0 - P)} = \left(\frac{c-1}{n_m c}\right)\frac{P}{P_0} + \frac{1}{n_m c} \tag{3.8}$$

where,

P = vapor pressure (MPa),

P_0 = saturated vapor pressure (MPa),

N = specific amount adsorbed on the surface of the absorbent (mg), and

n_0 = monolayer specific amount of vapor adsorbed on the surface of aggregate (mg).

For the type of isotherms associated with the pressure conditions in this USD test, n_m can be obtained from the slope and the intercept of the straight line that fits the plot of *P/n(P-Po)* versus *P/Po* best. The specific surface area (SSA) of the aggregate can then be calculated through the following equation:

$$SSA = \left(\frac{n_m N_o}{M} \right) \alpha \tag{3.9}$$

where,

α = $1.091 \left(\frac{M}{N_o \rho} \right)^{2/3}$ for a hexagonal close-packing model (m^2),

N_o = Avogadros' number (6.02×10^{23}),

M = molecular weight (g), and

ρ = density of the adsorbed molecule in liquid at the adsorption conditions (g/cm^3).

The result from the BET equation is used to calculate the spreading pressure at saturation vapor pressure (π_e) for each solvent using Gibb's adsorption equation:

$$\pi_e = \frac{RT}{A} \int_0^{p_0} \frac{n}{P} dP \tag{3.10}$$

where,

π_e = spreading pressure at saturation vapor pressure of the solvent ($ergs/cm^2$),

R = universal gas constant (83.14 cm^3 bar/mol.K), and

T = absolute temperature (Kelvin, K) ($K = 273 + ^\circ C$).

The work of adhesion of a liquid on a solid (W_A) can be expressed in terms of the surface energy of the liquid (Γ_l) and π_e as shown in Equations 3.11 and 3.12, where subscripts *s* and *l* represent solid (aggregate) and liquid (solvent), respectively:

$$W_a = \pi_e + 2\Gamma_l \tag{3.11}$$

$$\pi_e + 2\Gamma = 2\sqrt{\Gamma_s^{LW}\Gamma_l^{LW}} + 2\sqrt{\Gamma_s^{+}\Gamma_l^{-}} + 2\sqrt{\Gamma_s^{-}\Gamma_l^{+}} \tag{3.12}$$

Then, Equation 3.13 is used to calculate the Γ_s^{LW} of the surface for a nonpolar solvent on the surface of the solid (aggregate).

$$\Gamma_s^{LW} = \frac{\left(\pi_e + 2\Gamma_l\right)^2}{4\Gamma_l^{LW}} \tag{3.13}$$

For a known mono-polar basic liquid vapor (subscript m) and a known bipolar liquid vapor (subscript b), the Γ_s^{+} and Γ_s^{-} values are calculated using Equations 3.14 and 3.15 as follows.

$$\Gamma_s^{+} = \frac{\left(\pi_e + 2\Gamma_{lm} - \sqrt{\Gamma_s^{LW}\Gamma_{lm}^{LW}}\right)^2}{4\Gamma_{lm}^{-}} \tag{3.14}$$

$$\Gamma_s^{-} = \frac{\left(\pi_e + 2\Gamma_{lb} - \sqrt{\Gamma_s^{LW}\Gamma_{lb}^{LW}} - 2\sqrt{\Gamma_s^{+}\Gamma_{lb}^{-}}\right)^2}{4\Gamma_{lb}^{+}} \tag{3.15}$$

Finally, the total surface energy of the aggregate (Γ_s) is calculated as expressed by Equation 3.16.

$$\Gamma_s = \Gamma_s^{LW} + 2\sqrt{\Gamma^{+}\Gamma^{-}} \tag{3.16}$$

Surface free energy (SFE) of two aggregates studied (i.e., VG and GL) were measured by the USD method, and the results are listed in Table 3.8. The specific surface areas of the aggregate samples calculated using the adsorption isotherm of the three solvents are listed as well. The GL showed the higher acidic surface free energy, while the VG showed the higher basic components of surface free energy. The SSA of

VG was considerably greater than that of GL, which means that it had a relatively rougher surface texture than the GL. It is also correlated to the results from investigation of aggregate geometric properties, which will be reported later. Though the VG had a little lower SE value than GL; however, its product of SE and SSA (195.70×10^{-3} Joel/g) was much higher than that of GL (87.31×10^{-3} Joel/g).

Table 3.8. SE Components for the Aggregates.

SE Component (ergs/cm^2)	Γ^+	Γ^-	Γ^{AB}	Γ^{LW}	Γ^{Total}	SSA (m^2/g)	Γ^{Total}×SSA (10^{-3} Joel/g)
VG	1.10	426.85	43.31	81.34	124.65	1.57	195.70
GL	1.62	362.71	48.51	79.89	128.4	0.68	87.31

Further, the bond between the water and the aggregates was investigated, which is expressed by Equation 3.17.

$$\Delta G = \Delta G^{LW} + \Delta G^{AB} \tag{3.17}$$

where,

ΔG = the total bond Gibbs free energy of the material surface per unit surface area,

ΔG^{LW} = the nonpolar, Lifshitz-van der Waals bond Gibbs free energy of the material surface, and

ΔG^{AB} = the polar, acid-base bond Gibbs free energy of the material surface.

The adhesive nonpolar bond component is determined by Equation 3.18.

$$\Delta G^{LW} = -\Gamma_{ij}^{LW} + \Gamma_i^{LW} + \Gamma_j^{LW} \tag{3.18}$$

And the adhesive polar bond component is of the same form and is determined by Equation 3.19.

$$\Delta G^{AB} = -\Gamma_{ij}^{AB} + \Gamma_{i}^{AB} + \Gamma_{j}^{AB} \tag{3.19}$$

The interactive term for the nonpolar LW adhesive surface energy component, Γ_{ij}^{LW} is given by Equation 3.20.

$$\Gamma_{ij}^{LW} = \left(\sqrt{\Gamma_{i}^{LW}} - \sqrt{\Gamma_{j}^{LW}}\right)^2 \tag{3.20}$$

And the interactive term for the polar AB adhesive surface bond energy component, Γ_{ij}^{AB} is given by Equation 3.21.

$$\Gamma_{ij}^{AB} = 2\left(\sqrt{\Gamma_{i}^{+}} - \sqrt{\Gamma_{j}^{+}}\right)\left(\sqrt{\Gamma_{i}^{-}} - \sqrt{\Gamma_{j}^{-}}\right) \tag{3.21}$$

The results are summarized in Table 3.9. It shows that the total bond Gibbs free energy between water and VG was higher than that between water and GL. The total bond Gibbs free energy represents the ability of the solids to pull water. Immediately after pouring and before hardening, water-filled pockets form under coarse aggregates. It is expected that the VG has more preference to attract water than GL, which may have negative effect on concrete bonding performance.

Table 3.9. Bond between Water and Aggregates.

i=water, j=agg	Γ_{ij}^{AB}	Γ_{ij}^{LW}	ΔG^{LW}	ΔG^{AB}	ΔG (ergs/cm2)
Water-VG	-124.91	19.11	83.83	219.22	303.06
Water-GL	-105.72	18.41	83.08	205.23	288.31

Aggregate Shape and Texture Characteristics

Researchers have distinguished between different aspects that constitute aggregate geometry. It has been found that the particle geometry can be fully expressed in terms of three independent properties: form, angularity (or roundness), and surface texture (Barett 1980). A schematic diagram that illustrates the difference between these properties is shown in Figure 3.19. Shape or form, the first order property, reflects variations in the proportions of a particle. Angularity, the second order property, reflects variations at the corners, that is, variations superimposed on shape. Surface texture is used to describe the surface irregularity at a scale that is too small to affect the overall shape (Al-Rousan 2004).

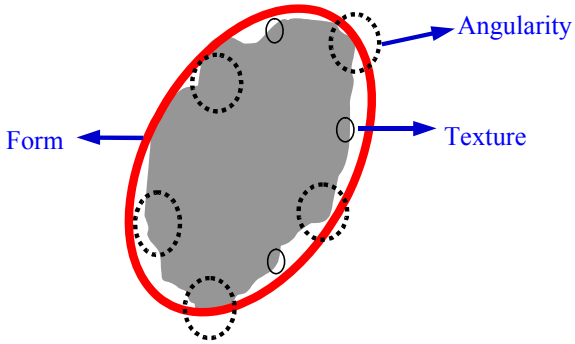

Figure 3.19. Aggregate Shape Components (Masad 2001).

Aggregate shape characteristics affect the proportioning of portland cement concrete mixtures, the rheological properties of the mixtures, aggregate-mortar bond, and the interlocking strength of the concrete joint/crack (Al-Rousan 2004). Previous studies (Mindness et al. 2002; Kosmatka et al. 2002; Will 2000) indicate that the bond strength between the cement paste and a given coarse aggregate generally increases as particles change from smooth and rounded to rough and angular. Rough, textured surfaces will improve the mechanical component of the bond by increasing the amount of surface area available for bonding with the paste for a given aggregate content. The interlocking of angular particles results in a strong aggregate skeleton under applied

loads, whereas round particles tend to slide by or roll over each other, resulting in an unsuitable and weaker structure. Using a high percentage of flat and elongated particles might cause problems when placing the concrete, which will result in voids and incomplete consolidation of the mix, and thus contribute to local distress. Therefore, three components—texture, angularity, and content—of flat/elongated aggregates have different (positive or negative) effects on bonding performance of concrete materials, which can be used to represent the effects of geometric properties of aggregates.

Table 3.10 (Al-Rousan et al. 2004) summarizes direct and indirect test methods that have been used by highway state agencies and research projects for measuring some aspects of aggregate shape properties. Direct methods are defined as those wherein particle characteristics are measured, described qualitatively and possibly quantified through direct measurement of individual particles. In indirect methods, particle characteristics are lumped together as geometric irregularities and determined based on measurements of bulk properties.

The comparative analysis and intensive evaluation conducted by Al-Rousan et al. (2004) highlighted the advantages of AIMS in measuring aggregate shape properties:

- able to capture images and analyze the shape of a wide range of aggregate sizes and types;
- measures all three aggregate shape properties (form, angularity, and texture) for all aggregate types and for different aggregate sizes;
- capable of performing two- and three-dimensional analysis as needed;
- captures images of aggregates at specified resolutions in order to minimize the influence of particle size on shape results;
- uses image analysis techniques that are based on sound scientific concept;
- rapid, computer automated, accurate, practical, and user friendly; and
- able to work in central and field laboratories.

Figure 3.20 shows the entire AIMS setup, which was utilized to facilitate this project.

Table 3.10. Summary of Methods for Measuring Aggregate Characteristics (Al-Rousan et al. 2004).

Test	References for the Test Method	Direct (D) or Indirect (I) Method	Field (F) or Central (C) Laboratory Application
Uncompacted void content of CA	AASHTO* TP56, National Cooperative Highway Research Program (NCHRP) Report 405, Ahlrich (1996)	I	F, C
Index for particle shape and texture	ASTM D3398	I	F, C
Angle of internal friction from direct shear test	Chowdhury and Button (2001)	I	C
Percentage of fractured particles in CA	ASTM D5821	D	F, C
Flat and elongated CA	ASTM D4791	D	F, C
Multiple ratio shape analysis	David Jahn (Martin Marietta, Inc.)	D	F, C
VDG-40 videograder	Emaco, Ltd. (Canada), Weingart and Prowell (1999)	D	F, C
Computer particle analyzer	Mr. Reckart (W. S. Tyler Mentor Inc.), Tyler (2001)	D	C
Micromeritics optisizer PSDA	Mr. M. Strickland (Micromeritics optisizer)	D	C
Video Imaging System (VIS)	John B. Long Company	D	C
Buffalo wire works PSSDA	Dr. Penumadu, University of Tennessee	D	C
Camsizer	Jenoptik Laser Optik System and Research Technology	D	C
WipShape	Marez and Zhou (2001)	D	C
University of Illinois Aggregate Image Analyzer (UIAIA)	Tutumluer et al. (2000), Rao et al.(2001)	D	C
Aggregate Imaging System (AIMS)	Masad (2003)	D	C
Laser-Based Aggregate Analysis System	Kim et al. (2002)	D	C

* AASHTO = American Association of State Highway and Transportation Officials

Figure 3.20. AIMS Setup.

Parameters Representing Aggregate Shape. In the AIMS analysis system a number of indices have been proposed to characterize particle form, angularity, and texture. Among the form parameters, sphericity is expressed in terms of three dimensions:

$$Spericity = \sqrt[3]{\frac{d_s * d_i}{d_l^2}} \tag{3.22}$$

where,

d_l = longest dimension of the particle,

d_i = intermediate dimension of the particle, and

d_s = shortest dimension of the particle.

The form index, describing form in two dimensions, uses incremental changes in the particle radius. The length of a line that connects the center of the particle to the

boundary of the particle is termed radius. The form index is expressed by the following equation:

$$Form\ Index = \sum_{\theta=0}^{\theta=360-\Delta\theta} \frac{\left|R_{\theta+\Delta\theta} - R_{\theta}\right|}{R_{\theta}} \tag{3.23}$$

where,

θ = the directional angle, and

R = the radius in different directions.

If a particle was a perfect circle, the form index would be zero. Although the form index is based on two-dimensional measurements, it can easily be extended to analyze the three-dimensional images of aggregates. Another way of presenting form of a particle is by using Flat and Elongated Ratio (FER), which is:

$$FER = \frac{d_l}{d_s} \tag{3.24}$$

The analysis methods of angularity have used mainly black and white images of two-dimensional projections of aggregates, with the assumption that the angularity elements in two-dimensions are a good measure of the three-dimensional angularity. For the gradient method, the angle of orientation values of the edge-points (θ), and the magnitude of the difference in these values (Δθ) for adjacent points on the edge are calculated to describe how sharp or how rounded the corner is, as illustrated in Figure 3.21. The angularity values for all boundary points are calculated and their sum accumulated around the edge to finally form a measure of angularity, which is noted, the gradient index (GI) (Chandan et al. 2004):

$$GI = \sum_{i=1}^{N-3} \left| \theta_i - \theta_{i+3} \right| \tag{3.25}$$

where,

i = the ith point on the edge of the particle, and

N = the total number of points on the edge of the particle.

Masad et al. (2003) proposed the angularity index, which is described by the following equations:

$$Angularity\ Index = \sum_{\theta=0}^{\theta=360-\Delta\theta} \frac{\left| R_{P\theta} - R_{EE\,\theta} \right|}{R_{EE\ \theta}} \tag{3.26}$$

where,

$R_{P\theta}$ = the radius of the particle at a directional angle, θ, and

$R_{EE\theta}$ = the radius of an equivalent ellipse at the same θ.

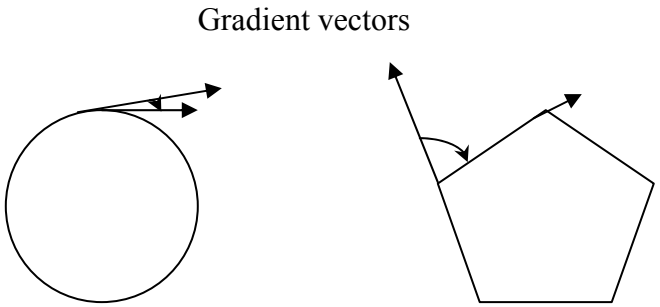

Figure 3.21. Difference in Gradient between Particles.

The index relies on the difference between the radius of a particle in a certain direction and a radius of an equivalent ellipse taken in the same direction as a measure of angularity. Both gradient and radius angularity results are presented in AIMS.

Wavelet analysis method is used in AIMS for texture characterization. The wavelet transform works by mapping an image onto a low-resolution image and a series of detailed images, as shown in Figure 3.22. The original image is shown in Figure 3.22a. It is decomposed into a low-resolution image (Image 1 in Figure 3.22b) by literally blurring the original image. The remaining images contain information on the fine intensity variation (high frequency) that is lost in Image 1. Image 1 can be further decomposed similarly to the first iteration, which gives a multi-resolution decomposition and facilitates quantification of texture at different scales. Image 2 contains the information lost in the y-direction, Image 3 has the information lost in the x-direction, and Image 4 contains the information lost in both the x- and y-direction. Texture index is taken at a given level as the arithmetic mean of the squared values of the detail coefficients at that level:

$$Texture\ Index_n = \frac{1}{3N}\sum_{i=1}^{3}\sum_{j=1}^{N}\left(D_{i,j}(x,y)\right)^2 \qquad (3.27)$$

where,

N = the level of decomposition,

i = 1, 2, or 3, for the three detailed images of texture, and

j = the wavelet coefficient index.

The output of the analysis software can be an Excel file with summary reports and graph illustrations for all sizes combined or individual sizes. It also shows the results in terms of a cumulative distribution curve and some statistics such as standard deviation, mean, and values of first, second, and third quartiles. Figures 3.23 and 3.24 show the examples of output from analysis software.

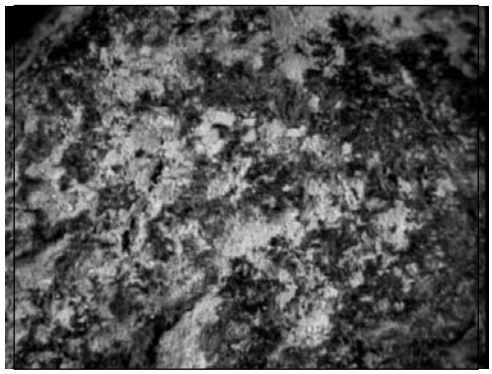

(a) Original image

Image 1 Image 2

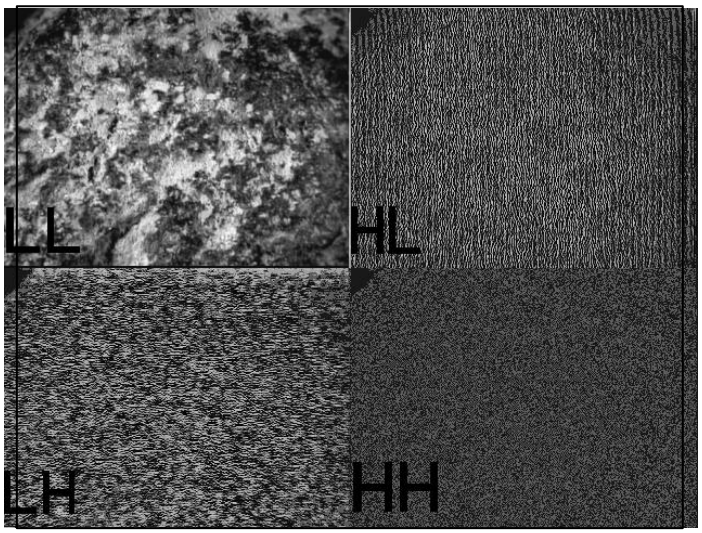

Image 3 Image 4

(b)

Figure 3.22. Illustration of the Wavelet Decomposition (Chandan et al. 2004).

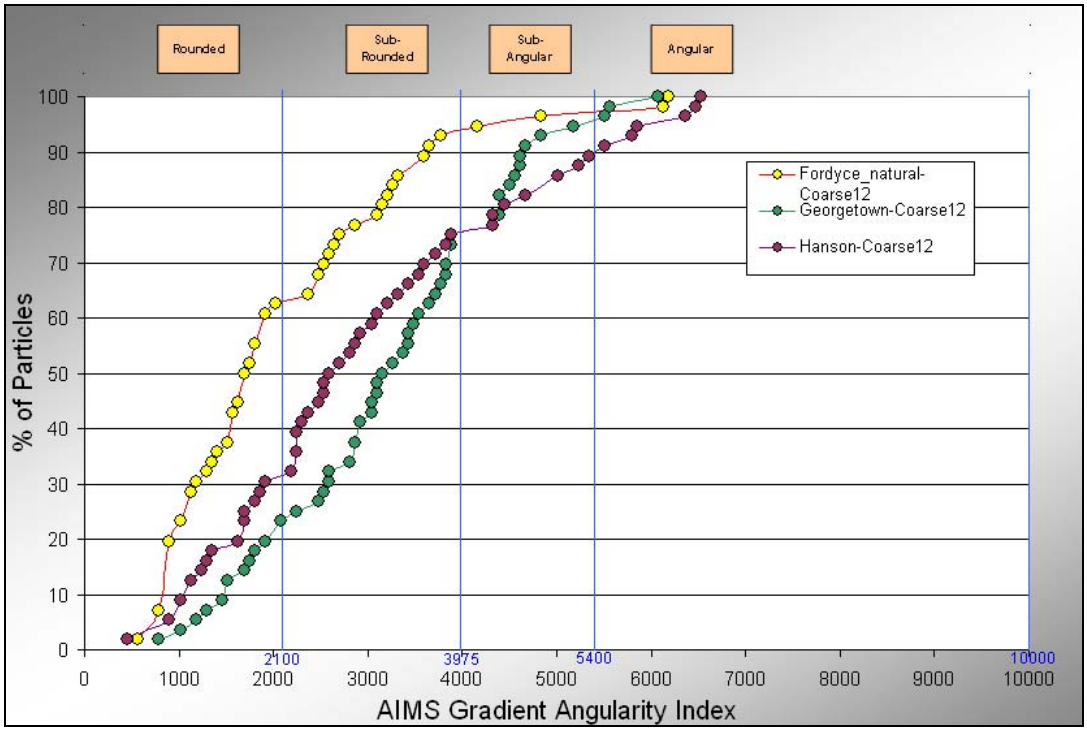

Figure 3.23. Example of AIMS Gradient Angularity Index Curve.

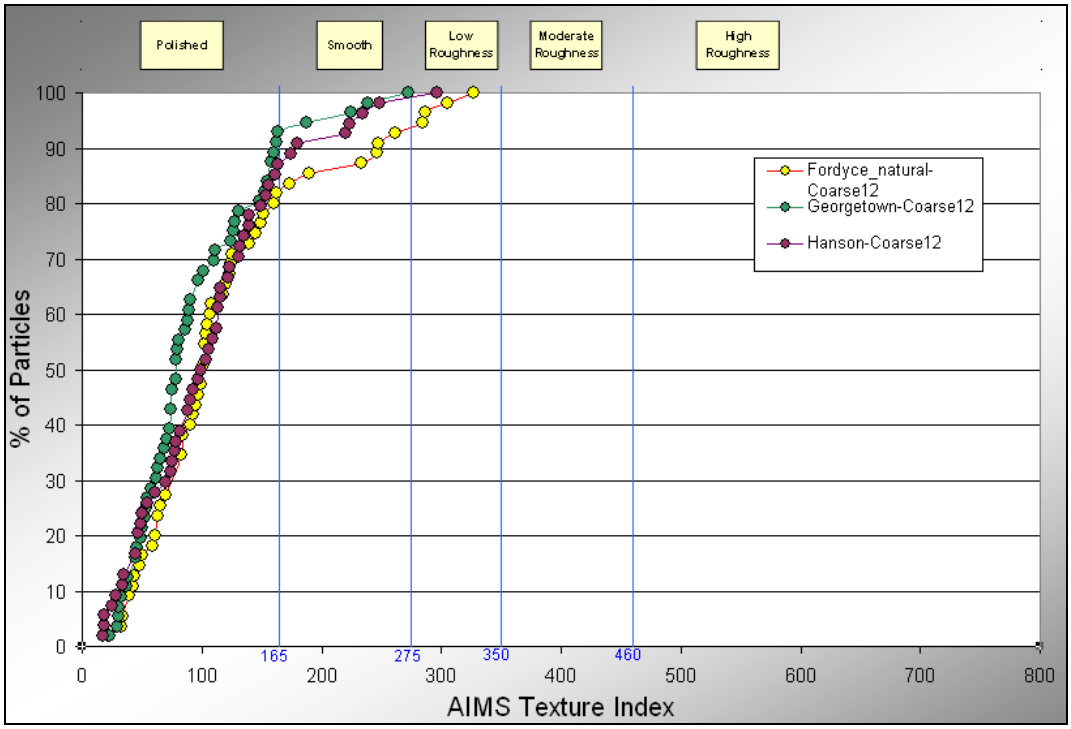

Figure 3.24. Example of AIMS Texture Index Curve.

Table 3.11 summarizes the features of each shape parameter used in AIMS. Texture index and gradient angularity index were picked up for this project. The sphericity value gives a very good indication on the proportions of a particle's dimensions. However, one cannot determine whether an aggregate has flat, elongated, or flat and elongated particles using the sphericity alone. Therefore, percentage of flat/elongated aggregates was used, which can be obtained from the AIMS analysis summary report.

The blue lines in Figures 3.23 and 3.24 show the aggregate shape classification limits, as also summarized in Figure 3.25. For example, if texture index of aggregate is below 165, it is defined as polished texture. If the value is higher than 460, it is defined as high roughness.

Table 3.11. Features of Analysis Methods in AIMS.

Method	Description	Features
Texture Index Using Wavelet	Used by AIMS analysis software (AIMSTXTR)	• Capable of separating aggregates with different texture characteristics • Most unique among the texture parameter
Gradient Angularity Index	Used by AIMS analysis software (AIMSGRAD)	• Capable of separating aggregates with different angularity characteristics • Capable of separating angularity from form • Most unique among angularity parameters
Radius Angularity Index	Used by AIMS analysis software (AIMSRAD)	• Captures angularity but it is not capable of separating two-dimensional form from angularity
2-D Form Index	Used by AIMS analysis software (AIMSFORM)	• Captures two-dimensional form but it is not capable of separating form from angularity
Sphericity	Used by AIMS analysis software (AIMSSPH)	• Capable of separating aggregates with different form characteristics • Captures unique characteristics of aggregates • Most unique among the form parameters

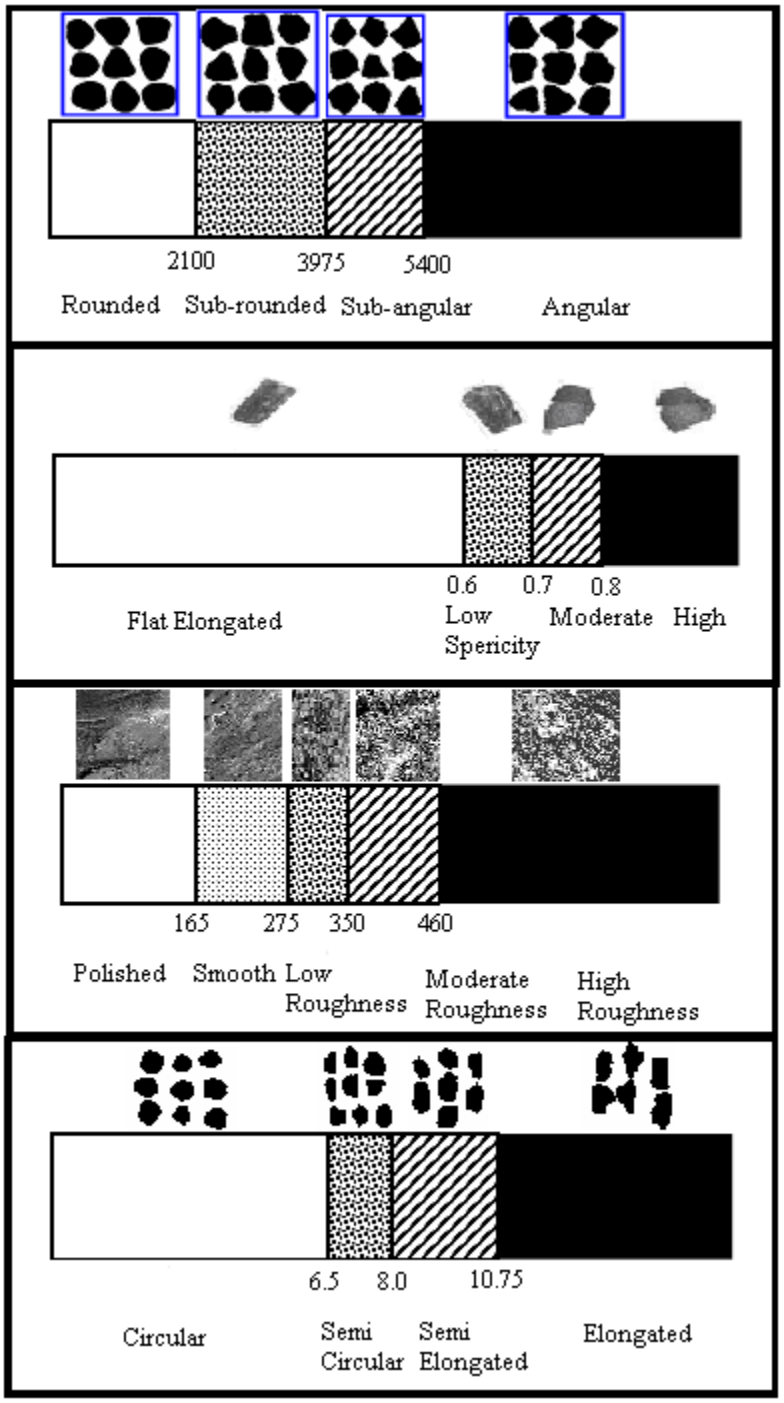

Figure 3.25. Aggregate Shape Classification Limits (Al-Rousan 2004).

For each size level of each aggregate type, AIMS analysis software provides the results in terms of cumulative distribution functions and statistical parameters such as average texture index (TI_k), angularity index (GI_k), and percentage of flat/elongated aggregates ($\%E_k$) based on 56 particles for each individual size level. To consider the overall contribution of aggregates at all size levels in concrete, overall shape and texture parameters were proposed based on these original statistical parameters from AIMS, which can be expressed as:

$$STI = \frac{\sum \%A_k \cdot TI_k}{460} \tag{3.28}$$

where,

STI = overall standardized texture index,

$\%A_k$ = percentage of aggregates on the size k sieve, and

460 = threshold value for high roughness particle in AIMS.

$$SGI = \frac{\sum \%A_k \cdot GI_k}{5400} \tag{3.29}$$

where,

SGI = overall standardized gradient angularity, and

5400 = threshold value for angular particle in AIMS,

and,

$$OS = \sum \%A_k \cdot \%E_k \tag{3.30}$$

where,

OS = overall percentage of flat/elongated aggregates.

After being standardized by the threshold value, STI ranges from 0 to 1. The higher the value of STI, the rougher the aggregate surface SGI ranges from 0 to 1 as well. The closer to 1, the more angular the aggregate is. In terms of OS, a higher value indicates more flat/elongated aggregates in the concrete. Therefore, these three parameters can represent various effects (positive or negative) of aggregate shape on concrete bonding performance.

Before measurements, aggregates were cleaned, dried, and sieved to four size levels: passing 1-in but retaining on ¾-in sieves; passing ¾-in but retaining on ½-in sieves; passing ½-in but retaining on 3/8-in sieves; and passing 3/8-in but retaining on #4 sieves. Table 3.12 shows sources and sizes of aggregates tested.

Table 3.12. Aggregate Sources and Sizes.

Aggregate	Source	Aggregate Description	Aggregate Sizes			
			25.4-19.0 mm (1-3/4″)	19.0-12.5 mm 3/4″-1/2″)	12.5-9.5 mm (1/2″-3/8″)	9.5-4.75 mm (3/8″-#4)
GG	Garwood, TX	Uncrushed river gravel	X	X	X	X
VG	Victoria, TX	Uncrushed river gravel	X	X	X	X
GL	Georgetown, TX	Limestone	X	X	X	X

A summary of these aggregate shape parameter results is illustrated in Figure 3.26. It can be seen that different aggregates showed different behaviors in terms of these three independent components. The decreasing rank orders of bonding performance as measured are GG, GL, and VG with respect to angularity; VG, GG, and GL with respect to texture; and VG, GG, and GL with respect to percentage of flat/elongated particles. GG is the most angular aggregate, and VG has the roughest aggregate surface and also the highest amount of flat/elongated particles

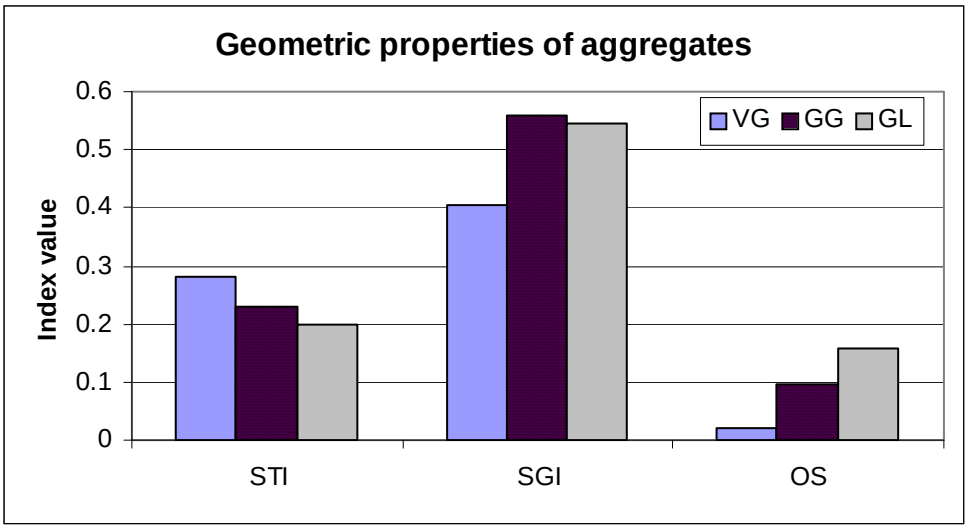

Figure 3.26. **Aggregate Geometric Properties Summary.**

Aggregate Physical Properties

Gradation (also called particle-size distribution or grain-size distribution) refers to the proportions—by mass or weight—of aggregate particles distributed in special particle-size ranges (Somayaji 2001). It affects the workability of concrete which may, in turn, affect the segregation of constituents, bleeding, water-cement requirements, handling, placing, and finishing characteristics. These factors may then affect strength, volume change, durability, and the economy of concrete.

The gradations for three aggregates studied are illustrated in Figure 3.27. Not only maximum size but also the fineness modulus can be calculated from the gradation curves of aggregates. It is useful as an indicator of the average size of an aggregate. A lower fineness modulus of aggregate indicates a larger percentage of finer materials; similarly, a higher number means fewer finer particles or plenty of coarser particles. The fineness modulus cannot be used as a single description of the grading of an aggregate, but it is valuable for measuring slight variations in the aggregate gradation. It gives an indication of the probable behavior of a concrete mix made with aggregate having a certain grading, and the use of the fineness modulus in assessment of aggregates and in mix proportioning has had many advocates (Neville 1995,

Popovics 1966). Therefore, both of these parameters were used to investigate size effect of aggregates studied, where the results are summarized in Table 3.13.

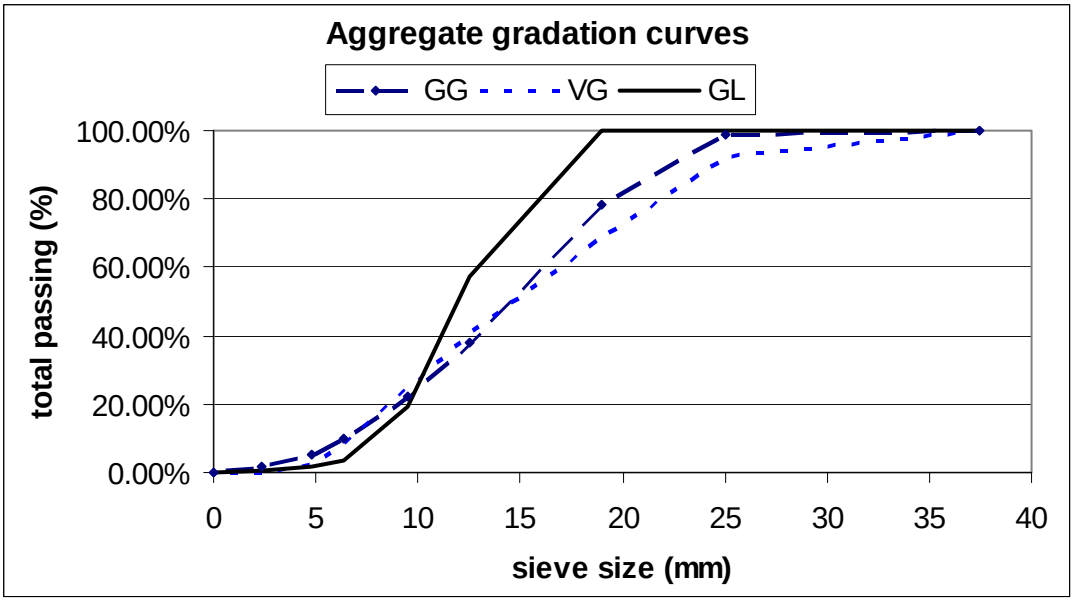

Figure 3.27. Aggregate Gradation Curves.

Table 3.13. Physical Properties of Aggregates.

Aggregate type	GL	VG	GG
Max. size (in)	3/4	1	1
Fineness Modulus	6.78	7.04	6.92
BSG-od	2.50	2.56	2.56
DRUW (lbs/ft^3)	94.17	103.3	102.74
AC (%)	4.79	1.42	1.05

It is obvious that there was a finer grading associated with GL aggregate than the gravel aggregates. The two gravel aggregates had the same maximum aggregate size; however, the VG aggregate had higher contents of particles at larger size levels than GG,

which can also be found from their fineness modulus data. Larger aggregate size can have a detrimental effect on the bonding due to the following reasons:

- for a given volume of coarse aggregate, a larger maximum size reduces the specific surface area of aggregate;
- an increased stress concentration and microcracks in the vicinity of the aggregate is expected with decreased surface area;
- larger aggregate size results in the increases of the perimeter and thickness of interfacial layer between mortar and aggregate so that a larger flaw can be formed and the bond strength decreased (Akçaoğlu et al. 2002); and
- larger aggregate particles tend to accumulate more bleed water around it, which could lead to a higher local w/cm and subsequently, a higher bulk porosity and the size and porosity in the ITZ than the ITZ around the smaller aggregates (Elsharief et al. 2003; Basheer et al. 1999).

Therefore, in terms of aggregate size effect, the decreasing rank order of bonding performance as evaluated is GL, GG, and VG.

Other physical properties are also summarized in Table 3.13. It can be seen from Table 3.13 that all three aggregate types, especially the two types of gravel, had very close values of BSG-od and DRUW. AC represents the maximum amount of water the aggregate can absorb. As for the AC, the two gravels had very close values. However, GL had much higher AC than the gravel aggregates, which means that the GL aggregate is much more porous and absorbent. Though abnormally high absorption capacities indicate high-porosity aggregates, which may have potential durability problems, this property is beneficial to the bond performance at early ages, because the process of absorption increases and improves the contact area between the mortar and the aggregate. Therefore, in terms of AC, the bonding performance rank can be predicted as GL, VG, and GG in a decreasing order.

Aggregate Chemical Properties

Struble et al. (1980) stated that one of the sources of the aggregate-mortar interfacial bond is a chemical bond resulting from a reaction between the aggregate and the cement paste. Therefore, in this project, an attempt was made to provide evidence elucidating the role played by aggregates in influencing ionic chemical interactions at the interface.

The total bond Gibbs free energy between water and aggregates could be a good parameter to represent the chemical characteristics of aggregate relative to the concrete bonding performance, since it represents the preference of aggregate to pull water. However, the equipment problem did not allow this test to be done. As an alternative, the mineralogy analysis of aggregates was conducted by visual observation and optical microscope analysis, as shown in the rock components table (Table 3.14). It was found that these two gravels are actually mixtures of several rock components. GG is a combination of chert (i.e., microcrystalline quartz), quartzite, and acid volcanic, while VG is composed of chert, quartzite, limestone, and acid volcanic. It can be seen that VG and GG have almost similar chert content. However, GG has a much higher content of quartzite than VG. GG has no limestone in it, but VG contains about 21.09 percent of limestone. Different compositions of rock components for these aggregates lead to different chemical activities and, subsequently, the aggregate-mortar bond.

Table 3.14. Rock Components of Aggregates.

Aggregate Type		GL	VG	GG
Rock components (%)	Chert	N/A	67.26	68.38
	Quartzite	N/A	8.03	24.21
	Limestone	100	21.09	N/A
	Volcanic	N/A	3.42	6.25

N/A = Non applicable

The study on ITZs of different rock types at varied curing ages conducted by Tasong et al. (1999) provided reasonable interpretations of the results obtained in this

project. Figure 3.28 compares the ITZs of limestone and quartzite at an early age by SEM analysis. It shows that very high porosity formed in the limestone ITZ (shown in Figure 3.28[a]), while it was not found in the quartzite ITZ. Instead, the cement paste side of the quartzite ITZ did not show any microstructural differences compared with its bulk paste (shown in Figure 3.28[b]). Different from previous findings by other researchers (Monteiro and Mehta 1986), carbon dioxide gas given off as a result of a chemical interaction between the limestone and the hydrating cement paste is considered to be the main reason for this high porosity (Tasong et al. 1999), which accounts for the weaker bond between this rock and the cement paste at an early age.

The study on $Ca(OH)_2$ orientation index at ITZ for different rock types proved similar conclusions as well, which represents the degree of preferred orientation of $Ca(OH)_2$ crystals with their c-axes normal to the aggregate surface (Grandet and Ollivier 1980). Higher values of $Ca(OH)_2$ orientation index represents more $Ca(OH)_2$ crystals orientated with their c-axes perpendicular to the ITZ, which weakens the ITZ structure and the associated bonding between aggregate and mortar. The $Ca(OH)_2$ orientation index at the limestone ITZ was higher than that of the bulk paste at all ages studied, while that at the quartzite ITZ was more or less the same as that of the bulk cement paste at all ages studied. In addition, for all ages studied, quartzite ITZ provided lower $Ca(OH)_2$ orientation index than limestone, which indicates the poorer ITZ of the former than the latter. The low $Ca(OH)_2$ orientation index at the quartzite ITZ could be due to a pozzolanic reaction between Si^{4+}, leached out of the rock, and the $Ca(OH)_2$ or the hydroxyl ion to produce calcium silicate (CSH), which is known to enhance the density of the ITZ and subsequently increase the bond strength.

Though detailed information of mineralogy analysis by XRD technique is recommended for further study, it is not surprising that due to the higher content of quartzite and no limestone in GG, GG was expected to provide the more beneficial chemical reaction than the other two aggregate types. The very porous nature of the ITZ associated with the reaction of limestone with the cement paste at an early age resulted in a negative effect on the bonding strength. Therefore, the decreasing rank order of

bonding strength as evaluated in terms of aggregate chemical properties is GG, VG, and GL.

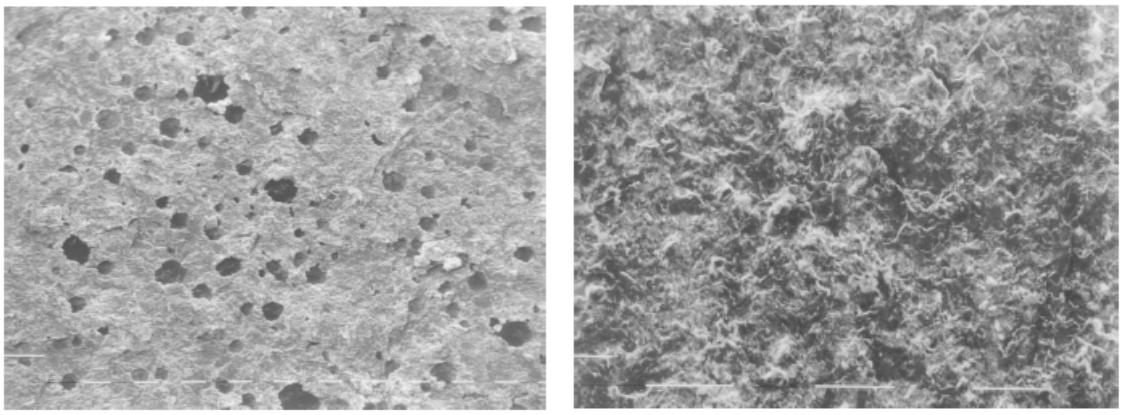

(a) Limestone ITZ (b) Quartzite ITZ

Figure 3.28. ITZ Comparisons of Limestone and Quartzite (Tasong et al. 1999).

UTILITY THEORY

To put it in its simplest form, utility theory is a way to compare dissimilar things (apples and oranges) based on the following concepts (Ledbetter et al. 1977):

- Value – the worth attached to an object or a service, and
- Utility – capability of a practice or measure to satisfy a particular need or provide a desirable result.

It can be used to synthesize and account for a variety of factors that play a role to varying degrees in decision or evaluation processes. A basic premise in utility theory is that decisions are arrived at using a rational basis, i.e., there is a set of transitive preferences for the outcome of the courses of action available, and the best of the alternatives will be chosen on the basis of maximizing some parameter. Furthermore, these preferences can be rated in terms of their relative power (utility) to satisfy the decision-maker's desires.

MacCrimmon has classified the various methods of formally modeling a multiple objective decision-making process into:

- weighting methods,
- sequential elimination methods,
- mathematical programming methods, and
- spatial proximity methods.

Among MacCrimmon's classification scheme, weighting methods are the most appropriate models relative to choosing a particular method. The weighting methods are further subdivided into:

- trade-offs,
- simple additive weighting,
- hierarchical additive weighting, and
- quasi-additive weighting.

Hierarchical additive weighting was selected in this case because of its relative simplicity.

A utility curve is a mapping from one scale of measurement to a second. The first scale represents a result variable that can be quantified, and the second scale is the level of value (satisfaction, utility) that is generated. Use of a utility curve provides a means to characterize the decision variable. It allows one to determine the utility of any decision variables once a particular value of that variable is known.

In accordance with the hierarchical additive weighting method of decision analysis, the individual utilities for each decision criterion must be weighted and added together to give an overall utility for each design method. Weighted expected values are added directly according to the following relation:

$$E(u) = \sum_{i=1}^{n} w_i E_i(u) \tag{3.31}$$

where,

$E_i(u)$ = the average rating of the i^{th} attribute component,

w_i = the weight of the i^{th} attribute component,

$E(u)$ = the overall expected rating of utility, and

n = the number of attribute components.

Overall Evaluation of Aggregate Contribution

Based on the investigation of the aggregate physical, geometric, and chemical properties described in the previous section, it can be seen that any property alone could not be used to completely evaluate bond strength. This is because the aggregate-mortar interfacial bond for a given cement paste was found not to be a simple function of any one of the aggregate properties, but a function of all three properties aggregated together. In addition, different relative importance existed in the different aggregate properties and different components within the property, which then affected the overall contribution of that particular property (i.e., physical, geometric, and chemical) to the interfacial bond of the concrete.

As previously introduced, utility theory facilitates a way to compare dissimilar things based on their values and utilities. Therefore, a rating system based on utility theory was applied to evaluate the overall contribution of aggregate properties on concrete bonding performance. A combined value can be generated to represent the integral overall contribution of the aggregate properties for each aggregate type by assigning a pre-determined weighting factor to the rating of each individual aggregate property allowing for all rating values to be combined into a single parameter in Equation 3.31.

Table 3.15 lists a summary of overall evaluation for aggregates investigated, where the rating system is on a scale of 0 (poor) to 10 (best). Higher overall expected

rating value indicates better overall aggregate contribution to the bonding performance, which is identified based on the combination of physical, geometric, and chemical properties with suggested weighting values of 4, 3, and 3, respectively. These weighting values were assigned on the basis that physical properties (with a value of 4) are the most basic properties relating to concrete mix and construction design. Geometric and chemical properties (with a value of 3 each) were assumed to have equal contribution and then were assigned equal weighting values.

Table 3.15. **Overall Evaluation for Aggregates.**

	Weight	**Attribute**	**Weight**	**Rating**		
				GG	**VG**	**GL**
Physical Properties	4	Size effect	5	5	3	8
		AC	5	4	4	8
Geometric Properties	3	Angularity	3.5	8	3	6
		Texture	3.5	6	8	3
		Percent flat particles	3	5	8	3
Chemical Properties	3	N/A	N/A	8	4	5
Overall Rating				6.1	4.5	5.9

N/A = Non applicable

Within each property, there are sub-attribute components with individual weighting values. Within the scope of this project, the aggregate contribution in terms of physical property was evaluated with respect to aggregate size effect, AC; angularity, texture, and percentage of flat/elongated particles were considered in the evaluation of the aggregate contribution in terms of geometric properties.

As shown in Table 3.15, different rating values were assigned to each aggregate type based on the analysis of bonding performance in each attribute component in the previous section. Higher rating values represented better performance of components for different aggregate types. Equation 3.31 was applied twice to:

- get overall rating values for physical and geometric property considering their sub-attributes, and
- obtain the combined rating values representing overall aggregate contribution in terms of all three properties.

The overall ratings considering all attributes and their sub-attributes were 6.1, 5.9, and 4.5 for GG, GL, and VG, respectively, which indicated that GG and GL provided the similar higher rating level (although GG is slightly higher than GL) while VG is characterized by the lower rating. The higher rating of GG is primarily due to higher quartzite content and presence of lesser amount of flat particles than VG. Higher quartzite contents make the SFE low and improve the mechanical aspect of bond strength. This result also matched the experimental design analysis very well.

Therefore, gravel aggregates containing considerable amount of quartzite can provide acceptable bonding performance between the aggregate and the mortar. In addition on this premise, for a given aggregate type, based on the overall evaluation of the aggregate contribution, aggregate blending at selected combination may also be a possible means to optimize the aggregate contribution to bond strength of concrete. Based on the composite contribution of the individual aggregate properties to the bonding strength of concrete as depicted by utility theory, this approach allows for the selection of the best aggregate type in concrete paving construction.

Feasibility Evaluation of Design Combinations

The previous Taguchi design analysis indicated the relative importance of the design factors relative to the bond strength, and different effects of levels for each factor. Therefore, utility theory can also be used to evaluate the feasibility of mixture design

combinations relative to the bonding performance. The basic idea behind the use of utility theory is that if there is a set of prerequisite preferences associated with the end result of a given design combination, then the best combination can be chosen on the basis of maximizing the rating.

It can be accomplished in a similar manner as that of the aggregate evaluation, but with respect to:

- aggregate contribution,
- w/cm,
- curing method, and
- ultra-fine fly ash content.

A combined value can be generated to represent the integral overall performance of a design combination by assigning a user defined weighting factor to the rating of each individual component allowing for all rating values to be combined into a single parameter using Equation 3.31. Figure 3.29 shows the correlation between the rating values and bonding performance in the utility curve, where the rating system is on a scale of 0 (poor) to 10 (best). It indicates that the higher the rating values, the better the bonding performance and the more feasible the design combinations.

Table 3.16 provides an example of this approach by comparison of test run 1 (i.e., VG + WMC + 0.4 of w/cm + 8 percent of ultra-fine fly ash), test run 3 (i.e., VG + WOC + 0.45 of w/cm + 20 percent of ultra-fine fly ash), and the optimum design (i.e., GG + WMC + 0.4 of w/cm + 8 percent of ultra-fine fly ash). As shown in Table 3.16, different weights and ratings were assigned to the design factors due to the different relative importance of each factor to K_{IC}. Higher weights represented greater importance given to the factors relative to K_{IC} and higher ratings represented better performance relative to bond strength. Optimum design combination provided the highest overall rating value, which was also correlated with the previous result from the experimental design. The overall rating values of test run 1 (i.e., 6.6) was higher than that of test run

3 (i.e., 5.6). Therefore, the design of test run 1 is more feasible (Figure 3.29), which is consistent with the 1 day K_{IC} results of these two designs (Figure 3.10). In addition, these two designs used the same aggregate type. However, they provided different bonding performance due to different selections of other factors. Therefore, for a given gravel aggregate type, it appears to be possible to improve the bonding performance of concrete by selecting optimum levels of other design factors.

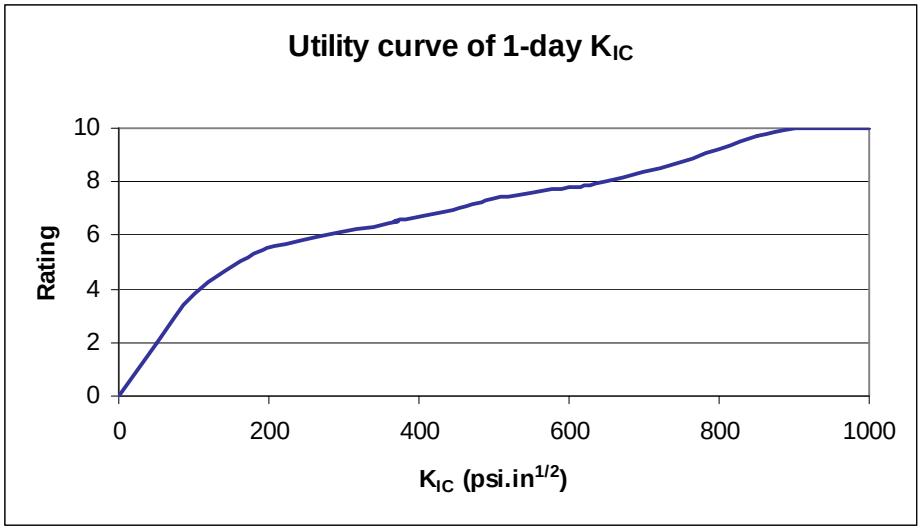

Figure 3.29. Utility Curve of One-day K_{IC}.

Table 3.16. Summary of Evaluations by Rating Systems.

	Weight	Rating		
		Test 1	Test 3	Optimum
Aggregate type	4	4.5	4.5	8.0
Curing method	3	8.0	5.4	8.0
W/cm	2	8.0	6.9	8.0
Ultra-fine fly ash content	1	7.5	8.0	7.5
Overall rating		6.6	5.6	8.0

The application of utility theory to the evaluation of the overall contribution of aggregate properties to the bonding performance of concrete, and feasibility of design combinations should enable the selection of the best available aggregate type and aggregate combination to optimize the mixture for concrete paving construction to minimize delamination and subsequent spalling distresses.

CHAPTER IV
DELAMINATION PREDICTION THROUGH STRESS ANALYSIS APPROACH

GENERAL

An approach to predict the delamination occurrence by numerical simulation and laboratory investigation was proposed. It is based on comparing K_I (stress intensity factors) and K_{IC} (critical stress intensity factor or fracture toughness) directly in terms of fracture criteria for unstable growth. One can then determine the crack stability of the material under given loading conditions. It can also be used for evaluating the effectiveness of pavement design methods to prevent delamination and spalling distress.

DELAMINATION OCCURRENCE PREDICTION

During the first three days after paving, the moisture gradients near the surface of the pavement slab can actually generate stresses large enough to create delaminations in the concrete. It is possible to predict early age delamination in the concrete. In this project, a fracture mechanics based approach is facilitated by numerical analysis to predict the time when delamination would occur. As described in previous chapters, one necessary condition for delamination to develop is the sufficient evaporation of pore water from the hydrating concrete resulting in differential drying shrinkage near the pavement surface. As a consequence of its dominating effect, the nature of the moisture profile in hardening concrete particularly near the evaporative surface was also considered in this prediction protocol.

Criterion for Delamination Occurrence

Stress intensity and fracture toughness are key fracture mechanics parameters that can be used by materials engineers and designers in design analysis (Boresi et al. 1993; Irwin 1957; Hertzberg 1976). By comparing K (stress intensity factors) and K_C (critical stress intensity factor or fracture toughness) directly, one can then determine the crack stability based on fracture criteria for unstable growth of the

material under the given loading conditions. In the previous chapters, fracture toughness was used to represent the nature of the interfacial bond between the aggregate and mortar relative to delamination. Therefore, it appears to be feasible to predict the occurrence of delamination by comparing the development of K and K_C.

The crack along the aggregate-matrix interfaces may have been caused either by tensile or by shear stresses or by combinations of tensile and shear stresses (Taylor and Broms 1964). Büyüköztürk and Lee (1993) stated that cracking of mortar-aggregate interfaces involves mixed mode fracture effects due to the difference in the properties between mortar and aggregate, as well as due to loading conditions, which means that the stress field in the vicinity of the crack front is defined not only by the stress intensity factor K_I, but also by K_{II} (Richard et al. 2005). In this case, plane mixed mode conditions are characterized by the superposition of the fracture modes I and II. As can be seen in Figure 4.1, the beginning of unstable crack growth can be described by a fracture limit curve. If the loading condition on a crack in a structure corresponds to the point P, no unstable crack growth is to be expected. If in contrast to this, the load level increases in such a way, which for example, point C of the fracture limit curve is reached, immediate unstable crack growth will occur.

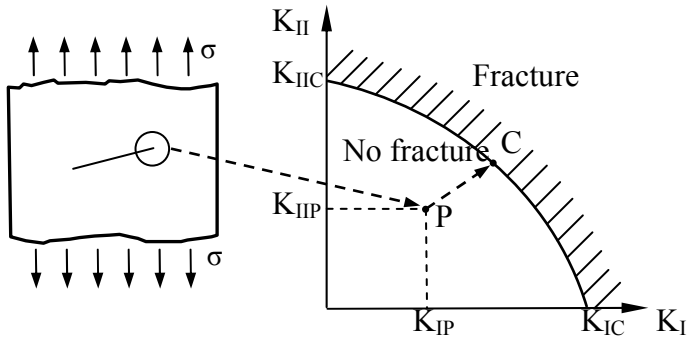

Figure 4.1. Fracture Limit Curve (Richard et al. 2005).

However, different researchers have different opinions about this. Previous research (Tan et al. 1995) showed that for the same interfaces the specific fracture energy in shear (mode II) is an order of magnitude higher than in tension (mode I). Since interfacial cracking precedes bulk cracking, initiation of interfacial cracks in mode I is the critical step for failure. The mode II fracture energy is found to be far larger than the mode I fracture energy (Bažant and Pfeifer 1987), and the critical stress intensity factor K_{IC} is about a fifth of K_{IIC}, which means that G_{IIF} is about 25 times as large as G_{IF} (Ozbolt et al. 1999). In addition, the predicted values of mode II stress intensity factor (K_{II}) were much smaller than those of mode I stress intensity factor (K_I), which will be shown later. Therefore, in this project, the crack initiation in mode I was considered the predominant type. Then the criterion for predicting early age delamination occurrence is that delamination occurs when $K > K_{IC}$.

Until now, many methods have been adopted to compute K, such as finite element method, boundary element method, and finite difference method, etc. Among these, finite element method is the most popular one. In this project, finite element software packages—Temperature and Moisture Analysis of Curing Concrete ($TMAC^2$) (Jeong 2003) and ABAQUS (2003) were applied to predict the development of K.

Concrete Moisture Diffusivity Profiles

The nature of the moisture profile in hardening concrete particularly near the evaporative surface and the associated drying shrinkage are subjects of great interest relative to their effects on the formation of early aged delamination at cracks and joints in concrete pavements. Moisture flow and diffusion in concrete have been a significant topic in the research of concrete pavement materials (Bažant and Najjar 1972; Parrott 1988; Parrott 1991; Xin et al. 1995; Buch and Zollinger 1993).

In freshly placed concrete, moisture movements are typically characterized by high rates of diffusion followed by gradually lower rates 10 to 12 hours after placement. This drying characteristic is inherently related to a material property referred to as the moisture diffusivity (D), which has been generally accepted to be dependent upon the

pore water content within the cement paste. It has been observed that moisture diffusivity may change significantly with variations in the moisture content or the relative humidity (from 100 to 70 percent) of the concrete (Pihlajavaara 1964; Kasi and Pihlajavaara 1969; Bažant 1970; Bažant and Najjar 1972). At constant water content (w), moisture diffusivity changes little with time in mature concrete in contrast with the dramatic changes fresh concrete undergoes during the first 24 hours after placement. In this regard, diffusivity in early aged concrete is not only a function of humidity but also of concrete age and porosity. The moisture diffusivity is important in modeling moisture flow in hardening concrete.

The rate of moisture flow through concrete can be expressed by the velocity of flow (J) representing the mass of evaporable water passing through a unit area perpendicular to the direction of flow per unit time. The velocity of flow by Darcy's law is derived from energy gradients (Bažant and Najjar 1972):

$$J = -C \cdot grad\ \mu \tag{4.1}$$

where, μ is Gibb's free energy (GFE) per unit mass of evaporable water, and the coefficient C characterizes the permeability of porous concrete. Equation 4.1 is restricted to small energy gradients and laminar flow conditions. Assuming water vapor behaves as an ideal gas, Gibb's free energy is (Bažant and Najjar 1972):

$$\mu = \left(\frac{RT}{MV_w}\right) \cdot \ln H + \mu_{sat}(T) \tag{4.2}$$

where,

R = universal gas constant (8.3143 J/mol/^{o}K),

T = absolute temperature (^{o}K),

M = molecular weight of water (18.015 g/mol),

V_w = specific volume of water (1 cm^3/g),

H = humidity of concrete $\left(= \frac{RH}{100}\right)$, and

RH = relative humidity of concrete (%).

Equation 4.1 can be rewritten in terms of temperature (T) and humidity (H) of concrete as (Bažant and Najjar 1972):

$$J = -c \cdot grad\ H \tag{4.3}$$

where, the coefficient c is permeability as a function of temperature and humidity of concrete as below:

$$c = \left(\frac{RT}{MV_w}\right) \times \left(\frac{C}{H}\right) \tag{4.4}$$

The relationship between humidity and water content within concrete at a constant degree of hydration and temperature is described by desorption or sorption isotherms as illustrated in Figure 4.2 (Bažant and Najjar 1972). It should be noted that the isotherm for sorption is different from the isotherm for desorption. This characteristic may be due to the various states of equilibrium of the pore water. An investigation by Parrott (1988) implied the significance of porosity with respect to the position of the desorption or sorption isotherm within concrete. The results indicated that a greater amount of moisture loss in drying concrete would occur in regions nearest to exposed drying surfaces, which also may be regions of greater porosity. Therefore, it can be explained that there is a greater volume of coarse pores at positions nearer to an exposed concrete surface and consequently the relationship between weight loss and relative humidity of concrete will vary with distance from the exposed surface. In this respect, the performance and behavior of a concrete pavement may be affected by the porosity of the surface. It should also be noted that the resulting desorption isotherm at

any time during hydration of the hardening slab concrete must be interpreted not only as a function of the degree of hydration, but also as a function of porosity. At a given porosity, the desorption isotherm may be expressed in the differential form as (Bažant and Najjar 1972):

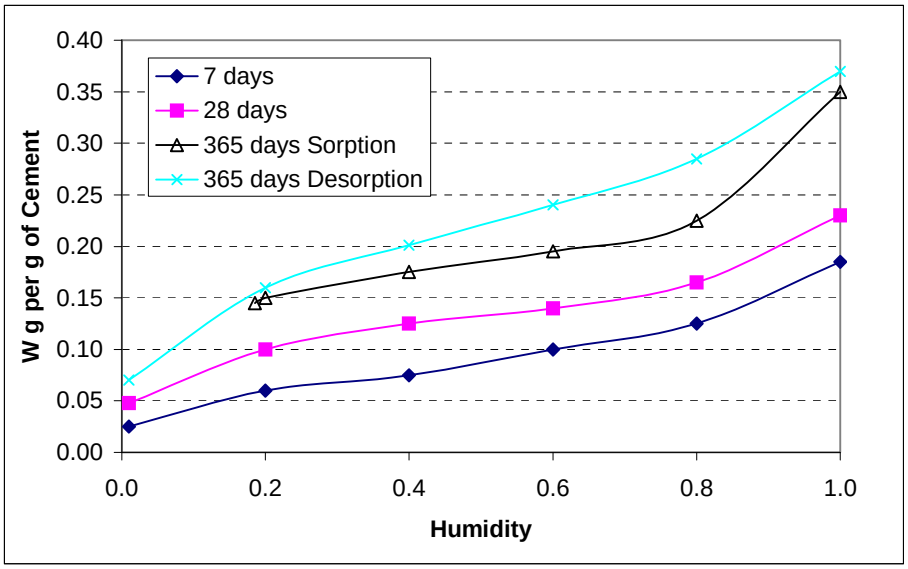

Figure 4.2. Example of Desorption-Sorption Isotherms of Cement Paste, Established by Powers (Bažant and Najjar 1972).

$$dH = kdw \tag{4.5}$$

$$k = \left(\frac{\partial H}{\partial w}\right)_w \tag{4.6}$$

where, the parameter *k* represents the slope of the moisture isotherm where the mass of water (w) is described as a function of humidity (H). Moisture movements in an unsaturated porous medium are effected by temperature profiles of the medium (Huang 1979; Suh et al. 1988; Somasundaram et al. 1989). Thus, the calculation of

humidity in hydrating concrete requires additional terms under variable temperature conditions as (Bažant and Najjar 1972):

$$dH = kdw + KdT + dH_s \tag{4.7}$$

where,

K = hygrothermic coefficient ($= \left(\frac{\partial H}{\partial T}\right)_w$), and

dH_s = change in humidity (H) due to hydration at a constant water content (w) and time (t).

The hygrothermic coefficient represents the change in humidity due to 1°F of change in temperature at a constant water content and a given level of hydration. It should be noted that the pore water content (w) includes both the evaporable or capillary water (w_c) and the non-evaporable water (w_n) per unit volume of materials.

The rate of moisture flow in unit volume of concrete is determined from:

$$\frac{\partial w}{\partial t} = -divJ \tag{4.8}$$

Substituting Equation 4.3 into Equation 4.8 and subsequently substituting Equation 4.8 into Equation 4.7 leads to:

$$\frac{\partial H}{\partial t} = k \cdot div(c \cdot gradH) + \frac{\partial H_s}{\partial t} + K\frac{\partial T}{\partial t} \tag{4.9}$$

which is the diffusion equation for the drying concrete under variable temperature conditions. Equation 4.9 is further developed to be Equation 4.10.

$$\frac{\partial H}{\partial t} = kc\frac{\partial^2 H}{\partial x^2} + k\frac{\partial c}{\partial x}\frac{\partial H}{\partial x} + \frac{\partial H_s}{\partial t} + K\frac{\partial T}{\partial t} \tag{4.10}$$

Permeability (c) is also a function of the porosity and indirectly a function of position x. Because permeability change with position x is assumed to be very small, the second term in Equation 4.10 is considered to be negligible and is consequently dropped from the diffusion equation as:

$$\frac{\partial H}{\partial t} = D\frac{\partial^2 H}{\partial x^2} + \frac{\partial H_s}{\partial t} + K\frac{\partial T}{\partial t} \tag{4.11}$$

where, D (= $k \cdot c$) is moisture diffusivity (L^2/t).

Governing Differential Equations

Drying shrinkage occurs as a result of evaporation of pore water to the surrounding environment; however, it is probably the least widely recognized cause of volume change in concrete paving. Stress occurs when the shrinkage is restrained. Though temperature variation is also a factor in the delamination development, this project specifically focused on early age concrete behavior associated with volumetric contraction due to moisture induced shrinkage. Delamination is caused by differential drying shrinkage induced stress. The drying process is mainly related to the moisture variation in concrete. Whether delamination occurs or not is mainly related to this stress level in concrete. Therefore, in this project, early-age concrete subjected to moisture induced shrinkage was modeled as an isotropic, time-dependent material subjected to coupled hygro-mechanical loading conditions.

For two-dimensional problems we consider three strain components, namely:

$$\varepsilon_x = \frac{\partial u}{\partial x} \tag{4.12}$$

$$\varepsilon_y = \frac{\partial \upsilon}{\partial y} \tag{4.13}$$

$$\gamma_x = \frac{\partial \upsilon}{\partial x} + \frac{\partial u}{\partial y} \tag{4.14}$$

The relations between the components of stress and the components of strain are presented as:

$$\varepsilon_x = \frac{1}{E_1}\left(\sigma_x - \nu_1 \sigma_y\right) + \left(1 + \nu_1\right)\alpha H \tag{4.15}$$

$$\varepsilon_y = \frac{1}{E_1}\left(\sigma_y - \nu_1 \sigma_x\right) + \left(1 + \nu_1\right)\alpha H \tag{4.16}$$

$$\gamma_{xy} = \frac{2\left(1 + \nu_1\right)}{E_1}\tau_{xy} \tag{4.17}$$

Compared with the original Hooke's law, there is one more term at the right side of Equations 4.15 and 4.16, which is the strain component due to the moisture variation.

The differential equations of equilibrium for two-dimensional problems are (Timoshenko and Goodier 1970):

$$\frac{\partial \sigma_x}{\partial x} + \frac{\partial \tau_{xy}}{\partial y} + X = 0 \tag{4.18}$$

$$\frac{\partial \sigma_y}{\partial y} + \frac{\partial \tau_{xy}}{\partial x} + Y = 0 \tag{4.19}$$

Converting Equations 4.15, 4.16, and 4.17 to equations represented by displacement components, then substituting them into Equations 4.12, 4.13, and 4.14, and subsequently substituting into Equations 4.18 and 4.19, the equilibrium equations are finally developed as:

$$\frac{\partial}{\partial x}\left(\frac{E}{(1+\nu)(1-2\nu)}\left((1-\nu)\frac{\partial u}{\partial x}+\nu\frac{\partial \upsilon}{\partial y}\right)\right)+\frac{\partial}{\partial y}\left(\frac{E}{2(1+\nu)}\left(\frac{\partial u}{\partial y}+\frac{\partial \upsilon}{\partial x}\right)\right)+\frac{\alpha E}{(1-2\nu)}\frac{\partial H}{\partial x}+X=0 \qquad (4.20)$$

$$\frac{\partial}{\partial x}\left(\frac{E}{2(1+\nu)}\left(\frac{\partial u}{\partial y}+\frac{\partial \upsilon}{\partial x}\right)\right)+\frac{\partial}{\partial y}\left(\frac{E}{(1+\nu)(1-2\nu)}\left(\nu\frac{\partial u}{\partial x}+(1-\nu)\frac{\partial \upsilon}{\partial y}\right)\right)+\frac{\alpha E}{(1-2\nu)}\frac{\partial H}{\partial y}+Y=0 \qquad (4.21)$$

where,

E = elastic modulus of concrete,

ν = Poisson's ratio of concrete,

α = coefficient of shrinkage, and

H = relative humidity of concrete.

For two-dimensional analysis, Equation 4.11 is converted to:

$$\frac{\partial H}{\partial t}=D\left(\frac{\partial^2 H}{\partial x^2}+\frac{\partial^2 H}{\partial y^2}\right)+\frac{\partial H_s}{\partial t}+K\frac{\partial T}{\partial t} \qquad (4.22)$$

If the dry bulb temperature, T, used in Equation 4.22 is assigned a constant temperature value (though it is not a realistic assumption), the third item in the right side of the equation will become zero, simplifying Equation 4.22 to:

$$\frac{\partial H}{\partial t}=D\left(\frac{\partial^2 H}{\partial x^2}+\frac{\partial^2 H}{\partial y^2}\right)+\frac{\partial H_s}{\partial t} \qquad (4.23)$$

If the humidity change due to self-desiccation is assumed to be insignificantly small, Equation 4.23 reduces to:

$$\frac{\partial H}{\partial t} = D\left(\frac{\partial^2 H}{\partial x^2} + \frac{\partial^2 H}{\partial y^2}\right) \tag{4.24}$$

Equations 4.20, 4.21, and 4.24 are governing equations used in this analysis. The third term on the left side of Equations 4.20 and 4.21 indicates that the relative humidity of the concrete influences the force equilibrium of the concrete by strains due to shrinkage or swelling. The proportionality between drying shrinkage and the decrease of pore humidity is dictated by the coefficient of shrinkage, which is analogous to the coefficient of thermal expansion, and it is equivalent to the ultimate shrinkage (Lim 2002).

It has been noted that there are some similarities between the coupled thermal stress problem and the coupled hygro-mechanical stress analysis warranted by dimension analysis and comparison, though time dependency is not addressed (Zhang 2004). For example, the relative humidity is corresponding to the temperature, and the moisture diffusivity is corresponding to the thermal conductivity. Heat transfer and the coupled thermal stress have been studied in mechanical engineering for decades. Some methods for conducting this type of analysis are already well-established and many commercial software packages, for example, ABAQUS and ANSYS have provided options to solve the differential equations numerically. Therefore, the program specifically for the coupled thermal stress approach in ABAQUS was used for the coupled hygro-mechanical stress analysis. Considering the time-dependency of E, H, and D in the above equations, subroutines were developed to facilitate the input and updating of those parameters.

Numerical Study

Although the definition of the term early age is somewhat arbitrary, the analysis of drying and stress development was conducted up to about 7 days (604,800 seconds).

Figure 4.3 shows the typical geometry and finite element mesh of the pavement section studied, and the mechanical boundary conditions are also shown. The concrete slab was 0.3 m (12-in) thick. Due to the symmetry of the pavement structure, a 1 m (3.3-ft) length was chosen. The finite element analyses were made with the ABAQUS program using rectangular mesh of 4-node quadrilateral elements. Full bond between concrete slab and foundation was modeled by fixing displacements in all directions. Only vertical displacements were allowed for the left and right side of the structure, since the section was considered as a part of the whole pavement. For some cases, the concrete slab was also notched to simulate the sawcut effects, with a notch width of 4 mm.

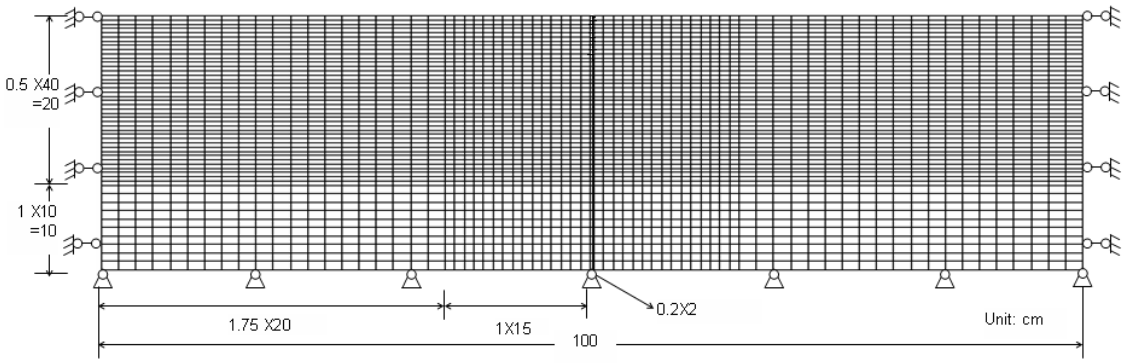

Figure 4.3. Geometry and Mesh of Modeling.

The ABAQUS program offers the contour integral method for the evaluation of stress intensity factors, which means that in a finite element model each evaluation can be thought of as the virtual motion of a block of material surrounding the crack tip. Each such block is defined by contours: each contour is a ring of elements completely surrounding the crack tip or crack front from one crack face to the opposite crack face. The beginning of unstable crack growth as well as the crack growth direction can be determined by the use of one fracture criteria (Erdogan and Sih 1963; Sih 1974; Bilby

and Cardew 1975). Here, the criterion of energy release rates by Nuismer (1975) was chosen for calculating the direction of cracking initiation.

At the time of concrete placement, a concrete mixture is assumed to be completely wet. Therefore, the initial boundary condition was as follows:

$$H = 1.0 \text{ at } t = 0 \tag{4.25}$$

The stress intensity factor at an early age was investigated by incorporating distribution and history of moisture relative to the material-related moisture transport property in the analysis. Since the moisture differences between ambient conditions and those inside the concrete cause moisture to migrate from the concrete to the surrounding atmosphere, the humidity at the surface and bottom of the concrete slab were considered as the boundary conditions.

The TMAC^2 program, a finite element program developed by TTI, produces the temperature and moisture profiles and accounts for the interaction between them at any points in a hydrating concrete slab as a function of time and ambient boundary conditions (Jeong 2003). The input data include climatic parameters, mix design, materials properties, parameters for hydration, and construction parameters. The finite element mesh of TMAC^2 has a total of 120 rectangular elements (5 columns × 24 rows) with 539 nodal points (9 nodal points per each element). This program was used to predict the humidity histories, with the assumption that the humidity at the concrete surface has been assumed to be the same as the humidity of ambient condition during the analysis period. Figure 4.4 shows an example of relative humidity trends at the bottom and the surface of the slab estimated from the TMAC^2 program.

A typical Poisson's ratio of 0.15 was used for the concrete. The history of elastic modulus of concrete was converted from that of compressive strength based on its relationship from the American Concrete Institute (ACI) building code formula (Equation 4.13) (ACI 1996), where compressive strength data were obtained from

laboratory testing. The coefficient of shrinkage, equivalent of the ultimate shrinkage, was determined by the BP model (Bažant and Panula 1978):

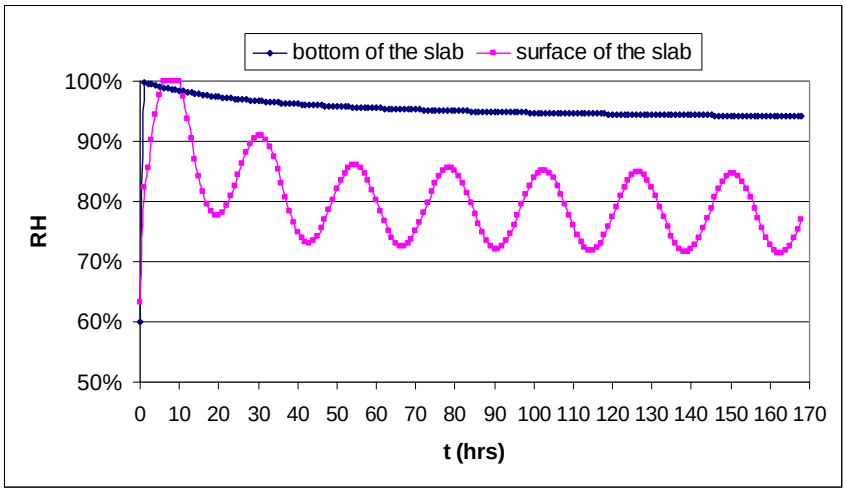

Figure 4.4. Relative Humidity Trends from TMAC[2].

$$\alpha = \varepsilon_{ult-shr} = 1330 - 970y \tag{4.26}$$

where,

$$y = \left(390z^{-4} + 1\right)^{-1}$$

$$z = 0.381\sqrt{f'_{cyl28}}\left[1.25\sqrt{\frac{a}{cm}} + 0.5\left(\frac{g}{s}\right)^2\right]\sqrt[3]{\frac{1+\frac{s}{cm}}{\frac{w}{cm}}} - 12$$

$\frac{a}{cm}$ = total aggregate/cementitious ratio,

$\frac{g}{s}$ = coarse aggregate/fine aggregate,

$\frac{s}{cm}$ = fine aggregate/cementitious ratio,

$\frac{w}{cm}$ = water/cementitious ratio, and

f'_{cyl28} = 28-day compressive strength of concrete (ksi).

Three subroutines (i.e., USDFLD, UMAT and UMTHT) were developed to facilitate the numerical analysis. Because all material properties used in the analysis were time dependent, USDFLD was used to obtain stress, strain, and relative humidity from previous a calculation step. UMAT was used to update the stiffness matrix of the FEM simulation and UMTHT was used to update the corresponding moisture diffusivity matrix during the simulation.

Example of Stress Intensity Factor Development

An example of typical concrete with material characteristics shown in Table 4.1 was selected for analysis purposes. The development of the concrete elastic modulus is illustrated in Figure 4.5.

Table 4.1. Material Parameters in the Example Analysis.

Parameters	w/cm	Cement factor	a/cm	g/s	s/cm	f'_{cyl28} (ksi)	α (micro-strain)
	0.45	5.5	6.336	4.351	1.985	5.207	424.5

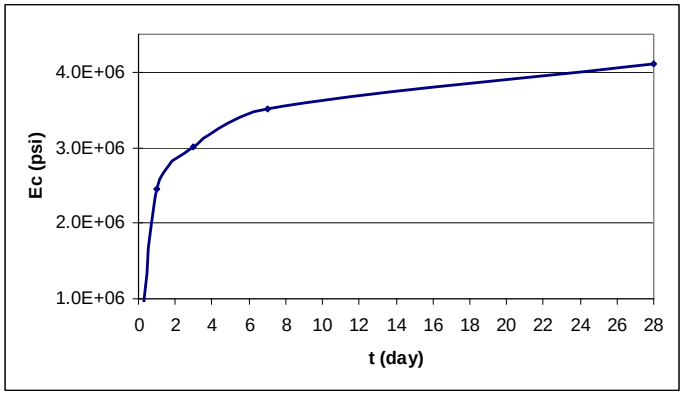

Figure 4.5. Development of Elastic Modulus of Concrete.

The distribution and history of moisture diffusivity was back-calculated from the TMAC[2] program by transforming the governing equations of moisture diffusion to calibrate predicted humidity. Details can be referred from the previous section and also the reference (Jeong 2003). It can be seen from Equation 4.26 that D is the function of both curing time and concrete dimensions. Figure 4.6 shows an example of the prediction of the diffusivity history at 8.02 cm (3.16 in) below the concrete surface.

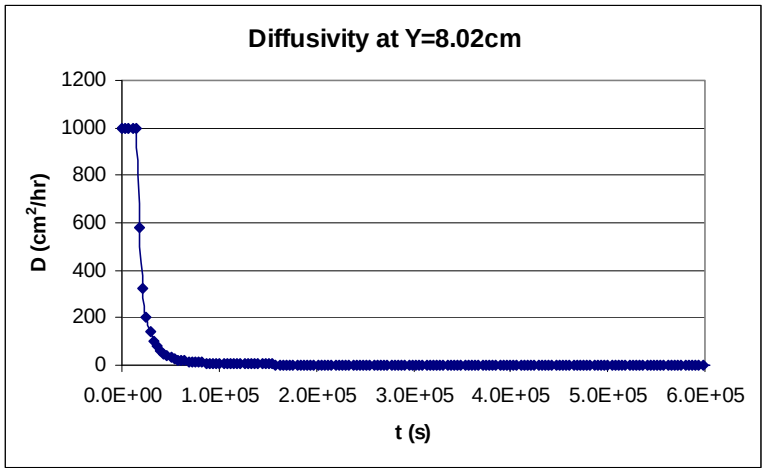

Figure 4.6. Diffusivity History at 8.02 cm below the Surface of Concrete.

The evaluation of the stress intensity factor, K_I, where the relative displacement of mating crack surfaces normal to the fracture plane, is shown in Figure 4.7. From Figure 4.7, it can be seen that instead of increasing with the time monotonically, the development of K_I with the time showed a cycling pattern with the cyclic change of relative humidity profiles, similar to the stress analysis. There were seven sets of peak-and-trough values within the analysis period, which indicates that every day there were maximum and minimum stress values consistent with the relative humidity profiles. In addition, with time, the maximum and minimum stress values increased with a gradually lower rate.

As mentioned before, the development of K_{II} was also conducted. The values of K_{II} associated with the K_I values in Figure 4.7, which correspond to in-plane shear, are

shown in Figure 4.8. Similarly, the development of K_{II} followed cyclic patterns as well, though toward the direction of negative values, where the negative symbol indicated the direction of the crack propagation. The values of K_{II} were much lower than those of K_I. This is the reason that we neglected mode II crack in our analysis.

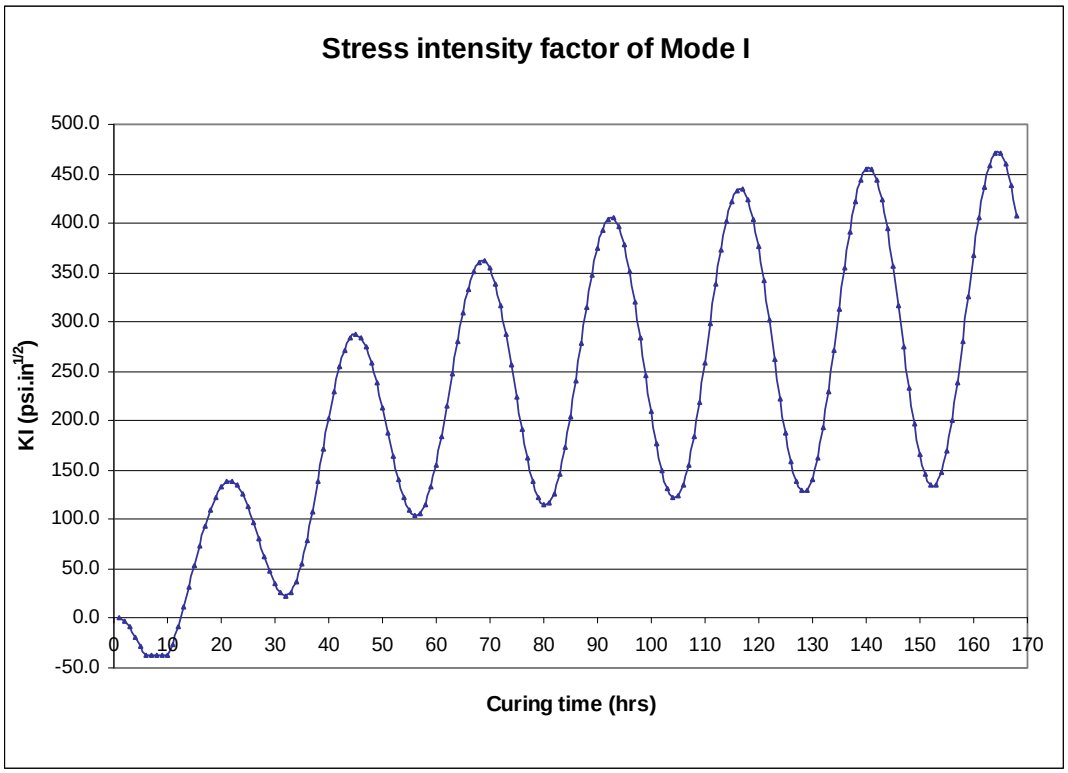

Figure 4.7. Mode I Stress Intensity Factor History.

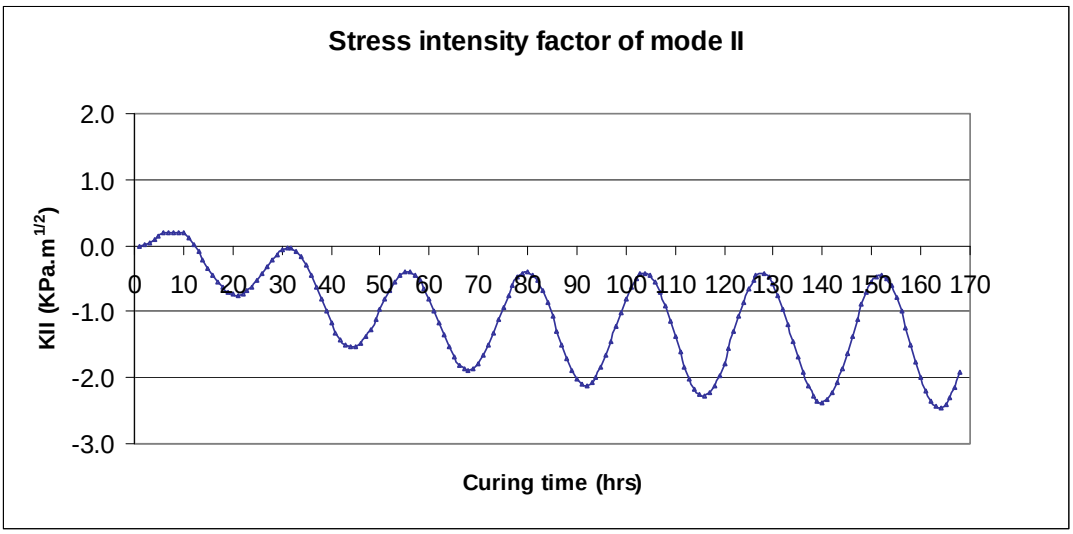

Figure 4.8. Mode II Stress Intensity Factor History.

Prediction of Delamination Occurrence

The occurrence of delamination can be determined by comparing K_I against the fracture toughness, K_{IC}, developed under laboratory investigation. Two examples were utilized to show the ability of this method to select and evaluate the effectiveness of pavement design methods to prevent delamination and spalling in concrete paving.

Crack Induction

The sawcutting technique has been used widely to form controlled cracking and relieve the stress level at the surface of concrete pavements (Tang et al. 1994), and it is considered as one of the remedial measures of delamination in concrete pavements. For the simulation of sawcutting, both horizontal and vertical directions were considered as the direction of crack initiation for K_I prediction. However, the results showed that for an induced sawcut (vertical), the predicted K_I values with vertical crack initiation were much higher than those with horizontal crack initiation. Therefore, K_I values with vertical crack initiation were used for comparison. Figure 4.9 compares the effect of sawcut depth on the K_I development of concrete pavement made with VG, 0.45 of w/cm, and without any curing treatment. The a/h represented the relative sawcut depth, where

a was the sawcut depth, and h was the thickness of the concrete slab. The notch depths were 0, 1, 2, 3, 4, and 6 in, respectively, corresponding to the relative sawcut depths of 0, 1/12, 1/6, 1/4, 1/3, and 1/2.

From Figure 4.9, it can be seen that without sawcut most of the K_I values were lower than K_{IC}, which means that the probability of delamination occurring at the sawcut front is very low. Instead it could occur at any other locations. With the increase of the sawcut depth, the local stress at the sawcut tip increased significantly, which greatly increased the probability of delamination occurring at the sawcut front, while reducing the stress at other locations. Among different relative sawcut depths, relative depth of 1/4 provided the highest K_I values through the period studied. In addition, almost all values of K_I exceeded the corresponding K_{IC}, which indicated that delamination would occur at the sawcut location through the early age of concrete instead of other locations in the pavement. Continually increasing relative notch depth (i.e., 1/3 and 1/2) resulted in a decreased K_I profile. It may be because of lower moisture gradient and associated strain energy. Therefore, within the scope of this project, cutting the pavement 1/4 of the whole slab thickness provided the best performance in terms of relieving delaminations in concrete pavements.

Optimization of Design Factors

As described in Chapter III and in this chapter, use of gravel aggregates in concrete paving suggested a way to optimize the combination of construction and material design factors for improving delamination resistance. These factors include aggregate type, w/cm, replacement with ultra-fine fly ash, and curing method. Figure 4.10 shows the results from two different design combinations:

- GG + 0.4 of w/cm + 8 percent of ultra-fine fly ash + WMC, which is the optimum design combination from analysis of the laboratory data; and
- VG + 0.45 of w/cm + 20 percent ultra-fine fly ash + WOC, which provided a low K_{IC} based on laboratory results.

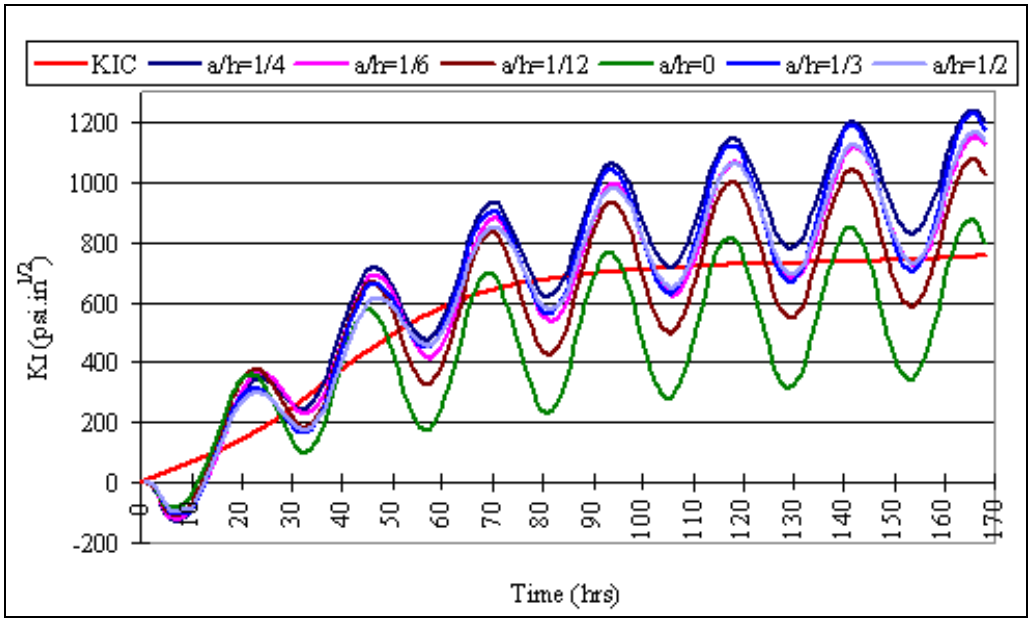

Figure 4.9. Sawcut Effect Comparison.

From Figure 4.10, it can be seen that for combination b, the earliest delamination occurs within 15 hours after the concrete is paved when the K_I development exceeds K_{IC}. However, for combination a, the stress level in the pavement is reduced, and over the analysis period, K_I did not surpass K_{IC}. Therefore, no delamination occurs, which signifies the effectiveness of this method. The result was also confirmed from field tests on SH 290, where a similar materials design was used at one of the 10 test sections and there was no delamination indicates from observations of concrete cores taken at that test section.

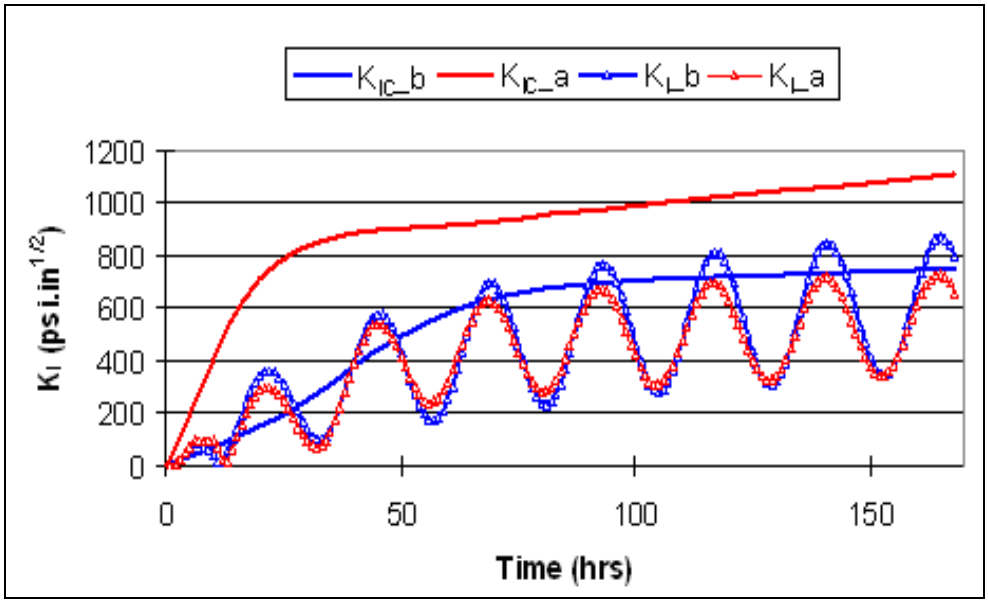

Figure 4.10. Design Methods Comparison.

CHAPTER V
DELAMINATION DETECTION PROTOCOL

INTRODUCTION

Many efforts were made to detect in advance of spalling, horizontal cracking or delamination in selected CRC pavements. Spalling related delamination is believed to occur at an early concrete age and at a rather shallow depth when stresses caused mainly by the moisture variation may surpass the concrete shear strength. This early delamination, can develop into spalling. Although delimination can also occur at the steel bar depth this type of delamination rarely spalls out. Spalling and pop-outs are believed to be associated with horizontal cracks propagating from the transverse cracks. Sansalone and Streett (1997) have used Impact Echo (IE) as an effective NDT method to detect both early delamination and spalling. Kim et al. (2006) combined the IE and the Spectral Analysis of Surface Wave (SASW) to evaluate concrete slabs containing voids. The Portable Seismic Pavement Analyzer (PSPA), a device developed by Baker et al. (1995), was used at several sites in the vicinity of Houston to evaluate the feasibility of locating debonding that may occur in concrete slabs constructed with crushed gravel aggregates. In this chapter, the operating principles of the PSPA, theoretical background on the IE and the SASW, and a delamination detection protocol with the PSPA for field testing are included. The operating principles of the PSPA and the theoretical background on the IE and the SASW are provided in Appendix A. A delamination detection protocol along with typical results of debonding detection is discussed below.

TYPICAL RESULTS OF DEBONDING DETECTION

The Impact Echo method was the primary method used to identify debonded areas. This can be easily done by observing the pattern of the distribution of energy in the amplitude spectrum of each record after it is transformed into the frequency domain.

Typical representations of the intact and debonded time records are shown in Figure 5.1. For an intact location (Figure 5.1a), an emerging surface record appears in the

first 0.3 millisecond of the record, followed by a harmonic response resembling a decaying sine-wave with smaller amplitude than the surface wave energy. The period of this sine-wave corresponds to standing waves propagating in the slabs representing twice the thickness of the slab. On the other hand, for the debonded area (Figure 5.1b), the surface wave energy, even though present, is contaminated with a low-frequency, high-amplitude response. This sine-wave corresponds to the flexural mode of vibration of the concrete in the debonded area.

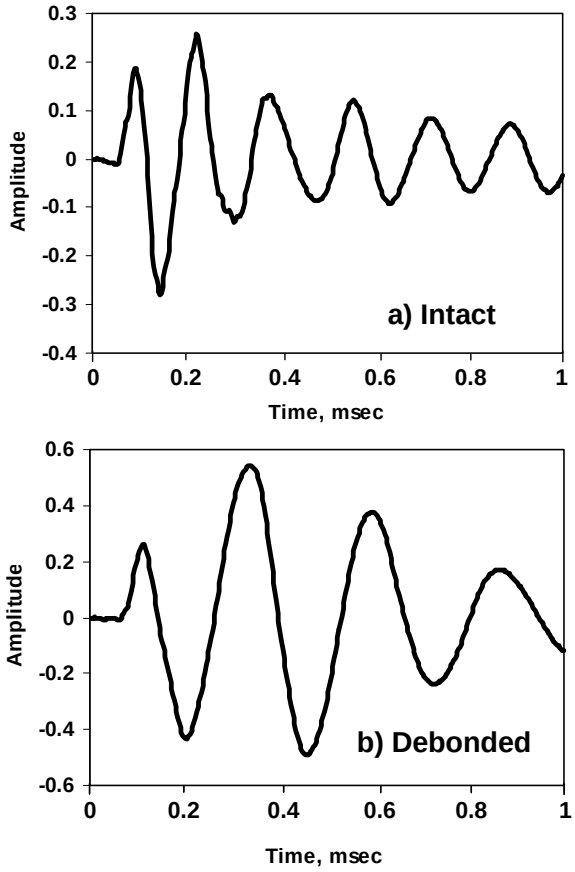

Figure 5.1. Typical Time Records from Intact and Debonded Areas.

To more objectively separate the two modes of vibration, a frequency-domain analysis is beneficial. The results from such an operation are shown in Figure 5.2. For an intact location (see Figure 5.2a), the energy is concentrated toward one frequency (in this case about 6500 Hz) corresponding to twice the thickness of the slab (see Equation 5.7 in Appendix A). A shallow debonded point exhibits one or several peaks with a frequency lower than the thickness frequency as shown in Figure 5.2d. This lower frequency is counterintuitive since according to Equation 5.7 for a shallower discontinuity the return frequency should be greater. The lower frequency occurs because the flexural mode of vibration would dominate the response. In other words, shallow debonding acts like a drum rather than a rigid layer that traps the compression waves propagating within it. A comprehensive description of the differences between the two modes of vibration can be found in Sansalone and Streett (1997). A horizontal crack within a concrete will contain two frequencies: one corresponding to the layer thickness and the second corresponding to the depth of crack; and depending on the amplitude of these peaks two intermediate stages are defined (see Figures 5.2b and 5.2c). The relative amplitudes at the two frequencies depend on the tightness of the crack. When the interfaces at the two sides of the crack are still in good contact, the amplitude related to the frequency corresponding to the crack is small as compared to the amplitude related to the thickness of the slab (see Figure 5.2b). However, when the crack is severe so that debonding occurs at the interface, the amplitude of the frequency related to the crack is dominant. In severe cases, as is the case for Figure 5.2c, additional frequencies related to possible vertical cracks or other modes of vibration will appear.

The quality of concrete can be assessed from the value of the moduli measured from the ultrasonic surface wave (USW) method. Typically, the modulus of a concrete varies from 4000 ksi to 6000 ksi. Any value below this level is an indication of low-strength concrete or a deteriorated pavement.

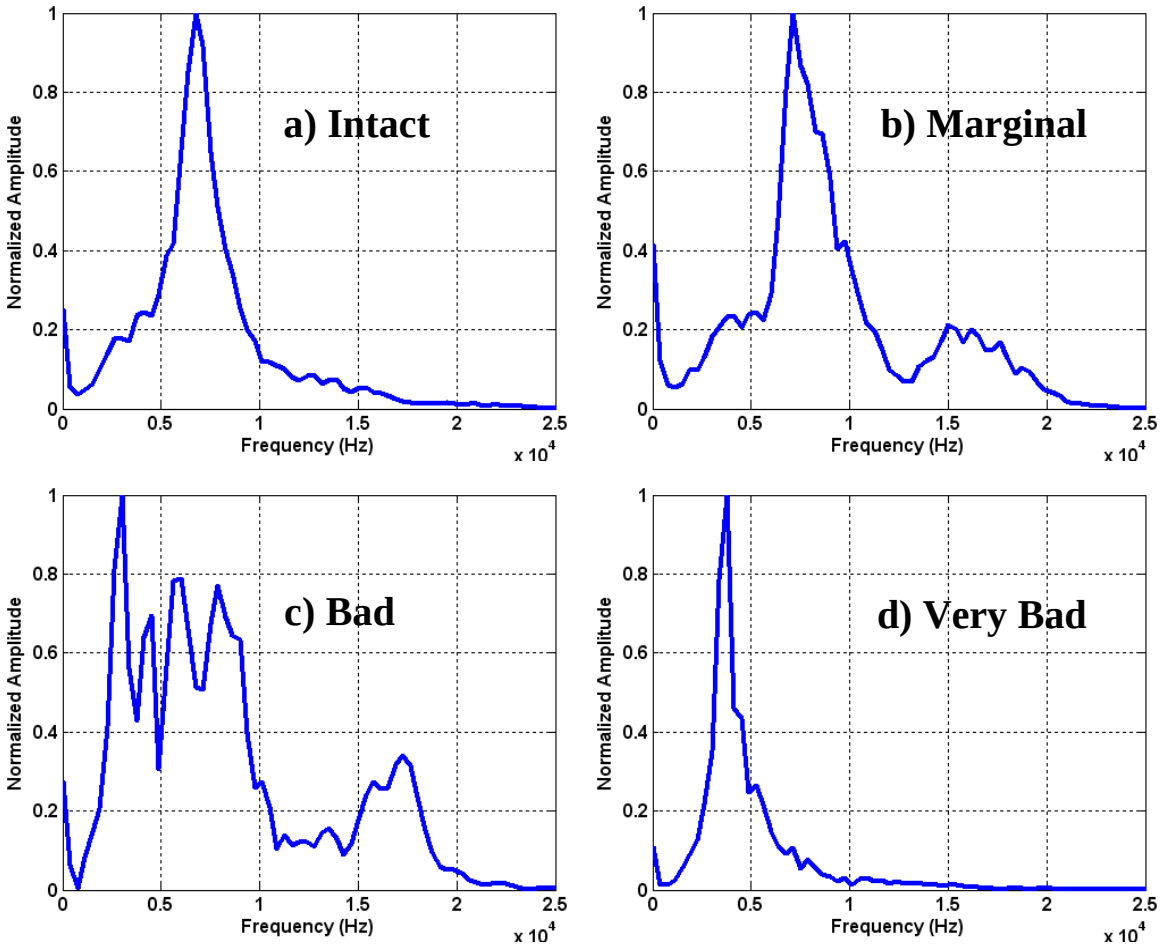

Figure 5.2. Typical Amplitude Spectra from Intact to Very Bad (Debonded) Locations.

The same four categories presented on Figure 5.2 to distinguish between intact and delaminated areas are illustrated on Figure 5.3 for the time-frequency analysis presented in this chapter. Again, four different categories were selected to identify each of the possible conditions of the concrete material. Red areas (close to a normalized amplitude of 1) in the spectrogram show concentration of the signal at a determined frequency and time and as it becomes blue (close to zero amplitude), the signal loses strength.

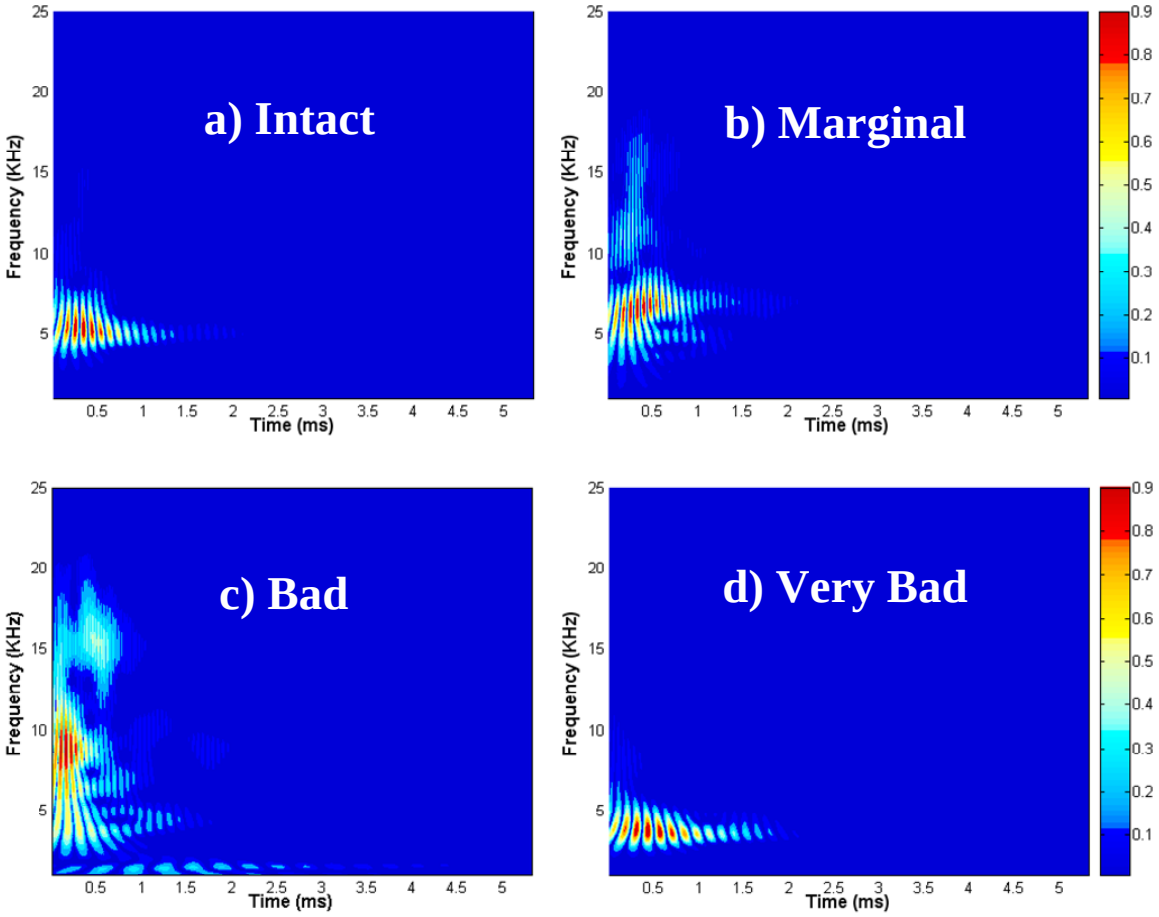

Figure 5.3. Typical Time-Frequency Results (Spectrograms) from Intact to Very Bad (Debonded) Locations.

By determining a simple scale from 0 to 3 (0 corresponding to intact, 1 to marginal, 2 to bad, and 3 to very bad), a contour map of the concrete condition can be generated. An example of a location tested with PSPA every 2 ft from the lane edge and at 1, 3, 6, and 12 in. from the crack on both sides is shown in Figure 5.4. This type of representation gives a good visual impression of the intensity and distribution of damaged areas in concrete materials.

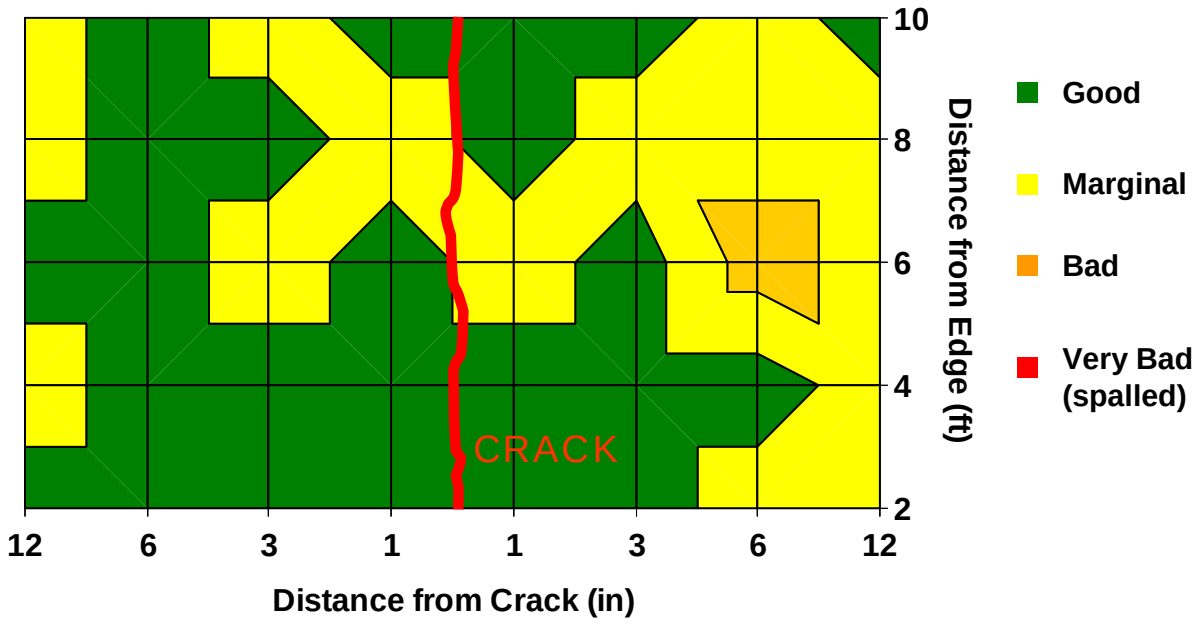

Figure 5.4. Contour Map of a Grid Area around a Crack from Time-Frequency Analysis.

A series of calibration tests were carried out to corroborate the PSPA setup. Results obtained from SH 225 on the east area of Houston are shown, since they presented the most extreme cases—intact and very bad or debonded. Four cores were obtained as part of the project. Cores 1 and 4 (obtained at a saw cut location) were intact after drilling and without any sign of delamination or cracks, while Cores 2 and 3 were debonded at a depth of about 4 in. to 5 in. Details of the four cores are shown in Figure 5.5. All cores were obtained at a distance of 2 to 3 inches from the selected location at each crack; therefore, the cores obtained approximately covered a range of 2 to 5 inches measured from the crack, since the cores were 4 inches in diameter. The spectrograms (following the procedure explained above) calculated at several locations (from 1 to 6 inches) from the selected cracks at the four core locations are shown in Figure 5.6.

Figure 5.5. Cores Retrieved from SH 225.

For Core 1 (Figure 5.6a), which was intact, all spectrograms match the intact pattern and exhibit a clear peak at about 6500 Hz, corresponding to the thickness of the slab (approximately 12 inches). No sign of debonding is apparent at this location. At locations 2 and 5 a very mild possibility of mid-depth crack can be observed.

As reflected in Figure 5.6b, all test points demonstrate responses that are representative of the flexural mode of vibration of the debonded portion of the slab (bad case). The dominant frequency at most points is about 3 kHz, being stronger at locations 2 to 4, as the colors in these locations are closer to red. For point 1 in the figure, the standing mode of vibration is also present at about 17 kHz, which indicates the thickness of the debonded layer is about 5 in. At points 5 and 6, the frequency related to the thickness of the slab is also becoming emergent, indicating that the debonding is becoming less severe.

The results from Core 3 are shown in Figure 5.6c. In this case, the debonding is more severe than Core 2. All points exhibit a very dominant frequency related to the flexural mode of vibration of the debonded concrete, corresponding to a very bad spectrogram. Only slight frequency related to the thickness of the slab is revealed from points 4 to 6, demonstrating that the debonding at this core location is severe.

For Core 4, as reflected in Figure 5.6d, all records exhibit a frequency that correspond to the thickness of the slab and as such can be considered intact.

DELAMINATION DETECTION PROTOCOL

To more objectively study the presence and extent of delamination, the field protocol proposed for the PSPA is shown in Figure 5.7. Based on the field test protocol recommended, for every crack suspected of having spalling, PSPA tests should be carried out on both sides of the crack at 2 ft intervals, from 2 to 10 ft measured from the edge of the lane, and at locations 1, 3, 6, and 12 inches, measured from the crack itself. The estimated time to perform these 40 tests for every crack is about 45 minutes. An example of the PSPA carrying out testing on the field at 1 inch from the crack around a core location is shown in Figure 5.8.

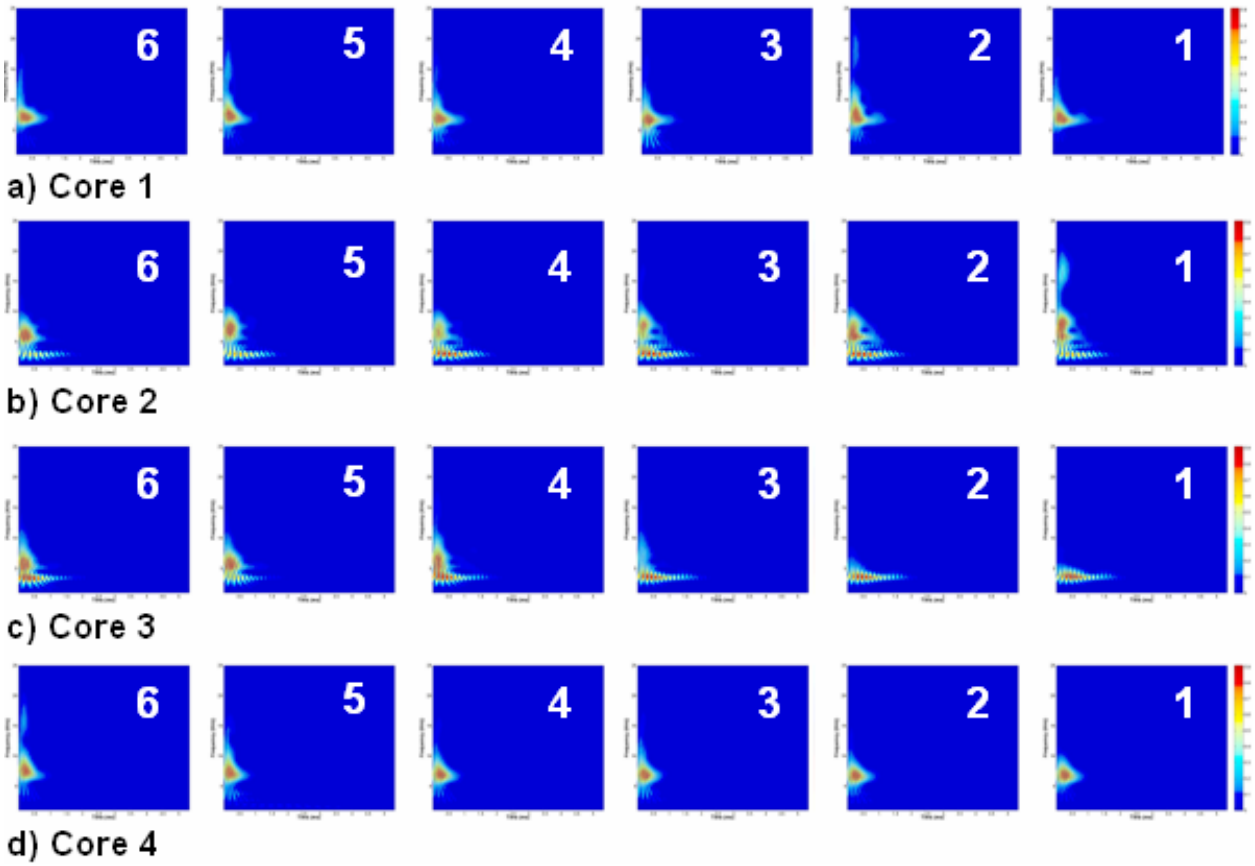

Figure 5.6. Results from Various Distances (in inches) from the Crack at Four Core Locations on SH 225.

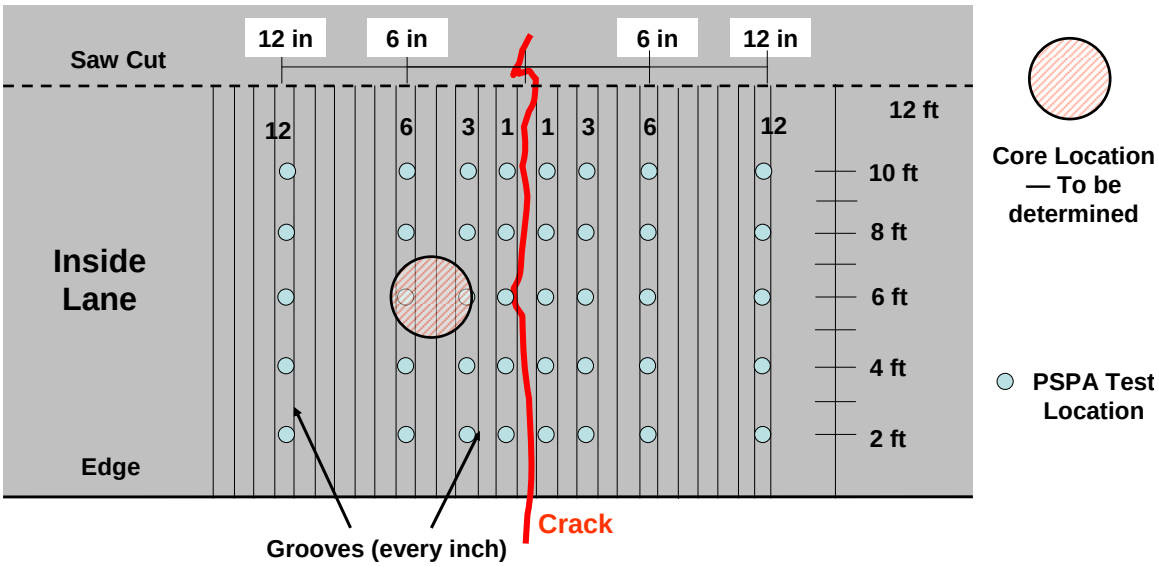

Figure 5.7. PSPA Test Protocol Proposed on a Crack Area.

Figure 5.8. Example of PSPA Testing around a Core Location Following Proposed Field Test Protocol.

CHAPTER VI
FIELD SECTIONS

GENERAL

Pavement test sections using gravel aggregates were established to validate measures and practices from laboratory investigation (Chapter III), and numerical analysis (Chapter IV). Field data were collected through various types of instrumentation and monitoring by personnel from TTI, TxDOT, UTEP, and CTR over a period of the first few days after paving. Weather data, concrete temperature and relative humidity profiles, and drying shrinkage development were monitored, and pavement surveys were conducted to monitor the crack pattern development over time in each test section. Bonding strength in the field was measured and non-destructive delamination detection protocol (Chapter V) was applied to track the delamination development. The stress analysis to predict delamination occurrence and field delamination detection protocol were further validated through visual observation of concrete cores taken from the selective locations (generally on the cracks) in the test sections.

Subsequently, a step-by-step recommendation for using gravel aggregates in concrete paving is presented based on an integrated approach developed by combining laboratory findings, analytical approaches, and field practices.

DEVELOPMENT OF TEST SECTION DESIGN

The field test section design was finalized through several discussions and meetings. The design has ultimately narrowed down to 3 factors: fly ash content, curing method, and batching sequence with a total of 10 test sections, as summarized in Table 6.1. Dense aggregate gradation, water to cementitious ratio (w/cm = 0.41), cement factor (CF = 6), and aggregate factor were considered as fixed parameters.

Table 6.1. Test Variables for the Field Program.

Test Section	FA Replacement (%)	Curing	Charging sequence
1	(10+15) *	HRC	Normal
2	(10+15)	HRC	Modified
3	(10+15)	NC	Normal
4	(10+15)	NC	Modified
5	25 **	HRC	Normal
6	25	Wet Mat	Modified
7	25	NC	Normal
8	25	NC	Modified
9	(10+15)	Wet Mat	Normal
10	25	Wet Mat	Normal

** 10% ultra-fine fly ash and 15% Class F fly ash*
*** 25% Class F fly ash*
HRC = High Reflective Curing Compound, and NC = Normal Curing Compound.

Use of two different levels of fly ash, i.e., (1) a combination of 10 percent ultra-fine fly ash and 15 percent Class F fly ash, and (2) 25 percent Class F fly ash allowed the researchers to maintain the same replacement levels but using both ultra-fine and conventional Class F fly ash in the same design. The curing methods consisted of high reflective resin-based curing (HRC) compound, normal (conventional) resin-based (NC) curing compound, and wet mat curing. Two time applications (10 minutes and 30 minutes after paving) for both the curing compounds were undertaken. The HRC was applied by hand spray. A modified charging sequence was formulated through trial batch at Dorsett Brothers Plant (described later in this section) to minimize the available water at the aggregate-paste interface. It was decided to use dense graded concrete mixture for the test sections. Dense graded mix using Fordyce aggregates (coarse, intermediate, and fine) was developed (described below) in the laboratory prior to paving the test sections.

Dense Gradation of Aggregates

In the laboratory, the researchers determined bond strength of concrete with both dense graded and normal graded aggregates using the same Fordyce aggregate (Victoria, Texas), 25 percent fly ash (10 percent ultra-fine fly ash and 15 percent Class F fly ash) by weight of total cementitious materials and w/cm ratio of 0.4. The specimens were cured in the moisture room before being tested. Mix proportion parameters are summarized in Table 6.2, where the workability factor represents the fraction of total aggregate passing the 2.36-mm sieve and coarseness factor represents ratio between the weight fraction of particles retained on the 9.5-mm sieve to the weight of all particles retained on the 2.36 mm sieve (Shilstone 1990). Table 6.3 shows the mix proportions of concrete on a 1 cubic yard batch basis.

Figure 6.1 compares the fracture toughness values for concrete with and without dense graded aggregates. It is obvious that dense graded aggregates greatly improved the interfacial bonding performance of concrete at the tested early ages. It is because after dense gradation the aggregate in the concrete mixture becomes more compacted and denser, which greatly reduces the voids and subsequently the potential defects in the interface zone of concrete.

Table 6.2. Mix Proportion Parameters for Mixes with and without Dense Gradation.

Tests	Cement Factor	Coarse agg. Factor	Intermediate Aggregate Factor	Workability Factor	Coarseness Factor
Normal	6	0.75	-	34.4	58.9
Dense	6	0.495	0.18	36	55.2

Table 6.3. Concrete Mix Proportion (1 cubic yard).

Mixture Component	Weight
Cement (lbs)	423
Total fly ash (lbs)	141
Coarse aggregate (1½ in, OD, lbs)	1370
Intermediate aggregate (3/8 in, OD, lbs)	498
Fine aggregate (sand, OD, lbs)	1215
Net water (lbs)	225
Air-entraining admixture (oz)	2
Water reducer (oz)	23
w/cm = 0.41 and cement factor = 6 sacks / cy	

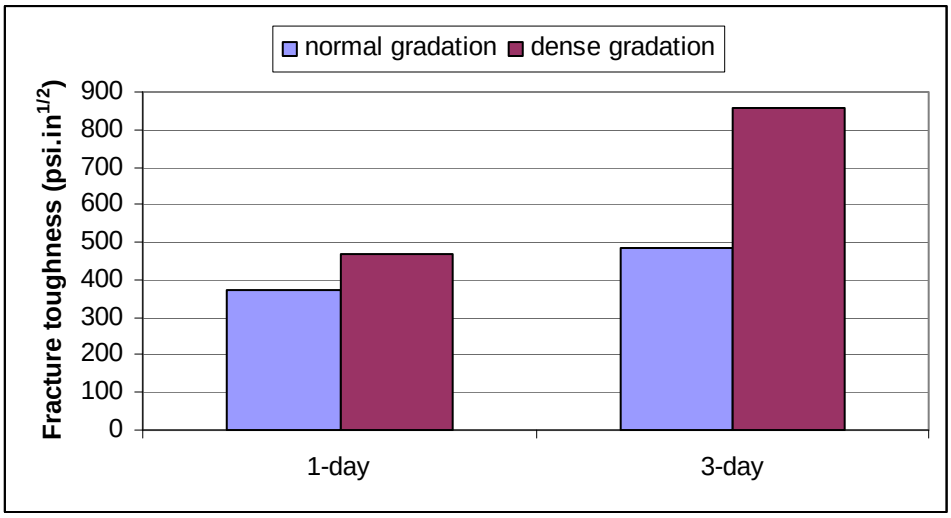

Figure 6.1. Fracture Toughness Comparisons between Concrete with and without Dense Graded Aggregates.

Laboratory-based, dense graded mix was verified in the field through trail batch application, and it successfully met the required strength and workability levels.

Charging Sequencing

Using the same mix developed with dense aggregate gradation (described above), experiments with two charging sequences (conventional and modified) were conducted in the field through trail batch application and the results were compared to check the possible improvement of bonding performance. The conventional charging sequencing (traditional mixing of the materials together at the same time) was based on ASTM C 192/C 192M (ASTM 2000) and the modified charging sequencing was carried out with the following steps:

- adding sand, total cementitious materials (cement and fly ash), and 75 to 80 percent of the total water in the mixer, and mixing for 50 seconds;
- charging coarse and intermediate aggregates to the mixer, and mixing for another 30 seconds; and
- adding the rest of the water to the mixer, and mixing for another 50 seconds.

Three-day fracture toughness results for mixes with both conventional and modified charging sequences are compared in Figure 6.2. Modified charging sequence provided higher concrete fracture toughness and better workability than the conventional one. As described in Chapter II, an effective way to improve the interfacial bond is to decrease the water layer at the interface. Figures 6.3 and 6.4 illustrate petrographic observation of ITZ for these two different concrete samples using a scanning electron microscope. It can be seen that coarse $Ca(OH)_2$ was well developed at the ITZ of concrete with conventional charging sequencing (Figure 6.3), while at the ITZ of concrete with modified charging sequencing, only scattered fine CH occurred (Figure 6.4). Moreover, its ITZ was less porous due to better intergrowth/interlocking of hydration products and densification of ITZ, which indicated that modifying charging

sequencing improved the ITZ structure, and then bonding performance of concrete. The results are consistent with the findings from other researchers (Hayakawa and Itoh 1982, Tamimi 1994).

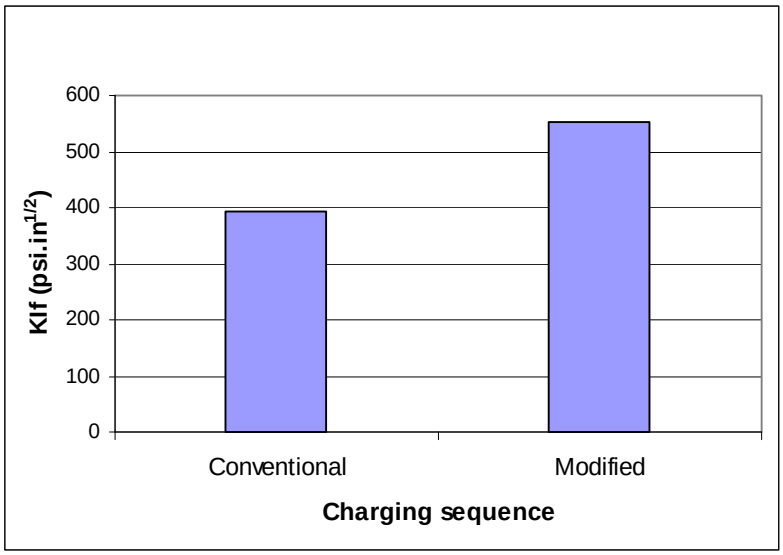

Figure 6.2. Effect of Charging Sequencing on 3-day Concrete Fracture Toughness.

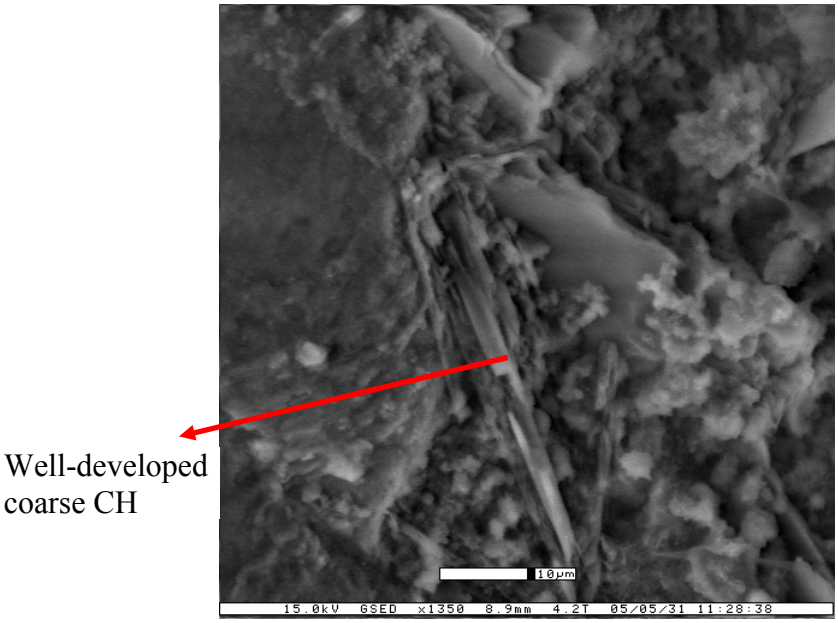

Figure 6.3. ITZ of Concrete with Conventional Charging Sequencing.

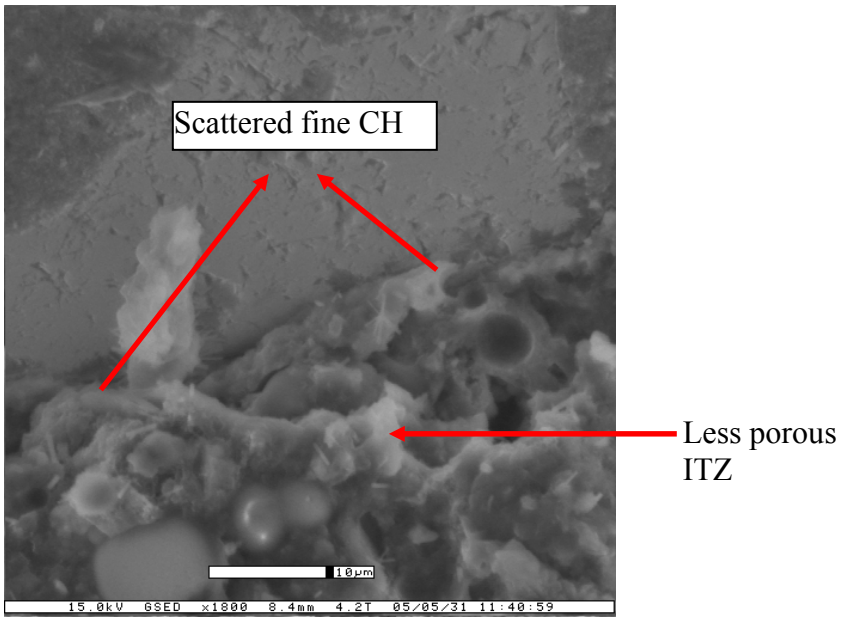

Figure 6.4. ITZ of Concrete with Modified Charging Sequencing.

SUMMARY OF WINTER SECTIONS

Test sections using Fordyce materials (coarse, intermediate, and fine aggregates) were established in November 2005 on SH 288 (3 miles south of Beltway 8 in Houston) to produce performance test data to validate measures and trends relative to the practices and techniques to minimize the development of spall related delamination in CRC paving. Three continuous days from November 16 to 18 were dedicated to paving a total of 10 sections (Table 6.4). A schematic test section layout is presented in Figure 6.5. The planned construction length for each test section was 175 ft. However, the actual lengths of 10 of the sections varied, as shown in Figure 6.5.

Table 6.4. Section Designation Used in the Test Section.

Section Description	SH 288 (Winter)		SH 35 (Summer)
	TTI and TxDOT	UTEP	
10+15, HRC, NM	Section 1	Section 5	Section 6
10+15, HRC, MM	Section 2	Section 2	Section 1
10+15, NC, NM	Section 3	Section 10	Section 5
10+15, NC, MM	Section 4	Section 3	Section 2
25, HRC, NM	Section 5	Section 6	Section 7
25, WM, MM	Section 6	Section 8	Section 4
25, NC, NM	Section 7	Section 1	Section 9
25, NC, MM	Section 8	Section 4	Section 3
10+15, WM, NM	Section 9	Section 9	Section 8
25, WM, NM	Section 10	Section 7	Section 10

TTI and TxDOT followed the original design serial numbers as section designation for SH 288; All the Universities in SH 35 and UTEP in SH 288 followed the actual paving sequence as section designation.
NM = Normal Mixing, MM = Modified Mixing, and WM = Wet Mat

Field Test Data and Analysis

The field test data and analysis presented here included:

1) weather data, concrete temperature and relative humidity profiles, and drying shrinkage development;
2) pavement condition such as the crack pattern development over time in each test section;
3) field bond strength of concrete; and
4) NDT data.

The data information in the first three items was further used as inputs for stress analysis to predict associated delamination occurrence, and NDT data was analyzed by the field delamination detection protocol. The results were further validated by associated concrete coring tests.

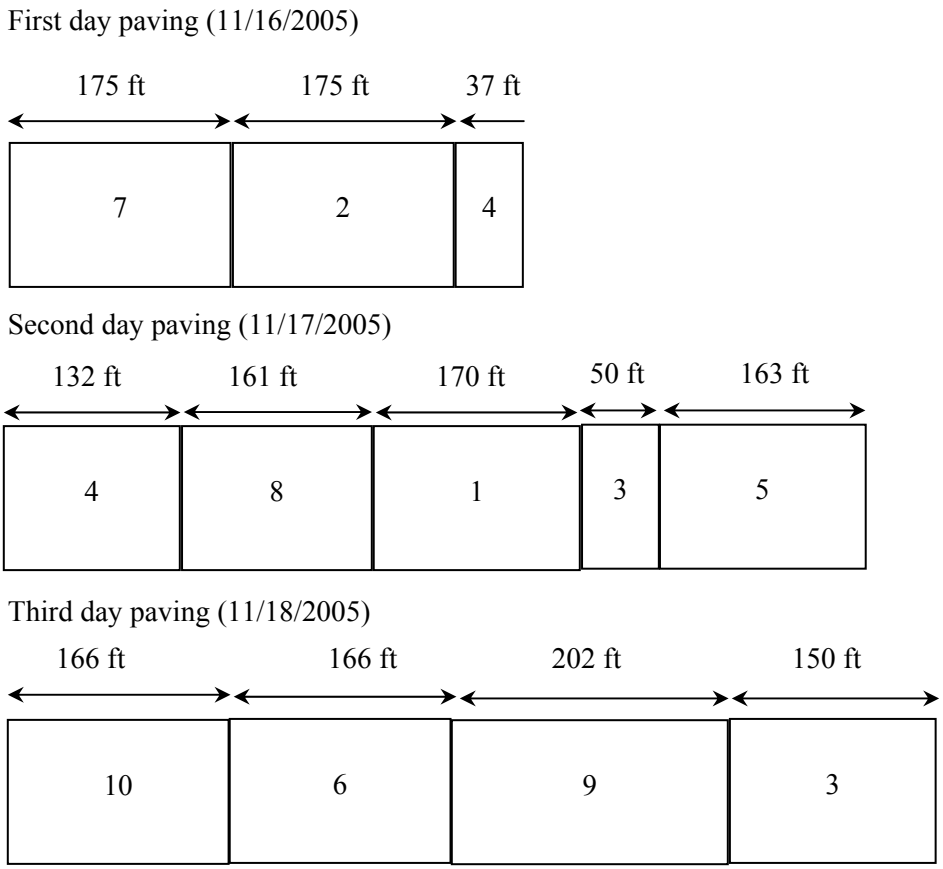

Figure 6.5. A Schematic Layout of the Test Sections.

Weather Data

The development of delaminations and spalling distresses in continuous reinforced concrete pavement (CRCP) at an early age is significantly affected by climatic factors. Therefore, a weather station (shown in Figure 6.6) was used to collect weather data in the field, which included ambient relative humidity, ambient temperature, solar radiation, wind direction, wind speed, and rainfall. These data were collected at hourly intervals on a continuous basis.

Figure 6.6. Weather Station Setup.

Figures 6.7 and 6.8 record the trends of relative humidity, temperature, solar radiation, and wind speed with time over the placement period and beyond (from 11/16/2005 to 11/21/2005). As shown in Figure 6.7, relative humidity shows the inverse relation with the temperature, i.e., the higher temperature associates with the lower relative humidity, and vice versa. Over the first several days after construction, ambient temperatures ranged from a low of 40 ^{o}F in the morning hours to a high of 65 ^{o}F in the afternoon. The relative humidity ranged from a low around 20 percent in the afternoon to a high of almost 100 percent in the morning. As shown in Figure 6.8, 0.65 kw/m^2 of maximum solar radiation and 6.2 m/s of wind speed were recorded over the monitored period.

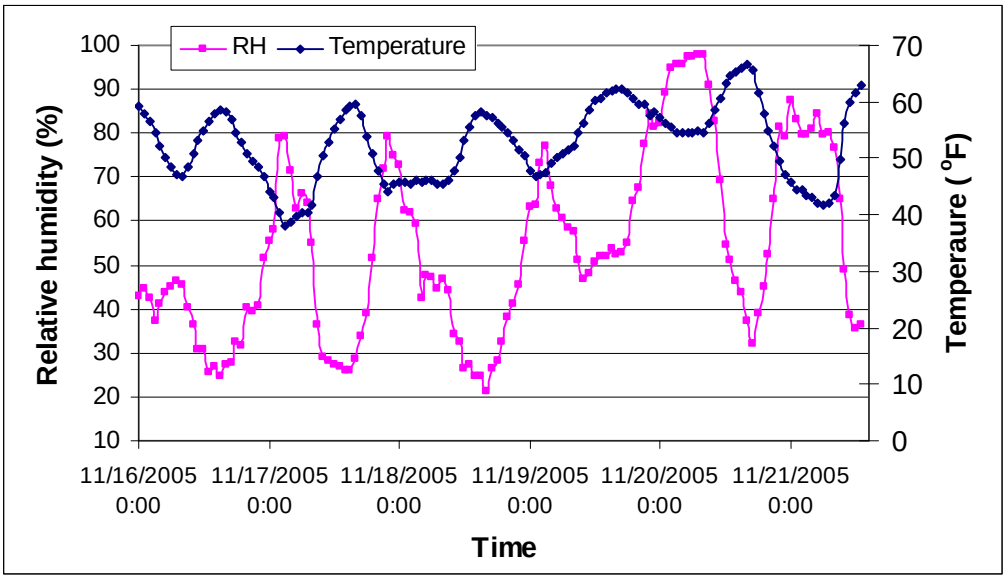

Figure 6.7. Ambient Temperature and Relative Humidity Cycles during Field Test Operation.

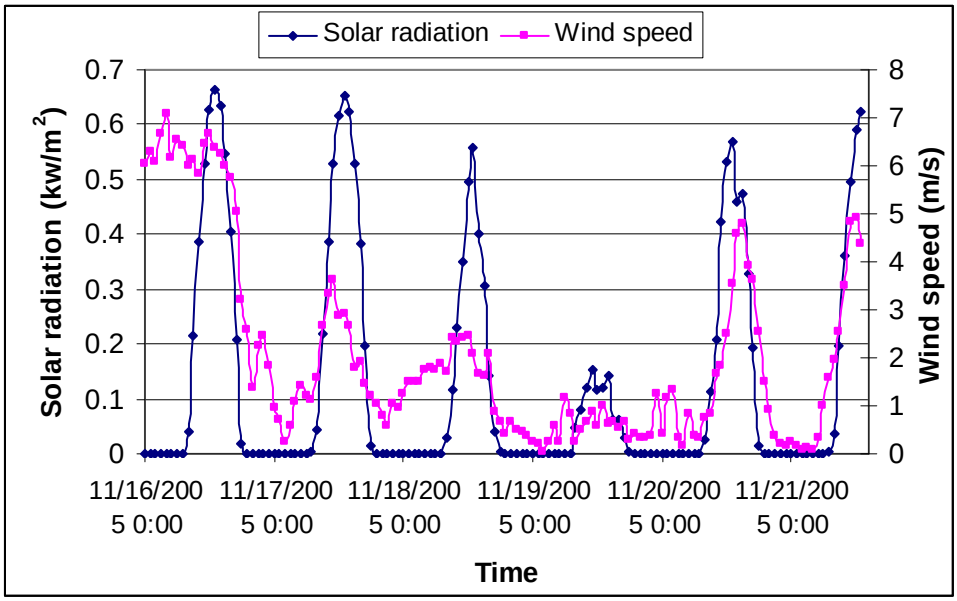

Figure 6.8. Solar Radiation and Wind Speed Cycles during Field Test Operation.

Concrete Temperature Profiles

Vertical temperature profiles through the thickness of the pavement for all the test sections were measured immediately after concrete placement by embedded I-buttons (as shown in Figure 6.9a) at three different locations in the concrete (1 inch from the top, mid-depth, and 1 inch from the bottom; and two different transverse locations: 2 ft and 6 ft from the edge). Figure 6.10 shows the temperature development in the concrete for one of the test sections (section 8). Figure 6.11 summarizes the maximum temperature at different locations in the pavement and the associated elapsed time when these temperatures were reached. A complete set of data is provided in Appendix B.

It can be seen that at each location, the development of concrete temperature with time followed a cycling pattern. For almost all test sections, there was an increase in temperature from top to bottom. Different maximum temperature existed for different test sections, which is related to the temperature at the time of placement. Generally, the higher the temperature at the time of placement, the higher the maximum temperature that the concrete can reach. Figure 6.12 illustrates the main effects plot for maximum temperature concrete at mid-depth, and Delta statistics (described in Chapter III) were again used to determine the significance of design factors related to the maximum concrete temperature. The higher Delta value represents the higher impact of the design factor on the target value of output (here, maximum concrete temperature). Based on Delta statistics, these factors followed a decreasing rank order with respect to their relative importance to the concrete maximum temperature: curing method, fly ash content, and charging sequencing. Compared with the experimental design in the laboratory, the same trend of the relative importance of design factors held, except that the factors of aggregate type and w/cm were not considered in the field design. Maximum temperature of concrete represents the maximum heat evolved during the hydration process. For the factor of curing method, WMC provided higher maximum concrete temperature than the other two curing methods. That is because the best curing quality provided by WMC enables the least loss of heat energy in the concrete.

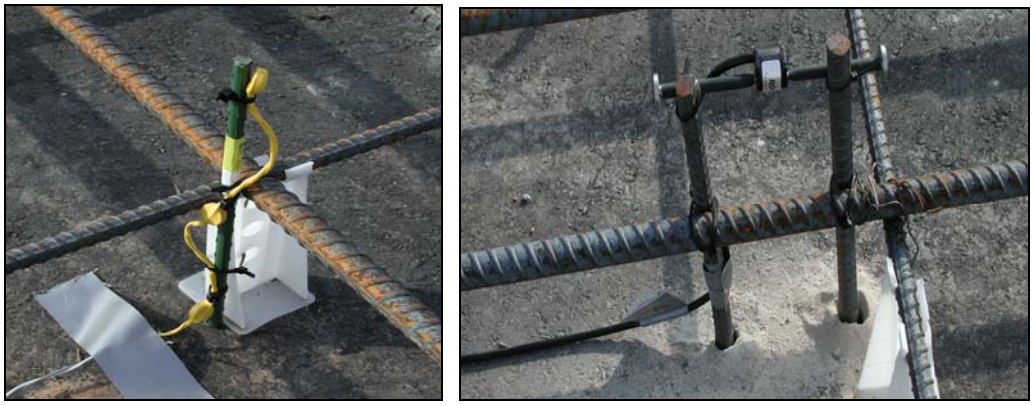

(a) (b)

Figure 6.9. I-Button (a) and VWG (b) Setup.

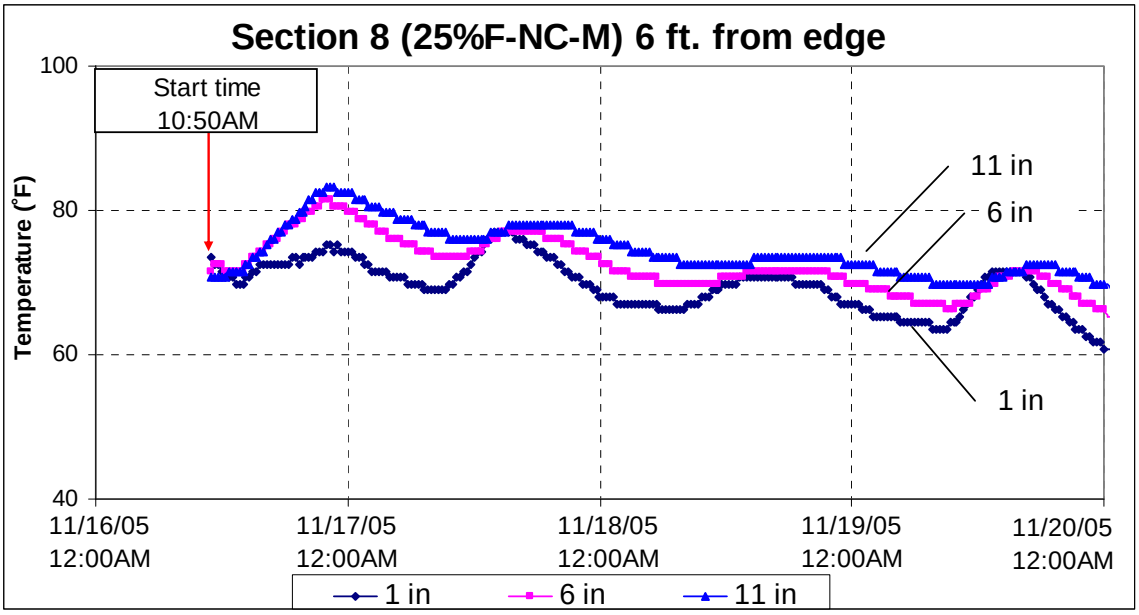

Figure 6.10. Temperature Profile of Test Section 8.

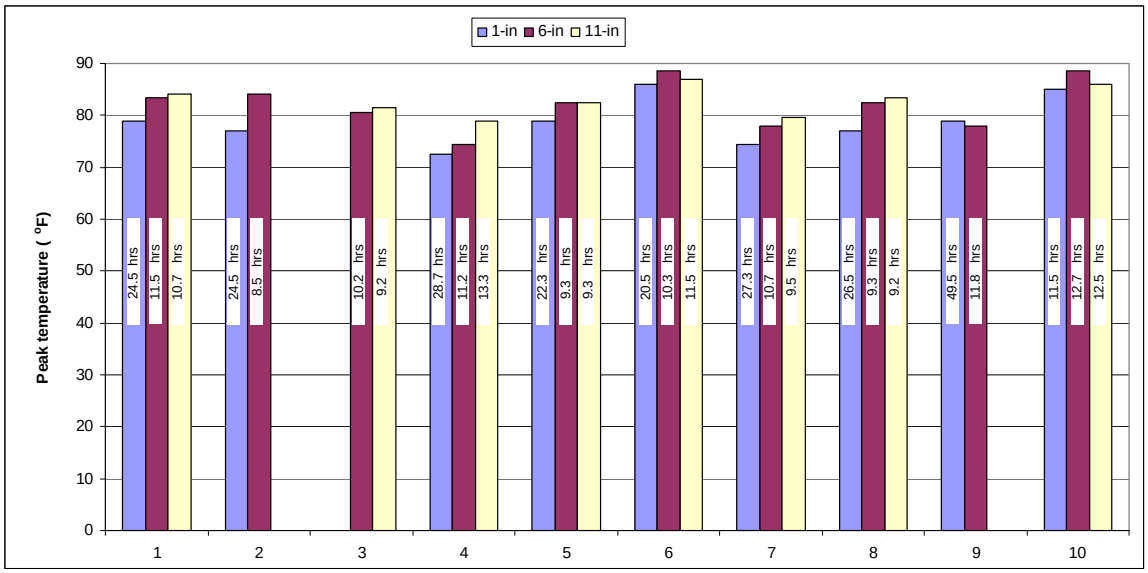

Figure 6.11. Maximum Temperature for Each Test Section.

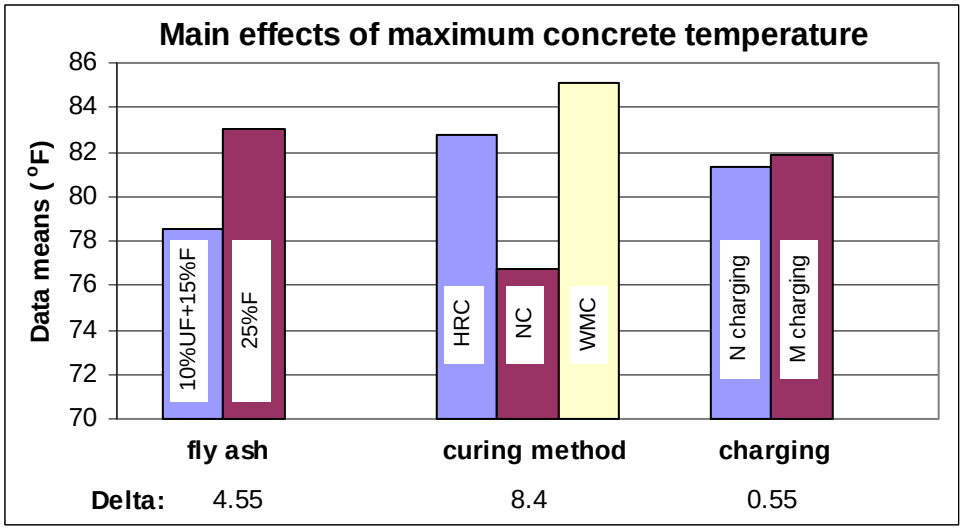

Figure 6.12. Main Effects Plot for Maximum Concrete Temperature.

As for the factor of fly ash, 25 percent Class F fly ash provided higher maximum concrete temperature than the combination of 10 percent ultra-fine fly ash and 15 percent Class F fly ash. Compared with ultra-fine fly ash, Class F fly ash is coarser. Therefore, the latter has less specific surface areas than the former. Under the same condition of w/cm, concrete made with 25 percent Class F fly ash may have more water to ensure the adequate reaction of hydration products than that made with 10 percent ultra-fine fly ash and 15 percent Class F fly ash, which then increases the concrete maximum temperature. In addition, the modified charging sequence provided higher concrete maximum temperature than the normal one. It may be that for the modified charging sequence, the coarse aggregates are added to the mixer later than other materials, which ensures the sufficient mixing of water with cementitious materials, and then improves the hydration process and increases the concrete maximum temperature.

In general, concrete at the mid-depth and at 1 in from the bottom reached their highest temperatures at almost the same elapsed time, while the concrete at 1 in from the top reached its highest temperature later than the other two locations. However, the small difference reflected the effects of different design parameters on the temperature development. Using concrete temperature at mid-depth and comparing sections 1 and 2, 6 and 10, and 7 and 8, the associated elapsed time when the maximum temperatures were reached for sections with modified charging sequence (sections 1, 7, and 10) was shorter than those with a normal charging sequence (sections 2, 6, and 8). It also may be due to the improvement of the hydration process by the modified charging sequence. As for the effect of curing method, in the case of wet mat curing, it took a longer time for concrete to reach its maximum temperature than the other two curing methods. However, the effect of fly ash combination is not that significant. It may be that at a very early age of concrete, fly ash mainly plays the role of being the filler. On this basis, there is not a big difference between the combination of 10 percent ultra-fine fly ash and 15 percent Class F fly ash, and 25 percent Class F fly ash only.

Moisture Profiles

Moisture profiles at different locations (i.e., surface, ambient, and 1 in below the surface) were measured by curing monitor system (CMS) (as shown in Figure 6.13). Figure 6.14 gives an example of time histories of relative humidity for one of the test sections (section 2), and complete data can be referenced in Appendix B**.** At any time, the ambient relative humidity was lower than that of the concrete. When the concrete was placed initially, the relative humidity values at the surface and 1 in below the surface of the concrete were very close to each other; however, with time, the surface relative humidity becomes lower than the relative humidity at 1 in below the surface. In addition, the development of ambient relative humidity with time follows a cyclic pattern. However, the moisture profile at the surface and 1 in below the surface varied with the different materials and curing methods. The data of relative humidity at both the top and bottom of the concrete slab were used as boundary conditions for stress analysis to assess the possibility of delamination occurrence for each test section, which will be reported later.

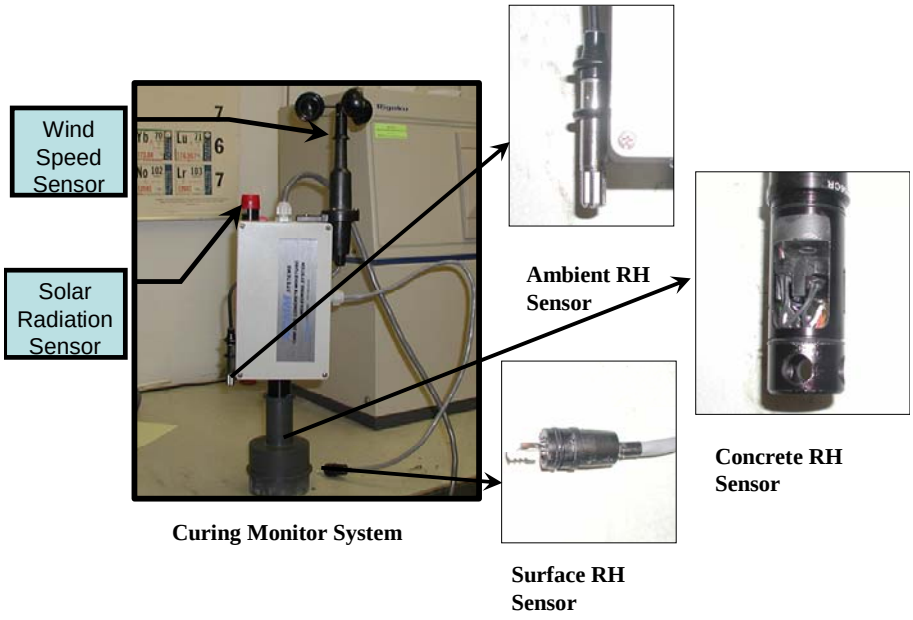

Figure 6.13. CMS Setup.

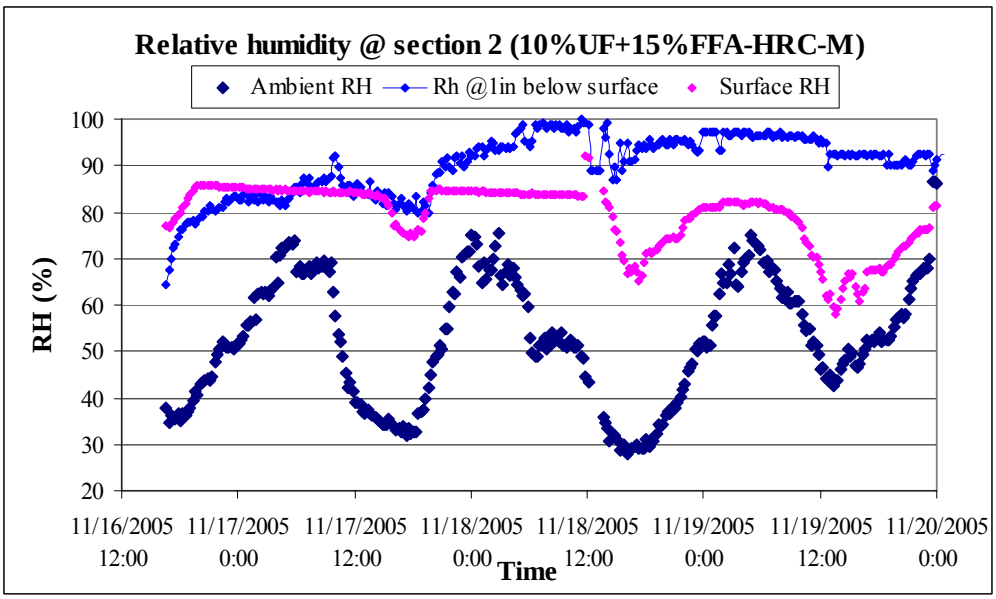

Figure 6.14. Moisture Profiles of Test Section 2.

Drying Shrinkage

To measure the strain in the concrete, 10 vibrating wire strain gages (VWG, shown in Figure 6.9b) (four from TTI and the other six from CTR) were installed at 1 inch below the surface for all test sections. Ten concrete shrinkage bar specimens were also cast according to ASTM C157 for unrestrained shrinkage strain measurements with VWGs placed within the specimens.

Figure 6.15 illustrates the free shrinkage strain development with time for all test sections. It can be seen that for most all sections free shrinkage strain increases with time, and maximum free shrinkage strain occurs at the later stage of the analysis period. Figure 6.16 illustrates the maximum free shrinkage strain within a 7-day analysis period. The comparisons between section 1 and 5, 3 and 7, 4 and 8, and 9 and 10 show that the combination of 10 percent ultra-fine fly ash and 15 percent Class F fly ash presented lower maximum free shrinkage than that of 25 percent of Class F fly ash. The comparisons between sections 2 and 4, 6 and 8, and also among 1, 3, and 9, and among 5, 7, and 10 show that HRC provided the highest maximum free shrinkage strain among these three curing methods, which implies that HRC appears to be effective at a very

early age of concrete, and become less effective with time. These results are also consistent with the result from experimental design analysis shown in Figure 6.17, which illustrates the main effects plot for maximum free shrinkage strain. Again, based on Delta statistics, these factors followed a decreasing rank order with respect to their relative importance to the maximum free shrinkage: curing method, fly ash content, and charging sequencing. Curing method has the most significant effect on the shrinkage development. Compared with the other two design factors, the effect of charging sequencing on the maximum free shrinkage strain was not significant.

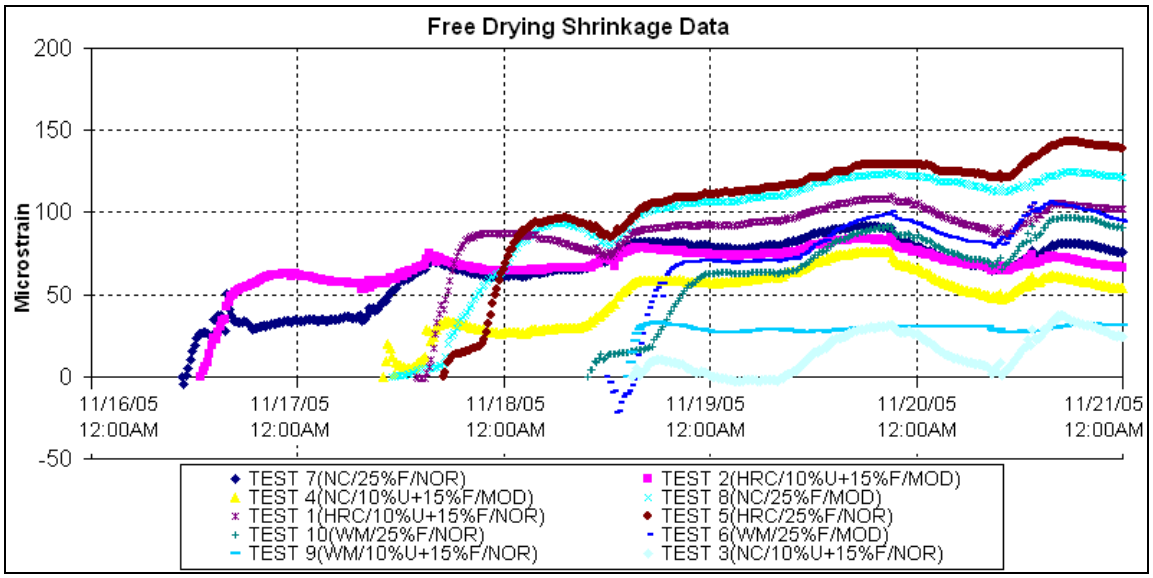

Figure 6.15. Free Shrinkage With Time for Different Sections.

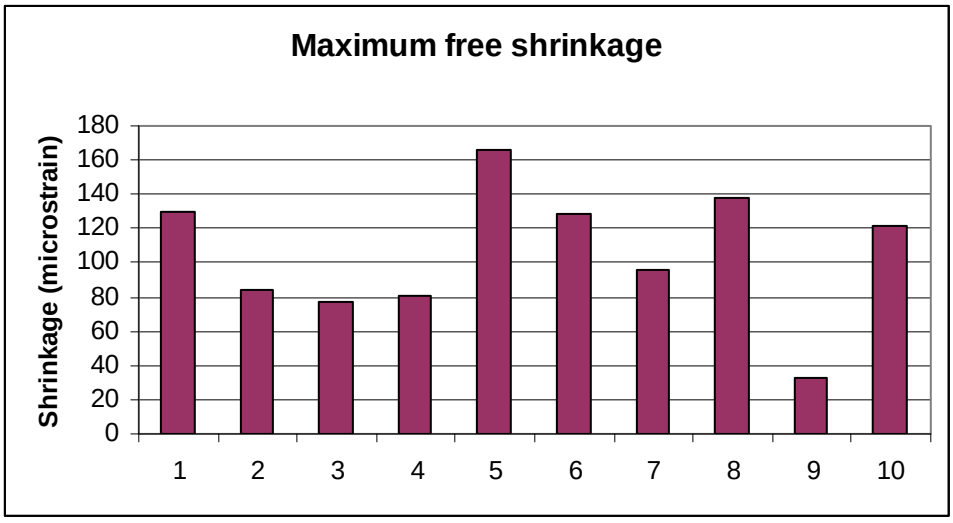

Figure 6.16. Maximum Free Shrinkage of Concrete.

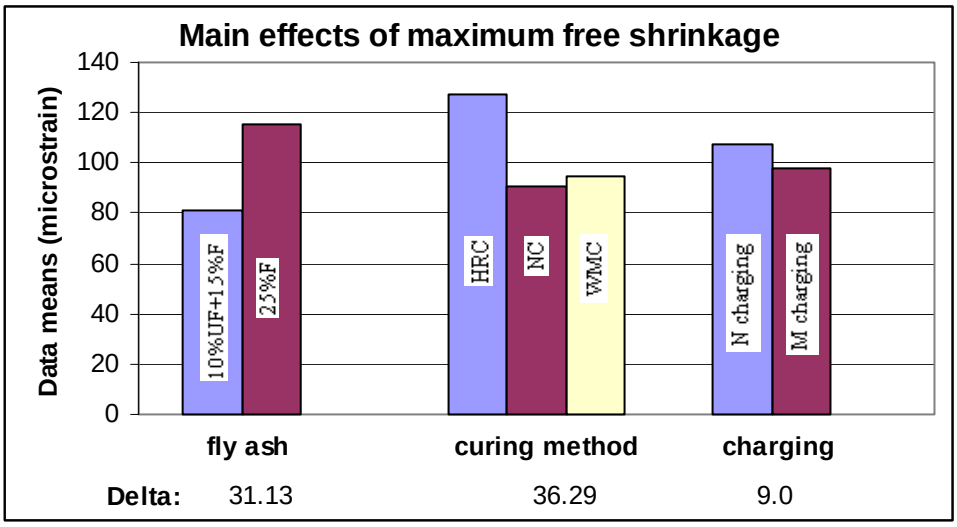

Figure 6.17. Main Effects Plot for Maximum Free Shrinkage.

Figure 6.18 presents the gage shrinkage strain development with time for test sections 2, 4, 7, and 8 from VWGs. For all test sections, the development of gage shrinkage in the concrete followed a cyclic pattern, which indicated the gage shrinkage

is a function of not only concrete material properties but also curing methods and environmental effects.

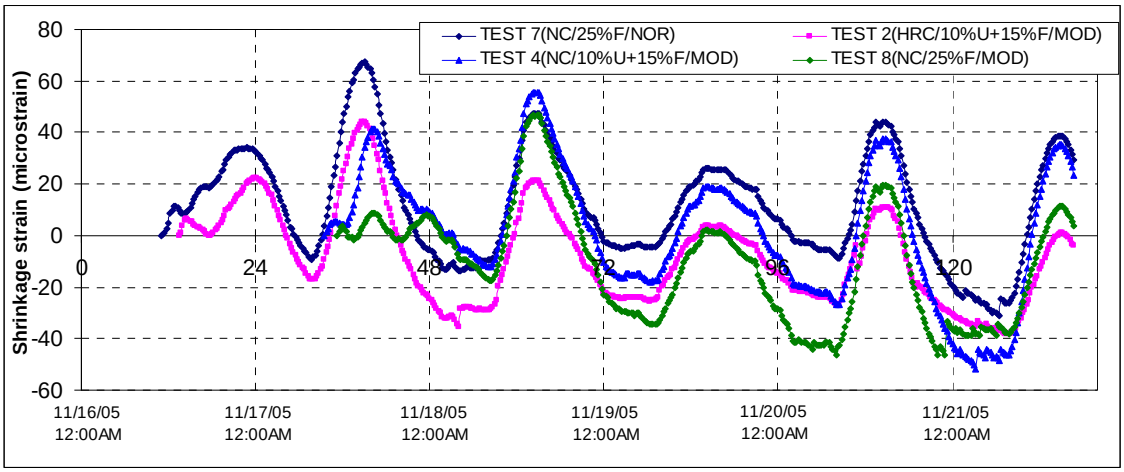

Figure 6.18. Gage Strains with Time for Different Sections.

Creep

Figure 6.19 illustrates the maximum creep strains for all test sections after subtracting thermal effect and drying shrinkage from the curves of gage shrinkage strains. Figure 6.20 indicates the significance of each design factor related to the maximum creep of concrete. It is found that these factors showed similar relative importance to the maximum creep strain. With respect to the maximum creep strain, these factors followed the same decreasing rank order as that for the maximum free shrinkage: curing method, fly ash content, and charging sequencing. Again, the combination of 10 percent ultra-fine fly ash and 15 percent of Class F fly ash presented lower maximum creep strain than that of 25 percent of Class F fly ash. HRC provided the highest maximum creep strain among these three curing methods, which again implies that HRC appears to be effective at a very early age of concrete, and become less effective with time. Compared with the other two design factors, the effect of charging

sequence on the maximum creep strain was not significant because of its very low Delta value.

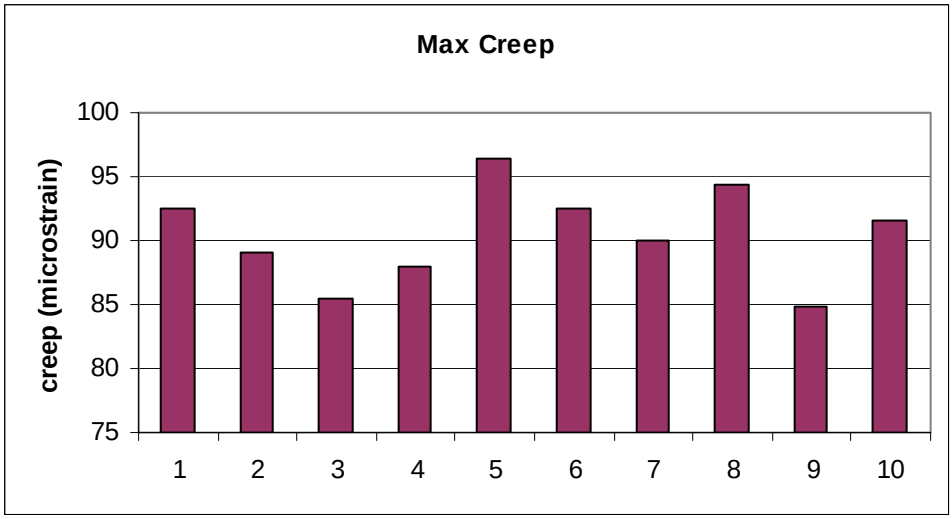

Figure 6.19. Maximum Creep for Different Sections.

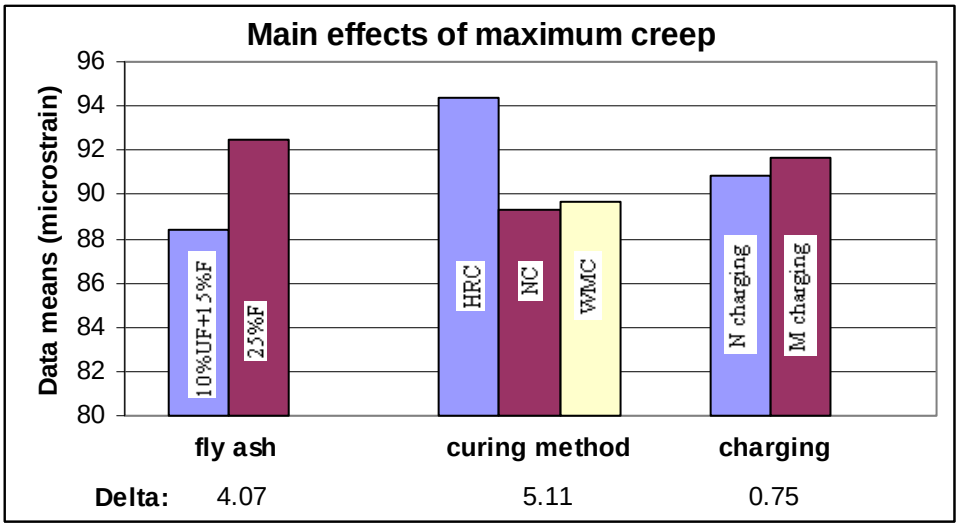

Figure 6.20. Main Effects Plot for Maximum Creep.

Pavement Survey

Pavement crack survey of 10 test sections was conducted on November 19, November 20, November 23, November 24, November 29, December 7, December 19, February 11, and March 24, which included collecting number of cracks, and crack spacing and crack width of each crack. The first crack was detected on section 7 in the morning of November 19 on the third day after paving. Figure 6.21 shows the probability of crack spacing at different concrete ages, using data from section 5 as an example. The probability of crack spacing less than a given value presented a sigmoidal shape. With the age, the curve shifted to the left gradually, which indicated that the probability of crack spacing less than a given value increased. Figure 6.22 compares the development of crack spacing for all test sections. At an early age of the concrete the crack spacing for each section was large due to only a few cracks developing. The increase in the numbers of cracks with time resulted in the decrease of average crack spacing for each section. In addition, the decrease of average crack spacing with time got slower, which can be reflected from close values for crack spacing at 20 days and 126 days of concrete age.

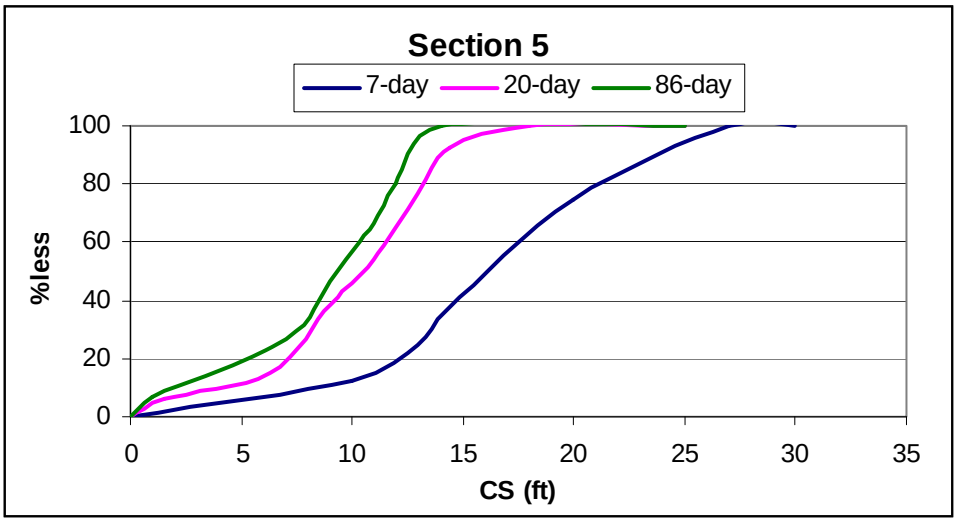

Figure 6.21. Crack Development with Time.

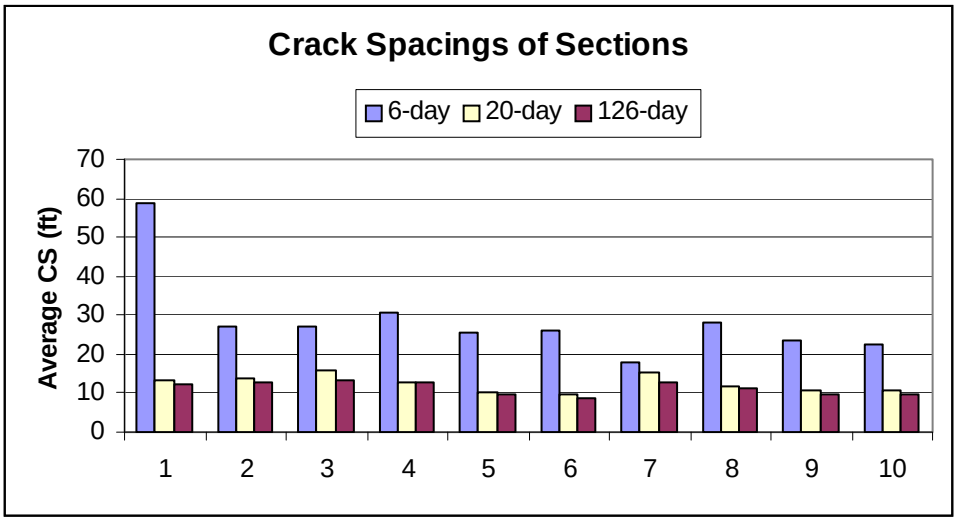

Figure 6.22. Crack Spacing for Concrete Sections.

Concrete Strength

Figure 6.23 illustrates the 4-day compressive strength of concrete for all sections, and data of other compressive strength, flexural strength, elastic modulus, and coefficient of thermal expansion are listed in Appendix B. It can be seen that except for section 7, other sections had very similar compressive strength values. This was because after the concrete specimens for all sections were cast, they were moved to the laboratory and cured in a water tank, which then made the design combinations different from the original designs. Instead, the design combinations for sections 1, 3, and 9 were the same, which was: water curing/10%U+15%F/NOR; those for sections 2 and 4 were the same, which was: water curing/10%U+15%F/MOR; those for sections 5, 7, and 10 were the same, which was: water curing/25%F/NOR; and those for sections 6 and 8 were the same, which was: water curing/25%F/MOR. The very close strength data resulted from the exclusion of the effect of curing method in the original designs, which has much more significant effect than the other factors. In addition, section 7 showed the lowest strength data. This is because the concrete mixture for section 7 was very dry, and it was difficult to place. Additional water was applied to facilitate casting, which at the same time compromised the strength development.

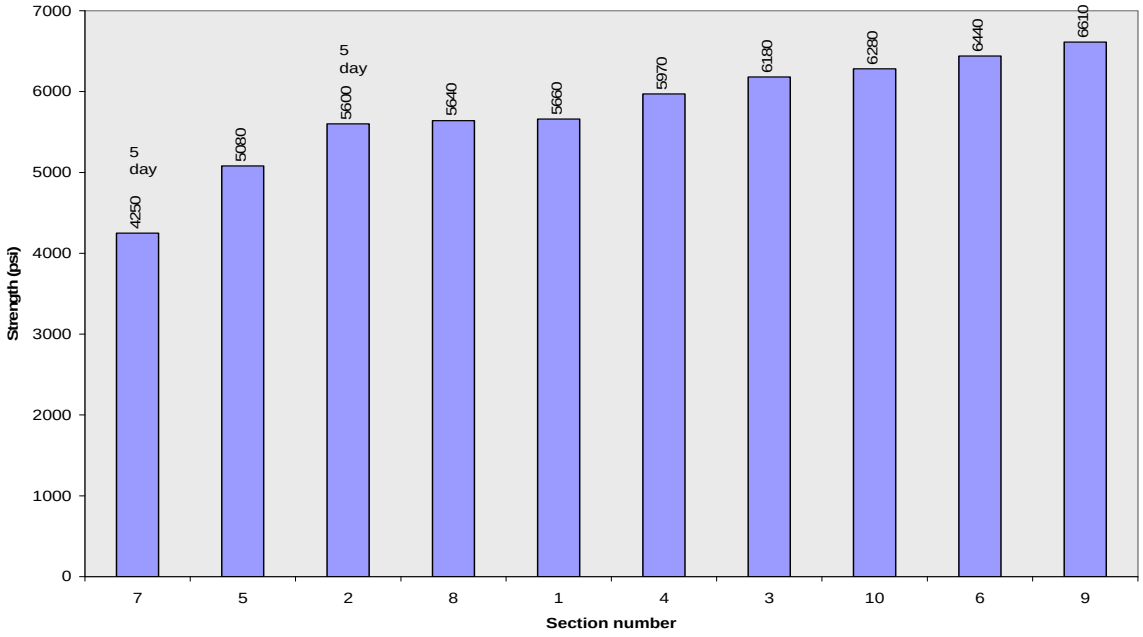

Figure 6.23. Four-day Compressive Strength of Concrete for All Test Sections.

Field Fracture Toughness Testing

As described in Chapter III, the fracture toughness value at early ages of concrete was used to represent the interfacial bond between aggregate and mortar, and the variable-notch one-size split-tensile test method developed at TTI was applied to facilitate measurement of fracture toughness values. During paving, concrete fracture specimens were cast in cylinder molds for the purpose of determining the interfacial bond between aggregate and mortar. Previous field experience has shown that a few days after paving is the most critical time for delaminations to form in concrete paving. On this basis, test results were obtained for concrete at ages of both 1-day and 3-day. Figure 6.24a and b show the specimens cast in the field and the equipment for split-tensile testing, respectively.

(a) (b)

Figure 6.24. Fracture Toughness Tests.

Figure 6.25 summarizes fracture toughness results for each test section. It can be seen that the interfacial bond between aggregate and mortar increased at different degrees with the time. Different design combinations produced different improvement of interfacial bond. Section 6 (i.e., 25% Class F fly ash + WMC + modified charging sequence) resulted in the highest bonding strength among all the test sections. The effectiveness of the wet mat curing method can be observed from comparison of sections 1, 3, and 9; sections 5, 7, and 10; and comparison between sections 2 and 4, and between 6 and 8. However, the effects of other factors on the bonding strength were not clear from results in Figure 6.25 only.

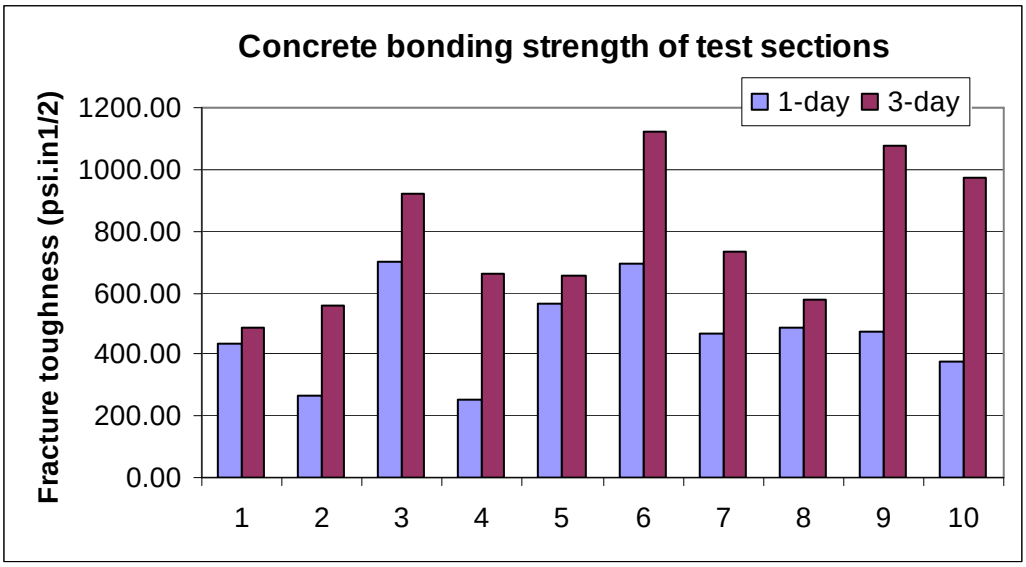

Figure 6.25. Summary of Fracture Toughness for Each Section.

Hence, experimental design analysis was further conducted to check the relative importance of each design factor and the best level for each factor. Figure 6.26 is the main effects plot for means of all design factors at concrete age of 1-day. Based on the Delta values, these factors showed a decreasing order related to their relative importance to the bonding performance: curing method > fly ash > charging sequence. The factor of curing method was identified as the most significant factor relative to the bonding performance. For each factor, higher level average indicates the better level of this factor in terms of the bonding performance. It can be seen that for curing methods, WMC showed the best performance, and HRC was better than NC. With respect to the 1-day bonding performance, the level of 25 percent of Class F fly ash was better than that of the combination of 10 percent ultra-fine fly ash and 15 percent of Class F fly ash. However, the level of the normal charging sequence was better than that of the modified charging sequence, which was not consistent with the result from the laboratory investigation.

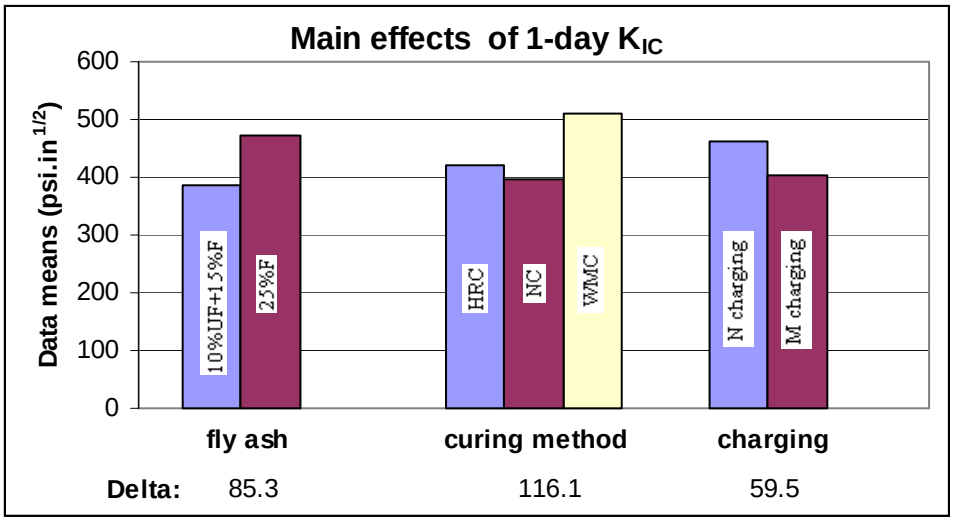

Figure 6.26. Main Effects Plot for One-day K_{IC}.

Figure 6.27 illustrates the main effects plot for means of all design factors at concrete age of 3-day. As with 1-day K_{IC}, these factors followed the same trend of their relative importances, and the factor of curing method was identified as the most significant factor relative to the bonding performance. Compared with the levels of each factor for the 1-day K_{IC} case, for curing method, NC showed better 3-day K_{IC} than HRC. The previous analysis also showed that HRC provided highest shrinkage and creep development at the later stage of the 7-day period. HRC may be only effective during a very short period after paving, which is needed to be tested. About the charging sequence, for output of 3-day K_{IC}, these two different charging sequences provided very close performance, which means that within the scope of the test sections, this factor was not significantly related to the K_{IC}. The main reason for this may be that, different from the experimental design for the laboratory described in Chapter III, all design combinations for test sections were designed with 0.4 of w/cm and dense-graded aggregates, which already ensured very low probability of delamination and good quality of concrete, as investigated in the laboratory. It will also be addressed in the next section about assessment of delamination probability. As a result, on the basis of low w/cm and dense-graded aggregates, the improvement of concrete bonding performance

provided by charging sequence appears to be not as significant as it should be. Furthermore, the actual operation of charging sequences in the field may cause the levels chosen for charging sequence to be not significantly different.

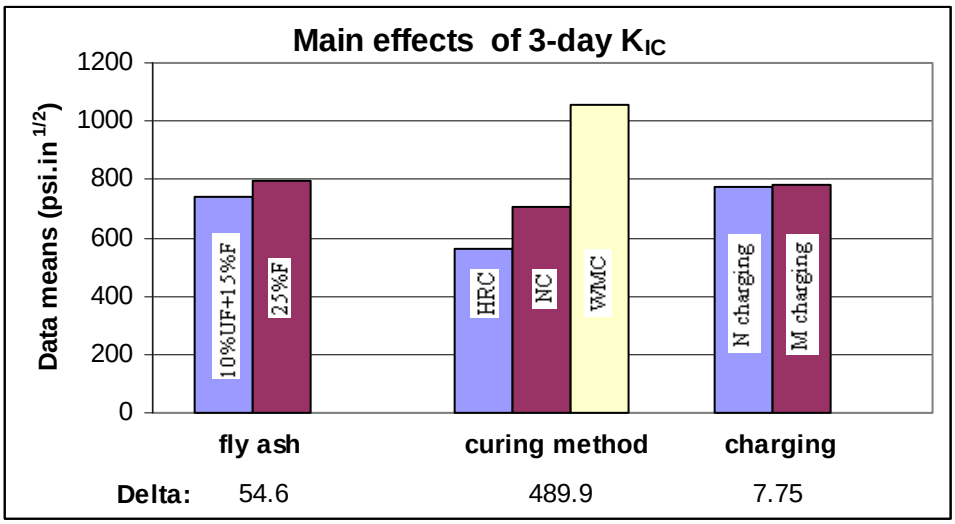

Figure 6.27. Main Effects Plot for 3-day K_{IC}.

Assessment of Delamination Probability

In Chapter IV, an approach to predict the delamination occurrence by comparing K_I (stress) and K_{IC} (strength) was proposed. Therefore, in this section, this approach was applied to assess the delamination occurrence probability. Because delamination results from a combination of material and environment effects, this analysis incorporated the net effect of climatic parameters, mix design parameters, material properties, hydration parameters, curing methods, and concrete properties such as elastic modulus, compressive strength, and shrinkage strains.

The stress analyses for all sections were conducted using the above data as inputs, and the complete results are shown in Appendix B. Here Figures 6.28, 6.29, and 6.30 give some examples. Figure 6.28a compares the development of stress and strength with time for section 3. Through the whole analysis period of over 150 hours, the stress

did not surpass the strength at any time, which indicates that there was no delamination. The result was also confirmed from the concrete core taken in section 3, as shown in Figure 6.28b. From the core, it can be seen that there was no horizontal delamination at a shallow depth below the surface from both the concrete core and also from the wall of the core hole. Instead, the concrete core broke at the location of the steel bar, which was due to the coring operation. The result was also consistent with analysis from the UTEP research team.

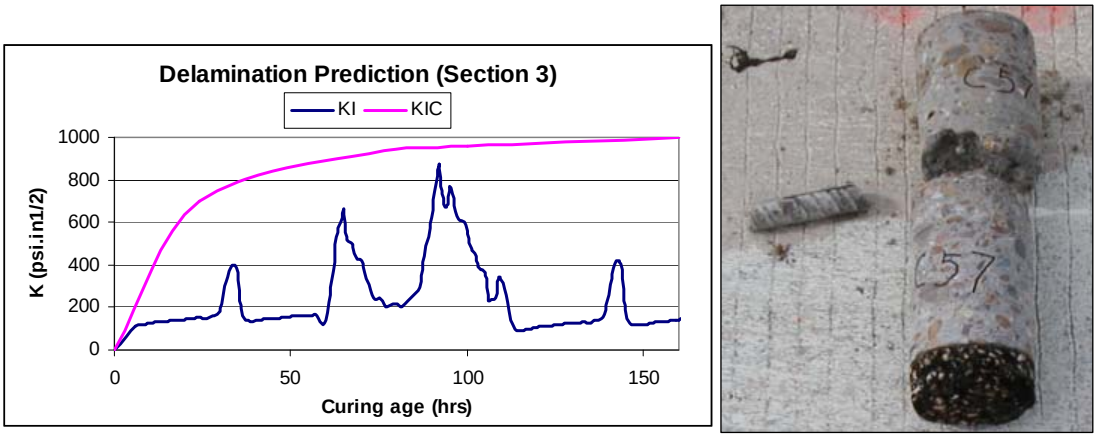

(a) (b)

Figure 6.28. Delamination Prediction for Section 3.

Figure 6.29 compares the development of stress and strength with time for section 2. It can be seen that through the whole analysis period of over 150 hours, there were a few occasions where the stress exceeded the strength, which indicates a greater possibility of delamination occurrence. The result was also correlated with the petrography analysis shown in Figure 6.30. At the aggregate-mortar interface, there was a low concentration of $Ca(OH)_2$, which tends to reduce the interfacial bonding and, subsequently, result in an increased probability of horizontal delamination occurrence.

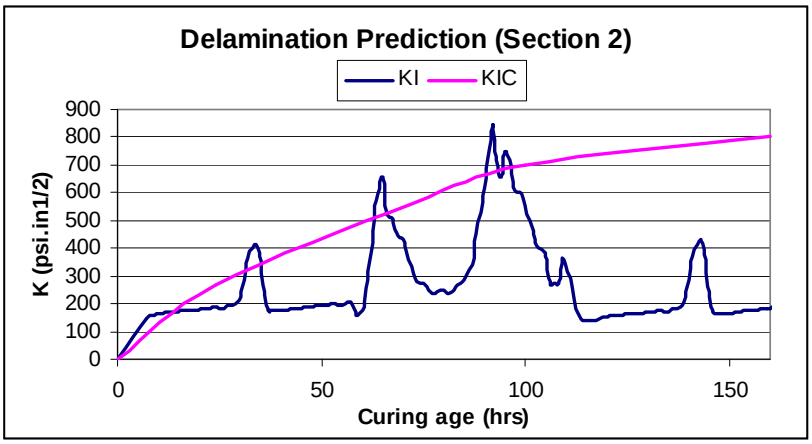

Figure 6.29. Delamination Prediction for Section 2.

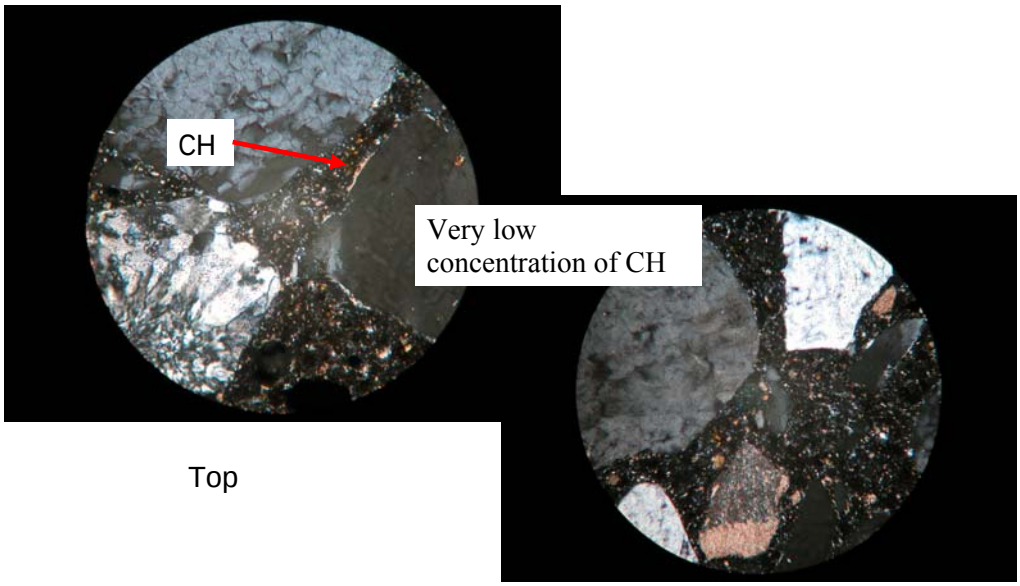

Figure 6.30. Petrography Analysis of Section 2.

Figure 6.31 compares the development of stress and strength with time for section 4. It can be seen that over the analysis period of over 150 hours, there were more occasions where the stress exceeded the strength than in section 2, which indicates the higher probability of delamination occurrence. The result was also correlated with the

petrography analysis shown in Figure 6.32, where at the aggregate-mortar interface, there was a very fine horizontal crack.

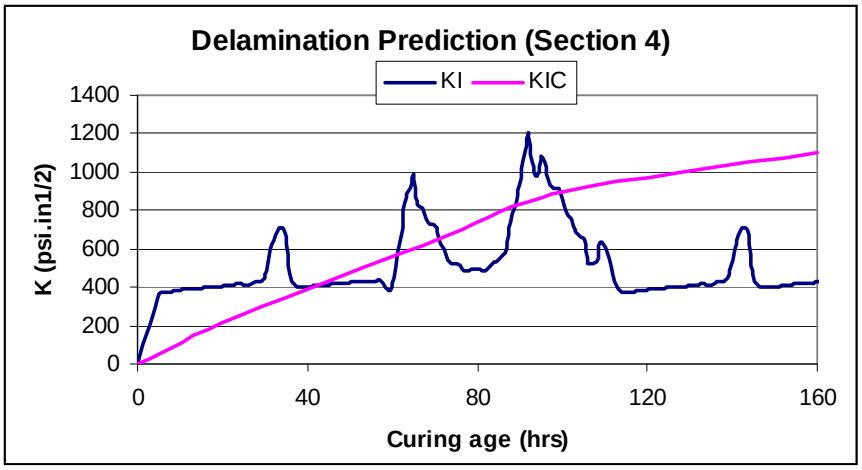

Figure 6.31. Delamination Prediction for Section 4.

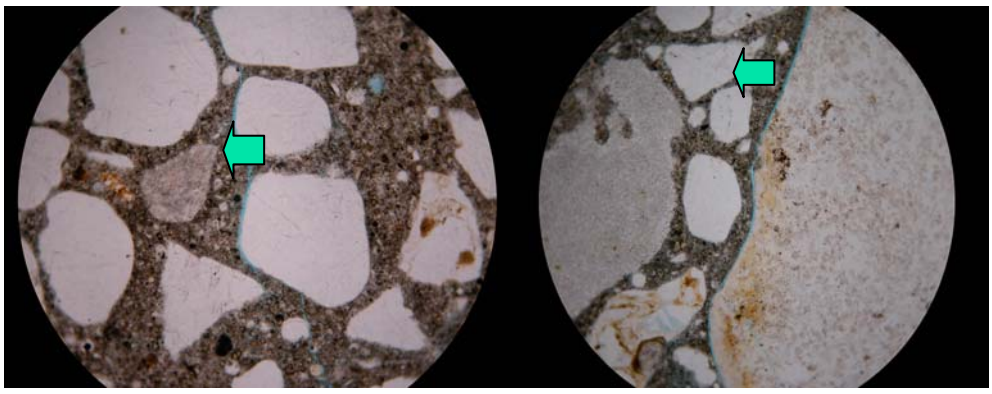

Fine Horizontal cracking at ~ 0.5 inch)

Figure 6.32. Petrography Analysis of Section 4.

Delamination Detection by NDT Protocol

In Chapter V, a NDT delamination detection protocol was developed. In this section, the application of that protocol to detect delamination in the field test section is verified.

The early age moduli obtained with the PSPA on the 10 sections measured near the locations of the maturity sensors are summarized in Figures 6.33a and b. At early ages, Mix 2 (10% UFFA+15% fly ash with modified charge cured with high-reflective compound) exhibited the highest strength. However, after 28 days, Mix 5 (10% UFFA+15% fly ash with normal charge cured with high-reflective compound) exhibited the highest strength.

The estimated compressive strengths of the 10 sections after 4 hr, 24 hr, and 28 days are shown in Figure 6.34. Under normal charge sequence and normal curing conditions, the mix with 10 percent UFFA exhibited higher strength after 24 hours.

In the same way, Figure 6.35 is completed with the information obtained from the TxDOT Lab. In this figure the compressive strengths for different mixes are compared.

The seismic modulus from Free-Free Resonant Column tests (FFRC) provided by TxDOT and obtained from samples prepared during construction for all the mixes was compared to the compressive strength measured on the same samples. Results are shown in Figure 6.36. A power equation was selected to obtain the correlation between the measured seismic modulus and the compressive strength in the form (Yuan et al. 2006):

$$Strength = \alpha\,(Seismic\ Modulus)^{\beta} \qquad (6\text{-}1)$$

The global relationship between the compressive strength and seismic modulus from all 10 mixes from Figure 6.36 shows that the two parameters correlate reasonably well as judged by the value of the R^2 of about 0.8. This global relationship can be used

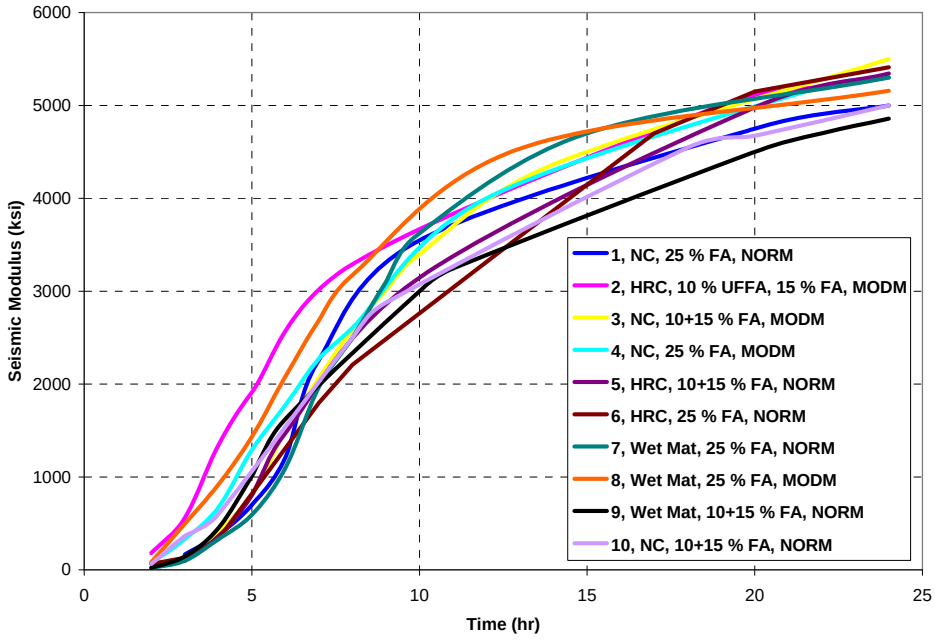

(a)

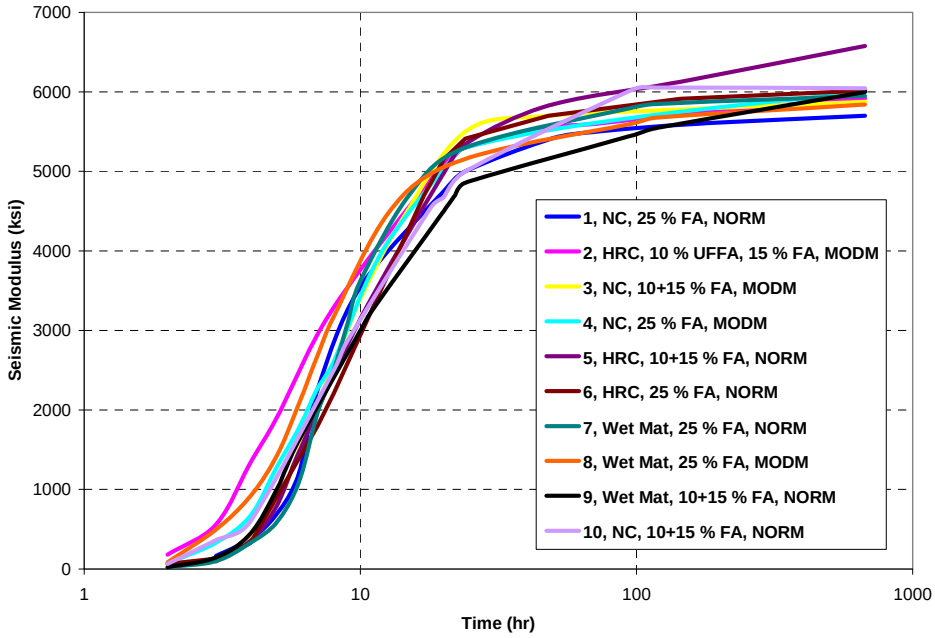

(b)

Figure 6.33. Variation of Early Age Properties (Field Seismic Modulus) Obtained with PSPA on the First 24 Hours and 28 Days.

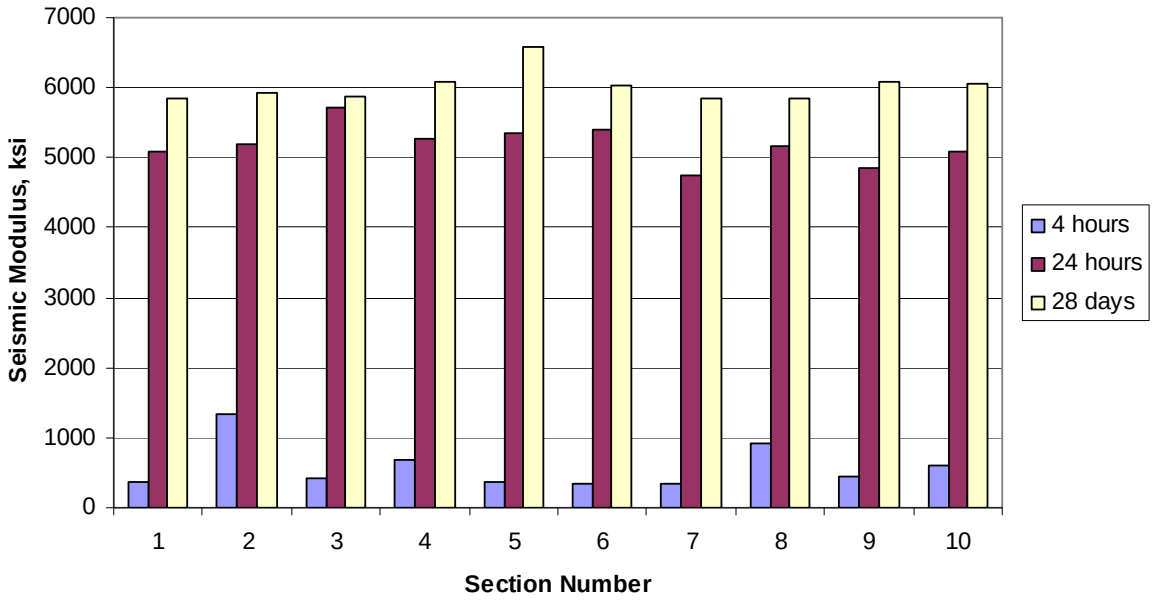

Figure 6.34. Comparison of Early Age Properties (Field Seismic Modulus) with PSPA for the 10 Sections on SH 288.

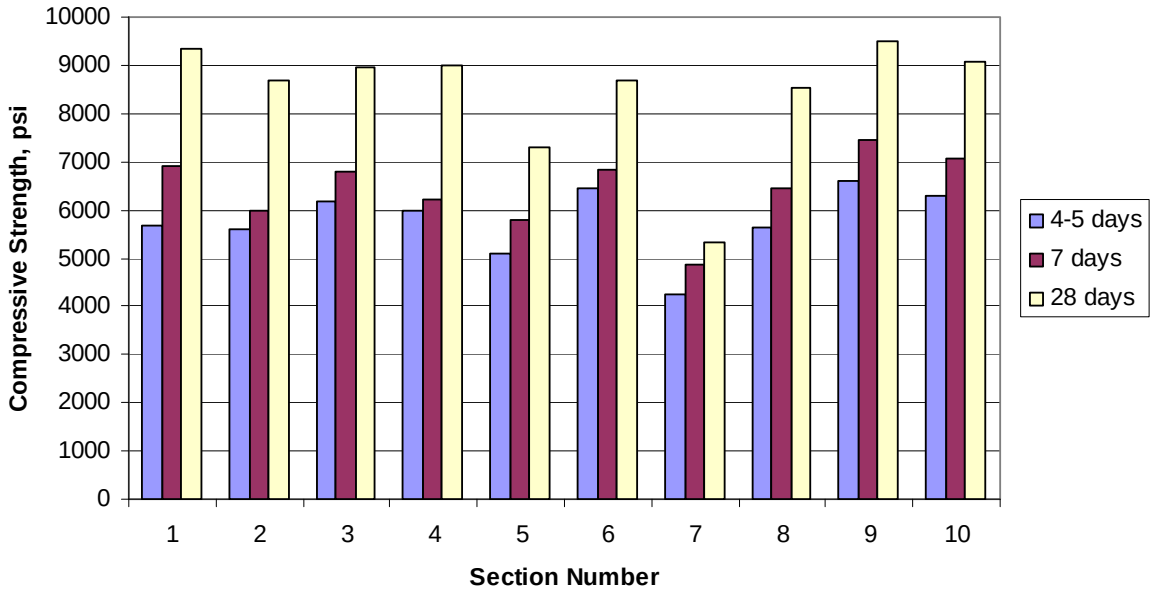

Figure 6.35. Variation in Compressive Strength for the 10 Sections on SH 288 (source: TxDOT Lab).

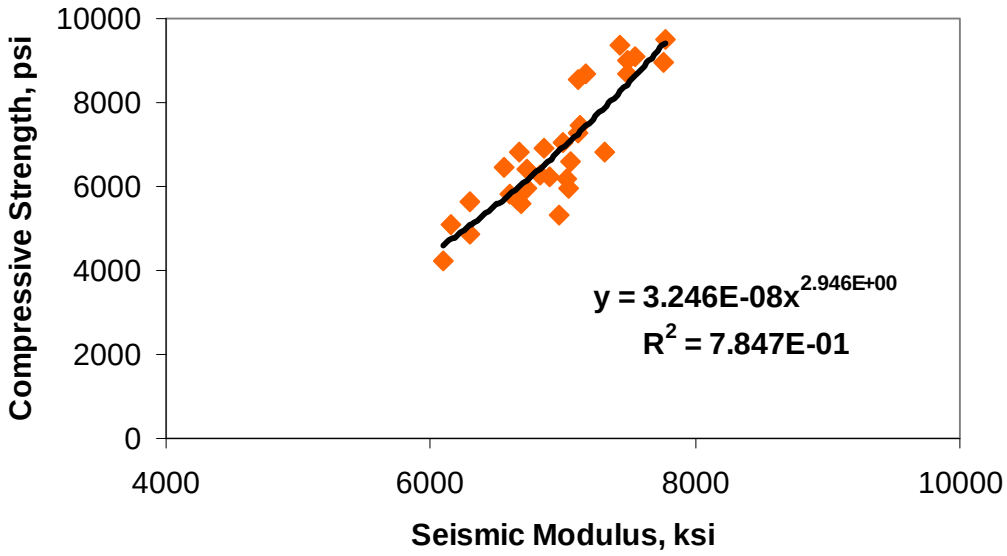

Figure 6.36. Compressive Strength vs. Lab Seismic Modulus (from TxDOT Results).

Table 6.5. Strength-Modulus Fit Parameters for All Mixes Used at SH 288.

Section	Parameter α*	Parameter β	R^2
1	5.119E-14	4.461	0.98
2	9.259E-11	3.601	0.90
3	5.546E-12	3.908	0.98
4	3.694E-12	3.970	0.98
5	1.264E-06	2.532	0.98
6	2.120E-09	3.271	1.00
7	5.560E-04	1.819	0.85
8	4.715E-10	3.438	0.94
9	3.544E-10	3.452	0.95
10	3.315E-11	3.724	0.98
GLOBAL	3.519E-8	2.936	0.80

* Power equation used: *Compressive strength* = α *(Seismic Modulus)*$^{\beta}$

in the absence of a mix-specific relationship. The same approach was used on each of the individual mixes used on SH 288. The parameters (α,β) of the power equation for each mix and for all 10 mixes together are summarized in Table 6.5 and also shown in Appendix C. The R^2 values of all the mix-specific relationships are greater than 0.9 except for Mix 7. According to TxDOT personnel, the quality of the specimens prepared for that mix was less than desirable. These relationships can be used to predict compressive strength from seismic modulus when the same type of aggregate and cement type is used for construction.

PSPA moduli obtained for each of the 10 mixes were used to predict compressive strength from individual relationships shown in Table 6.5. The comparison with measured results from the TxDOT Lab is presented in Figure 6.37. Different curing conditions between specimens tested at TxDOT facilities and in-placed material tested with the PSPA might explain the discrepancies between the results as depicted by Figure 6.37. These differences can also be observed in terms of measured seismic modulus at TxDOT lab facilities and in the field with the PSPA after 28 days (see Figure 6.38). For the majority of the 10 mixes the results obtained by TxDOT are consistently greater than the ones measured by the PSPA.

For each one of the 10 mixes from SH 288 a crack that developed after curing of the concrete was selected to test with the PSPA on a grid around the crack. The test protocol for each of the cracks selected on SH 288 is depicted in Figure 6.39.

Following the PSPA tests, core samples were extracted from selected locations around each crack. Using a time-frequency analysis (Kim et al. 2004, Shokouhi and Gucunski. 2003), spectrograms were generated for each crack investigated and with the information obtained from them, contour maps were also created. An example from section 9 of SH 288 is presented in Figures 6.40 and 6.41. Appendix D contains these final results for all 10 sections of SH 288.

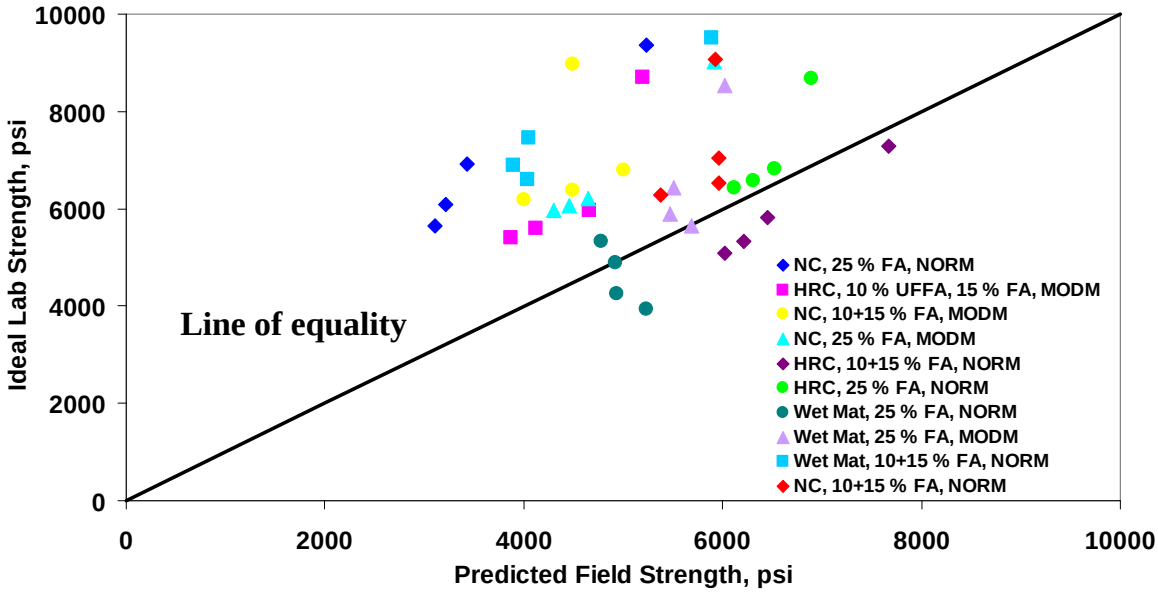

Figure 6.37. Predicted Compressive Strength (Field) vs. Measured Strength (Lab).

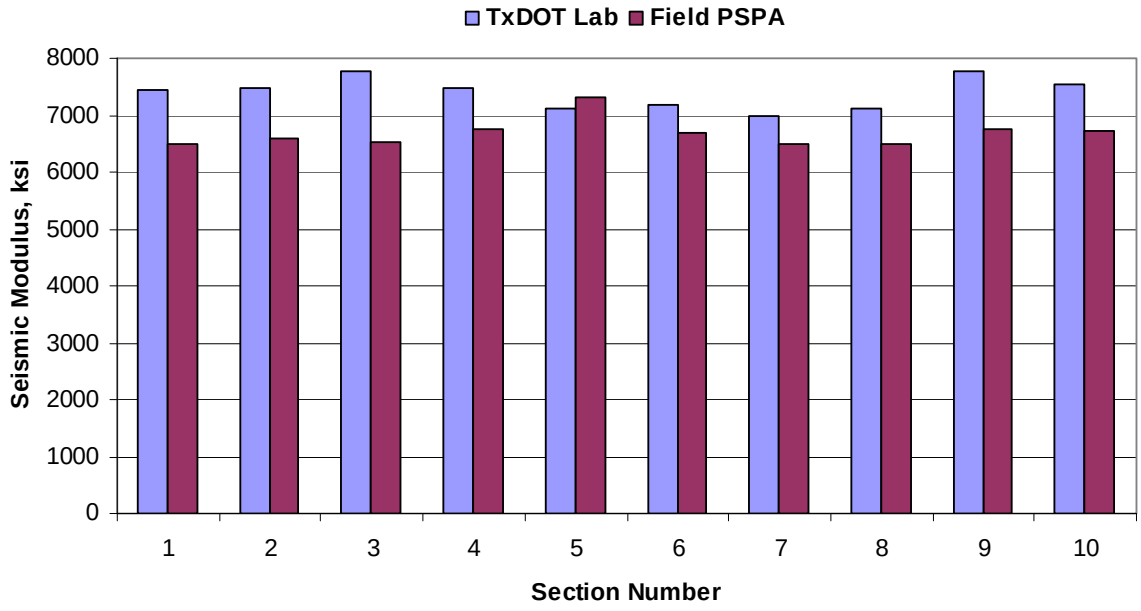

Figure 6.38. Comparison of Lab Seismic Modulus vs. Field PSPA Modulus on SH 288 at 28 days.

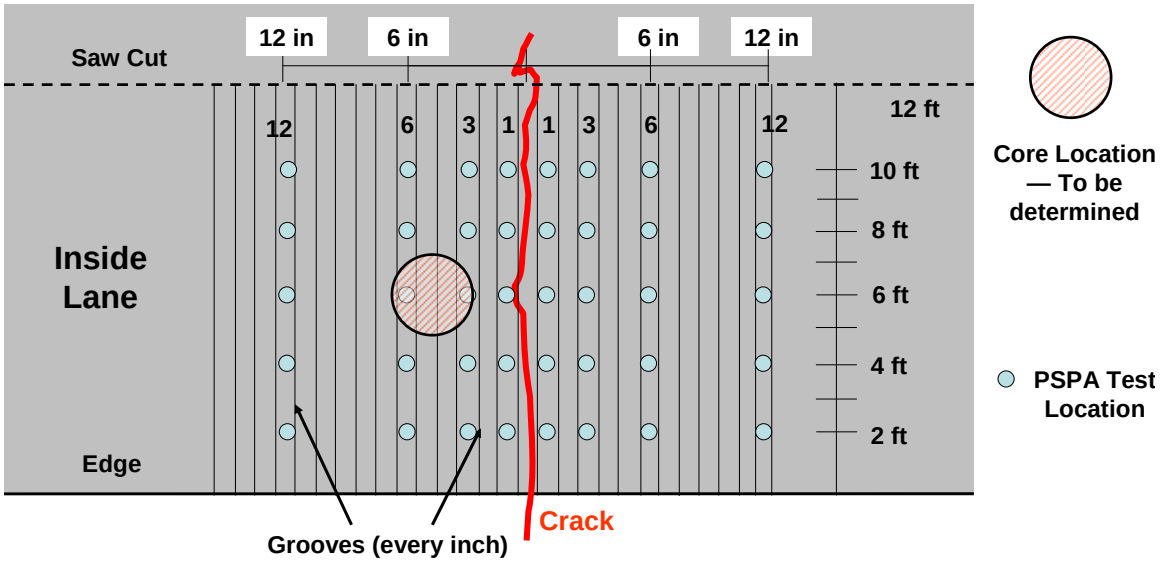

Figure 6.39. Test Protocol Followed around Cracks on SH 288.

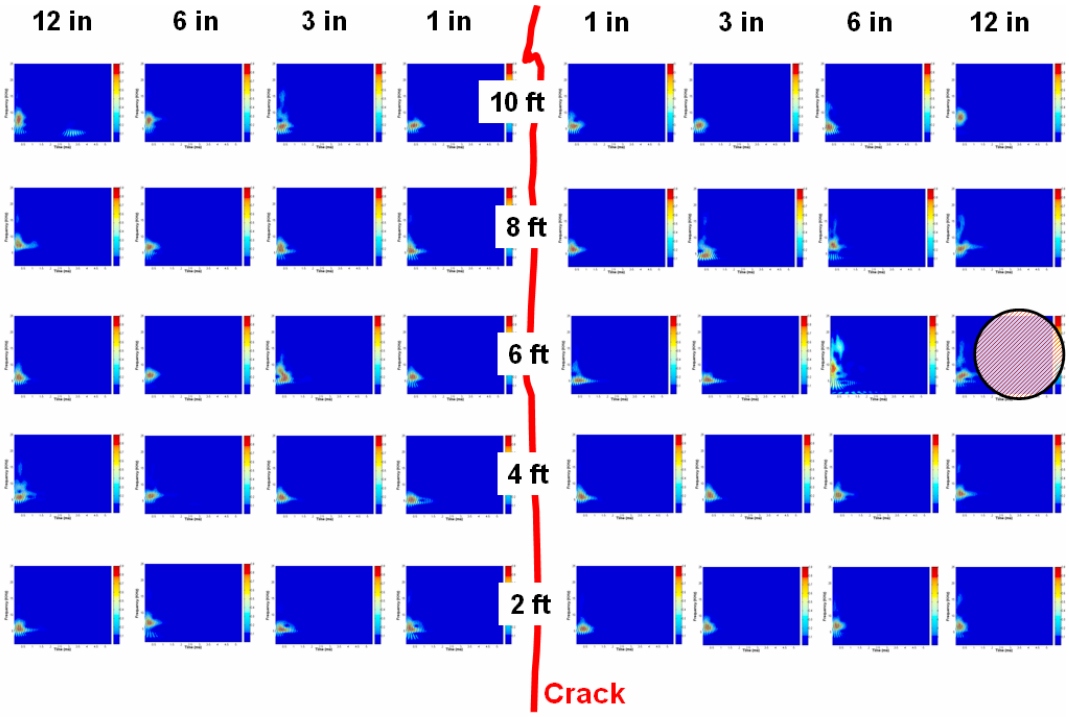

Figure 6.40. Spectrograms Obtained from Crack Selected on Section 9 of SH 288.

As part of the quality control, seven of the 10 mixes of SH 288 were tested at 10 equally spaced points (every 100 ft) and on both wheel paths and the center of the inside lane. An example of the variation in the seismic modulus obtained with the PSPA is presented in Figure 6.42 as a color coded map. Appendix E contains results for the seven sections subjected to this test. Tests were carried out 24 hours after placing the concrete.

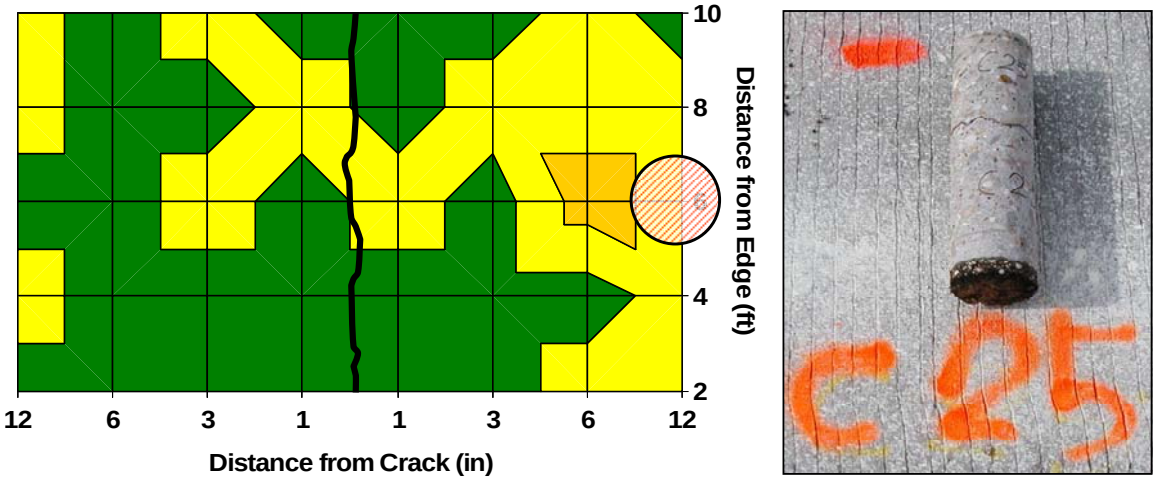

Figure 6.41. Contour Map Representing Material Condition from Crack Selected on Section 9 and Detail of Core Extracted at Same Location.

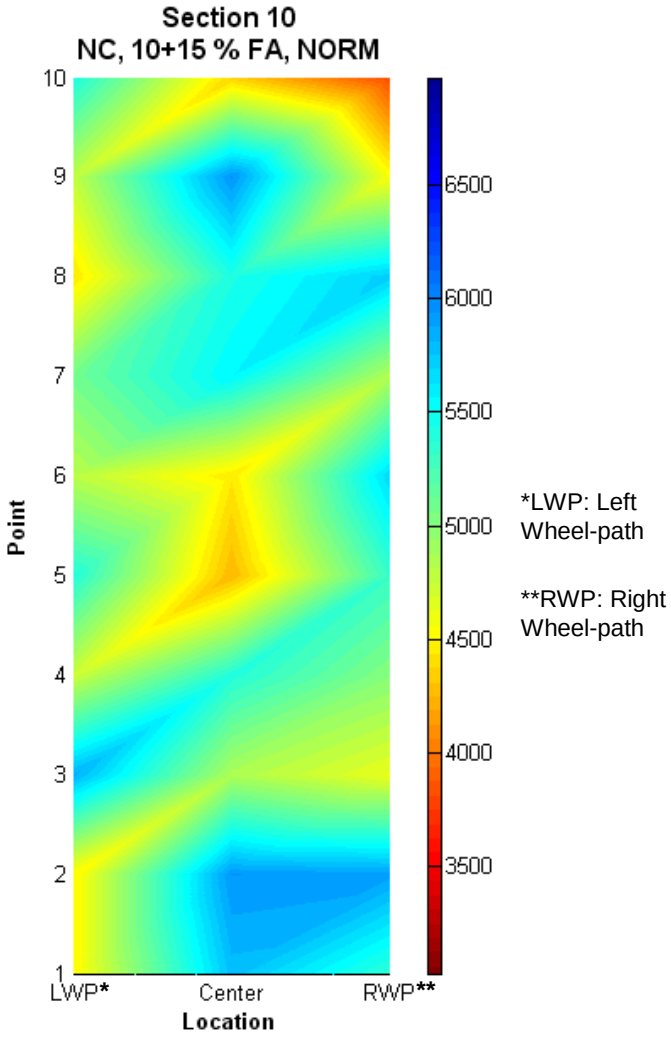

Figure 6.42. Example of Variation in Seismic Modulus along Section 10 on SH 288.

SUMMARY OF SUMMER SECTIONS

On the basis of the winter test sections, another 10 test sections on SH 35 in West Columbia in late April 2006 (summer) were constructed to further validate measures and trends relative to the practices and techniques to minimize the development of spall-related delamination, and to formulate a framework of the construction recommendations for using gravel aggregates in concrete paving. The test section designations are provided in Table 6.4. Ten sections were paved in two continuous days from April 26 - 27.

Field Test Data and Analysis

The field test data and analysis presented here include:

1) weather data, concrete temperature and relative humidity profiles, and drying shrinkage development;
2) pavement condition such as the crack pattern development over time in each test section;
3) field bond strength of concrete; and
4) NDT data.

The data information in the first three items was further used as inputs for stress analysis to predict associated delamination occurrence, and NDT data were analyzed by the field delamination detection protocol. The results were further validated by associated concrete coring tests.

Weather Data

As in the tests in the SH 288 test sections, a weather station (shown in Figure 6.6) was used to collect weather data in the field. This station recorded ambient relative humidity, ambient temperature, solar radiation, wind direction, wind speed, and rainfall. These data were collected at hourly intervals on a continuous basis.

Figures 6.43 and 6.44 record the trends of relative humidity, temperature, solar radiation, and wind speed with time over the placement period and beyond (from 04/26/2006 to 04/29/2006). As shown in Figure 6.43, relative humidity shows the inverse relation with the temperature, i.e., the higher temperature associates with the lower relative humidity, and vice versa. Over the first several days after construction, ambient temperature ranged from a low of 60 ^{o}F in the morning hours to a high of 83 ^{o}F in the afternoon, and the relative humidity ranged from a low of around 50 percent in the afternoon to a high of 95 percent in the morning (Figure 6.43). As shown in Figure 6.44, 0.45 kw/m^2 of maximum solar radiation and 10 mph of maximum wind speed were recorded over the monitored period.

Concrete Temperature Profiles

Vertical temperature profiles through the thickness of the pavement for all the test sections were measured immediately after concrete placement at three different locations in the concrete (1 inch from the top, mid-depth, and 1 inch from the bottom). Figure 6.45 shows the temperature development in the concrete for one of the test sections (section 5). Figure 6.46 summarizes the maximum temperature at different locations in the pavement and the associated elapsed time when these temperatures were reached. A complete set of data is provided in Appendix F.

It has been observed that at each location, the development of concrete temperature with time followed a cyclic pattern (similar to Figure 6.45). The different maximum temperatures in different sections are mainly a reflection of differences in placement temperatures. In general, the concrete at the three different locations reached their highest temperature in this time order: 1 in from the top, mid-depth, and 1 in from the bottom.

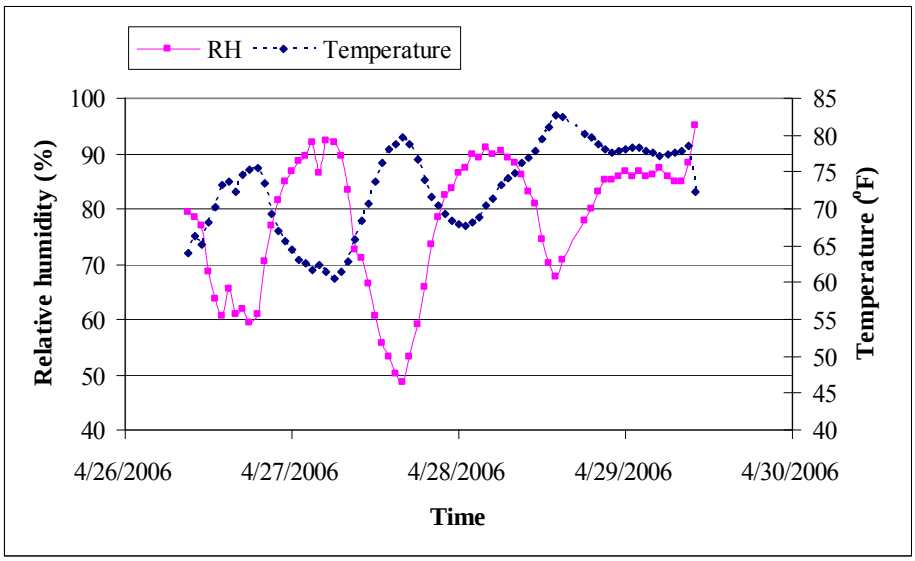

Figure 6.43. Ambient Temperature and Relative Humidity Cycles at SH 35 Test Sections.

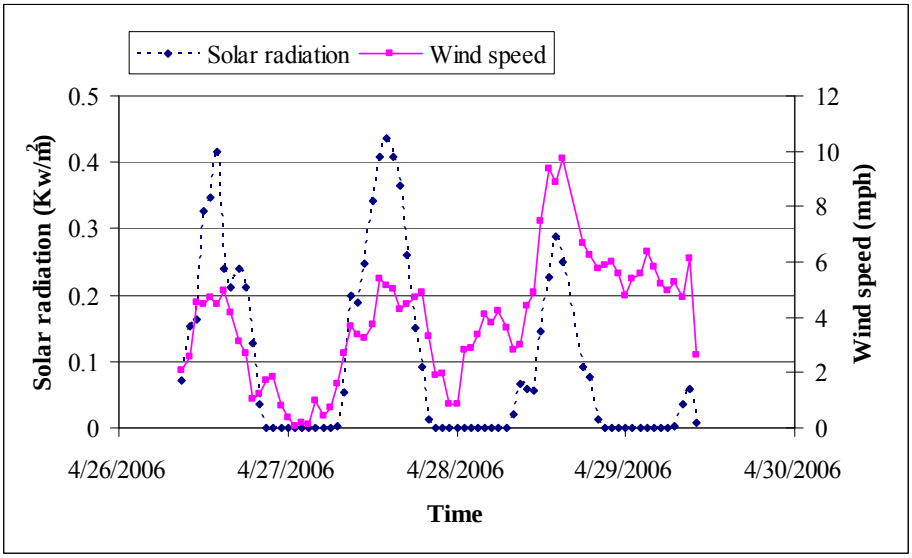

Figure 6.44. Solar Radiation and Wind Speed Cycles at SH 35 Test Sections.

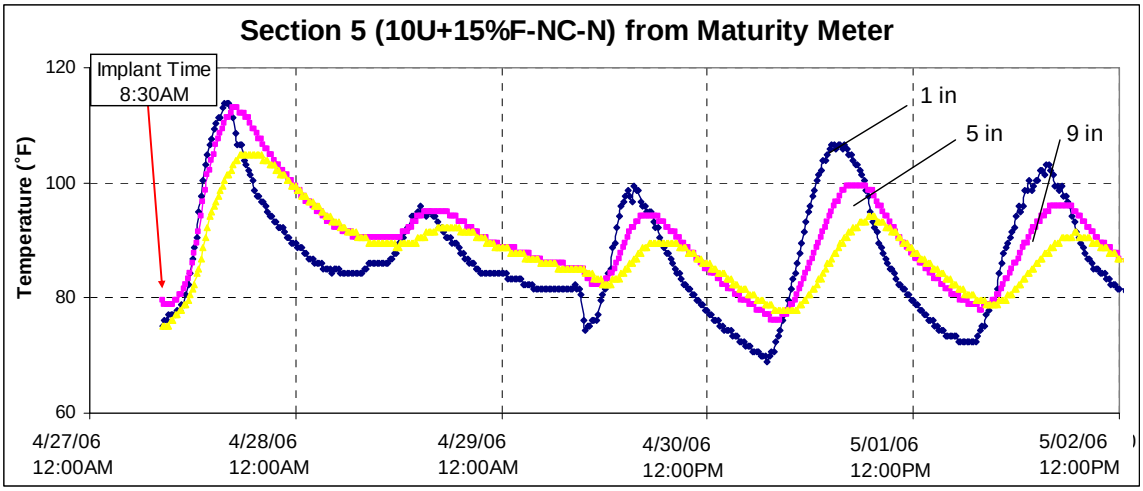

Figure 6.45. Temperature Profile of Test Section 5 at SH 35.

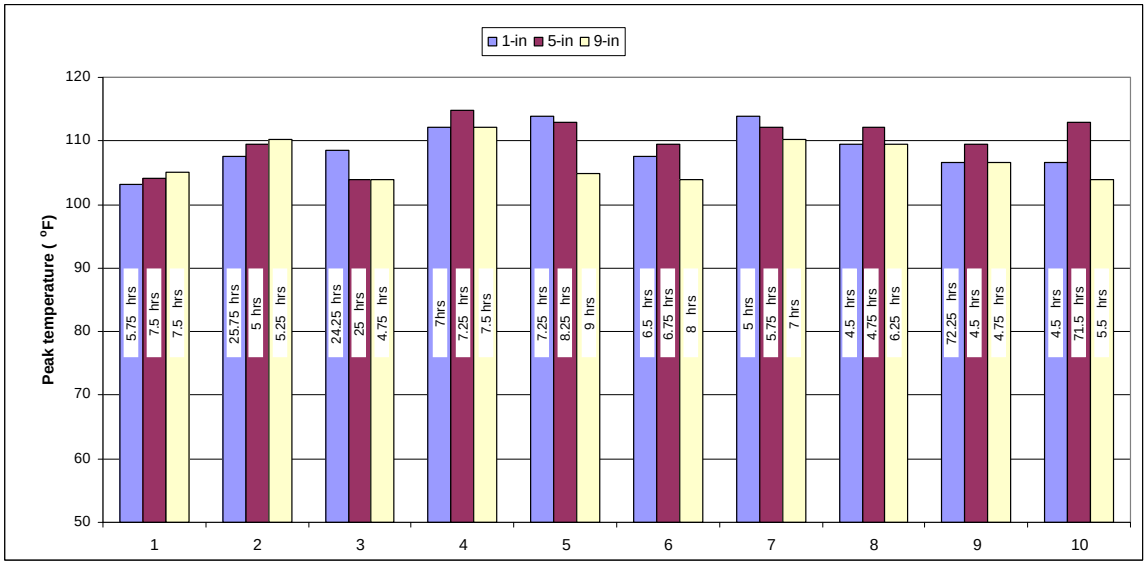

Figure 6.46. Maximum Temperature for Each Test Section at SH 35.

Moisture Profiles

Moisture profiles at different locations (i.e., surface, ambient, and 1 in below the surface) were measured by curing monitor system (as shown in Figure 6.13). Figure 6.47 gives an example of time histories of relative humidity for one of the test sections (section 1), and complete data can be referenced in Appendix F. Most of the time, the ambient relative humidity was lower than those of the concrete, and relative humidity at 1 in below the surface showed the highest values. In addition, the development of ambient relative humidity with time follows a cyclic pattern. However, the moisture profile at the surface and 1 in below the surface varied with the different materials and curing methods.

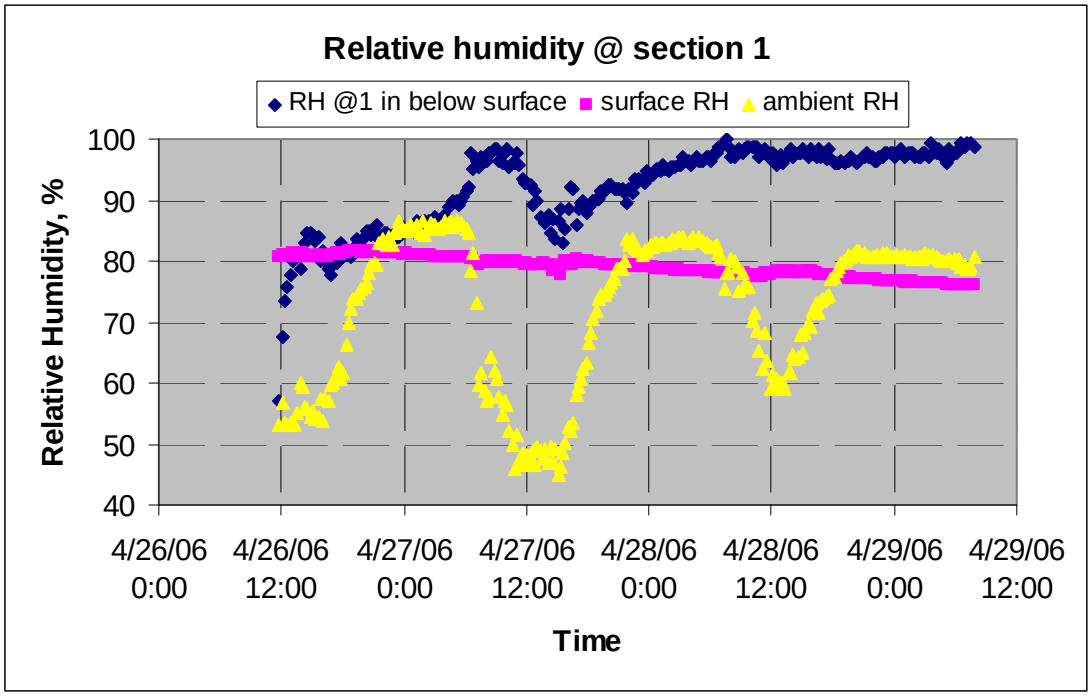

Figure 6.47. Moisture Profiles of Test Section 1 at SH 35.

Drying Shrinkage

To measure the strain in the concrete, 10 vibrating wire strain gages (shown in Figure 6.9b) (four from TTI and the other six from CTR) were installed at 1 inch below the surface for all test sections. Ten concrete shrinkage bar specimens were also cast according to ASTM C157 for unrestrained shrinkage strain measurements with VWGs placed within the specimens.

Figure 6.48 illustrates the free shrinkage strain development with time for all test sections. It can be seen that for most all sections free shrinkage strain increases with time, and maximum free shrinkage strain occurs at the later stage of the analysis period. Figure 6.49 illustrates their maximum free shrinkage strain within the 7-day analysis period. Sections 3 and 9 showed the higher maximum free shrinakage; however, a similar conclusion drawn from the winter sections cannot be obtained from the summer sections.

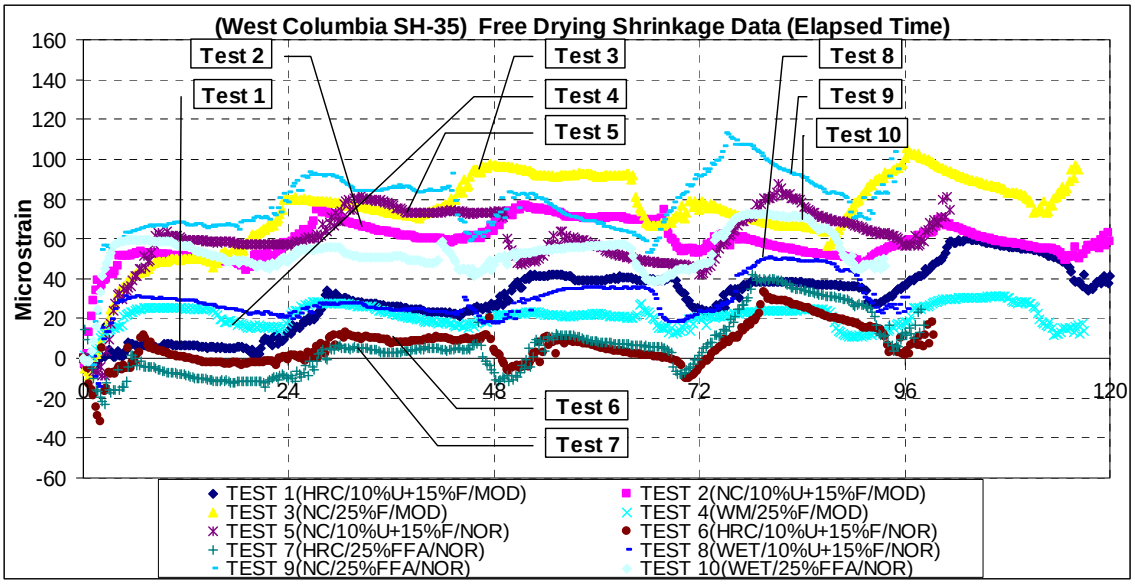

Figure 6.48. Free Shrinkage with Time for Different Sections.

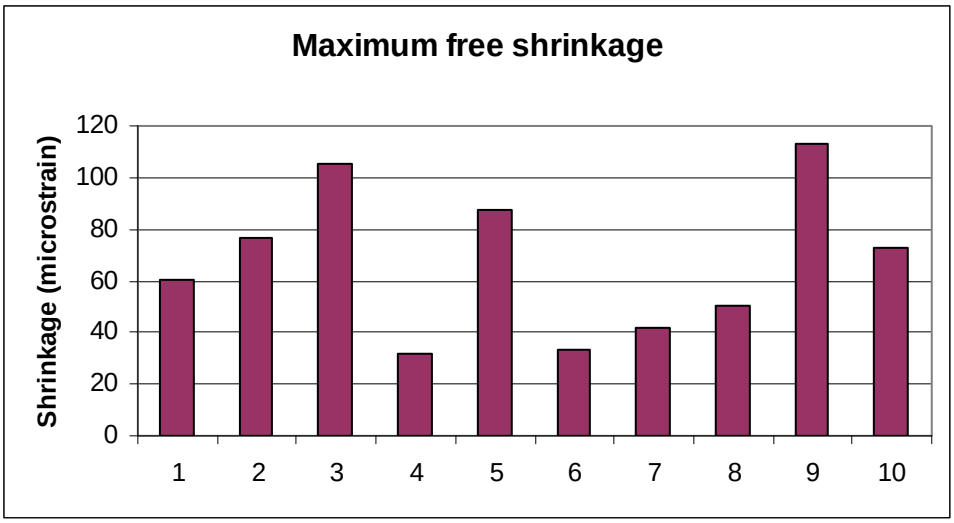

Figure 6.49. Maximum Free Shrinkage of Concrete.

Figure 6.50 presents the gage shrinkage strain development with time for test sections 1 to 6 from the VWGs. For all test sections, the development of gage shrinkage in the concrete followed a cyclic pattern, which indicated the gage shrinkage is a function of not only concrete material properties but also curing methods and environmental effects.

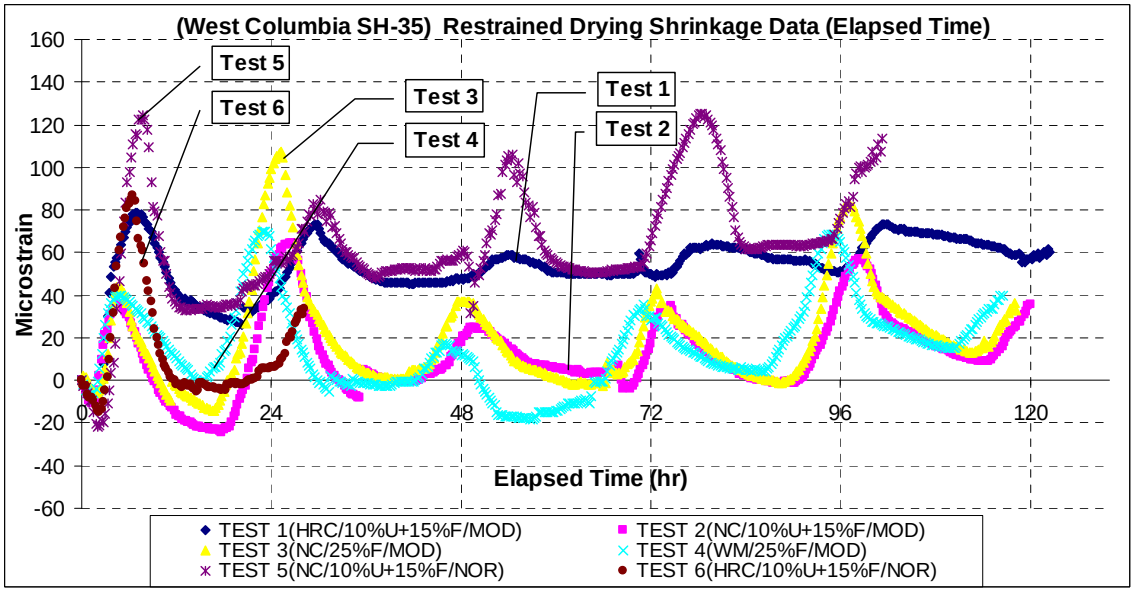

Figure 6.50. Gage Strains with Time for Different Sections.

Pavement Survey

Pavement crack survey of the 10 test sections were conducted several times during May and June, which included collecting the number of cracks, and crack spacing and crack width of each crack. The first crack was detected on section 1 in the morning of May 5. Figure 6.51 shows the probability of crack spacing at different concrete ages, using data from section 3 as an example. The probability of crack spacing less than a given value presented a sigmoidal shape. With age, the curve shifted to the left gradually, which indicated that the probability of crack spacing less than a given value increased. Figure 6.52 compares the development of crack spacing for all test sections. At an early age of the concrete, the crack spacing for each section was large due to only a few cracks developing. The increase in the numbers of cracks with time resulted in the decrease of average crack spacing for each section.

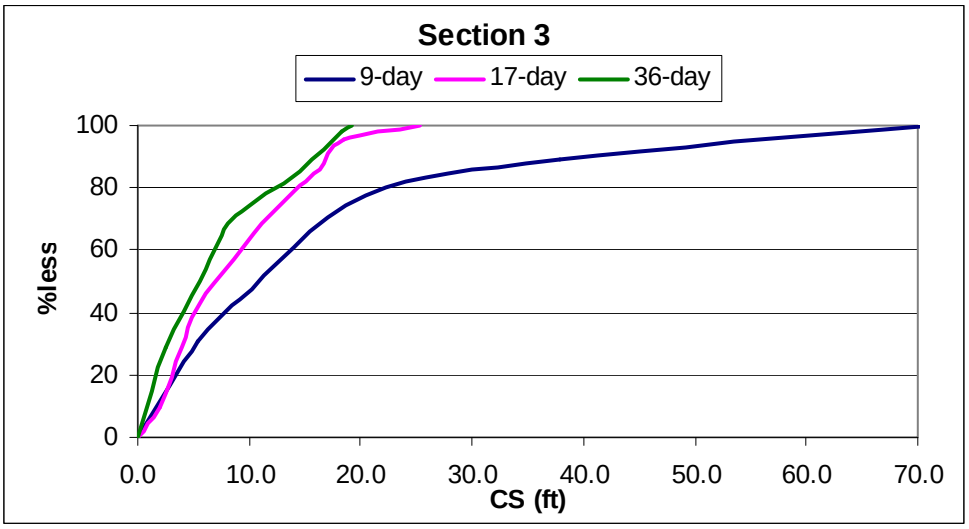

Figure 6.51. Crack Development With Time.

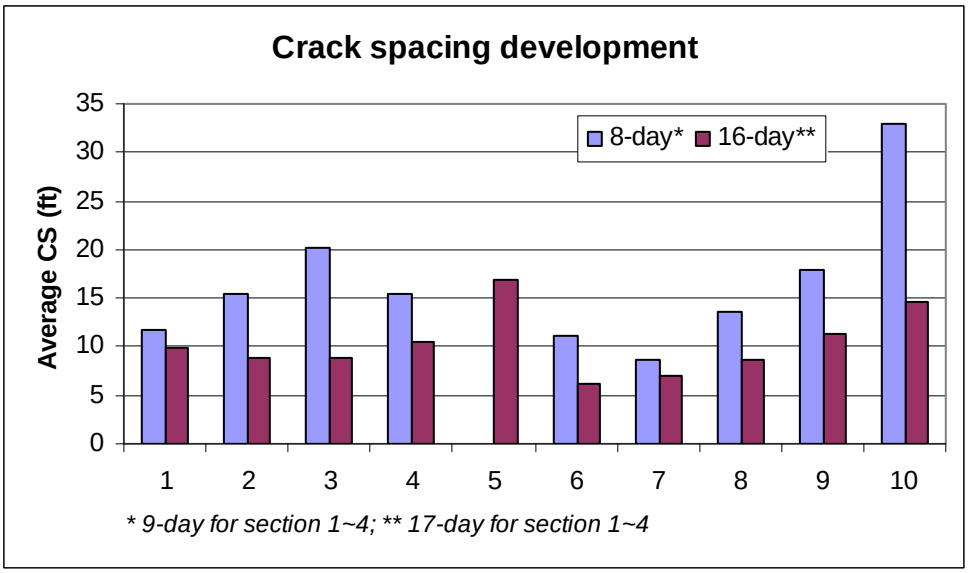

Figure 6.52. Crack Spacing for Concrete Sections.

Concrete Strength

Figure 6.53 illustrates the compressive strengths of concrete for all sections at four different ages, and Figure 6.54 illustrates the 7-day concrete modulus of rupture (MOR) for all sections with the time concrete compressive strength increased for all sections. Section 5 showed both highest 28-day compressive strength and 7-day MOR value. Modified charging sequencing showed more benefit to the development of MOR than normal charging sequencing by comparing sections 1 and 2, 3 and 4, and 6 and 10. However, the effect of wet mat curing was not as significant as what it presented in the winter test sections.

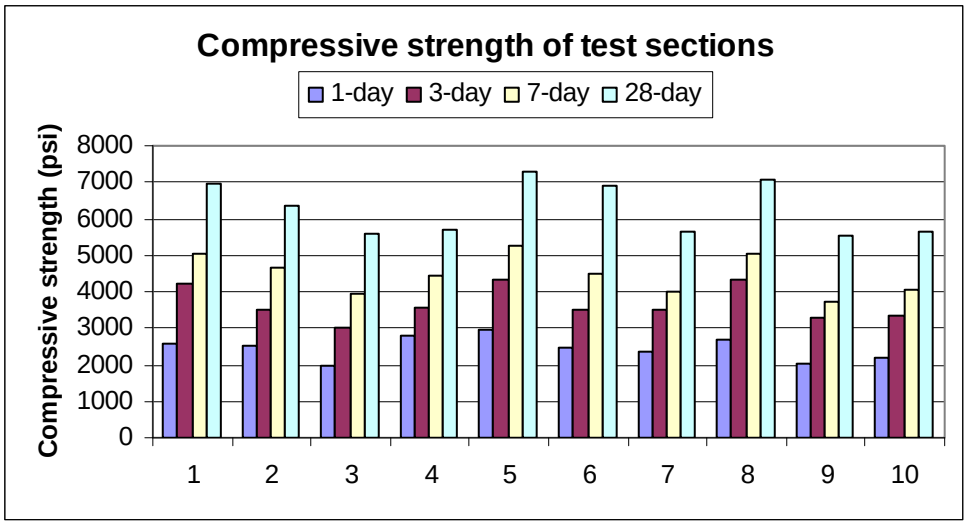

Figure 6.53. Compressive Strength of Concrete for All Test Sections.

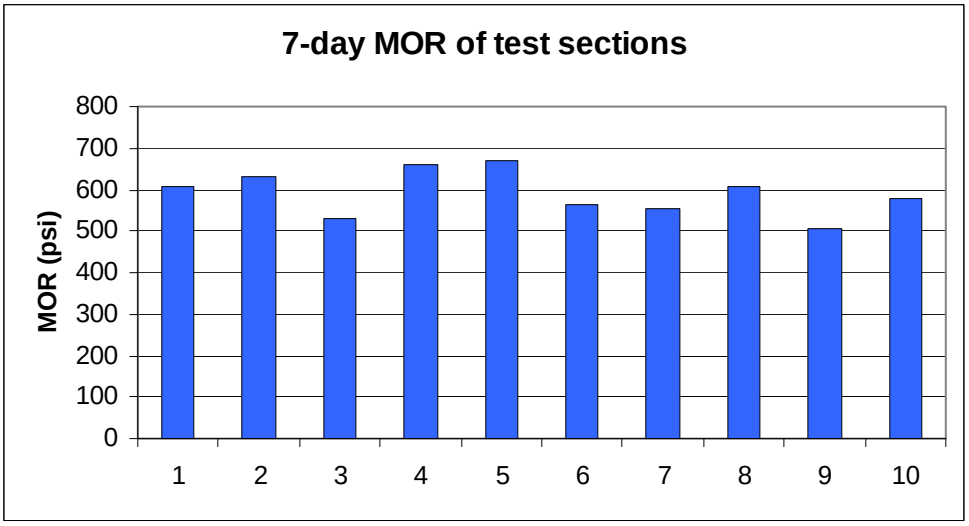

Figure 6.54. Concrete MORs for All Test Sections.

Field Fracture Toughness Testing

Fracture toughness testing for the summer sections were performed in the field for concrete at ages of both 1-day and 3-day, and Figure 6.55 summarizes the results for

each test section. A difference ranging from 7 to 10 percent between the results from the same combinations in the two test sections from both winter and summer sections is perhaps due to the variation in the field construction operations. It can be seen that the interfacial bond between aggregate and mortar increased at different degrees with time. Section 6 (i.e., a design combination of using 25 percent Class F fly ash, WMC, and a modified charging sequence) resulted in the highest bonding strength among all test sections. The effectiveness of the wet mat curing method can be observed from comparison among sections 1, 3, and 9; sections 5, 7, and 10; comparison between sections 2 and 4, and between 6 and 8.

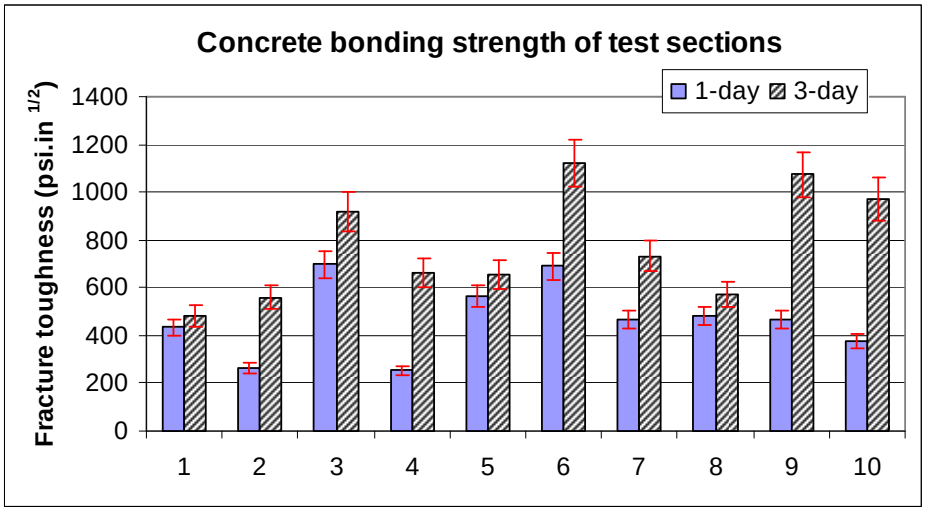

Figure 6.55. Summary of Fracture Toughness for Each Section.

Further experimental design analysis identified the factor of curing method as the most significant factor relative to the bonding performance for both 1-day and 3-day performance. For curing methods, WMC showed the best performance, and HRC was better than NC. In addition, within the scope of the test sections, the factor of charging sequencing was not significantly related to the K_{IC}. Although the possible reason could be on the basis of low w/cm and dense-graded aggregates; the improvement of concrete

bonding performance provided by charging sequence appears to not be as significant as it should be.

Assessment of Delamination Probability

The comparison between K_I (stress) and K_{IC} (strength) was again applied to assess the delamination occurrence probability for the summer test sections. As an example, Figure 6.56 compares the development of K_I and K_{IC} with time for section 5 on SH 35. Again it can be seen that over the analysis period of 7 days, there were a few occasions where the K_I exceeded the K_{IC}, which indicated there were critical times where there was a possibility of delamination occurrence. However, from the core taken on this section, there was again no horizontal delamination at a shallow depth below the surface from both the concrete core and the wall of the core hole, as shown in Figure 6.57. Instead, the concrete core broke at the mid-depth of the slab at the level of the steel reinforcing bars due to the stress concentration at the interface of the concrete and the steel bar.

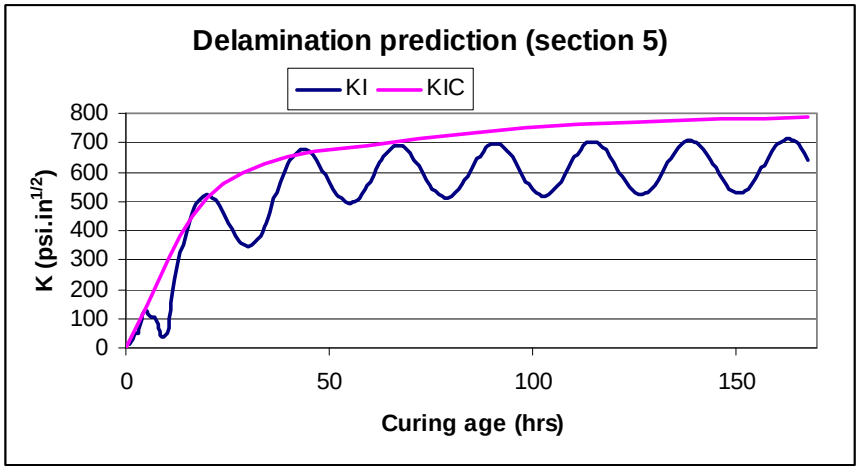

Figure 6.56. Delamination Prediction for Section 5.

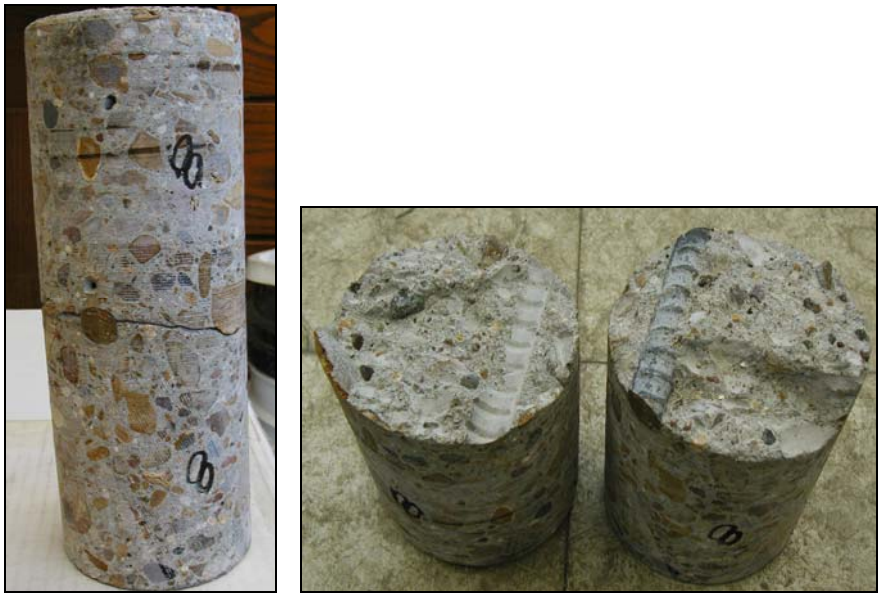

Figure 6.57. Assessment of Delamination for Section 5 on SH 35.

Delamination Detection by NDT Protocol

The developed NDT detection protocol (Chapter V) is applied in this test section to verify its applicability.

The early age moduli obtained with the PSPA on the 10 sections measured near the locations of the maturity sensors are summarized in Figures 6.58a and 6.58b. At early ages, Mix 8 (10 percent UFFA+15 percent fly ash with normal charge cured with a wet mat) exhibited the highest modulus. However, after 28 days, Mix 1 (10 percent UFFA+15 percent fly ash with modified charge cured with high-reflective compound) exhibited the highest modulus.

The estimated compressive strengths from PSPA moduli of the 10 sections after 4 hr, 24 hr, and 28 days are shown in Figure 6.59. Under normal charge sequence and normal curing conditions, the mix with 10 percent UFFA exhibited higher strength after 24 hours (same as in SH 288).

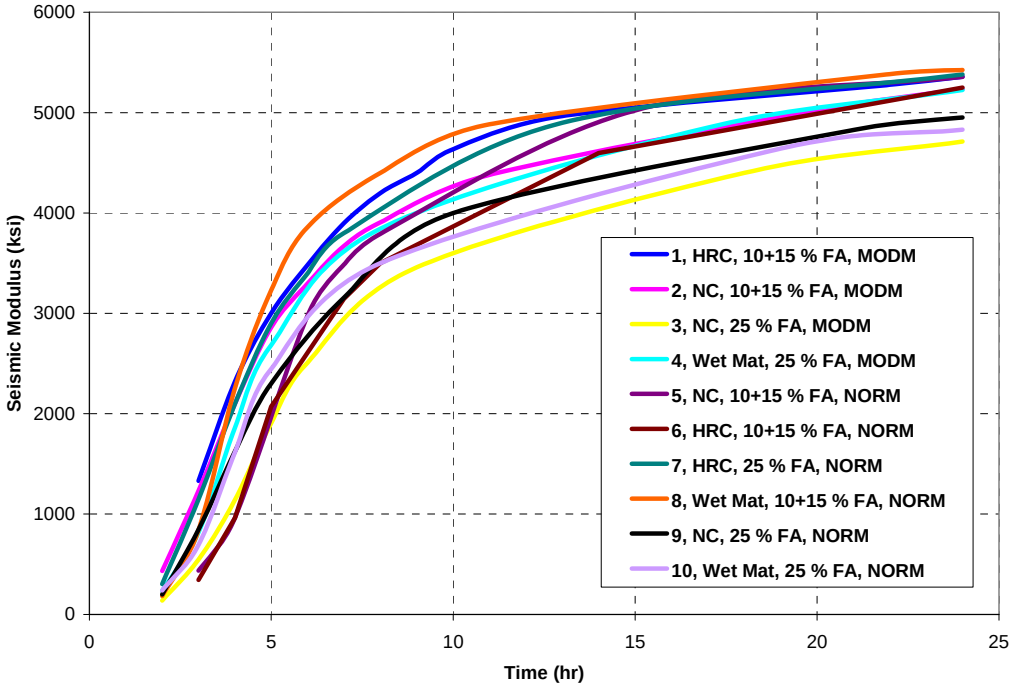

(a)

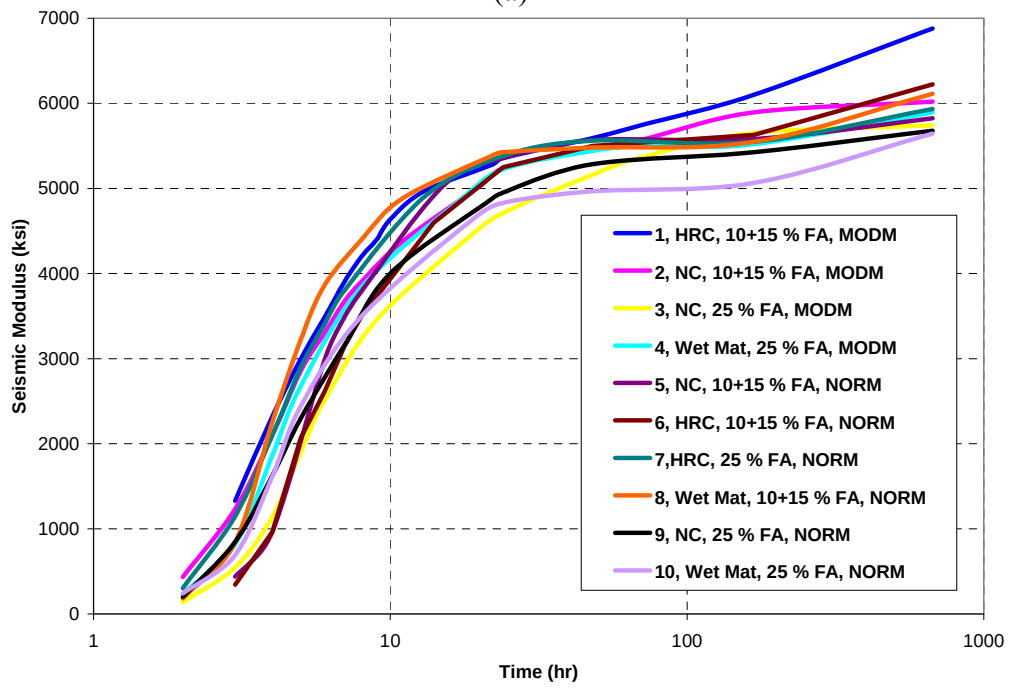

(b)

Figure 6.58. Variation of Early Age Properties (Field Seismic Modulus) Obtained with PSPA on the First 24 Hours and 28 Days.

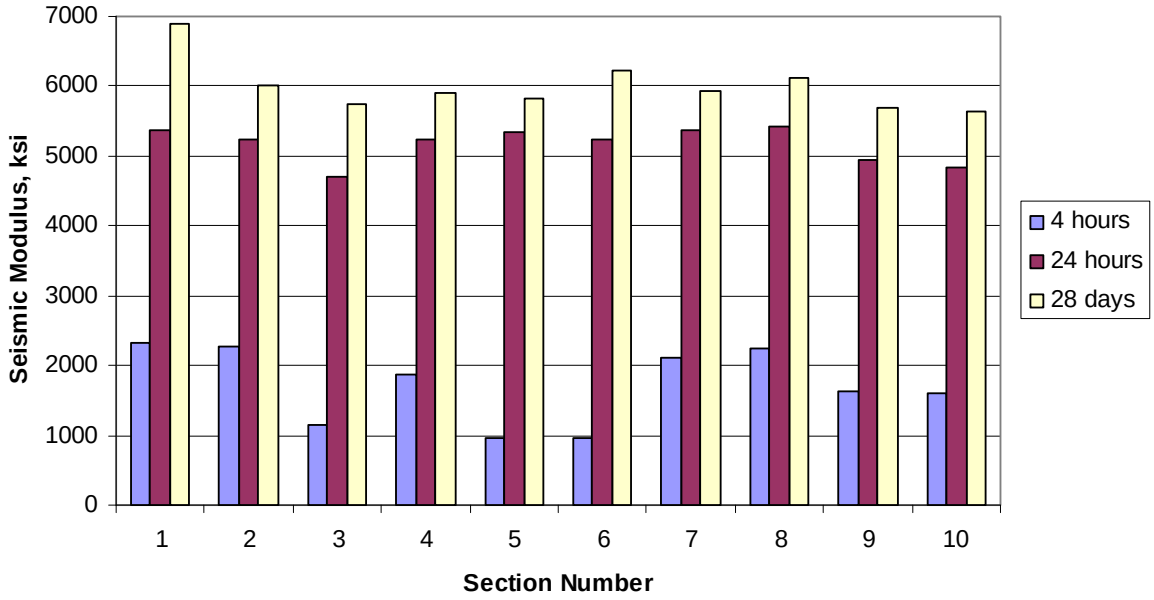

Figure 6.59. Comparison of Early Age Properties (Field Seismic Modulus) with PSPA for the 10 Sections on SH 35.

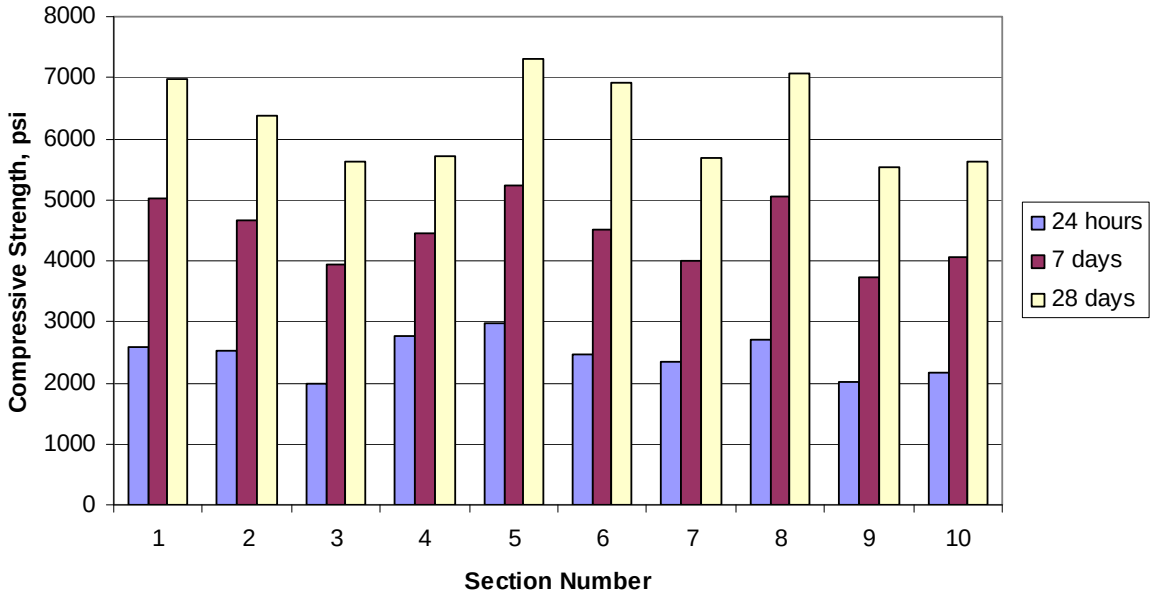

Figure 6.60. Variation in Compressive Strength for the 10 Sections on SH 35 (Source: TxDOT Lab).

The compressive strengths from the TxDOT Lab for different mixes are shown in Figure 6.60. PSPA tests were carried out on the 10 sections at different times to measure the early age properties of the different mixes. Results obtained with the PSPA were also compared to those obtained from TxDOT. In addition, eight cracks were selected to compare seismic testing and core samples. From these eight locations, four cores were distributed among the first five sections and the rest were obtained on locations around saw cut sections.

The seismic modulus from tests FFRC provided by TxDOT and obtained from samples prepared during construction for all the mixes was compared to the compressive strength measured on the same samples. Results are shown in Figure 6.61. The power equation previously introduced was selected to obtain the correlation between the measured seismic modulus and the compressive strength. The global relationship between the compressive strength and seismic modulus from all 10 mixes from Figure 6.61 shows that the two parameters correlate reasonably well as judged by the value of the R^2 of about 0.92. The same approach was used on each of the individual mixes used on SH 35. The parameters (α,β) of the power equation for each mix and for all 10 mixes together are summarized in Table 6.6 and are shown in Appendix G. The R^2 values of all the mix-specific relationships are greater than 0.97.

PSPA moduli obtained for each of the 10 mixes were used to predict compressive strength from individual relationships shown in Table 6.6. The estimated and measured strengths are compared in Figure 6.62. Different curing conditions between specimens tested at TxDOT facilities and in-placed material tested with the PSPA might explain the higher strengths obtained from lab tests. These differences can also be observed in terms of measured seismic modulus at the TxDOT Lab facilities and on the field with the PSPA after 28 days (see Figure 6.63). For the majority of the 10 mixes the results obtained by TxDOT are consistently greater than the ones measured by the PSPA.

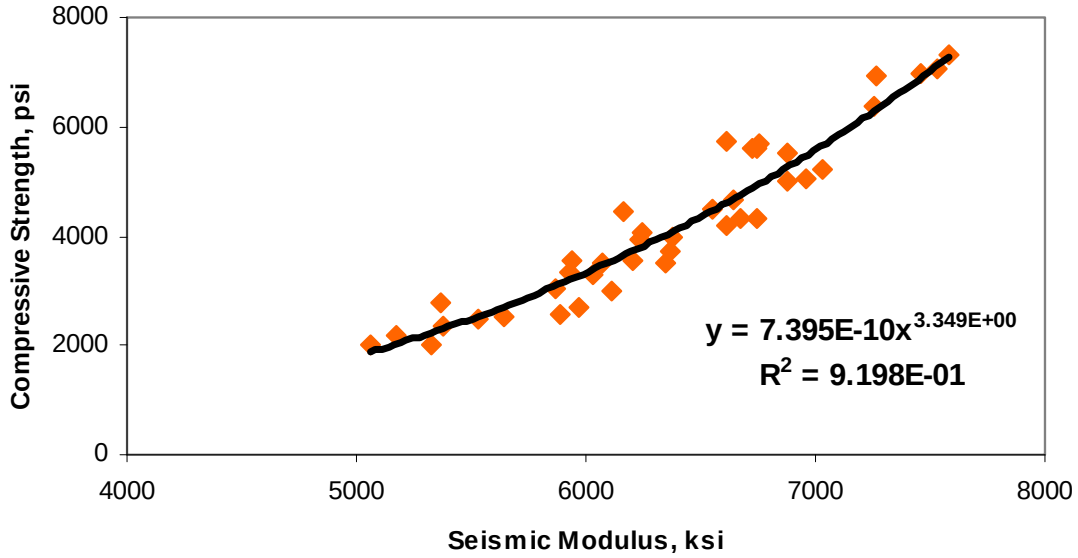

Figure 6.61. Comparison of Early Age Properties (Field Seismic Modulus) with PSPA for the 10 Sections on SH 35.

Table 6.6. Power Equation Parameters from All Mixes Used at SH 35.

	Alfa	Beta	R^2
GLOBAL	**7.395E-10**	**3.349**	**0.920**
Section	**INDIVIDUAL**		
1	3.453E-13	4.211	1.000
2	2.799E-11	3.717	0.979
3	1.189E-10	3.566	0.980
4	2.385E-10	3.499	0.970
5	4.425E-13	4.179	0.998
6	1.613E-11	3.786	0.994
7	4.251E-11	3.681	0.972
8	8.950E-13	4.100	1.000
9	7.187E-12	3.876	0.989
10	1.692E-10	3.528	0.994

* Power equation used: *Compressive strength* = α *(Seismic Modulus)*$^{\beta}$

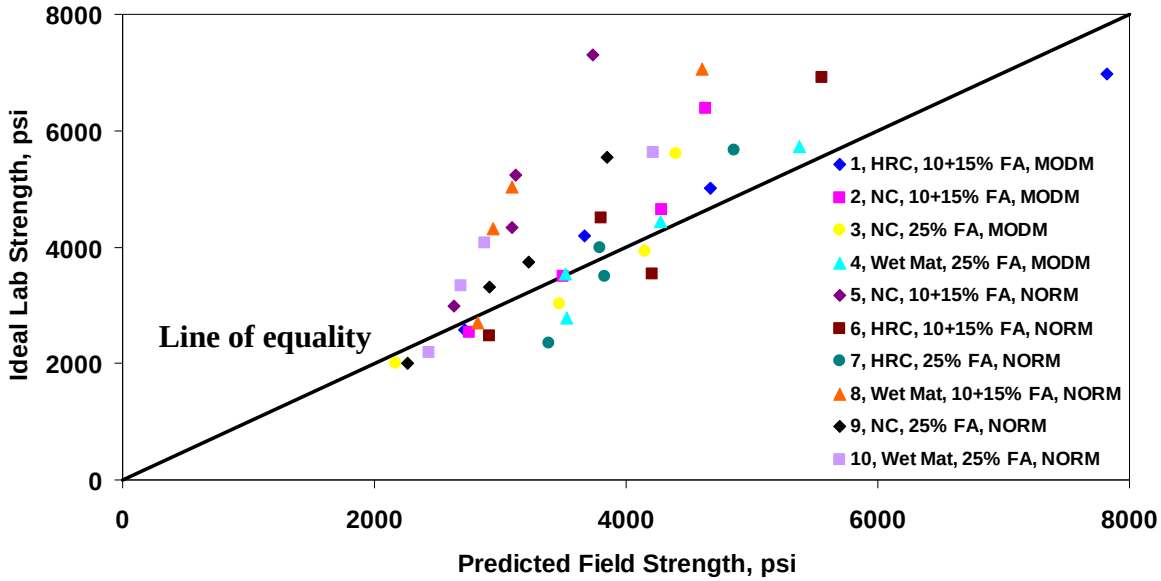

Figure 6.62. Predicted Compressive Strength (Field) vs. Measured Strength (Lab) for SH 35.

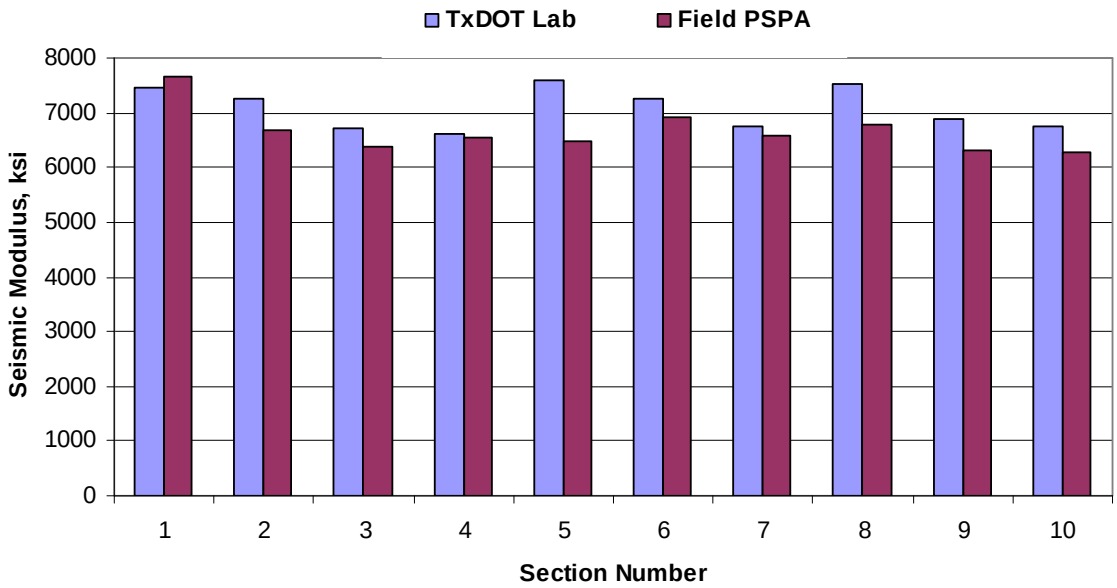

Figure 6.63. Comparison of Lab Seismic Modulus vs. Field PSPA Modulus on SH 35 at 28 days.

For four of the 10 mixes, a crack developed after curing of the concrete was selected for testing with the PSPA on several locations around the cores. The cores were obtained before the cracks were tested with the PSPA. The test protocol for each of the cracks selected on SH 35 is depicted in Figure 6.64. In addition, four more cores were obtained in saw cut areas and also tested with the PSPA. An example from section 1 of SH 35 is presented in Figure 6.65. Appendix H contains these final results for all eight cores from SH 35.

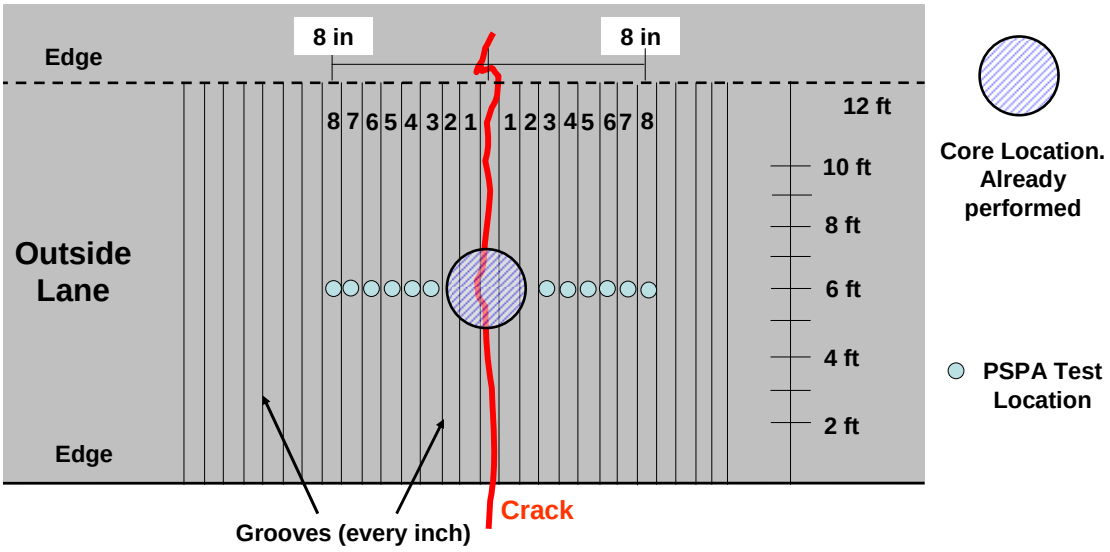

Figure 6.64. Test Protocol Followed around Cracks on SH 35.

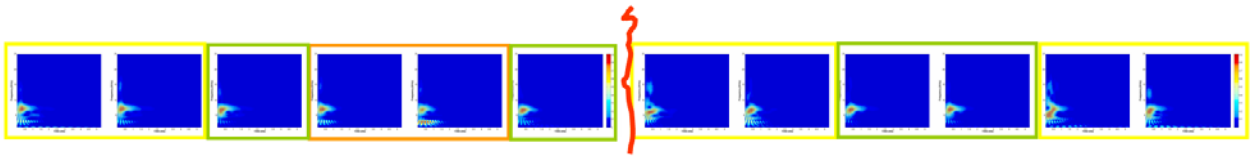

Figure 6.65. Results on Core 1 (Section 1) of SH 35.

As part of the quality control, eight of the 10 mixes of SH 35 were tested at 10 equally spaced points (every 100 ft) and on both wheel paths and the center of the outside lane. An example of the variation in seismic modulus obtained with the PSPA in the field is presented in Figure 6.66 as a color coded map. Appendix I contains results

for the seven sections subjected to this test. Tests were carried out 7 days after placing the concrete.

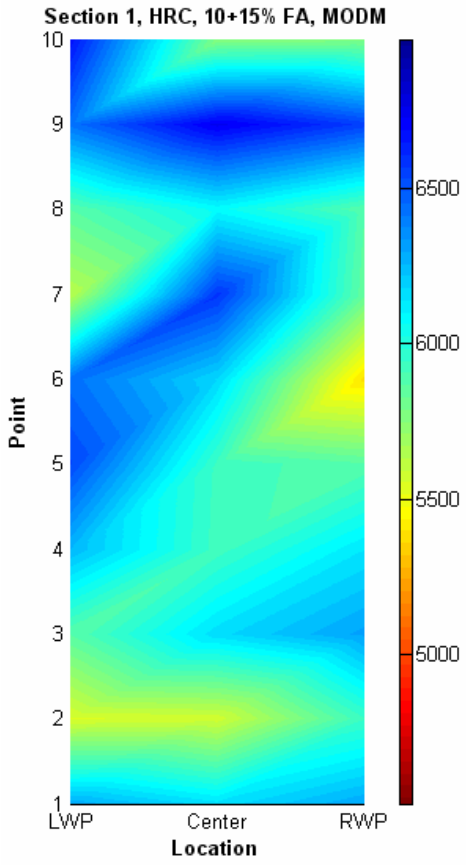

Figure 6.66. Example of Variation in Seismic Modulus along Section 1 on SH 35.

Probability of Delamination Occurrence for Both Winter (SH 288) and Summer (SH 35) Test Sections

For each test section, the probability density function of the difference between K_I and K_{IC} was assumed to follow a normal distribution, as shown in Figure 6.67. As suggested previously, delamination occurs when the K difference (i.e., $x = K_{IC} - K_I$) is a negative value. Therefore, the shaded area in Figure 6.67 represents the probability of delamination at a given time, K_I and K_{IC}. For each test section, the probability of delamination occurrence for every hour during the analysis period was calculated.

Table 6.7 summarizes the maximum probability of delamination occurrence and the associated time over the analysis period for each test section. Within the scope of the field testing programs, most of the test sections showed very low probabilities of delamination occurrence. The highest probability of delamination occurrence was 24 percent, which occurred at the curing age of 38 hours in test section 4 of SH 288. The results of the coring tests and NDT analysis indicated that no horizontal delamination at a shallow depth below the pavement surface was detected. Therefore, the probability of delamination occurrence below 25 percent was defined as a very low chance of delamination.

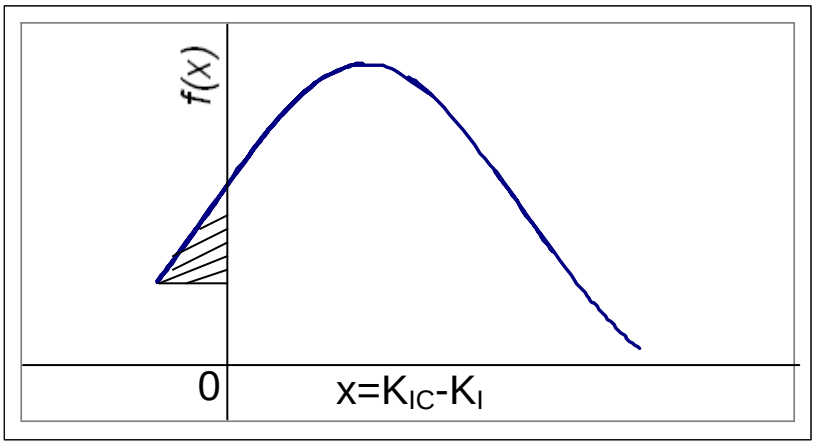

Figure 6.67. Probability Density Function of K Difference.

Table 6.7. Maximum Probability of Delamination Occurrence.

	SH 288 (winter)		SH 35 (summer)	
Section	**Maximum Probability (%)**	**Curing Age (hrs)**	**Maximum Probability (%)**	**Curing Age (hrs)**
1	0.24	100	0	/
2	10.44	15	8.38	23
3	0	/	0	/
4	24	38	13.4	51
5	3.82	100	2.08	48
6	0	/	0	/
7	0	/	0	/
8	0	/	5.4	45
9	10.87	64	8.18	55
10	0	/	1.1	20

CHAPTER VII
GUIDELINES FOR USING GRAVEL AGGREGATES IN CONCRETE PAVING

DETERMINE AGGREGATE RATING

The step-by-step procedure to determine aggregate rating is described below

1) Measure aggregate properties, including:
   - gradation, fineness modulus (FM), and AC (*ASTM C 136 and C127*); and
   - mineralogy analysis to determine the percentage of quartzite (*ASTM C 294 and C 295*).
2) Calculate geometric parameters STI, SGI and OS, including:
   - Wash, dry, and sieve aggregates to four size levels: passing 1 in but retaining on 3/4 in sieves; passing 3/4 in but retaining on 1/2 in sieves; passing 1/2 in but retaining on 3/8 in sieves; and passing 3/8 in but retaining on #4 sieves.
   - Conduct aggregate shape analysis by Aggregate Imaging System (AIMS) (*TxDOT Report 5-1707-01*).
   - Obtain average texture index (TI_k), angularity index (GI_k), and percentage of flat/elongated aggregates ($\%E_k$) at each size level from output spreadsheets of AIMS analysis workbook (*TxDOT Report 5-1707-01*).
   - Calculate STI, SGI, and OS based on Table 7.1 after filling data in it.

Table 7.1. Summary of Geometric Parameters.

Size level	% A_k	TI_k	GI_k	%E_k
1—3/4				
¾—1/2				
½—3/8				
3/8—#4				
Thresholds	/	460	5400	/
Sum ($\sum \%A_k \cdot TI_k$(or GI_k or $\%E_k$))				
STI/ SGI/ OS (Sum/threshold)				

3) Determine rating values for all components based on utility curves in Figure 7.1.

4) Fill in rating values for all individual attributes in Table 7.2, and calculate combined ratings of physical and geometric properties, and then overall aggregate rating. The rating system is on a scale of 0 (poor) to 10 (best). The gravel is considered desirable if the aggregate rating value is greater than 5.

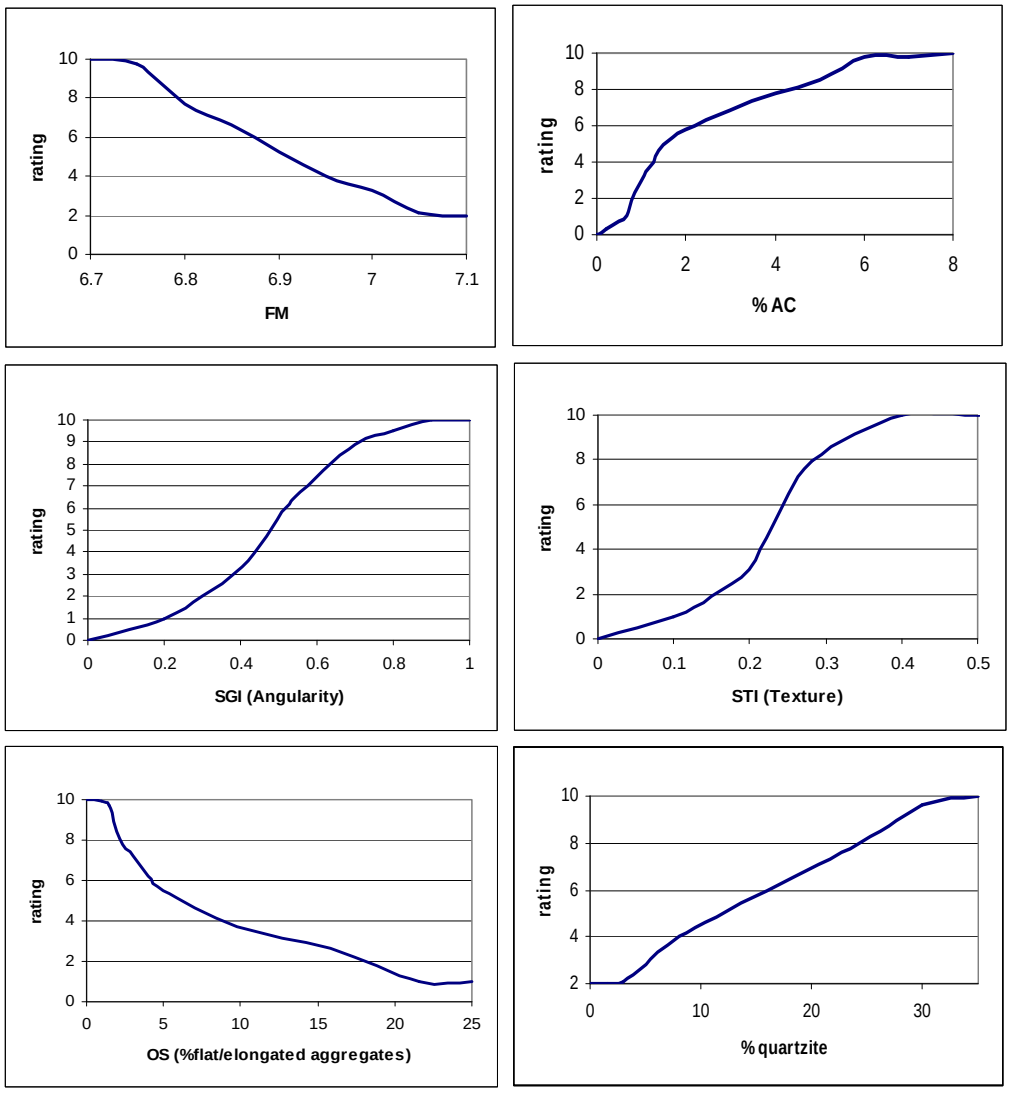

Figure 7.1. Utility Curves for Aggregate Properties.

Table 7.2. Summary of Aggregate Rating.

	Weight	Attribute	Weight	Rating	
				Individual attribute	Combined properties
Physical properties	4	FM	5		
		%AC	5		
Geometric properties	3	angularity	3.5		
		texture	3.5		
		%flat particles	3		
Chemical property	3	%quartzite	/		
Overall rating					

Determine Probability of Delamination

The probability of delamination for the method of curing can be determined from the following inputs:

- Divide the expected wind speed by the ambient relative humidity at the time of paving; this ratio determines the effective wind speed (eff WS).
- Find the probability of delamination (low, medium, or high) along the "y" axis of Figure 7.2 corresponding to the eff WS on the "x" axis.

Determine Method of Construction

The flowchart in Figure 7.3 provides construction recommendations for using gravel aggregates in concrete paving. Inputting the aggregate rating and the probability of delamination, different construction combinations are possible to prevent delamination. The methods of construction are:

- use of dense graded aggregate (DG),
- use of early aged sawcutting (SC), and
- use of modified charging sequence (MMS).

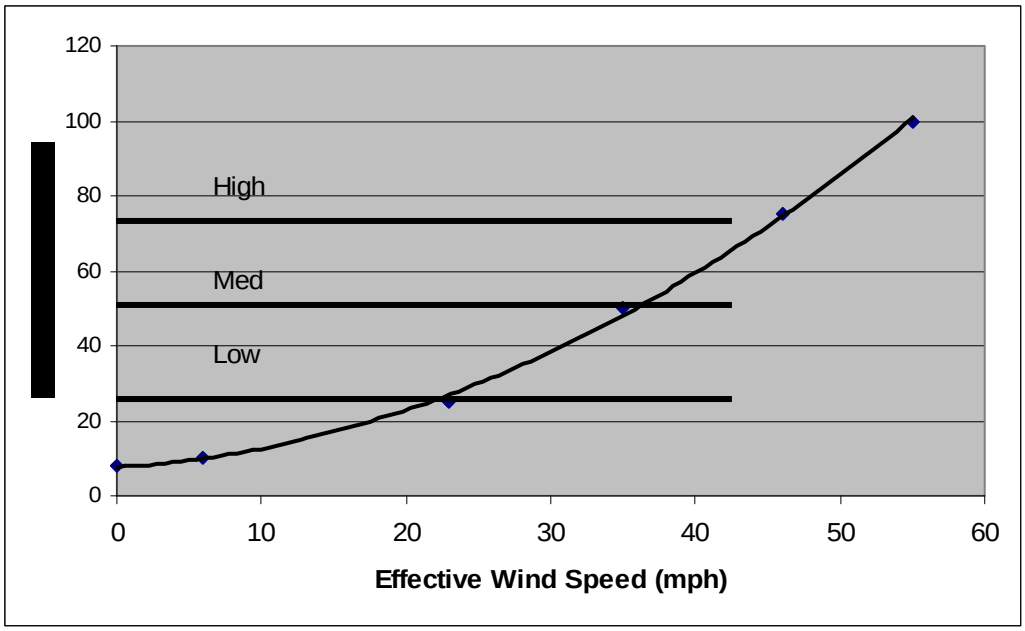

Figure 7.2. Assessment of Probability of Delamination Occurrence.

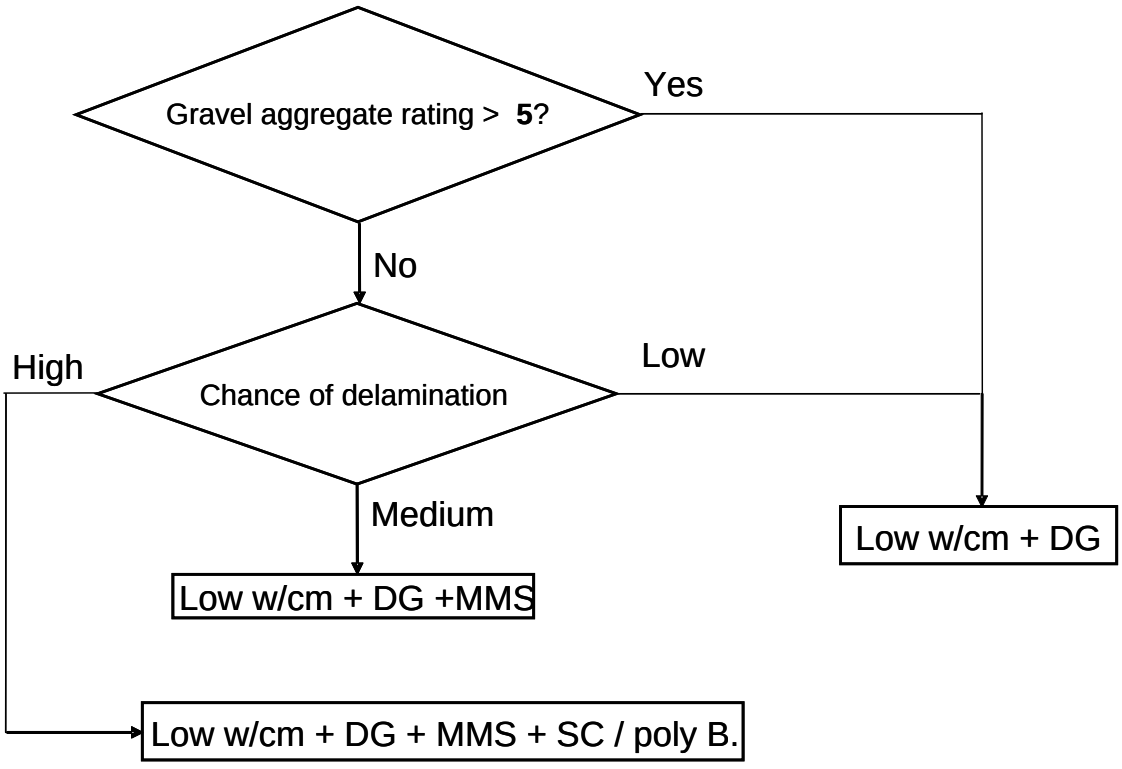

Figure 7.3. Flowchart Structure of Guideline.

Example Demonstration of Guideline

1) Determine Aggregate Rating

The aggregate used for this example is Fordyce gravel from Victoria, Texas.

- FM calculation (ASTM C 136):

Sieve size	Total %passing	Cumulative %
$1^{1/2}$	100	0
1	92.34	7.66
¾	68.73	31.27
½	41.10	58.90
3/8	24.96	75.04
¼	8.59	81.41
#4	2.44	97.56
#8	0.06	99.94
pan	0	100

For coarse aggregate,

$$FM = \frac{\sum\left[\text{Cumulative percent retained on standard sieves (\#4, \#8, 3/8, } 1^{1/2}\text{, and larger)} + 400\right]}{100}$$

$$= \frac{0 + 31.27 + 75.04 + 97.56 + 99.94 + 400}{100} = 7.04$$

Rating of FM is determined as 3 from the utility curve of FM in Figure 7.1.

- AC measurement (ASTM C 127):

%AC of gravel = 1.42, and rating of AC = 4 from the utility curve of AC in Figure 7.1.

- Results from AIMS analysis (TxDOT Report 5-1707-01):

Size level	% A_k*	TI_k	GI_k	%E_k
1—3/4	23.43	145.5	2963.6	3.6
¾—1/2	44.50	120.1	2116.7	0
½—3/8	20.78	157.9	1830.4	5.4
3/8—#4	11.29	111.2	1704.8	1.8
Thresholds	/	460	5400	/
Sum ($\sum$%A_k·TI_k(or GI_k or %E_k))		132.94	2208.6	2.17
STI/ SGI/ OS (Sum/threshold)**		0.289	0.409	2.17

$$* \ \%A_k = \frac{\text{weight of retained aggregates on the size k sieve}}{\text{weight of total aggregates}}$$

$$** \ STI = \frac{23.43\% * 145.5 + 44.50\% * 120.1 + 20.78\% * 157.9 + 11.29\% * 111.2}{460} = 0.289$$

$$** \ SGI = \frac{23.43\% * 2963.6 + 44.50\% * 2116.7 + 20.78\% * 1830.4 + 11.29\% * 1704.8}{5400} = 0.409$$

$$** \ OS = 23.43\% * 3.6\% + 44.50\% * 0 + 20.78\% * 5.4\% + 11.29\% * 1.8\% = 2.17\%$$

Ratings of STI, SGI, and OS are determined as 8, 3.3, and 8, respectively, according to the associated utility curves in Figure 7.1.

- Mineralogy analysis to determine the percentage of quartzite (*ASTM C 294* and *C-295*):

%quartzite = 8.03, and the associated rating is 4 from its utility curve in Figure 7.1.

- Calculation of aggregate rating:

Summary of Fordyce gravel ratings

	Weight	Attribute	Weight	Rating	
				Individual attribute	Combined properties
Physical properties	4	FM	5	3	3.5*
		%AC	5	4	
Geometric properties	3	angularity	3.5	3.3	6.3**
		texture	3.5	8	
		%flat particles	3	8	
Chemical property	3	%quartzite	/	4	4
Overall rating					4.5***

* *Combined rating of physical properties:* $E_1(u) = \sum_{i=1}^{n} w_i E_i(u) = \frac{5*3+5*4}{10} = 3.5$

** *Combined rating of geometric properties:* $E_2(u) = \frac{3.5*3.3+3.5*8+3*8}{10} = 6.3$

*** *Overall rating of aggregate:* $E = \frac{E_1 w_1 + E_2 w_2 + E_3 w_3}{10} = \frac{4*3.5+3*6.355+3*4}{10} = 4.5$

The rating value of Fordyce gravel is less than 5, which means for this aggregate type, further assessment of probability of delamination occurrence is needed.

2) For a mild weather condition with 75 percent of relative humidity (RH) and 15 mph wind speed (WS), an effective WS is 20 mph. According to Figure 6.69, the probability of delamination occurrence is 23 percent, which is within the low probability range.
3) From Figure 6.70, the combination of low w/cm + DG aggregates is chosen as the construction method

CHAPTER VIII
CONCLUSIONS AND RECOMMENDATIONS

GENERAL

The purpose of this project was to gain a better understanding of the construction practices to successfully use gravel aggregates, establish a test protocol to measure the bond strength between coarse aggregate and mortar, and provide guidelines and recommendations to minimize early age delamination in concrete pavements made with gravel aggregates.

CONCLUSIONS

The following conclusions can be made from this project:

1) Fracture toughness (K_{IC}) value at early ages of concrete was used to represent the interfacial bond between aggregate and mortar in the studied concrete mixtures. The variable-notch one-size split-tensile test method based on the size effect law and its generalized theory was applied to facilitate the measurements. This method allows the use of specimens of the same size and shape but with different notch lengths, which provided for a greater amount of convenience in specimen preparation.
2) The effect of crushing of gravel as possible corrective measures to improve the interfacial bonding between gravel aggregate and mortar were investigated in the laboratory. It is observed that the crushing of gravel consisting of low quartzite content did not improve the bonding performance. It was found that the gravel (especially VG in this project) consists of mainly chert (e.g., crypto-crystalline silica) generated smoother surfaces than the original surfaces and consequently didn't improve the bonding performance. However, this was not the case for gravels containing mainly quartzite particles made of crystalline quartz (e.g., gravel from Canada River, Amarillo). It is known that quartz develops conchoidal fracture during crushing and therefore, quartzite gravel particles

generate surfaces that are rougher than the original surfaces. Therefore, aggregate crushing can be an effective measure to improve surface texture for gravels consisting of mainly quartzite particles.

3) A fractional factorial design based on Taguchi's orthogonal array using four factors (i.e., aggregate type, w/cm, replacement of ultra-fine fly ash, and curing method) was selected to conduct the detailed laboratory study. The purpose of the laboratory investigation was to identify the key material and construction parameters, which significantly affect the bond strength of concrete at early ages and the relative importance of those parameters in design combinations. The significances of each factor to achieve better K_{IC} were determined, and the optimum design combination (a combination of all the four factors with their best levels) was subsequently chosen and validated. The statistical analysis indicated the following decreasing rank order with respect to the relative importance of each factor to achieve the best K_{IC}: aggregate type, curing method, w/cm, and ultra-fine fly ash content. Aggregate type was identified as the factor that most strongly affects the bond between aggregate and the mortar. Test results indicated the concrete made of gravel with relatively higher quartzite contents (e.g., Garwood, Texas) should provide adequate resistance against spalling provided w/cm, curing and fly content are properly selected and controlled.
4) The AIMS at TTI was used to measure the geometric properties (i.e., shape, texture, and angularity) of the aggregate used in the lab program. Three geometric parameters, i.e., STI, SGI, and OS were considered to characterize the overall shape and texture properties of aggregates of all sizes. The values for all the three parameters range from 0 to 1. The higher the value of STI, the rougher the aggregate surface. The closer to 1 the value of SGI, the more angular the aggregate is. In terms of OS, a higher value indicates more flat/elongated particles in the aggregate. Therefore, these three parameters can quantify the effects of aggregate shape, texture and angularity on concrete bonding performance. As for example, aggregate made of particles with higher texture

with lesser presence of flat and elongated particles creates stronger interfacial bond and thereby, reduces the chances of de-lamination.

5) A comprehensive investigation of aggregate properties relative to physical, geometric and chemical characteristics was conducted. The research findings indicated that the aggregate-mortar interfacial bond for a given cement paste was not a simple function of any one of the aggregate properties, but a function of all three properties aggregated together. Different relative importance existed in different aggregate properties and different components within the property as well, which then affected the overall contribution of aggregates to the interfacial bond of concrete.
6) A combined rating system based on utility theory was applied to develop guidelines and to evaluate the overall aggregate contribution to the concrete bonding performance and feasibility of design combinations. Commonly occurring gravel aggregates can be evaluated by the newly developed rating system, as a means to screen for potential aggregates requiring special consideration during construction. The combined aggregate rating has to be above certain threshold value (yet to be established as further work with more no. of gravel aggregates is necessary) in order to be used successfully in the pavement construction with conventional construction practices. If the combined aggregate rating falls below the threshold value, special construction requirements such as aggregate blending, special curing (an optimum rate of application to achieve a high quality of curing or wet mat curing etc.), saw-cut etc, are recommended to potentially relieve delamination and further spalling distresses.
7) A fracture mechanics based approach was employed along with of numerical analysis to predict the occurrence of delamination. The criterion for early age delamination was when $K_I > K_{IC}$. Two finite element software packages—TMAC[2] and ABAQUS—were utilized to predict the development of shear-related stress at an early age. In this numerical effort, the effect of shrinkage was

investigated by including the effect of the distribution and time history of moisture and the time dependent moisture diffusivity. In addition, the numerical analysis incorporated both moisture and thermal effects in the stress analysis which was principally dominated by the moisture (i.e. shrinkage) component. The results showed that the development of K_I with time followed cycling patterns consistent with the cyclic changes of relative humidity profiles within the analysis period. Through examples of practical design and construction methods, this approach is able to assess the probability of delamination occurrence, which will facilitate selection and evaluation of the effectiveness of pavement design methods to prevent delamination and spalling in concrete pavement construction.

8) Test sections for both winter and summer were established based on the research findings from laboratory investigation, previous field testing, theoretical modeling, and numerical analysis. The field testing verified the measures and trends relative to the practices and techniques to minimize the development of spall related delamination in CRC paving. It shows that among three design factors, curing method was the most significant factor to the concrete performance in the field. For all levels within each design factor, WMC and 25 percent Class F fly ash provided the best contribution to the early age concrete bonding performance. It is suggested that curing quality control is the most feasible means for minimizing early age delamination in the field. Also it is not necessary to apply ultra-fine fly ash, due to the role of mineral admixture being filler for early age concrete instead of pozzolanic reactivity.
9) A step-by-step process of selecting construction recommendations for the use of gravel aggregates in concrete paving was preliminarily established (requiring further validation), including determining aggregate rating, probability of delamination, and the method of construction.

RECOMMENDATIONS

1) A special field study should be undertaken to validate the role of the noted aggregate characteristics and weather conditions at the time of construction on the incidence of spalling. To the extent possible, each factor should be checked against field performance to verify the influence on the incidence of spalling by surveying several past projects where gravel was used as the coarse aggregate. This type of information should help to further establish the viability of the guidelines to address the use of gravel to avoid spalling distress.
2) Verify that chipping along the transverse cracks of gravel projects is at a different level of severity than delamination and spalling. Verification of the severity levels and dormancy of chipping over time should also be included in this verification.
3) If the test sections constructed under this project perform well (monitoring of the sections is being done by another research project), the validity of this process will still need to be verified. More case studies are needed to calibrate the curve of probability of delamination occurrence as a function of effective wind speed, curing quality, and construction practice (such as better curing practices and early-age sawcutting). The threshold vales for different levels of probability of delamination occurrence and the calibration of the curves need to be established through detailed future research.
4) Relative to the guidelines, further efforts should be undertaken to streamline and validate the procedures and methods as outlined in them to reduce the probability of delamination based both on historical and generated data through implementation. This validation would focus on the effectiveness of select combinations of materials and construction measures (improved curing, aggregate blending, early saw cutting) and relative to the effects of wind speed, and related climatic factors.

REFERENCES

ABAQUS, Inc. (2003). "ABAQUS version 6.4 documentation."

ACI. (1996). "Building code requirements for structural concrete." *ACI 318-95, ACI Manual of Concrete Practice Part 3: Use of Concrete in Buildings—Design, Specifications, and Related Topics*, American Concrete Institute, Detroit, Michigan.

Ahlrich, R.C. (1996). "Influence of Aggregate Gradation and Particle Shape/Texture on Permanent Deformation of Hot-Mix Asphalt Pavement." *Technical Report GL-96-1*, U. S. Army Corps of Engineers, Vicksburg, Mississippi.

Ahsan, T., and Taylor, D.A. (1999). "The Influence of Surface Energies of Calcium Carbonate Minerals on Mineral—Polymer Interaction In Polyolefin Composites." *Fundamentals of Adhesion and Interfaces*, Gordon and Breach Science Publishers, Amsterdam, The Netherlands, 69—79.

Akçaoğlu, T., Tokyay, M., and Çelik, T. (2002). "Effect of Coarse Aggregate Size on Interfacial Cracking Under Uniaxial Compression." *Materials Letters*, 57, 828—833.

Alexander, K.M., Wardlaw, J., and Gilbert, D.J. (1965). "Aggregate—Cement Bond, Cement Paste Strength and the Strength of Concrete." *Proceedings of an International Conference*, *The Structure of Concrete and Its Behavior under Load,* Cement and Concrete Association, London, England 59—81.

Alexander, M.G. (1993). "Two Experimental Techniques for Studying the Effects of the Interfacial Zone Between Cement Paste and Rock." *Cement and Concrete Research*, 23, 567—575.

Al-Rousan, T., Masad, E., Myers, L., and Speigelman, C. (2004). "Aggregate Shape Classification System Using AIMS." *83rd Annual Meeting of Transportation Research Board*, Washington, D.C. (CD-ROM).

Al-Rousan, T. (2004). "Characterization of Aggregate Shape Properties Using a Computer Automated System." Ph.D. Dissertation, Texas A&M University, College Station, Texas.

Asbridge, A.H., Page, C.L., and Page, M.M. (2002). "Effects of Metakaolin, Water/Binder Ratio and Interfacial Transition Zones on the Microhardness of Cement Mortars." *Cement and Concrete Research*, 32, 1365—1369.

ASTM C 192/C. (2000). "Standard Practice for Making and Curing Concrete Test Specimens in the Laboratory." Section 4, 04.02, Concrete and Aggregates, *Annual Book of ASTM Standards*, ASTM, West Conshohocken, Pennsylvania.

ASTM C 496-90 (1995). "Standard Test Method for Splitting Tensile Strength of Cylinders Concrete Specimens.

Baker, M.R., Crain, K., and Nazarian, S. (1995). "Determination of Pavement Thickness with a New Ultrasonic Device." Research Report 1966-1, Center for Highway Materials Research, The University of Texas at El Paso, Texas, 1995.

Barrett, P.J. (1980). "The Shape of Rock Particles, a Critical Review." *Sedimentology*, 27, 291—303.

Basheer, L., Basheer, P., and Long, A. (1999). "Influence of Aggregate Type, Size and Grading on Interfacial Transition Zone in Concrete." *Proceedings of the International Conference*, *Utilizing Ready-Mixed Concrete and Mortar,* University of Dundee, Scotland, 107—119.

Bažant, Z.P., and Pfeifer, P.A. (1987). "Determination of Fracture Energy from Size Effect and Brittleness Number." *ACI Materials Journal*, 84(6), 463—480.

Bažant, Z.P., and Panula, L. (1978). "Practical Prediction of Time-Dependent Deformations of Concrete. Part I: Shrinkage; Part II: Basic Creep." *Materials and Structures*, 11, 307—328.

Bažant, Z.P., and Najjar, L.J. (1972). "Nonlinear Water Diffusion in Nonsaturated Concrete." *Materials and Structures*, 5(25), 3—20.

Bažant, Z.P. (1970). "Constitutive Equation for Concrete Creep and Shrinkage Based on Thermodynamics of Multiphase Systems." *Materials and Structures*, 3(13), 3—36.

Beach, E.R., Tormoen, G.W., and Drelich, J. (2002). "Pull-off Forces Measured Between Hexadecanethiol Self—Assembled Monolayers in Air Using an Atomic Force Microscope: Analysis of Surface Free Energy." *Journal of Adhesion Science Technology*, 16(7), 845—868.

Beaudoin, J.J. (1982). "Microhardness-Fracture Studies: High Alumina Cement Systems." *Cement and Concrete Research*, 12, 289—299.

Bentur, R.A., and Cohen, M.D. (1987). "Effect of Condensed Silica Fume on the Microstructure of the Interfacial Zone in Portland Cement Mortars." *Journal of the American Ceramic Society*, 70, 738—743.

Bentz, D.P., Garboczi, E.J., and Stutzman, P.E. (1992). "Computer Modelling of the Interfacial Zone in Concrete." *International RILEM Conference*, Toulouse, France, E&FN Spon, London, England 107—116.

Bentz, D.P., and Garboczi, E.J. (1991). "Simulation Studies of the Effects of Mineral Admixtures on the Cement Paste-Aggregate Interfacial Zone." *ACI Materials Journal*, 88, 518—529.

Bentz, D.P., Schlangen, E., and Garboczi, E.J. (1987). "Computer Simulation of Interfacial Zone Micro Structure and Its Effects on the Properties of Cement Based Composites." *Material Science of Concrete, Vol IV*, J. Skalny and S. Mindess, eds., The American Ceramic Society, Westerville, Ohio, 155—199.

Bijen, J., and Selst, I. (1992). "Fly Ash as Addition to Concrete." *CUR Report 144*, INTRON, Institute for Material and Environmental Research B.V., A.A. Balkema, Rotterdam.

Bilby, B.A., and Cardew, G.E. (1975). "The Crack with a Kinked Tip." *International Journal of Fracture*, 11(4), 708—712.

Boresi, A., Schmidt, R.J. and Sidebottom, O.M. (1993). *Advanced Mechanics of Materials.* John Wiley & Sons, Inc., New York.

Brandt, A.M. (1995). *Cement-Based Composites: Materials, Mechanical Properties and Performance.* E&FN Spon, London, England.

Buch, N., and Early, J. (1999). "The Importance of Mechanical Bond between Cement Paste and Aggregate." *Proceedings of the International Conference on University of Dundee, Scotland, UK, Concrete Durability and Repair Technology*, Thomas Telford Publishing, London, England 133—141.

Buch, N., and Zollinger, D.G. (1993). "Preliminary Investigation on Effects of Moisture on Concrete Pavement Strength and Behavior." *Transportation Research Record 1382*, Transportation Research Board, National Research Council, Washington, D.C., 26—31.

Büyüköztürk, O., and Lee, K. (1993). "Assessment of Interfacial Fracture Toughness in Concrete Composites." *Cement & Concrete Composites*, 15, 143—151.

Carette, G., Bilodeau, A., Chevrier, R.L., and Malhotra, V.M. (1993). "Mechanical Properties of Concrete Incorporating High Volumes of Fly Ash from Sources in the U.S." *ACI Materials Journal*, 90, 535—–544.

Chandan, C., Sivakumar, K., Fletcher, T., and Masad, E. (2004). "Geometry Analysis of Aggregate Particles Using Imaging Techniques." *Journal of Computing in Civil Engineering, ASCE*, 18(1), 75—82.

Charles-Gibergues, A., Grandet, J., and Ollivier, J.P. (1982). "Contact Zone Between Cement Paste and Aggregate in Bond in Concrete." *Bond in Concrete*, P. Bartos ed., Applied Science Publishers, London, England 24—33.

Cheng, D. (2002). "Surface Free Energy of Asphalt—Aggregate System and Performance Analysis of Asphalt Concrete Based on Surface Energy." Ph.D. Dissertation, Texas A&M University, College Station, Texas.

Cheng-yi, H., and Feldman, R.F. (1985). "Influence of Silica Fume on the Microstructural Development in Cement Mortars." *Cement Concrete Research*, 15 (2), 285——294.

Chowdhury, A., and Button, J.W. (2001). "Fine Aggregate Angularity: Conventional and Unconventional Approach, Aggregate Contribution to Hot-Mix Asphalt HMA Performance." *American Society for Testing and Materials ASTM*, Special Technical Publication, 1412, 144—159.

Elsharief, A., Cohen, M.D., and Olek, J. (2003). "Influence of Aggregate Size, Water Cement Ratio and Age on the Microstructure of the Interfacial Transition Zone." *Cement and Concrete Research*, 33, 1837—1849.

Erdogan, F., and Sih, G.C. (1963). "On the Crack Extension in Plates Under Plane Loading and Transverse Shear." *Journal of Basic Engineering*, 85, 519—525.

Farran, J. (1956). *Contribution mineralogique a l'etude de l'adherence entre les constituents hydrates des ciments et les materiaux enrobes.* Rev. Material Construction Trav. Publics, Ed. C.

Fowkes, F.M. (1962). "Determination of Interfacial Tensions, Contact Angles, and Dispersion Forces in Surfaces by Assuming Additivity of Intermolecular Interactions in Surfaces." *Journal of Physical Chemistry*, 66, 382.

Fowler, D.W., Zollinger, D.G., Carrasquillo, R.L., and Constantino, C.A. (1996). "Aggregate Tests Related to Performance of Portland Cement Concrete." *Phase 1 Interim Report. NCHRP Project 4-20*, Transportation Research Board, National Research Council, Washington, D.C.

Goldman, A., and Bentur, A. (1992). "Interface in Cementitious Composites." *RELEM International Conference*, Toulouse, France, 53—61.

Goldman, A., and Bentur, A. (1989). "Bond Effects in High-Strength Silica Fume Concrete." *ACI Materials Journal*, 86, 440—447.

Good, R.J. (1992). "Contact Angle, Wetting, and Adhesion: a Critical Review." *Journal of Adhesion Science and Technology*, 6, 1269—1302.

Grandet, J., and Ollivier, J.P. (1980). "New Method for the Study of Cement-Aggregate Interfaces." *Seventh International Congress on Chemistry of Cement*, Paris, France 3(7), 85—89.

Guinea, G.V., El-Sayed, K., Rocco, C.G., Elices, M., and Planas, J. (2002). "The Effect of the Bond Between the Matrix and the Aggregates on the Cracking Mechanism and Fracture Parameters of Concrete." *Cement and Concrete Research*, 32, 1961—1970.

Gutierriz de Velasco, M., and McCullough, B.F. (1981). "Summary Report for 1978 CRCP Condition Survey in Texas." *Research Report 177-20*, Center for Transportation Research, University of Texas at Austin, Austin, Texas.

Hayakawa, M., and Itoh, Y. (1982). "A New Concrete Mixing Method for Improving Bond Mechanism." *Bond in Concrete,* P. Bartos, ed., Applied Science Publishers, London, England 282—288.

Hefer, A.W. (2004). "Adhesion in Bitumen—Aggregate Systems and Quantification of the Effects of Water on the Adhesive Bond." Ph.D. Dissertation, Texas A&M University, College Station, Texas.

Hertzberg, R.W. (1976). *Deformation and Fracture Mechanics of Engineering Materials*. John Wiley & Sons, New York.

Hsu, T.T.C., and Slate, O.F. (1963). "Tensile Bond Strength Between Aggregate and Cement Paste or Mortar." *ACI Journal*, 60(4), 465—486.

Huang, C.L.D. (1979). "Multi-Phase Moisture Transfer in Porous Media Subjected to Temperature Gradient." *International Journal of Heat and Mass Transfer*, 22(9), 1295 —1307.

Hutchinson, J.R. (1990). "Mixed Mode Fracture Mechanics of Interfaces." *Metal-Ceramic Interfaces*, M. Rühle et al., eds., Pergamon Press, New York, 295—306.

Irwin, G.R. (1958). *Fracture Encyclopedia of Physic*, Vol. VI, S. Flugge, ed, Springer, Berlin, Germany 551—590.

Irwin, G.R. (1957). "Analysis of Stresses and Strains Near the End of a Crack Traversing a Plate." *Journal of Applied Mechanics*, 79, 361—364.

Jeong, J. (2003). "Characterization of Slab Behavior and Related Material Properties Due to Temperature and Moisture Effects." Ph.D. Dissertation, Department of Civil Engineering, Texas A&M University, College Station, Texas.

Kasi, S.S.H., and Pihlajavaara, S. E. (1969). "An Approximate—Solution of a Quasi-Linear Diffusion." *Publication No. 153*, The State Institute for Technical Research, Helsinki, Finland.

Kim, D.S., Seo, W.S., and Lee, K.M. (2006). "IE–SASW Method for Nondestructive Evaluation of Concrete Structure." NDT&E International 39, 143—154.

Kim, D.S., Kim, N.R., and Seo, W.S., (2004). "Time-Frequency Analysis for Impact Echo-SASW (IE-SASW) Method, Key Engineering Materials," Vols. 270-273, 1529-1534, © 2004 Trans Tech Publications, Switzerland.

Kim, H., Haas, C., Rauch, A.F., and Browne, C. (2002). "Wavelet-Based 3D Descriptors of Aggregate Particles." *Transportation Research Record 1787*, Transportation Research Board, Washington, D.C.

Kosmatka, S.H., Kerkhoff, B., and Panarese, W.C. (2002). *Design and Control of Concrete Mixtures*. Portland Cement Association, Skokie, Illinois.

Langley, W.S., Carette, G.G., and Malhotra, V.M. (1989). "Structural Concrete Incorporating High Volumes of ASTM Class F Fly Ash." *ACI Materials Journal*, 86, 507—514.

Langton, C.A., and Roy, D.M. (1980). "Morphology and Microstructure of Cement Paste/Rock Interfacial Regions." *7th International Congress on the Chemistry of Cement*, Paris, France, 127—132.

Larbi, J.A., and Bijen, J.M. (1990). "Orientation of Calcium Hydroxide at the Portland Cement Paste-Aggregate Interface in Mortars in the Presence of Silica Fume: A Contribution." *Cement Concrete Research*, 20(3), 461—470.

Ledbetter, W.B. et al. (1977). "Techniques for Rehabilitating Pavements Without Overlay—A Systems Analysis Vol.1—Analysis." *Report FHWA-RD-77-132*, Texas Transportation Institute, Texas A&M University, College Station, Texas.

Lim, S. (2002). "Viscoelastic Age-Dependent Analysis of Restrained Shrinkage Stress Development in Early-Age Concrete." Ph.D. Dissertation, Department of Civil Engineering, Texas A&M University, College Station, Texas.

Liu, J., Mukhopadhyay, A., and Zollinger, D.G. (2006). "Contribution of Aggregates to the Bonding Performance of Concrete." *The 85th Transportation Research Board Annual Meeting*, Washington, D.C. (CD-ROM).

Marez, N.H., and Zhou, W. (2001). "Flat and Elongated: Advances Using Digital Image Analysis." *Proceedings of the 9th Annual Symposium of the International Center for Aggregates Research (ICAR),* Austin, Texas (CD-ROM).

Masad, E. (2003). "The Development of a Computer Controlled Image Analysis System for Measuring Aggregate Shape Properties." *National Cooperative Highway Research Program NCHRP-IDEA Project 77 Final Report*, Transportation Research Board, National Research Council, Washington, D.C.

Masad, E. (2001). "Review of Imaging Techniques for Characterizing the Shape of Aggregates Used in Asphalt Mixes." *Proceedings of the 9th Annual Symposium of the International Center for Aggregate Research (ICAR)*, Austin, Texas (CD-ROM).

Mason, R.L., Gunst, R.F., and Hess, J.L. (1989). *Statistical Design and Analysis of Experiments: with Application to Engineering and Science.* John Wiley & Sons, Inc., New York.

Mathews, P.G. (2004). *Design of Experiments with MINITAB.* American Society of Quality, Quality Press, Milwaukee, Wisconsin.

Mehta, P.K., and Monteiro, P.J.M. (1988). "Effect of Aggregate, Cement, and Mineral Admixtures on the Microstructure of the Transition Zone." *Proceedings of the Symposium, Bonding in Cementitious Composites,* Materials Research Society, Pittsburgh, Pennsylvania, 114, 65–75.

Meininger, R.C. (1998). "Aggregate Test Related to Performance of Portland Cement Concrete Pavement." *National Cooperative Highway Research Program Project 4-20A Final Report*, Transportation Research Board, National Research Council, Washington, D.C.

Mindness, S., Young, J.F., and Darwin, D. (2002). *Concrete*, Prentice-Hall Inc., Englewood Cliffs, New Jersey.

Mitsui, K., Li, Z., Lange, D., and Shah, S.P. (1993). "Influence of Rock and Cement Types on the Fracture Properties of the Interfacial Zone." *Interfaces in Cementitious Composition*, J.C. Maso, ed., E&FN, Spon, London, England.

Mitsui, K., Li, Z., Lange, D., and Shah, S.P. (1994). "Relationship Between Microstructure and Mechanical Properties of the Paste-Interface." *ACI Materials Journal*, 91, 30—39.

Mohamed, A.R., and Hansen, W. (1999). "Micromechanical Modeling of Crack-Aggregate Interaction in Concrete Materials." *Cement & Concrete Composites*, 21, 349-359.

Monteiro, P.J.M., Maso, J.C., and Ollivier, J.P. (1985). "The Aggregate Mortar Interface." *Cement and Concrete Research*, 15, 953-958.

Monteiro, P.J.M., and Mehta, P.K. (1986). "Interaction Between Carbonate Rock and Cement Paste." *Cement and Concrete Research*, 6, 127-134.

Monteiro, P.J.M., and Ostertag, C.P. (1989). "Analysis of the Aggregate-Cement Paste Interface Using Grazing Incidence X-ray Scattering." *Cement and Concrete Research*, 19, 987—988.

Nazarian, S., Baker, M., and Crain, K. (1993), "Developing and Testing of a Seismic Pavement Analyzer." Research Report SHRP-H-375, Strategic Highway Research Program, Washington, D.C.

NCHRP. (1996). "Nondestructive Testing to Determine Material Properties of Pavement Layers." Interim Report, NCHRP 10-44, Washington, D.C.

Nehdi, M., and Mindess, S. (1997). "Computer Assisted Electron Microscopy of High-Performance Concrete Made with Composite Cement." *Proceedings of the 19th International Conference on Cement Microscopy*, Cincinnati, Ohio, 261-274.

Neville, A.M. (1995). *Properties of Concrete.* 4th edition, John Wiley & Sons, Inc., New York.

Nuismer, R.J. (1975). "An Energy Release Rate Criterion for Mixed Mode Fracture." *International Journal of Fracture*, 11(2), 245-250.

Ozbolt, J., Reinhardt, H.W., and Xu, S. (1999). "Numerical Studies on the Double-Edge Notched Mode II Geometry." *Proceedings of Fracture Mechanics of Concrete Structures FRAMCOS-3*, Aedificatio Publishers, Freiburg, Germany, 773-782.

Parrott, L.J. (1991). "Factors Influencing Relative Humidity in Concrete." *Magazine of Concrete Research*, 43(154), 45-52.

Parrott, L.J. (1988). "Moisture Profiles in Drying Concrete." *Advances in Cement Research*, 1, 164-170.

Perry, C., and Gillot, J.E. (1977). "The Influence of Mortar-Aggregate Bond Strength on the Behavior of Concrete in Uniaxial Compression." *Cement and Concrete Research*, 7, 553—564.

Pihlajavaara, S.E. (1964). *Introductory Bibliography for Research on Drying of Concrete.* The State Institute for Technical Research, Helsinki, Finland.

Ping, X., and Beaudoin, J.J. (1992). "Effects of Transition Zone Microstructure on Bond Strength of Aggregate-Portland Cement Paste Interfaces." *Cement and Concrete Research,* 22, 23—26.

Pope, W.A., and Jennings, M.H. (1992). "The Influence of Mixing on the Microstructure of the Cement Paste/Aggregate Interfacial Zone and on the Strength of Mortar." *Journal of Materials Society*, 27, 6452—6462.

Popovics, S. (1966). "The Use of the Fineness Modulus for the Grading Evaluation of Aggregates for Concrete." *Magazine of Concrete Research*, 18(56), 131-140.

Prokopski, G., and Halbiniak, J. (2000). "Interfacial Transition Zone in Cementitious Materials." *Cement and Concrete Research*, 30, 579—583.

Prokopski, G., and Langier, B. (2000). "Effect of Water/Cement Ratio and Silica Fume Addition on the Fracture Toughness and Morphology of Fractured Surfaces of Gravel Concretes." *Cement and Concrete Research*, 30, 1427—1433.

Prokopski, G., Halbiniak, J., and Langier, B. (1997). "The Examination of the Fracture Toughness of Concretes with Diverse Structure." *Journal of Materials Society*, 33, 1819—1825.

Prokopski, G. (1991). "Influence of Water-Cement Ratio on Micro-Cracking of Ordinary Concrete." *Journal of Materials Society*, 26, 6352—6356.

Pye, G.B., and Beaudoin, J.J. (1992). "An Energy Approach to Bond Strength Determinations in Cement Systems." *Cement and Concrete Research*, 22, 551—558.

Ramachandran, V.S. (1995). *Concrete Admixture Handbook Properties, Science, and Technology.* 2nd Edition, Noyes Publications, Norwich, New York.

Rao, C., Tutumluer, E., and Stefanski, J.A. (2001). "Coarse Aggregate Shape and Size Properties Using a New Image Analyzer." *ASTM Journal of Testing and Evaluation*, JTEVA, 29(5), 79—89.

Rao, G.A., and Prasad, B.K.R. (2002). "Influence of the Roughness of Aggregate Surface on the Interface Bond Strength." *Cement and Concrete Research*, 32, 253 —257.

Rice, J.R. (1988). "Elastic Fracture Concepts for Interfacial Cracks." *Journal of Applied Mechanics*, 55, 98—103.

Richard, H.A., Fulland, M., and Sander, M. (2005). *Fatigue & Fracture of Engineering Materials & Structure*, Blackwell Publishing Ltd., Malden, Maryland.

Saito, M., and Kawamura, M. (1989). "Effect of Fly Ash and Slag on the Interfacial Zone Between Cement and Aggregate." *Fly Ash, Silica Fume, and Natural Pozzolans in Concrete, SP-114*, v.1, American Concrete Institute, Detroit, Michigan, 669—688.

Saito, M., and Kawamura, M. (1986). "Resistance of the Cement-Aggregate Interfacial Zone to Propagation of Cracks." *Cement and Concrete Research*, 16(5), 653—661.

Sansalone, M.J., and Streett, W.B. (1997). "Impact-Echo: Nondestructive Evaluation of Concrete and Masonry." Bullbrier Press, Ithaca, New York, 339.

Sansalone, M., and Carino, N.J. (1986). "Impact-Echo: A Method for Flaw Detection in Concrete Using Transient Stress Waves." Report NBSIR 86-3452. National Bureau of Standards, Gaithersburg, Maryland.

Scholer, C.F. (1967). "The Role of Mortar-Aggregate Bond Strength in the Strength of Concrete." *Highway Research Record, 210*, National Research Council, 108-—117.

Scrivener, K.L., and Gartner, E.M. (1988). "Micro Structural Gradients in Cement Paste Around Aggregate Particles." *Proceedings of a Symposium of Materials Research Society*, 114, 77—85.

Scrivener, K.L., and Pratt, P.L. (1986). "A Preliminary Study of the Microstructure of the Cement/Sand Bond in Mortars." *Proceedings, 8th International Congress on the Chemistry of Cement*, Vol. III, FINEP, Rio de Janeiro, Brazil, 466—471.

Senadheera, S., and Zollinger, D.G. (1996). "Influence of Coarse Aggregate in Portland Cement Concrete on Spalling of Concrete Pavements." *Research Report 1244-11*, Texas Transportation Institute, The Texas A&M University System, College Station, Texas.

Shelby, M.D., and McCullough, B.F. (1960). "Experience in Texas with Continuously Reinforced Concrete Pavement." *Highway Research Board Bulletin 274*, Highway Research Board, National Research Council, Washington, D.C., 1-29.

Shilstone, J.M., Sr. (1990). "Concrete Mixture Optimization." *Concrete International*, 12(6), 33-39.

Sih, G.C. (1974). "Strain-Energy-Density Factor Applied to Mixed Mode Crack Problems." *International Journal of Fracture*, 10(3), 305-321.

Shokouhi, P., and Gucunski, N. (2003). "Application of Wavelet Transform in Detection of Shallow Cavities by Surface Waves." Symposium on the Application of Geophysics to Engineering and Environmental Problems, EEGS, San Antonio, Texas.

Simeonov, P., and Ahmad, S. (1995). "Effect of Transition Zone on the Elastic Behavior of Cement-Based Composites." *Cement and Concrete Research*, 25(2), 165—175.

Soares, J.B., and Zollinger, D.G. (1998). "Mechanistic Evaluation of Spalling Distress." *Proceeding, 8th International Symposium on Concrete Roads*; Theme III: Pavement Performance and Evaluation, Lisbon, Portugal, 91—109.

Somasundaram, S., Anand, N.K., Suh, Y.B., and Aung, W. (1989). "Analysis of Moisture Migration in Two-Dimensional Unsaturated Porous Media with Impermeable Boundaries." *International Journal of Heat and Mass Transfer*, 32(9), 1733-1739.

Somayaji, S. (2001). *Civil Engineering Materials.* 2nd edition, Prentice-Hall, Inc., Englewood Cliffs, New Jersey

Strategic Highway Research Program (SHRP). (1993). "Distress Identification Manual for the Long-Term Pavement Performance Project." *Report No. SHRP-P338*, Transportation Research Board, Washington, DC.

Struble, L., Skalny, J., and Mindess, S. (1980). "A Review of the Cement-Aggregate Bond." *Cement and Concrete Research*, 10, 277—286.

Subramanian, S. (1999). "Interface in Concrete-Achieving Performance." *Proceedings of the International Seminar, Role of Interfaces in Concrete*, University of Dundee, Scotland, United Kingdom, 97—109.

Suh, Y.B., Anand, N.K., Aung, W., and Somasundaram, S. (1988). "Steady-State Moisture Profile in an Unsaturated Porous Medium with Impermeable Boundaries." *International Journal of Heat and Mass Transfer*, 11(12), 2587—2589.

Taguchi, G., Yokoyama, Y., and Wu, Y. (1993). *Taguchi Methods: Design of Experiment.* American Supplier Institute, Inc. in conjunction with the Japanese Standards Association, Livonia, Michigan.

Tamimi, A.K. (1994). "The Effect of a New Mixing Technique on the Properties of the Cement Paste-Aggregate Interface." *Cement and Concrete Research*, 24(7), 1299-1304.

Tan, D.M., Tschegg, E.K., Rotter, H., and Kirchner, H.O.K. (1995). "Cracks at Mortar-Stone Interfaces." *Acta Metal Materials*, 43(10), 3701-3707.

Tang, T., Yang, S., and Zollinger, D.G. (1999). "Determination of Fracture Energy and Process Zone Length Using Variable-Notch One-Size Specimens." *ACI Materials Journal*, 96(1), 3—10.

Tang, T., Bazant, Z.P., Yang, S., and Zollinger, D.G. (1996). "Variable-Notch One-Size Test Method for Fracture Energy and Process Zone Length." *Engineering Fracture Mechanics*, 55(3), 383—404.

Tang, T., Zollinger, D.G., and McCullough, B.F. (1994). "Field Tests and Analyses of Concrete Pavement in Texarkana and La Porte, Texas." *Research Report 1244-7,* Texas Transportation Institute, The Texas A&M University System, College Station, Texas.

Tang, T., Zollinger, D.G., and Senadheera, S.P. (1993). "Analysis of Concave Curling in Concrete Slabs." *ASCE Journal of Transportation Engineering*, 119(4), 618-633.

Tasong, W.A., Lynsdale, C.J., and Cripps, J.C. (1999). "Aggregate-Cement Paste Interface: Part I. Influence of Aggregate Geochemistry." *Cement and Concrete Research*, 29, 1019—1025.

Tasong, W.A., Cripps, J.C., and Lynsdale, C.J. (1998). "Aggregate-Cement Chemical Interaction." *Cement and Concrete Research*, 28, 1037—1048.

Taylor, M.A., and Broms, B.B. (1964). "Shear Bond Strength Between Coarse Aggregate and Cement Paste or Mortar." *Journal of the American Concrete Institute*, 939—957.

Timoshenko, S.P., and Goodier, J.N. (1970). *Theory of Elasticity*, 3rd Edition, McGraw-Hill Book Company, New York.

Toutanji, H.A., Liu, L., El-Korchi, T. (1999). "The Role of Silica Fume in the Direct Tensile Strength of Cement-Based Materials." *Materials and Structure*, 32, 203–209.

Trende, U., and Büyüköztürk, O. (1998). "Size Effect and Influence of Aggregate Roughness in Interface Fracture of Concrete Composites." *ACI Materials Journal*, 95(4), 331—338.

Tschegg, E.K., Rotter, H.M., Roelfstra, P.E., Bourgund, U., and Jussel, P. (1995). "Fracture Mechanical Behavior of Aggregate-Cement Matrix Interfaces." *Journal of Materials in Civil Engineering*, ASCE, 7, 199—203.

Tutumluer, E., Rao, C., and Stefanski, J. (2000). "Video Image Analysis of Aggregates." *Final Project Report, FHWA-IL-UI-278*, Civil Engineering Studies UILU-ENG-2000-2015, University of Illinois Urbana-Champaign, Urbana, Illinois.

Tyler, W.S. (2001). *Particle Size and Shape Analyzers (CPA).* Product Brochure, Mentor, Ohio.

Wainwright, P. J., and Cabrera, J.G. (1990). "Assessment of the Efficiency of Chemical Membranes to Cure Concrete." *Proceedings of an International Conference on the Protection of Concrete*, Dundee, Scotland, 907-920.

Wang, L., and Zollinger, D.G. (2000). "A Mechanistic Design Framework for Spalling Distress." *Transportation Research Record 1730*, Transportation Research Board, Washington, D.C., 18—24.

Weingart, R.L., and Prowell, B.D. (1999). "Specification Development Using the VDG-40 Videograder for Shape Classification of Aggregates." *Proceedings of the 7th Annual Symposium*, International Center for Aggregate Research (ICAR), University of Texas, Austin, Texas, B1-2-1-B1-2-12.

Westergaard, H.M. (1927). "Analysis of Stresses in Concrete Pavements Due to Variation of Temperature." *Proceedings of Highway Research Board*, Highway Research Board, Washington, D.C., 6, 201—215.

Will, J.J. (2000). "High-Performance Concrete Using Nevada Aggregates." Ph.D. Dissertation, University of Nevada, Reno.

Winslow, D.N., Cohen, M.D., Bentz, D.P., Snyder, K.A., and Garboczi, E.J. (1994). "Percolation of Interfacial Zone Pores in Cement Mortar and Concrete." *Cement and Concrete Research*, 24, 25—37.

Wong, Y.L., Lam, L., Poon, C.S., and Zhou, F. P. (1999). "Properties of Fly Ash-Modified Cement Mortar-Aggregate Interfaces." *Cement and Concrete Research*, 29 1905 -1913.

Wu, K., Liu, J., Zhang, D. and Yan, A. (1999). "Rupture Probability of Coarse Aggregate on Fracture Surface of Concrete." *Cement and Concrete Research*, 29, 1983-1987.

Xin, D., Zollinger, D.G., and Allen, G.D. (1995). "An Approach to Determine Diffusivity in Hardening Concrete Based on Measured Humidity Profiles." *Advanced Cement Based Materials*, 2, 138—144.

Xu, G., Beaudoin, J.J., Jolicoeur, C., and Pagé, M. (2000). "The Effect of a Polynaphthalene Sulfonate Superplasticizer on the Contribution of the Interfacial Transition Zone to the Electrical Resistivity of Mortars Containing Silica and Limestone Fine Aggregate." *Cement and Concrete Research*, 30, 683—691.

Yildirim, I. (2001). "Surface Free Energy Characterization of Powers." Ph.D. Dissertation, Virginia Polytechnic Institute and State University, Blacksburg, Virginia.

Yuan, D., Nazarian, S., and Perea, A., (2006). "Nondestructive Testing Techniques for Assessing the Early Age Properties of Concrete." Transportation Research Board. Annual Meeting 2006, Paper #06-2725.

Yuan, D., and Nazarian, S. (2000), "Feasibility of Detecting Flaws in Concrete Walls of Nuclear Power Plants," Research Report submitted to JPL by Center for Highway Materials Research, Pasadena, California.

Yuan, C., and Gud, W.J. (1998). "Effect of Bond Between Aggregate and Cement Paste on the Mechanical Behavior of Concrete." *MRS Symposium Proceedings 114*, 41—47.

Zhang, X. (2004). "Consolidation Theories for Saturated-Unsaturated Soils and Numerical Simulations of Residential Buildings on Expansive Soils." Ph.D. Dissertation, Department of Civil Engineering, Texas A&M University, College Station, Texas.

Zhang, M.H., Lastra, R., and Malhotra, V.M. (1996). "Rice-Husk Ash Paste and Concrete: Some Aspects of Hydration and the Microstructure of the Interfacial Zone Between the Aggregate and Paste." *Cement and Concrete Research*, 26(6), 963—977.

Zhang, M.H., and. Gjorv, O.E. (1990). "Microstructure of the Interfacial Zone Between Lightweight Aggregate and Cement Paste." *Cement and Concrete Research*, 20(4), 610—618.

Zimbelmann, R. (1987). “A Method for Strengthening the Bond Between Cement Stone and Aggregates.” Cement and Concrete Research, 17(4), 651—660.

Zimbelmann, R. (1985). “A Contribution to the Problem of Cement Aggregate Bond.” *Cement and Concrete Research*, 15, 801—808.

Zollinger, D.G., Tayabji, S., and Smith, K. (2004). “Repair and Rehabilitation of Concrete Pavement: Volume I.” *Report FHWA-01-00080*, Texas Transportation Institute, Texas A&M University System, College Station, Texas.

Zollinger, D.G., Senadheera, S.P., and Tang, T. (1994). “Spalling of Continuously Reinforced Concrete Pavements.” *ASCE Journal of Transportation Engineering*, 120(3), 394—411.

Zollinger, D.G., Tang, T., and Yoo, R.H. (1993). “Fracture Toughness of Concrete at Early Ages.” *ACI Materials Journal*, 90(5), 463—471.

APPENDIX A

THE OPERATING PRINCIPLES OF THE PSPA AND THE THEORETICAL BACKGROUND ON THE IE AND THE SASW

PORTABLE SEISMIC PAVEMENT ANALYZER

The Portable Seismic Pavement Analyzer, as shown in Figure A.1, is an instrument designed to determine the variation in modulus with depth of exposed layer being concrete or asphalt. The operating principle of the PSPA is based on generating and detecting stress waves in a medium. The PSPA consists of two transducers and a source packaged into a hand-portable system, which can perform the Ultrasonic Surface Wave, and Impact Echo tests. The USW method can be used to determine the modulus of the material. The Impact Echo method can be used as a tool to determine the thickness or the bonding condition of concrete slabs.

The PSPA is operable from a computer. This computer is tethered to the hand-carried transducer unit through a cable that carries power to the transducers and hammers and returns the measured signals to the data acquisition board in the computer. To collect data with the PSPA, the technician initiates the testing sequence through the computer. The high-frequency source is activated four to six times. The outputs of the two transducers from the last three impacts are saved and averaged (stacked). The other (pre-recording) impacts are used to adjust the gains of the pre-amplifiers. The gains are set in a manner that optimizes the dynamic range.

Typical voltage outputs of the two accelerometers are shown in Figure A.2. To ensure that an adequate signal-to-noise ratio is achieved in all channels, signals are normalized to an amplitude of one. In this manner, the main features of the signals can be easily inspected.

The data, collected in this fashion, have to be processed using signal processing and spectral analyses. The processes for each of the test methods are described in the following paragraphs.

Ultrasonic Surface Wave Method

The relationship amongst velocity, V, travel time, Δt, and receiver spacing, ΔX, can be written in the following form:

$$V = \frac{\Delta X}{\Delta t} \qquad \text{(A.1)}$$

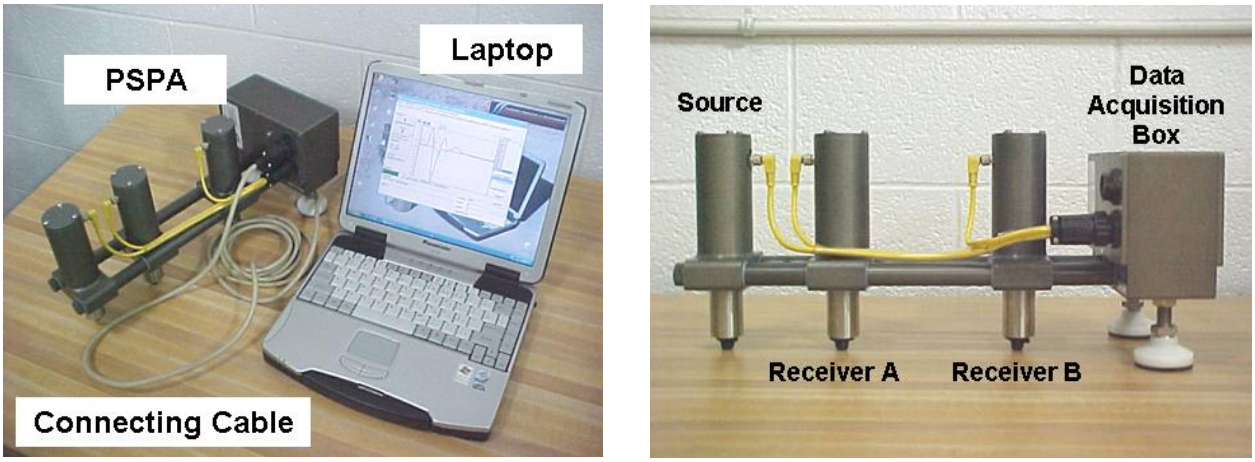

Figure A.1. Portable Seismic Pavement Analyzer.

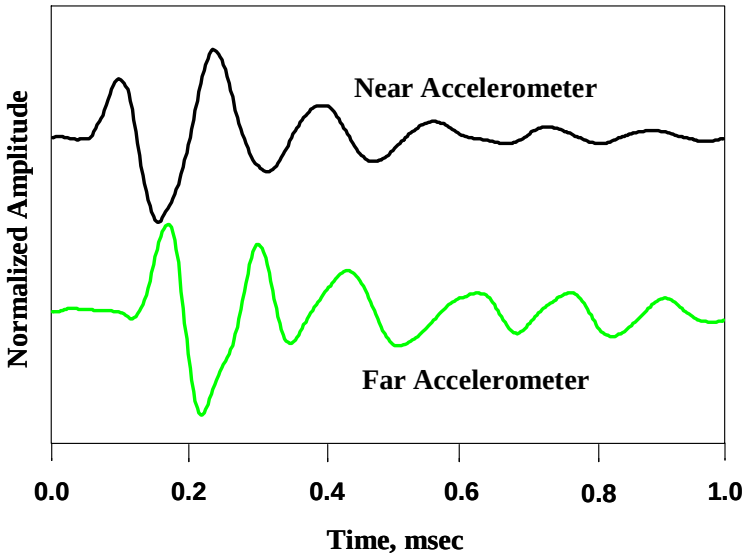

Figure A.2. Typical Time Records from PSPA.

In the equation, V can be the propagation velocity of any of the three waves (i.e., compression wave, V_P; shear wave, V_S; or surface (Rayleigh) wave, V_R). Knowing wave velocity, the modulus can be determined in several ways. Young's modulus, E, can be determined from shear modulus, G, through the Poisson's ratio, ν, using:

$$E = 2\,(1+\nu)\,G \tag{A.2}$$

Shear modulus can be determined from shear wave velocity, V_S, using:

$$G = \frac{\gamma}{g} V_s^2 \tag{A.3}$$

To obtain the modulus from surface wave velocity, V_R is first converted to shear wave velocity using:

$$V_S = V_R\,(1.13 - 0.16\nu) \tag{A.4}$$

The shear modulus is then determined by using Equation A.3.

Surface waves (or Rayleigh, R-wave) contain about two-thirds of the seismic energy. As such, the most dominant arrivals are related to the surface waves, making it easy to measure. The USW method is an offshoot of the SASW method (Nazarian et al., 1993). The major distinction between these two methods is that in the USW method the modulus of the top pavement layer can be directly determined without an inversion algorithm.

As sketched in Figure A.3, at wavelengths less than or equal to the thickness of the uppermost layer, the velocity of propagation is independent of wavelength. Therefore, if one simply generates high-frequency (short-wavelength) waves and if one assumes that the properties of the uppermost layer are uniform, the shear wave velocity of the upper layer, V_s, can be determined from:

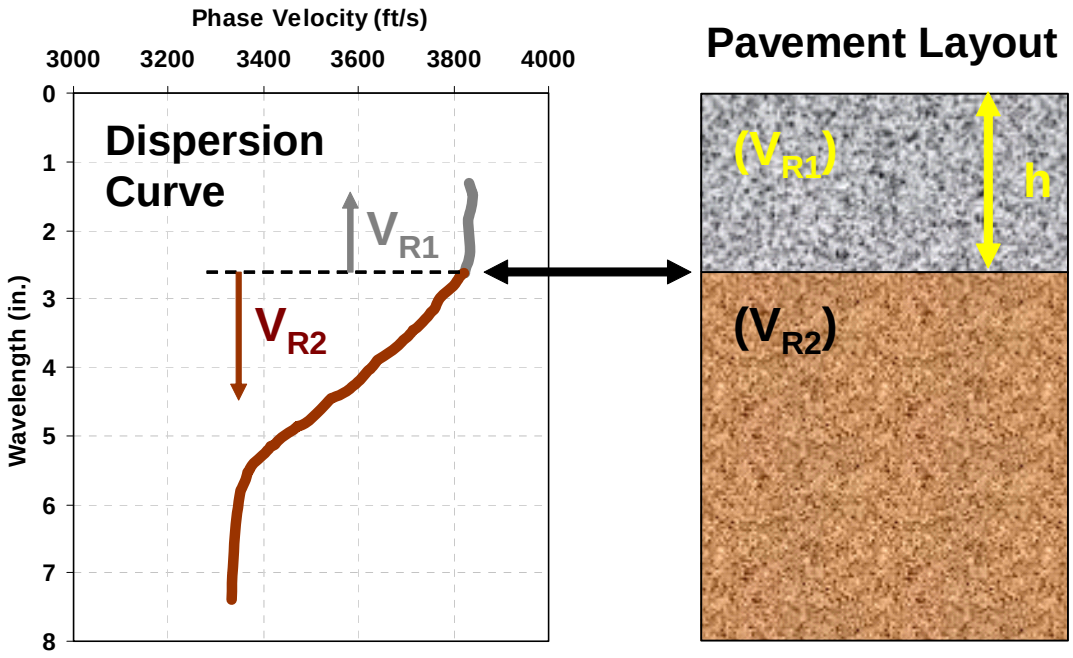

Figure A.3. Schematic of USW Method.

$$V_s = (1.13 - 0.16\nu)\, V_{ph} \qquad \text{(A.5)}$$

The modulus of the top layer, E, can be determined from:

$$E = 2\,\rho\, V_s^2\,(1 + \nu). \qquad \text{(A.6)}$$

where, V_{ph} = velocity of surface waves, ρ = mass density, and ν = Poisson's ratio.

To obtain the average velocity and as such, the average modulus, the dispersion curve from a wavelength of about 2 in. to about 0.5 in. less than the nominal thickness of the deck is used.

Impact Echo Method

The Impact Echo method primarily provides information about the thickness of and delamination within a PCC layer or slab. Sansalone and Carino (1986) have also used the method to locate defects, voids, cracks, and zones of deterioration within concrete.

Yuan and Nazarian (2000) conducted an extensive study to verify the applicability of the Impact Echo in detecting discontinuities, such as voids, cracking and debonding within a concrete member. The study consisted of both numerical and experimental phases. The objective of the numerical study, which was conducted using finite-element (FE) analyses, was to understand the full wave-field transient response from a variety of concrete walls or slabs containing voids and horizontal cracks. To ensure that the results from the numerical simulation were realistic, experiments were performed in a facility consisting of eight different concrete slabs built for that project. The facility was designed and constructed so that the impact of construction parameters (such as steel reinforcement and backfill density) on the measurements can also be documented. The PSPA was employed in the experiments. Defects in a concrete wall or slab were found to be detectable by analyzing the combined characteristics of wave propagation in both time and frequency domains. Close agreement between the results from numerical simulation and field measurements was shown.

The transducer closer to the source, shown in Figure A.1, is used in the IE measurements. The method, as sketched in Figure A.4, is based on detecting the frequency of the standing wave reflecting from the bottom and the top of the top PCC layer. Upon an impact on a PCC layer, some of the energy is reflected from the bottom of the layer, and some is transmitted into the base and subgrade. Since on a bridge deck, the top and bottom of the layer is in contact with air, almost all of the energy is reflected from that interface. The receiver senses the reflected energy at periodic intervals. The period depends on the thickness and compression wave of the layer. To conveniently determine the frequency associated with the periodic arrival of the signal, one can utilize a fast Fourier transform algorithm. The frequency associated with the reflected wave appears as a peak in the amplitude spectrum. Once the compression wave velocity of concrete, V_p, is known, the depth-to-reflector, h, can be determined from:

$$h = V_p / 2f \quad \text{(A.7)}$$

where f is the resonant frequency obtained by transforming the deformation record into the frequency domain. The compression wave velocity can be determined if the surface wave velocity is known from:

$$V_P = V_R \left[(1 - \nu) / (0.5\text{-}\nu)\right]^{0.5} / (1.13 - 0.16\,\nu) \quad \text{(A.8)}$$

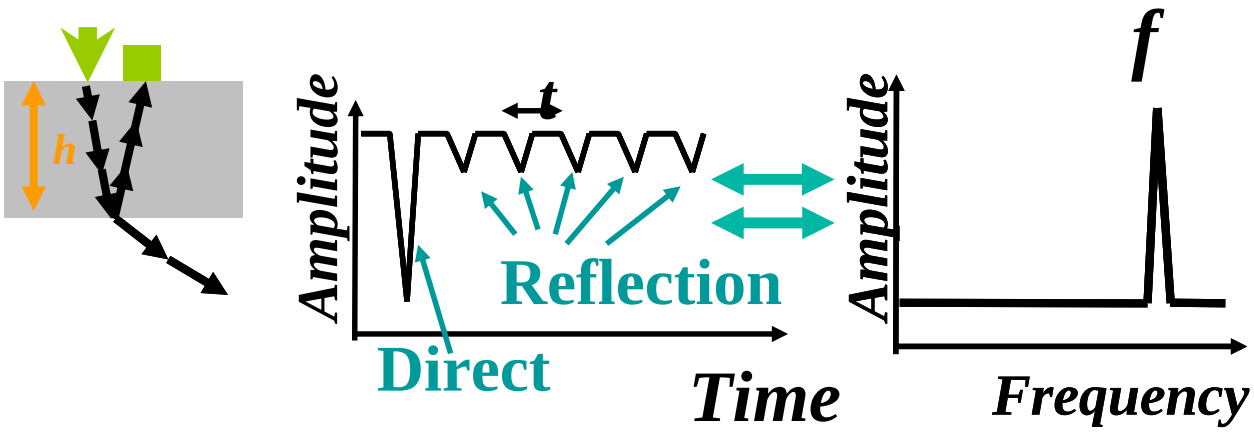

Figure A.4. Schematic of Impact Echo Method.

Time-Frequency Analysis. In the Impact Echo test, the main goal is to obtain information about the material integrity. The signal received by the PSPA receiver is a sum of the direct surface wave, surface echo, bottom or defect echo, and ambient noise. In the Impact Echo analysis, the objective is to detect the information on the bottom or the defect (target). Possible shifting or overshadowing of the target signal can cause difficulty in detecting it. In order to correct this shortcoming, a time-frequency analysis (Kim et al. 2004, Shokouhi and Gucunski 2003) can be performed on the signal. In this analysis, the time records and the frequency spectrum are combined to obtain a spectrogram, improving the identification of the damaged areas. The time-frequency analysis can provide the temporal variation in frequency components of the signal,

therefore improving the interpretation of the IE signal. Figure A.5 shows an example of the time-frequency analysis results on an intact 12 in. thick concrete slab. The signal is concentrated in the first millisecond of the time record at a frequency of the thickness of the slab.

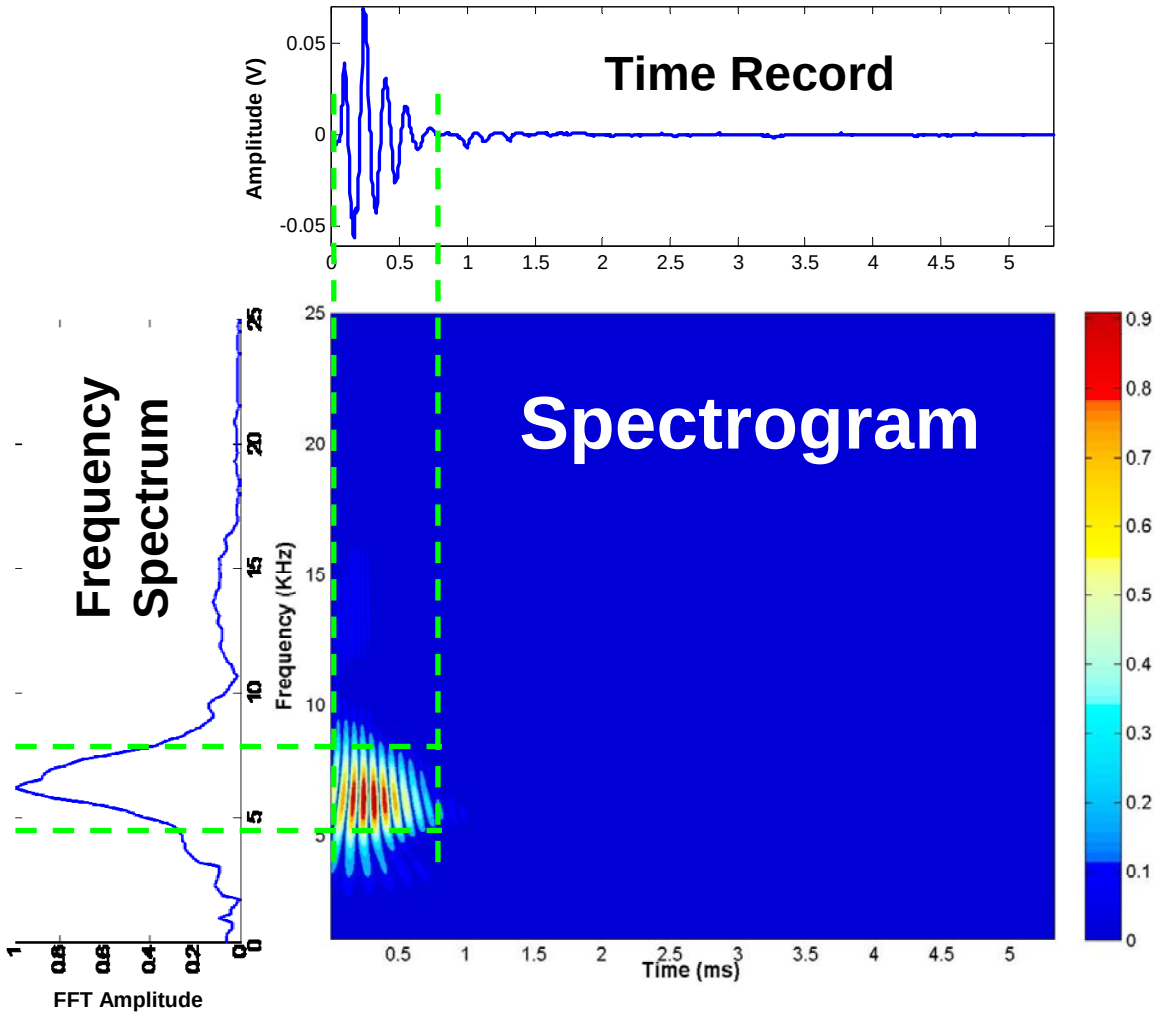

Figure A.5. Example of Time-Frequency Analysis.

APPENDIX B

DATA DETAILS OF FIELD TESTS AT SH 288

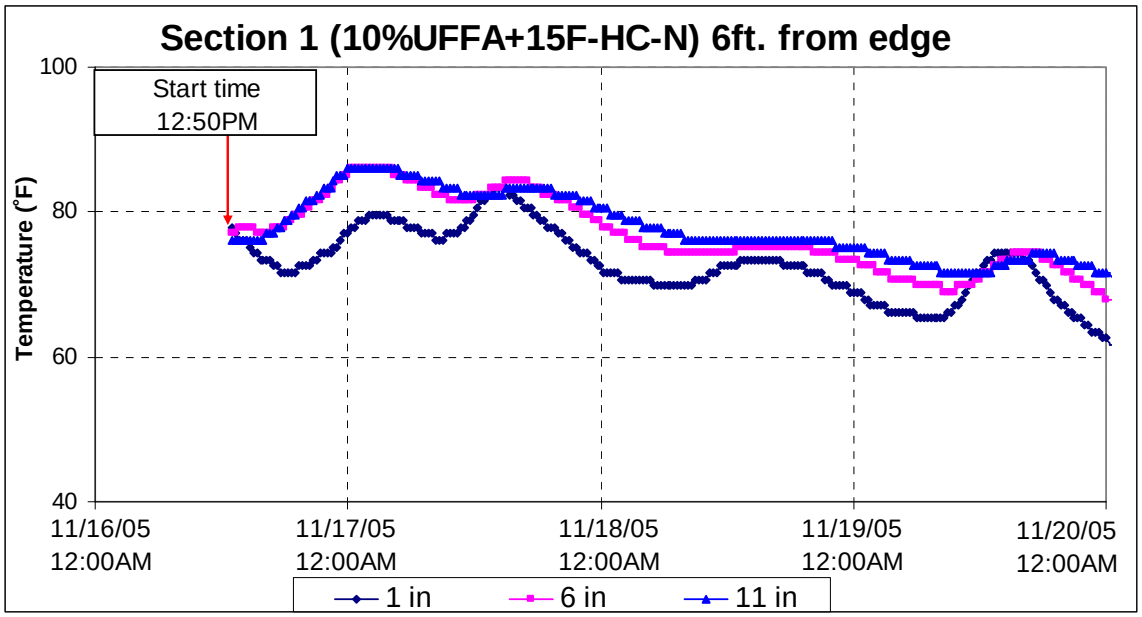

Figure B.1. Temperature Profile of Test Section 1.

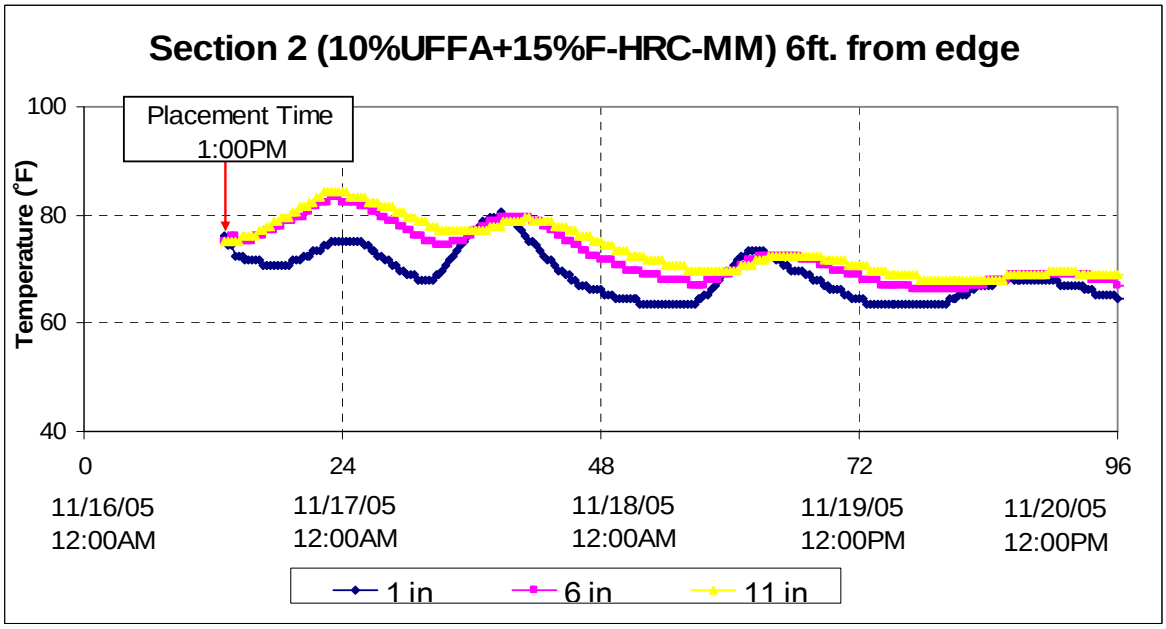

Figure B.2. Temperature Profile of Test Section 2.

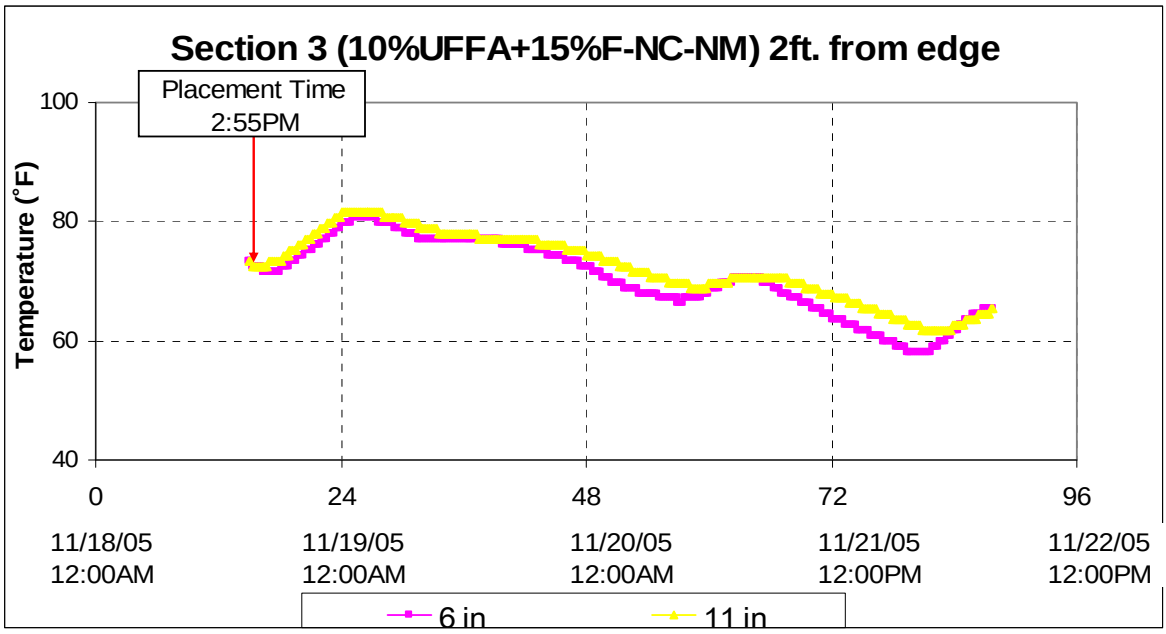

Figure B.3. Temperature Profile of Test Section 3.

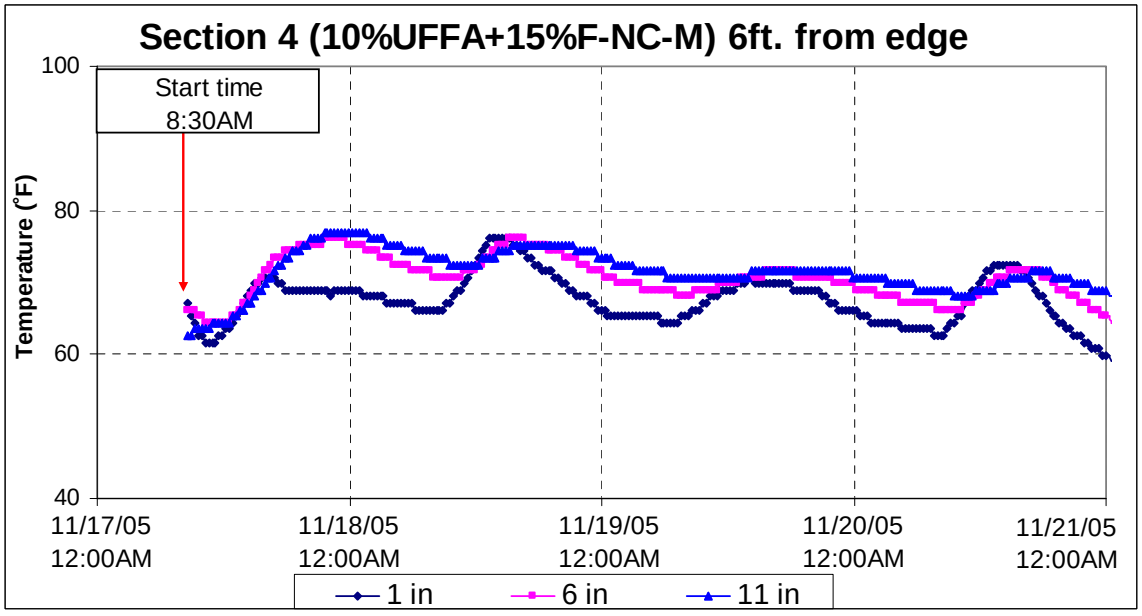

Figure B.4. Temperature Profile of Test Section 4.

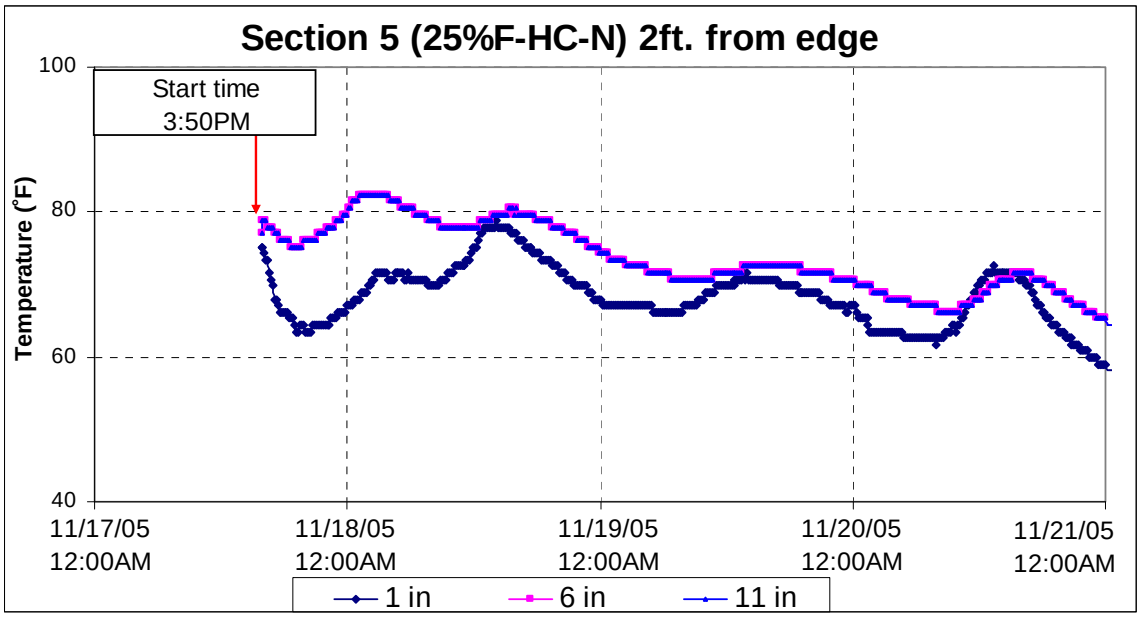

Figure B.5. Temperature Profile of Test Section 5.

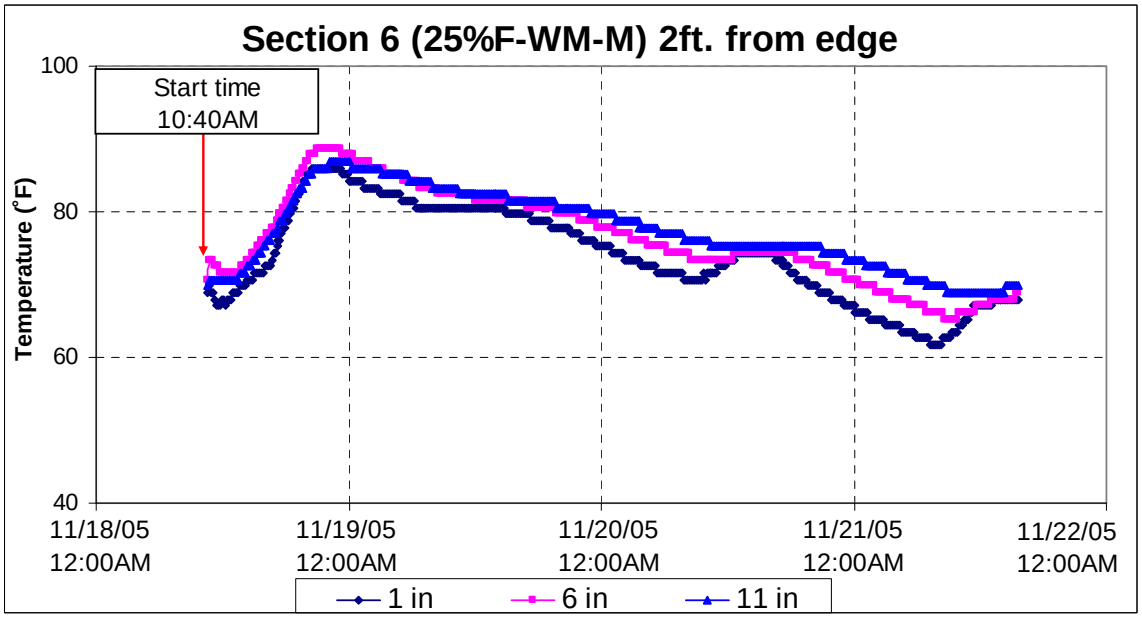

Figure B.6. Temperature Profile of Test Section 6.

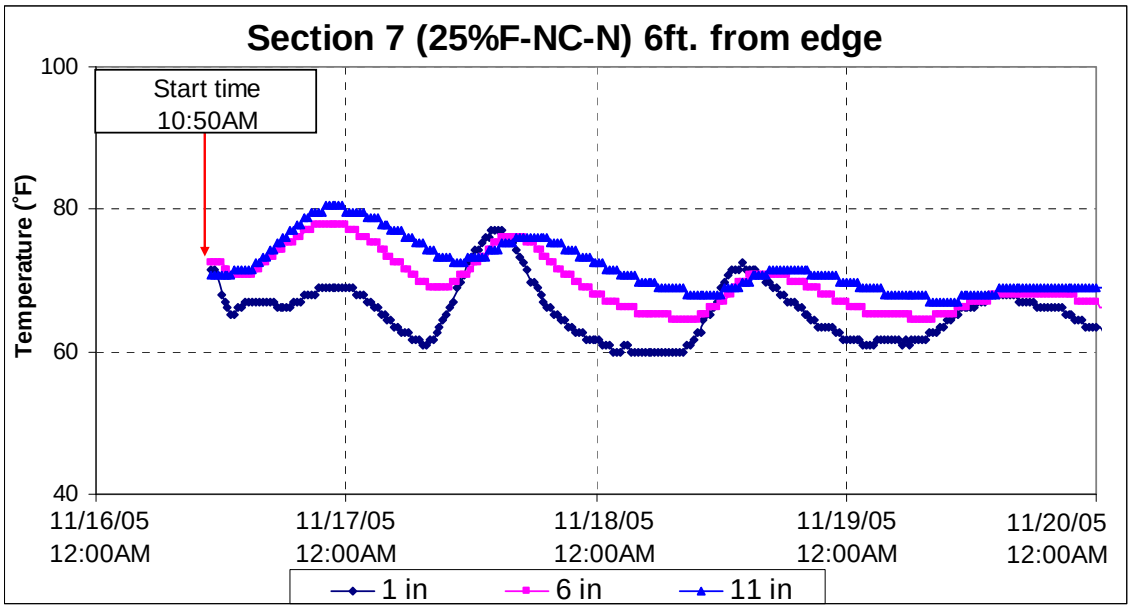

Figure B.7. Temperature Profile of Test Section 7.

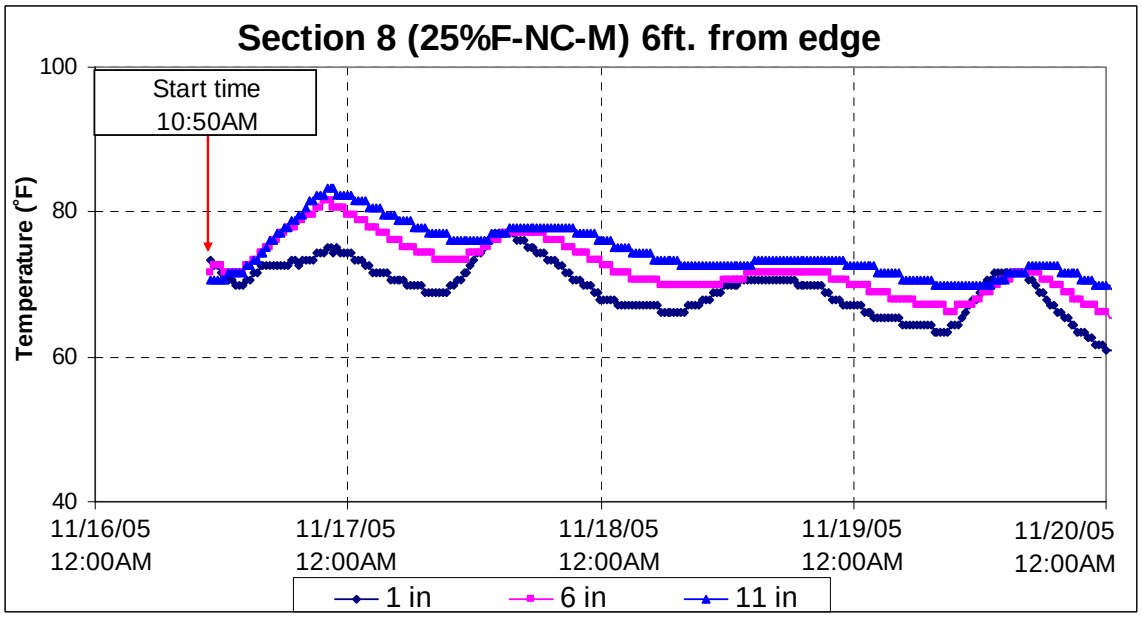

Figure B.8. Temperature Profile of Test Section 8.

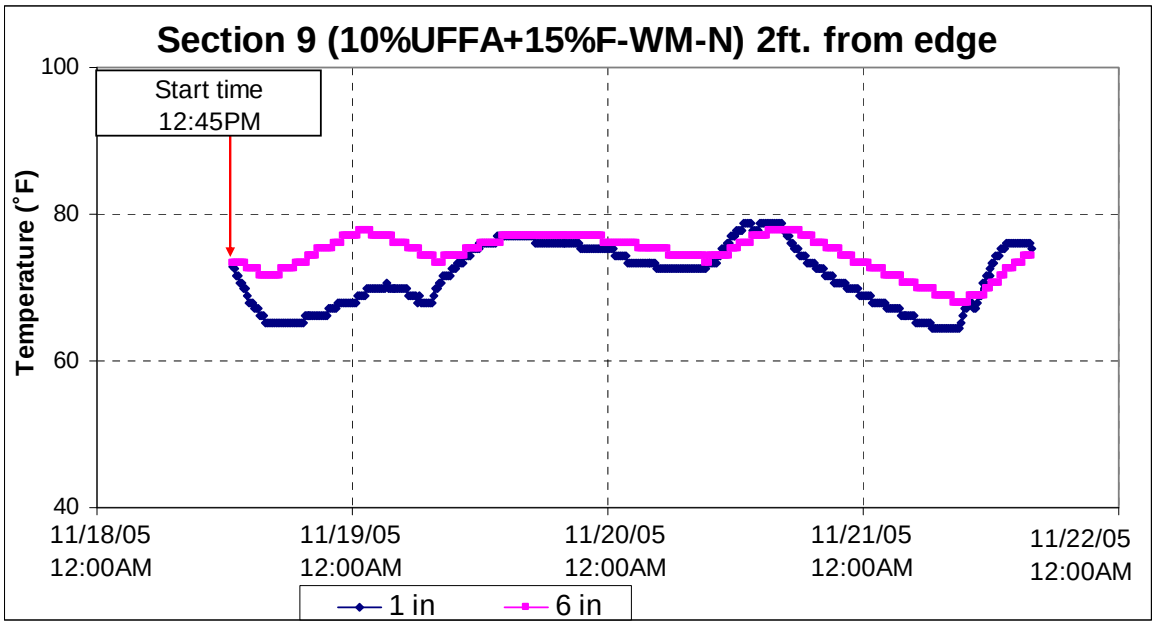

Figure B.9. Temperature Profile of Test Section 9.

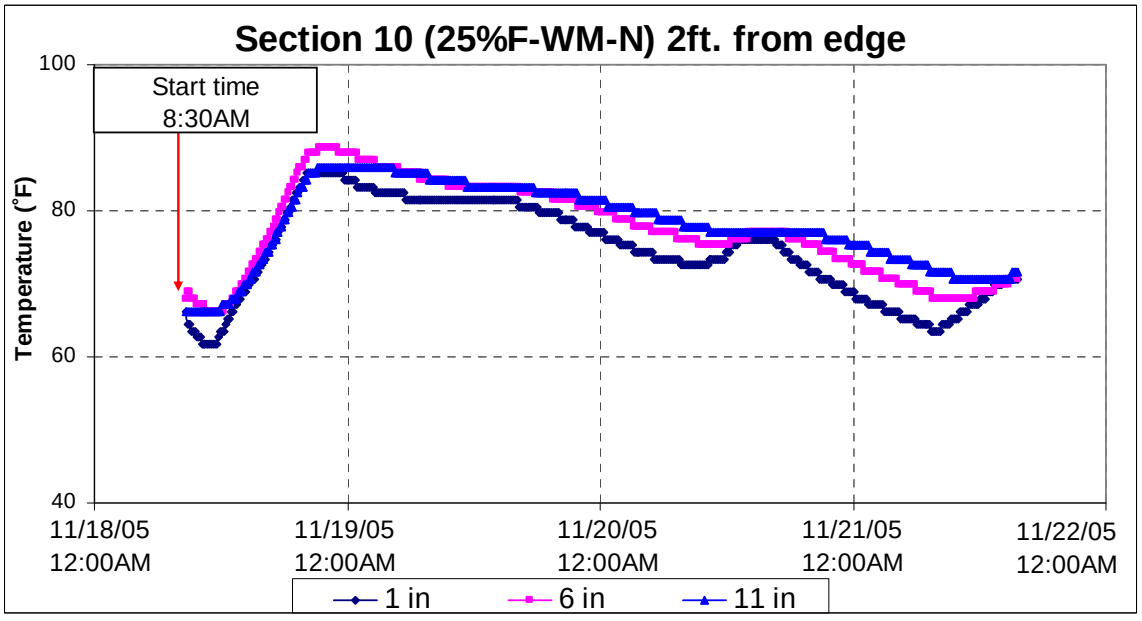

Figure B.10. Temperature Profile of Test Section 10.

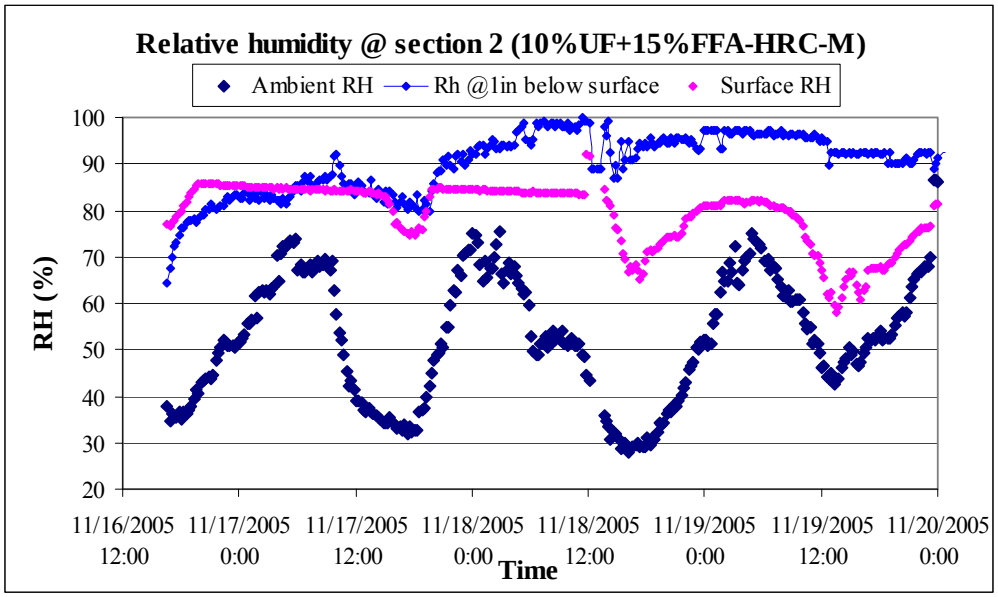

Figure B.11. Moisture Profiles of Test Section 2.

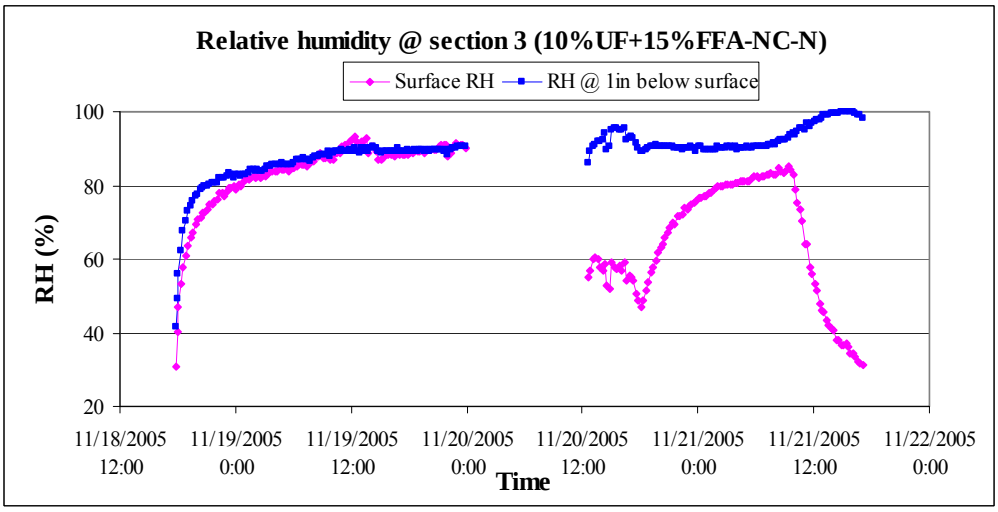

Figure B.12. Moisture Profiles of Test Section 3.

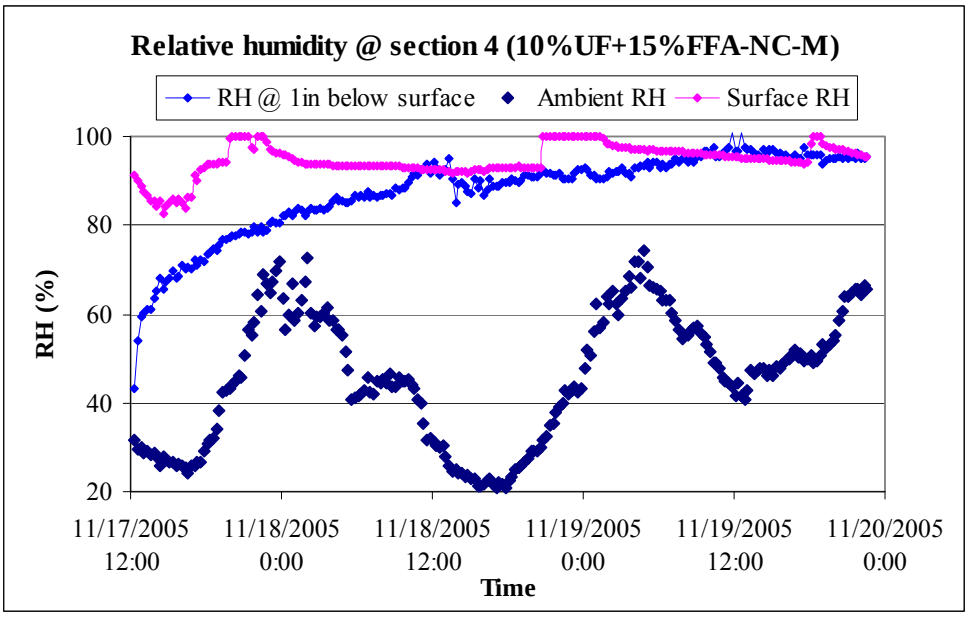

Figure B.13. Moisture Profiles of Test Section 4.

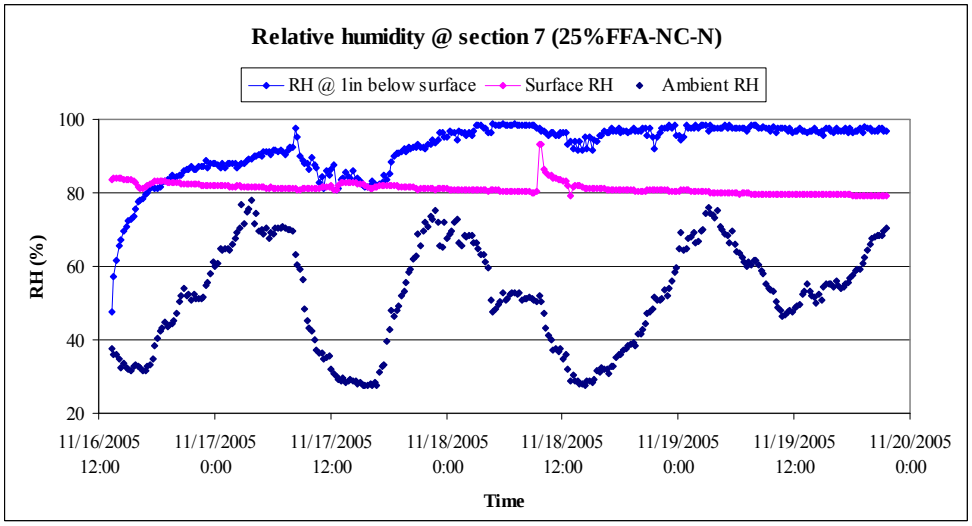

Figure B.14. Moisture Profiles of Test Section 7.

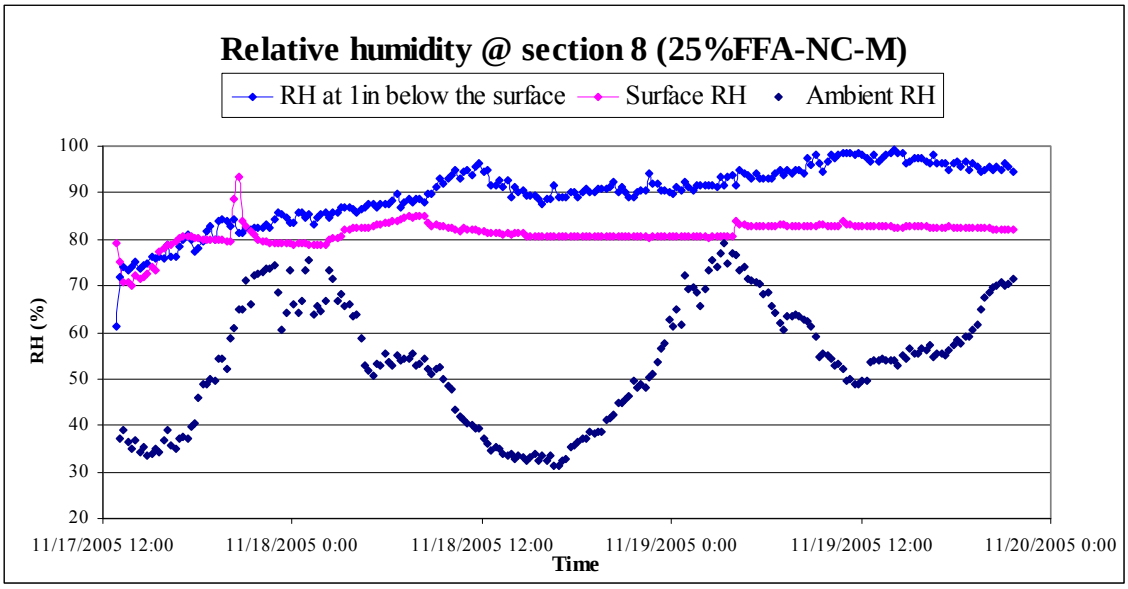

Figure B.15. Moisture Profiles of Test Section 8.

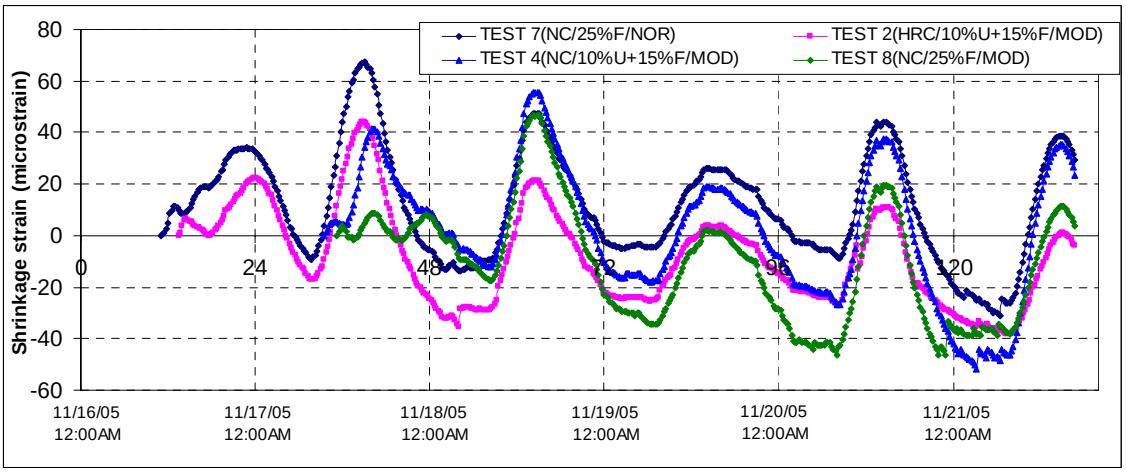

Figure B.16. Drying Shrinkage with Time for Different Sections.

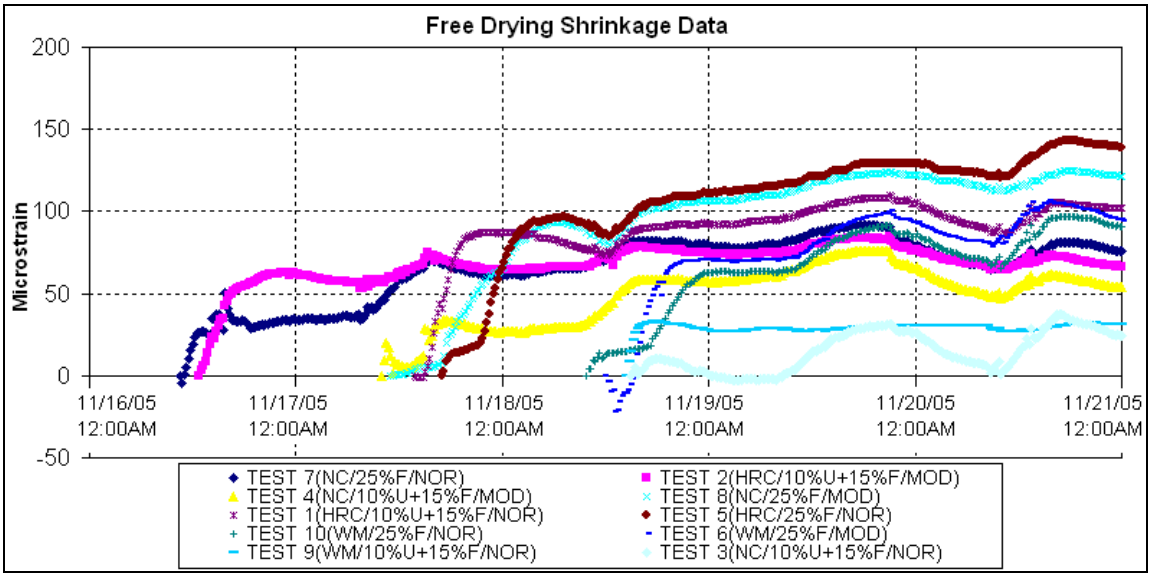

Figure B.17. Free Shrinkage with Time for Different Sections.

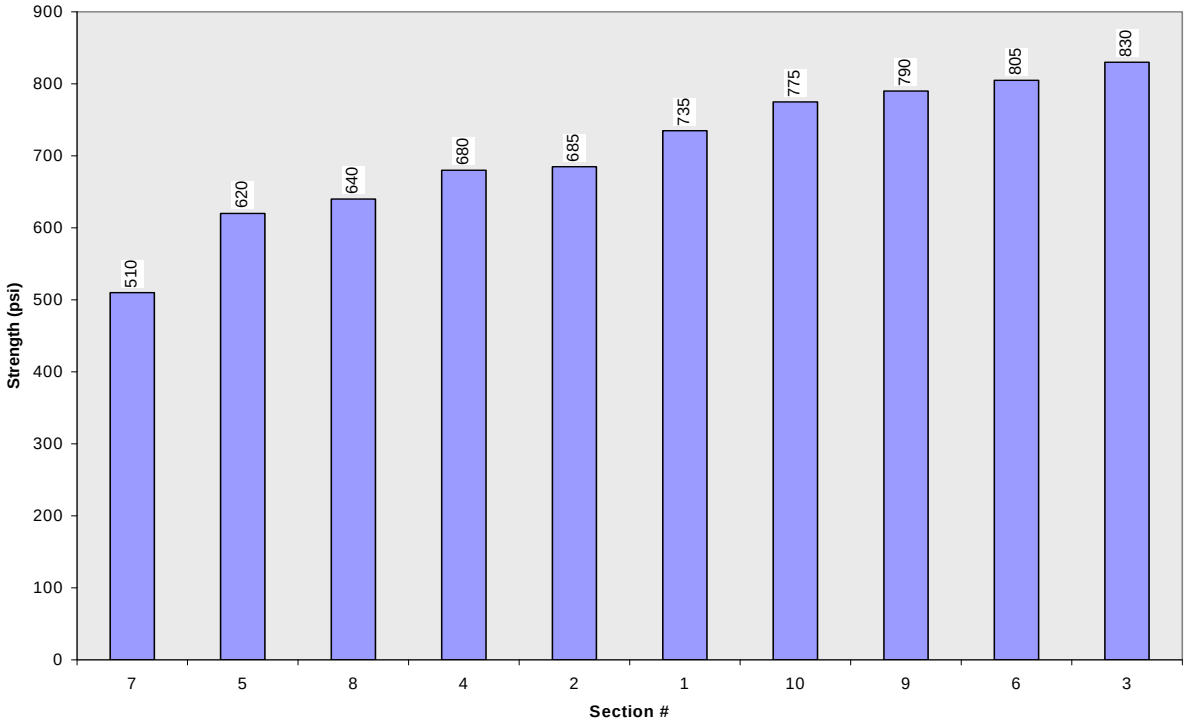

Figure B.18. Seven-day Flexural Strength of Concrete for All Test Sections.

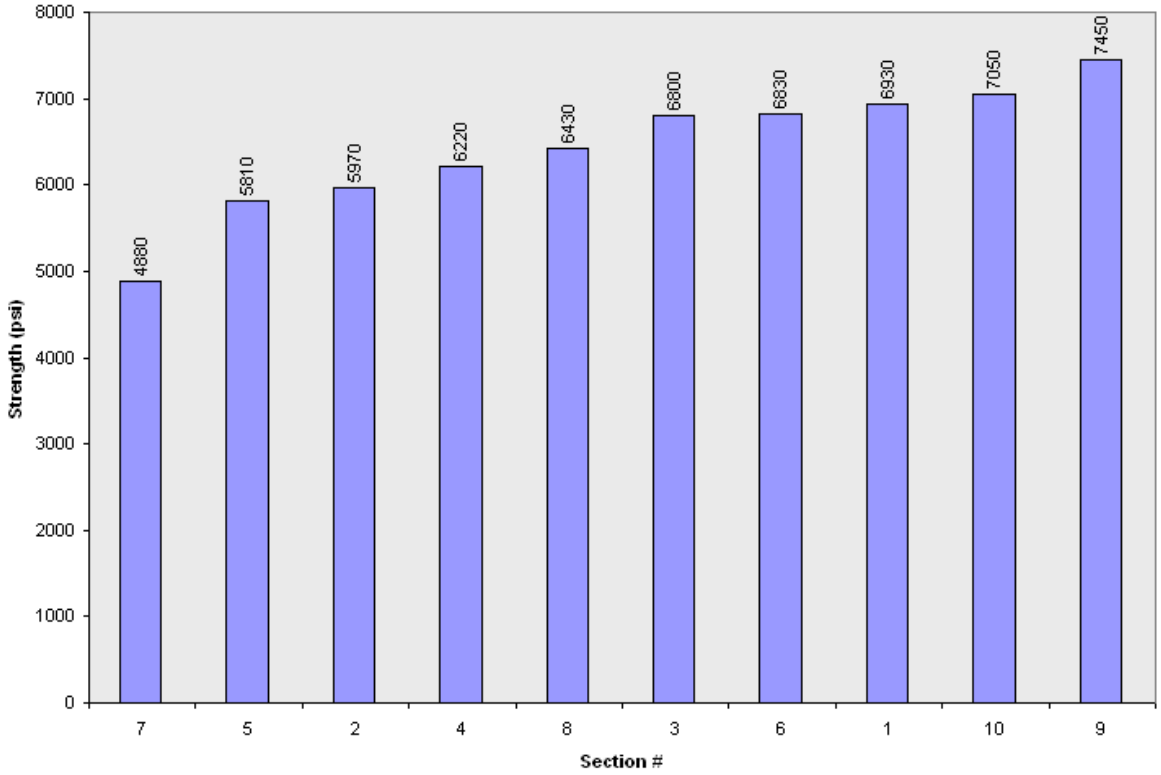

Figure B.19. Seven-day Compressive Strength of Concrete for All Test Sections.

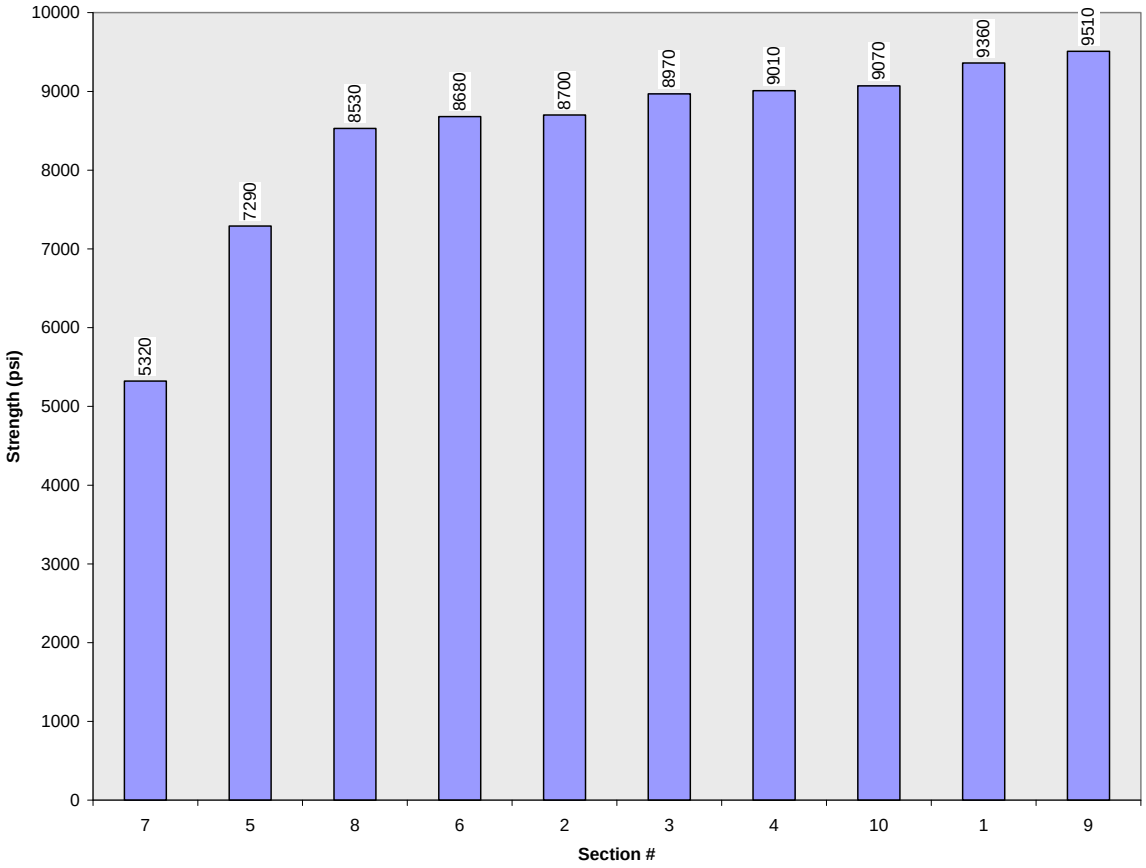

Figure B.20. Twenty-eight-day Compressive Strength of Concrete for All Test Sections.

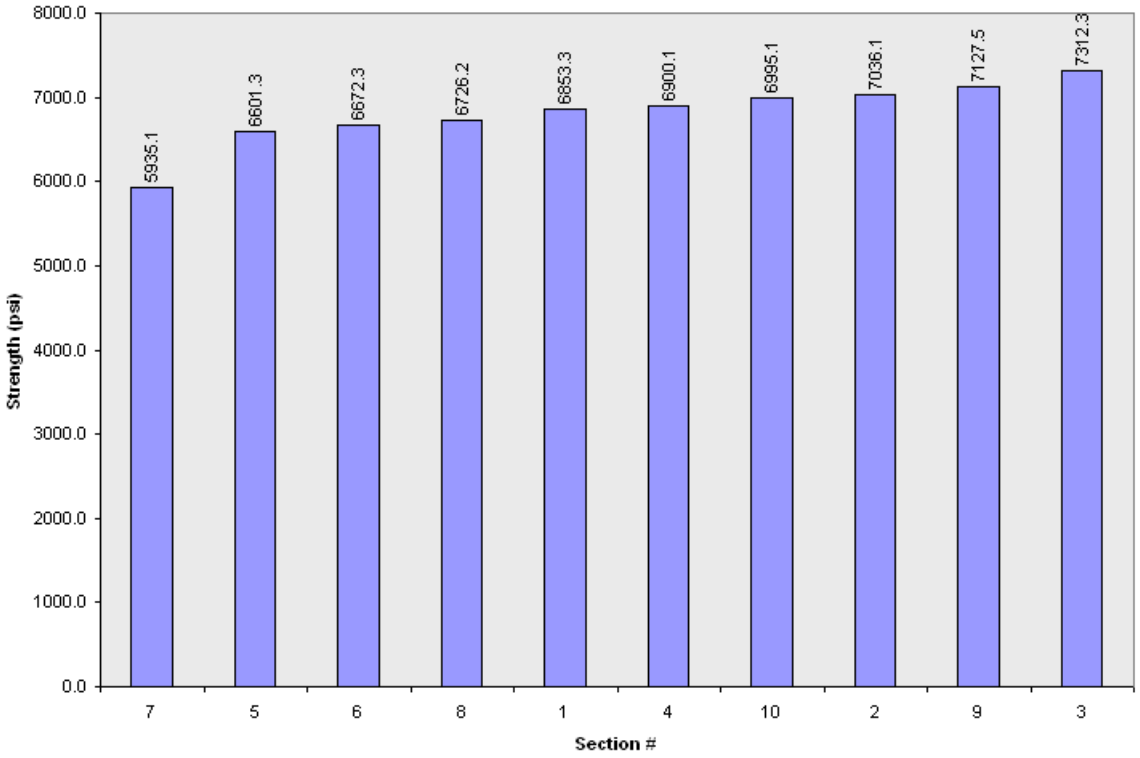

Figure B.21. Seven-day Elastic Modulus of Concrete for All Test Sections by Free-Free Test.

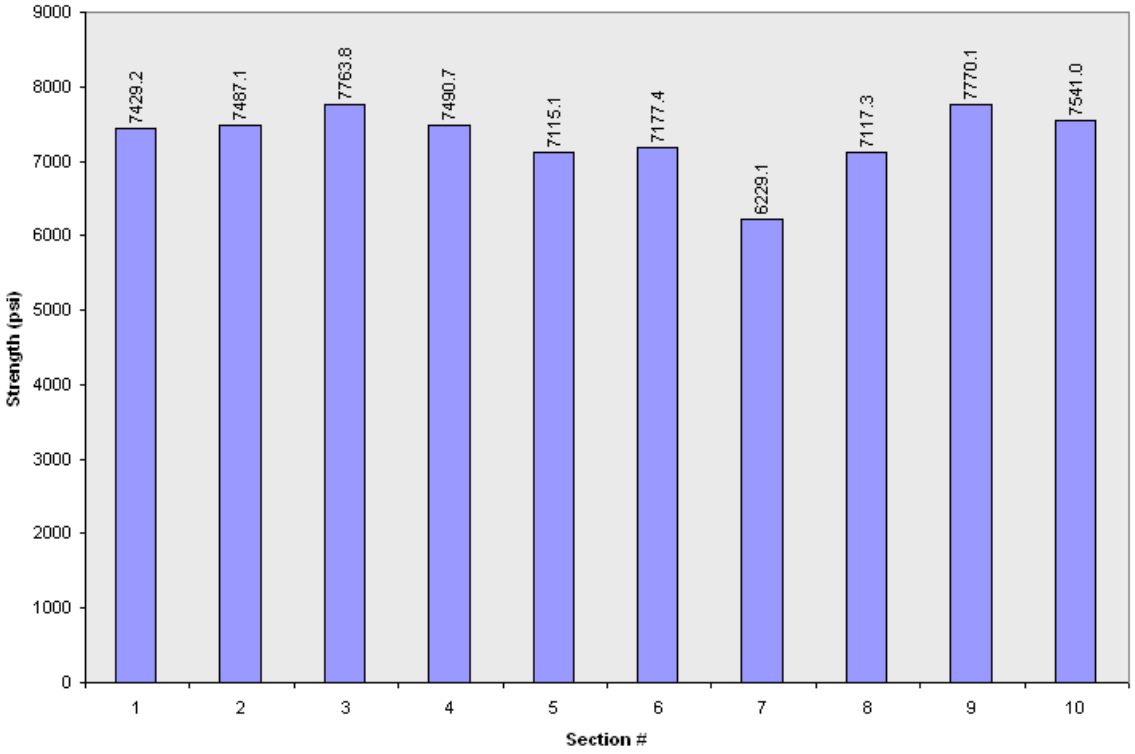

Figure B.22. Twenty-eight-day Elastic Modulus of Concrete for All Test Sections by Free-Free Test.

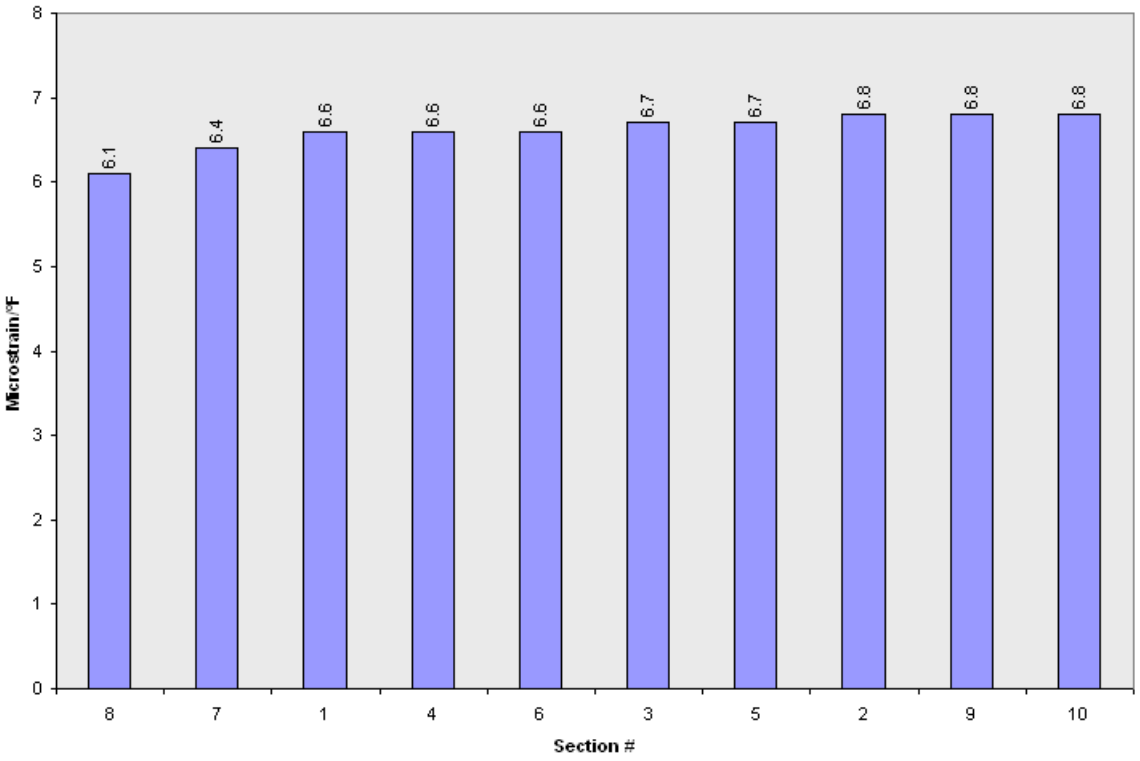

Figure B.23. Nineteen—Twenty-six-day Coefficient of Thermal Expansion of Concrete for All Test Sections.

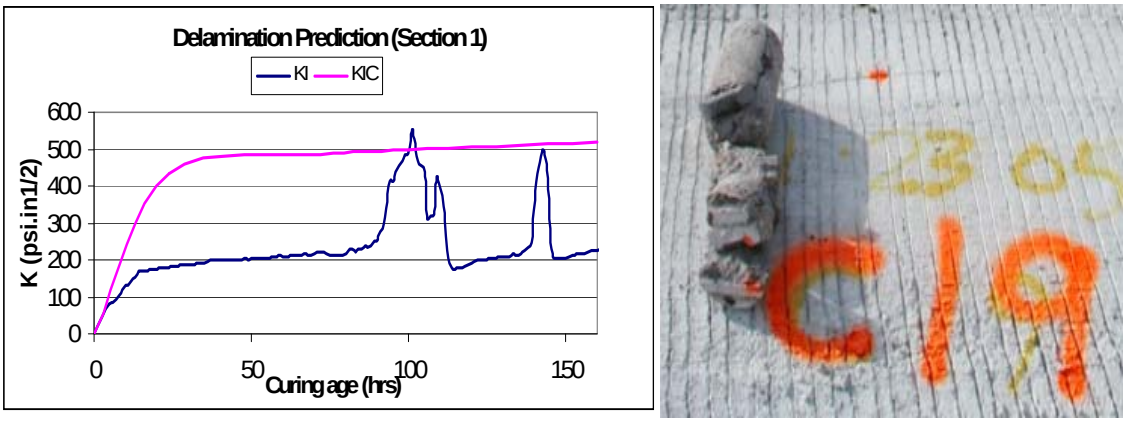

(a) (b)

Figure B.24. Delamination Prediction for Section 1.

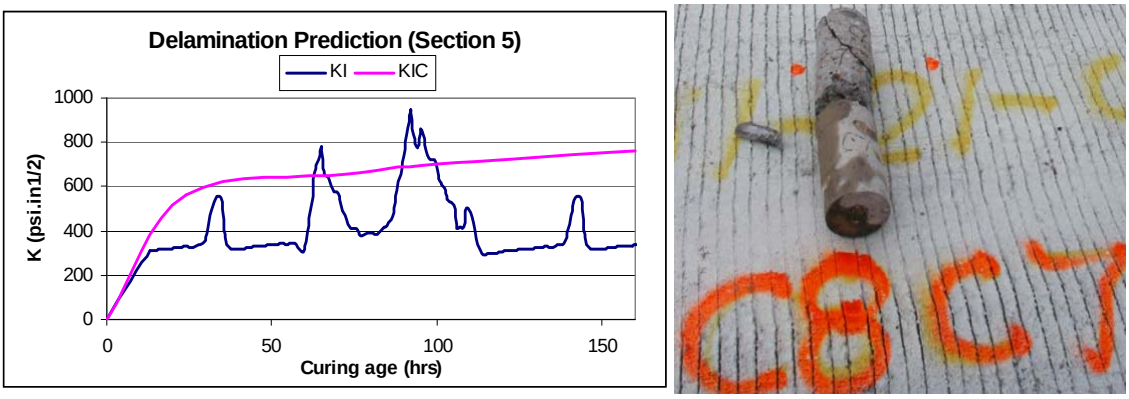

(a) (b)

Figure B.25. Delamination Prediction for Section 5.

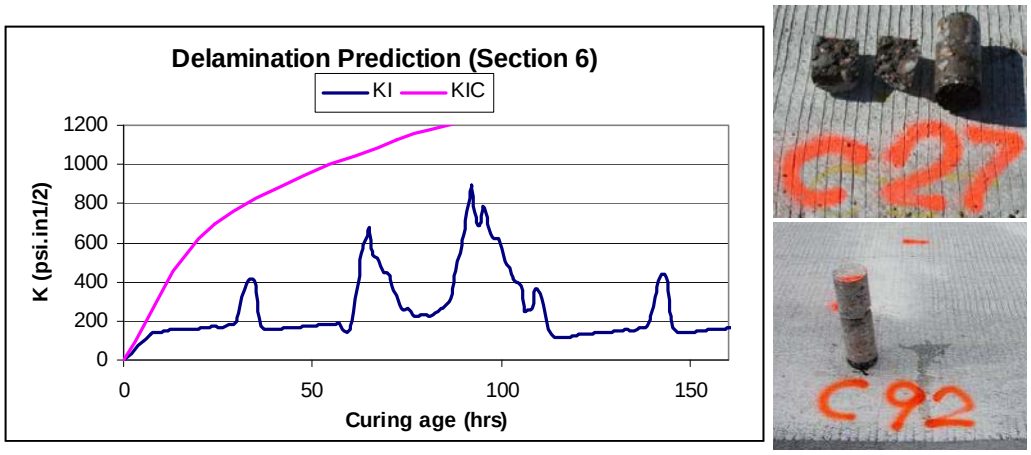

(a) (b)

Figure B.26. Delamination Prediction for Section 6.

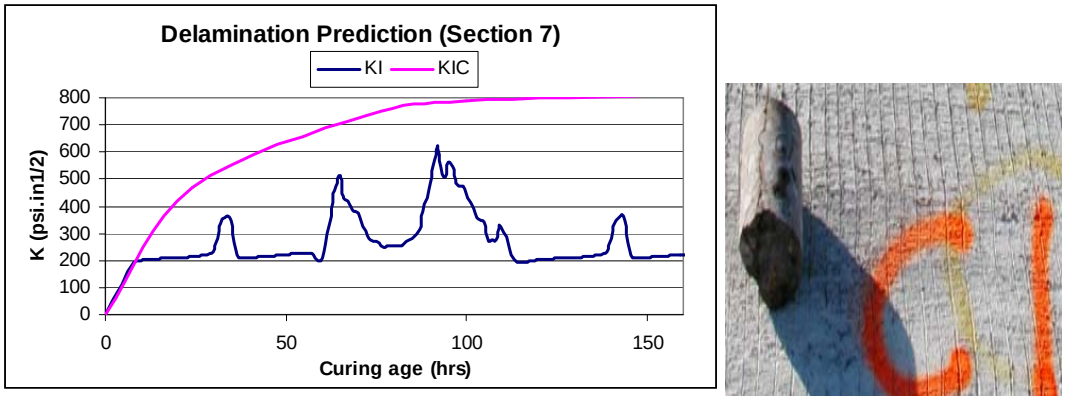

(a) (b)

Figure B.27. Delamination Prediction for Section 7.

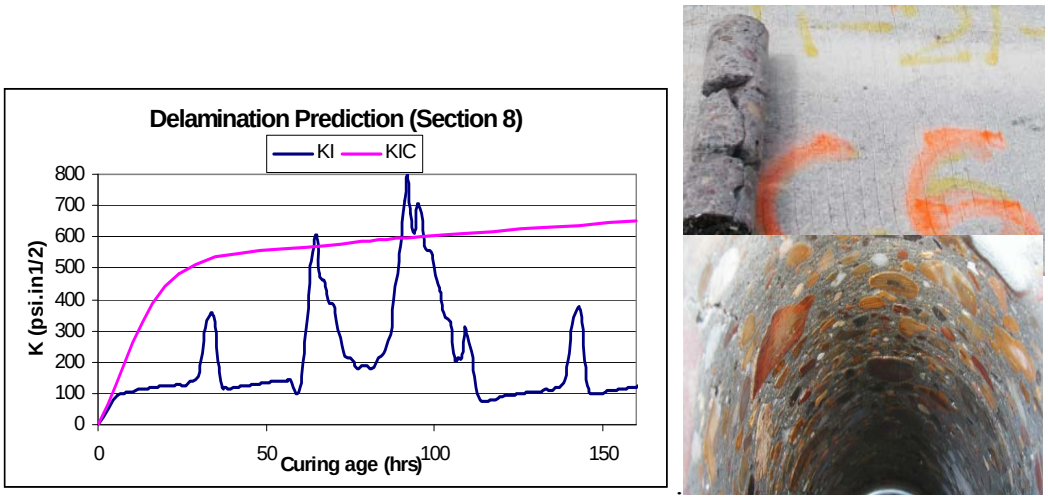

(a) (b)

Figure B.28. Delamination Prediction for Section 8.

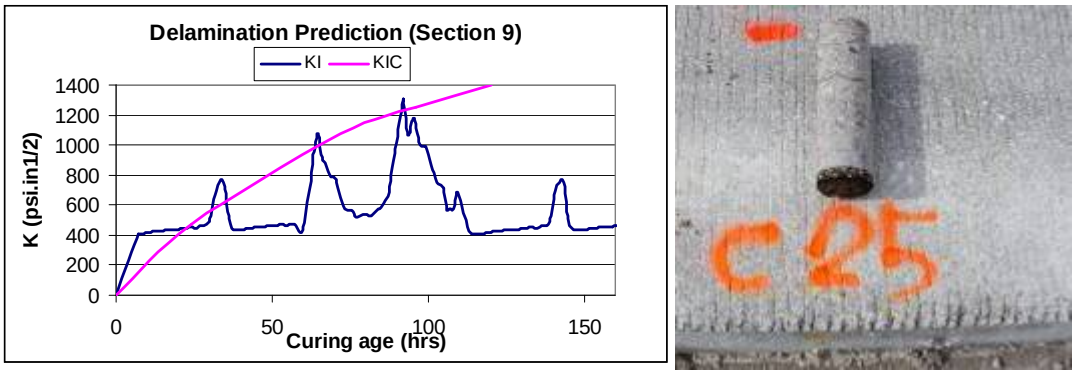

(a) (b)

Figure B.29. Delamination Prediction for Section 9.

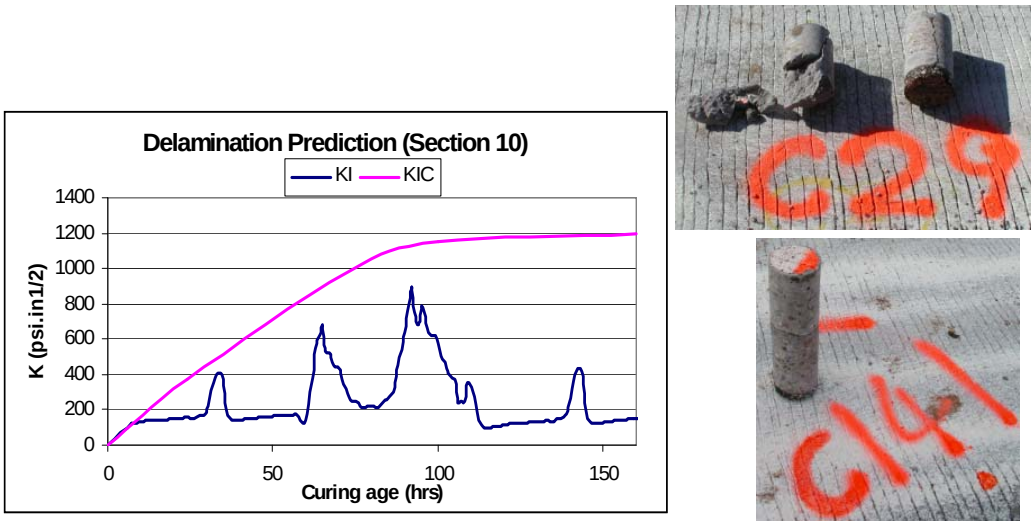

(a) (b)

Figure B.30. Delamination Prediction for Section 10.

APPENDIX C

TxDOT COMPRESSIVE STRENGTH AND FFRC RESULTS OF SH 288

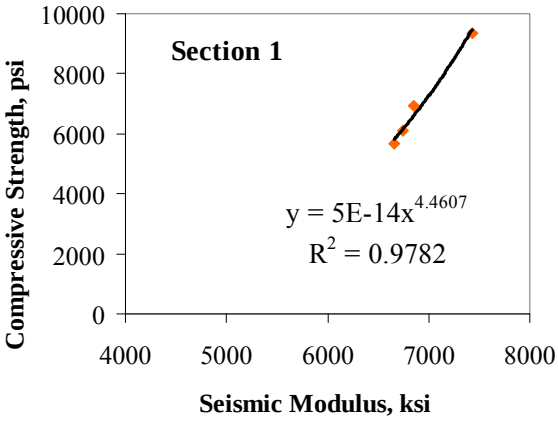
Section 1
Compressive Strength, psi
Seismic Modulus, ksi
y = 5E-14x^4.4607
R^2 = 0.9782
10000
8000
6000
4000
2000
0
4000
5000
6000
7000
8000

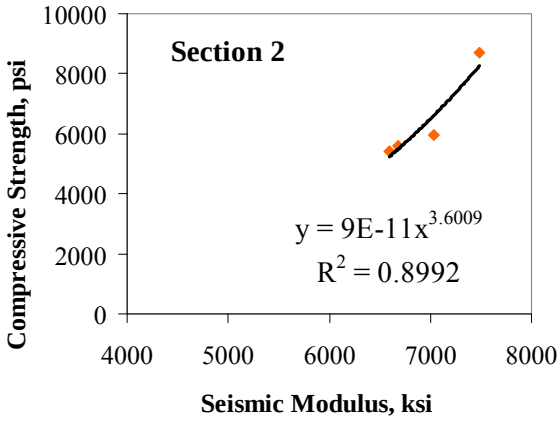
Section 2
Compressive Strength, psi
Seismic Modulus, ksi
y = 9E-11x^3.6009
R^2 = 0.8992
10000
8000
6000
4000
2000
0
4000
5000
6000
7000
8000

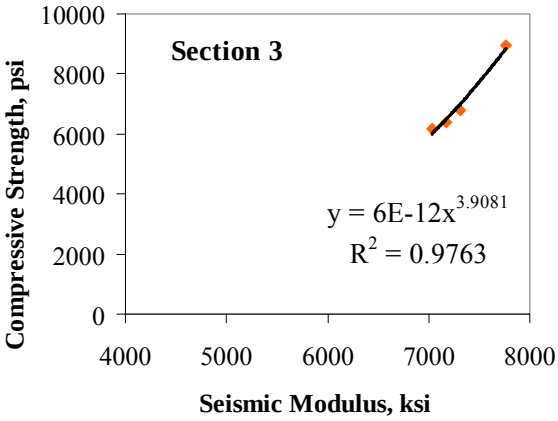
Section 3
Compressive Strength, psi
Seismic Modulus, ksi
y = 6E-12x^3.9081
R^2 = 0.9763
10000
8000
6000
4000
2000
0
4000
5000
6000
7000
8000

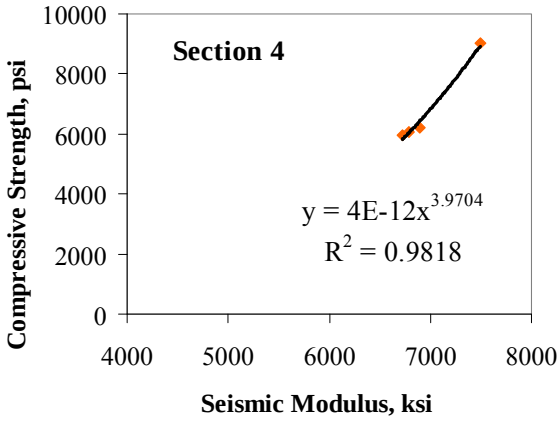
Section 4
Compressive Strength, psi
Seismic Modulus, ksi
y = 4E-12x^3.9704
R^2 = 0.9818
10000
8000
6000
4000
2000
0
4000
5000
6000
7000
8000

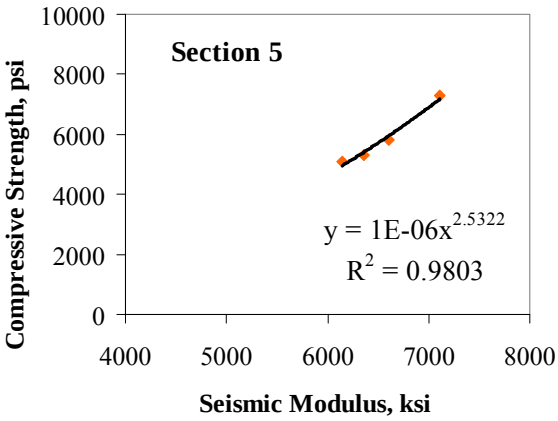
Section 5
Compressive Strength, psi
Seismic Modulus, ksi
y = 1E-06x^2.5322
R^2 = 0.9803
10000
8000
6000
4000
2000
0
4000
5000
6000
7000
8000

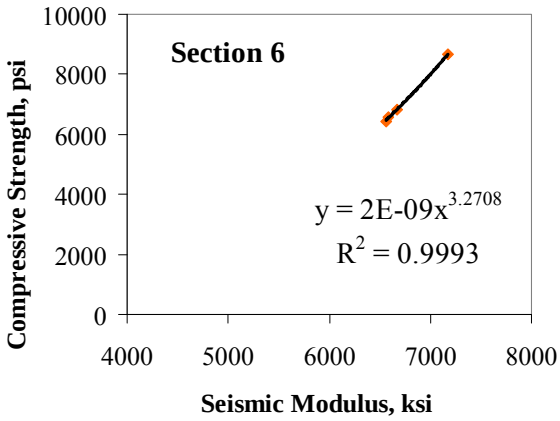
Section 6
Compressive Strength, psi
Seismic Modulus, ksi
y = 2E-09x^3.2708
R^2 = 0.9993
10000
8000
6000
4000
2000
0
4000
5000
6000
7000
8000

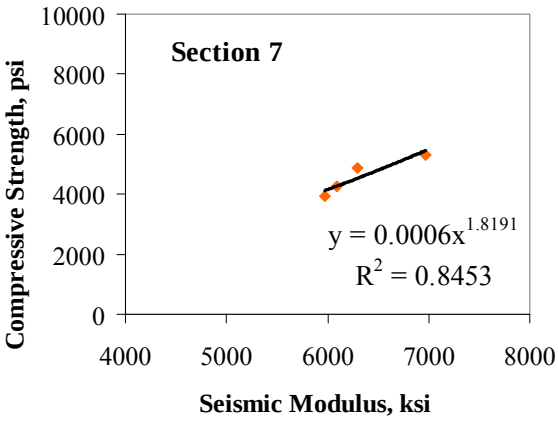
Section 7
Compressive Strength, psi
Seismic Modulus, ksi
y = 0.0006x^1.8191
R^2 = 0.8453
10000
8000
6000
4000
2000
0
4000
5000
6000
7000
8000

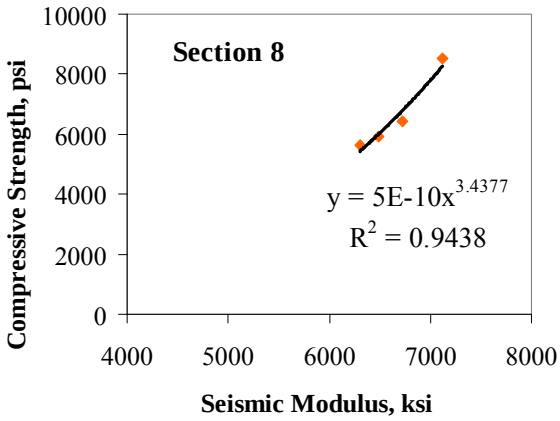
Section 8
Compressive Strength, psi
Seismic Modulus, ksi
y = 5E-10x^3.4377
R^2 = 0.9438
10000
8000
6000
4000
2000
0
4000
5000
6000
7000
8000

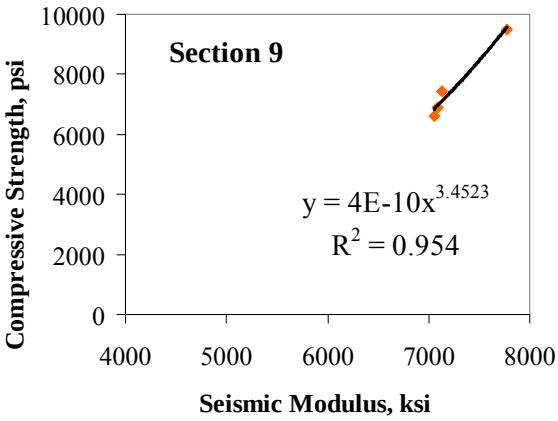
Section 9
Compressive Strength, psi
Seismic Modulus, ksi
y = 4E-10x^3.4523
R^2 = 0.954
10000
8000
6000
4000
2000
0
4000
5000
6000
7000
8000

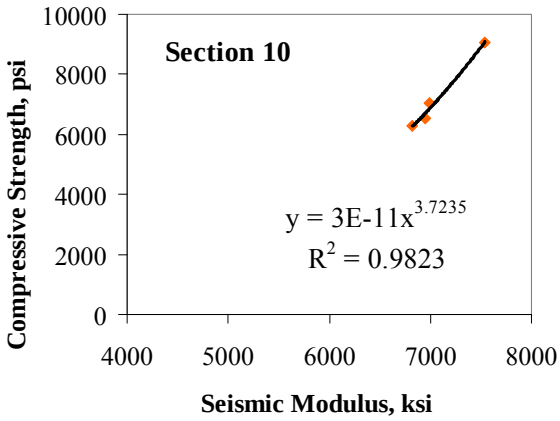
Section 10
Compressive Strength, psi
Seismic Modulus, ksi
y = 3E-11x^3.7235
R^2 = 0.9823
10000
8000
6000
4000
2000
0
4000
5000
6000
7000
8000

APPENDIX D

CONTOUR MAPS FOR CONCRETE CONDITION ON CRACKS OF SH 288

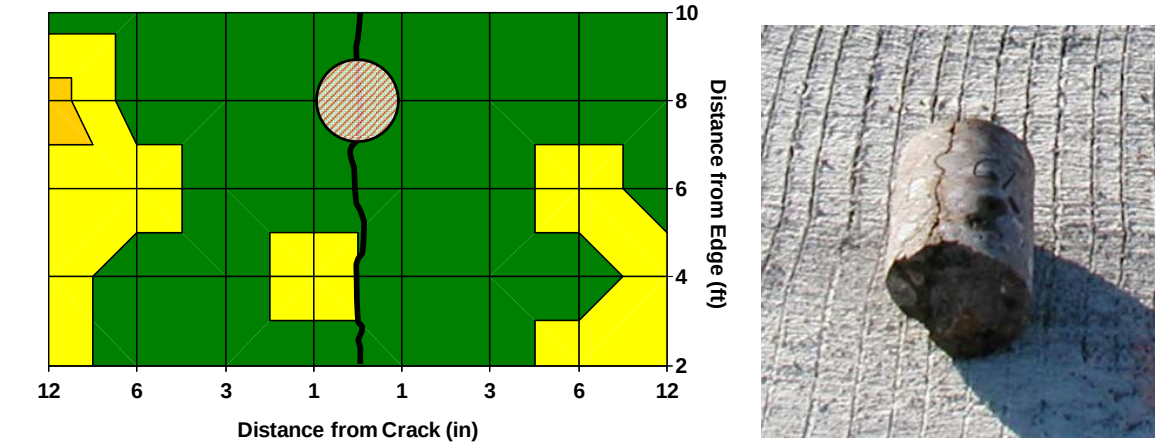

Figure D.1. Contour Map around Crack on Section 1 of SH 288.

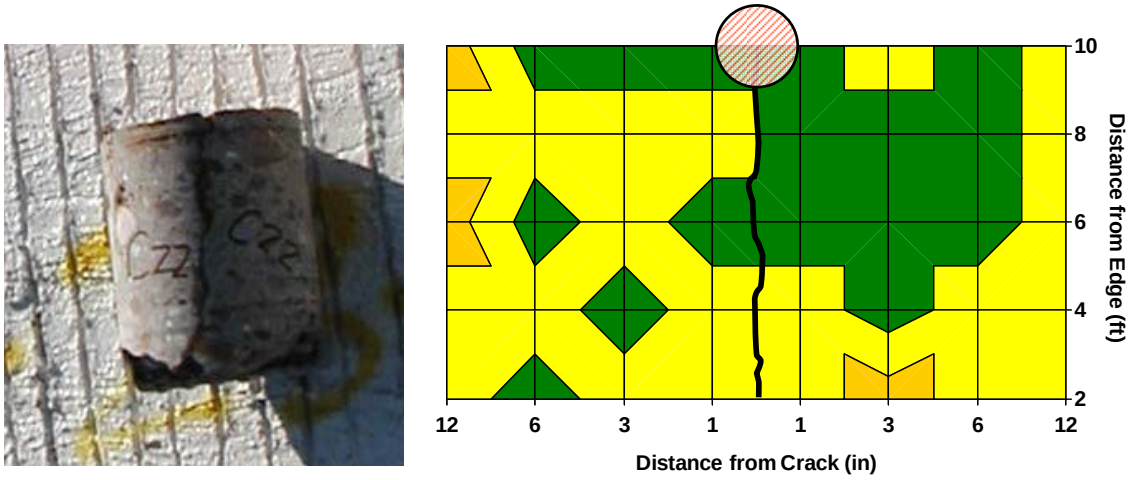

Figure D.2. Contour Map around Crack on Section 2 of SH 288.

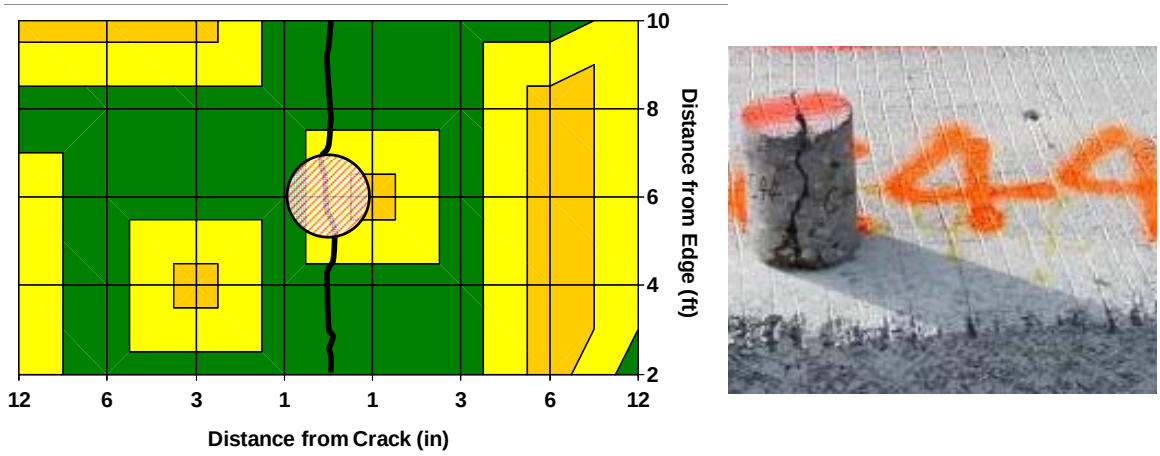

Figure D.3. Contour Map around Crack on Section 3 of SH 288.

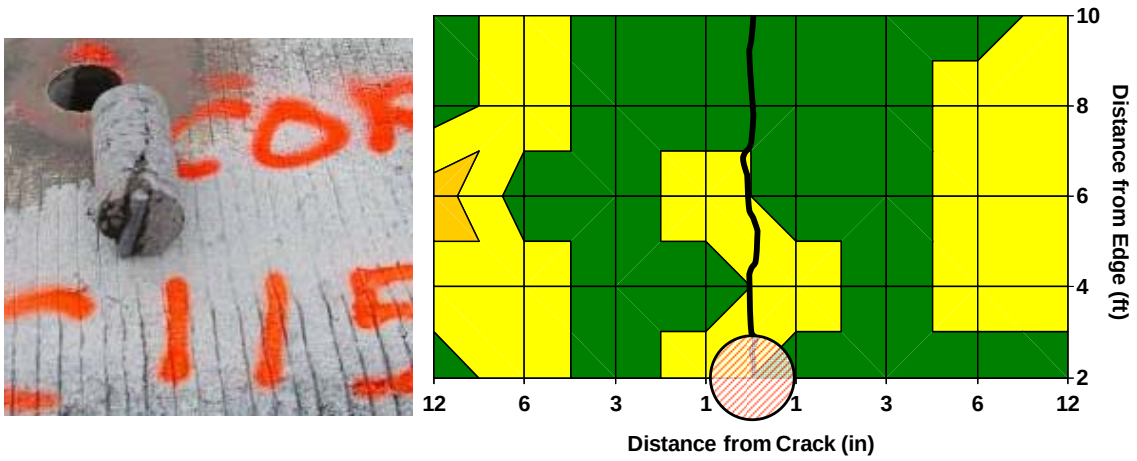

Figure D.4. Contour Map around Crack on Section 4 of SH 288.

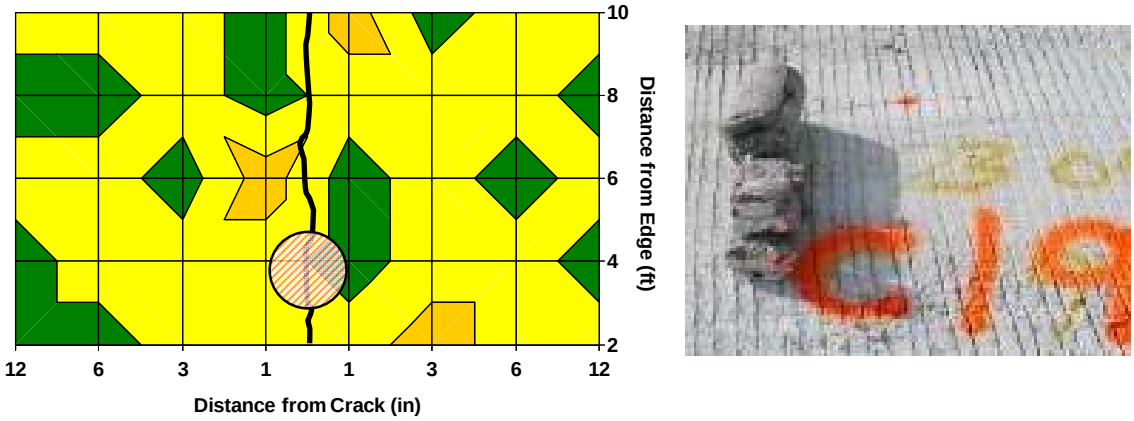

Figure D.5. Contour Map around Crack on Section 5 of SH 288.

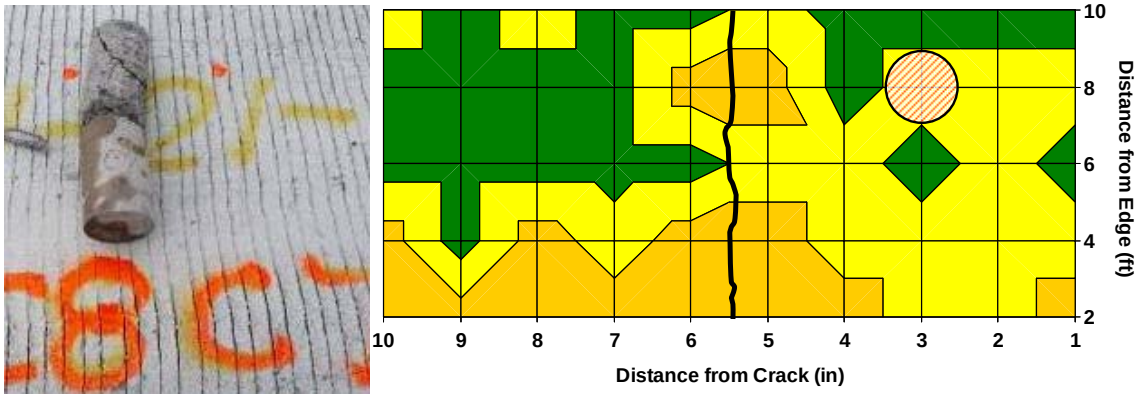

Figure D.6. Contour Map around Crack on Section 6 of SH 288.

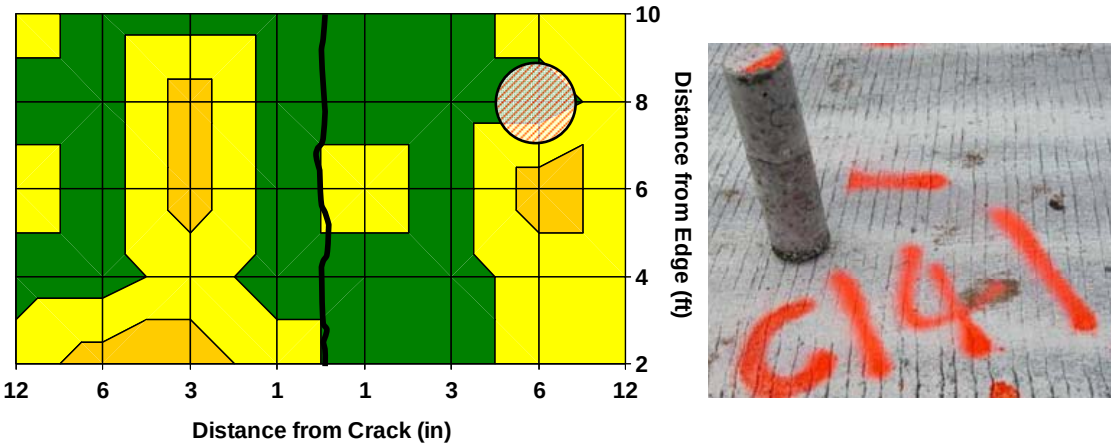

Figure D.7. Contour Map around Crack on Section 7 of SH 288.

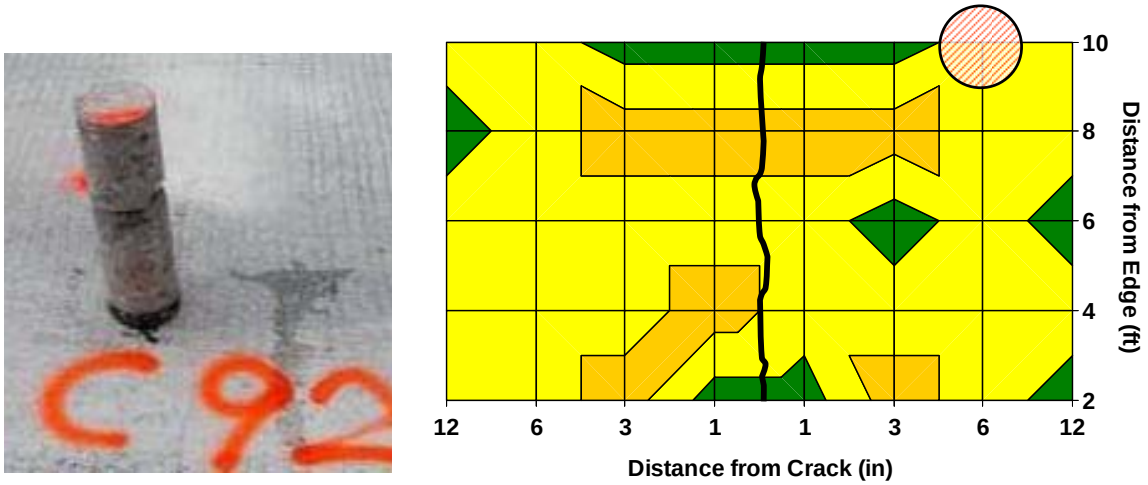

Figure D.8. Contour Map around Crack on Section 8 of SH 288.

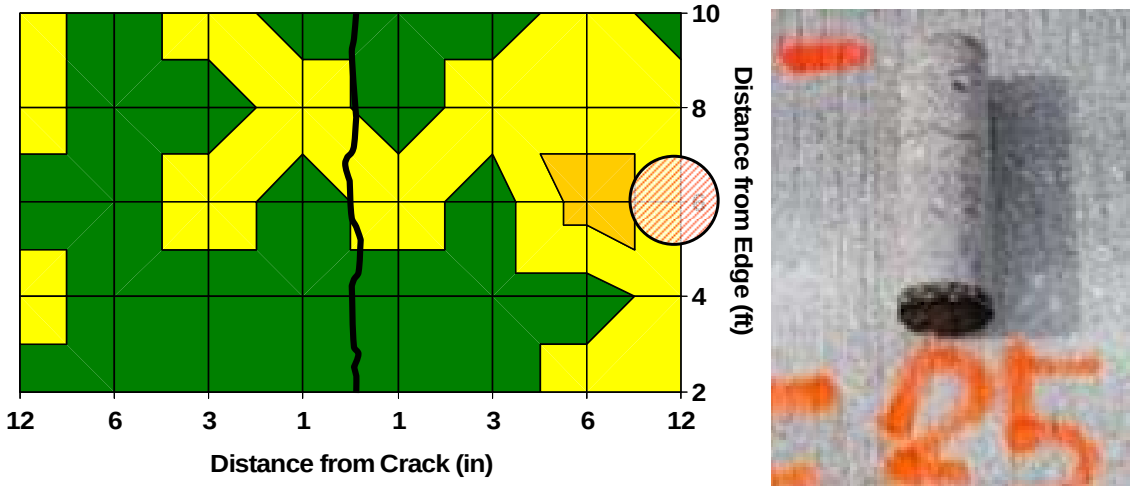

Figure D.9. Contour Map around Crack on Section 9 of SH 288.

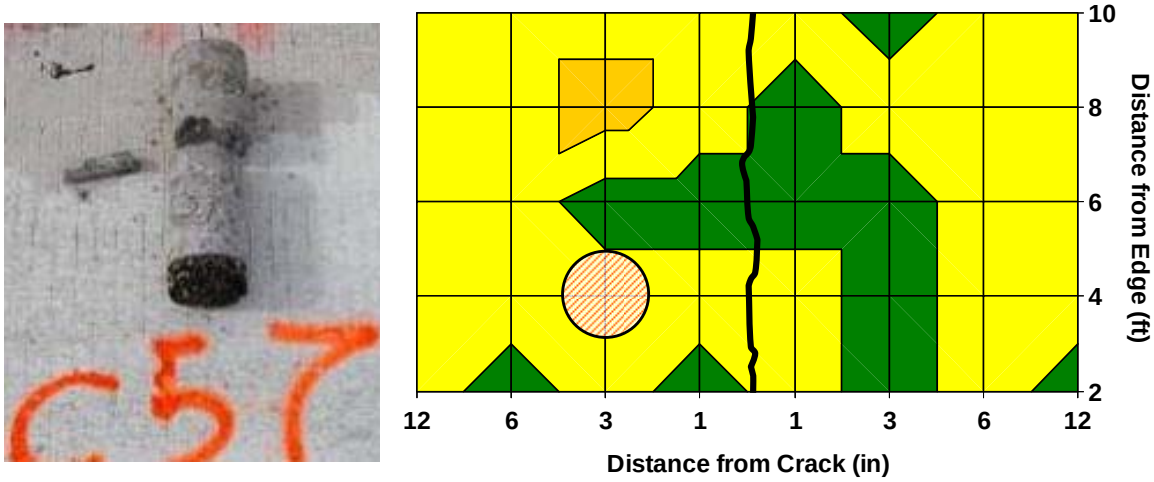

Figure D.10. Contour Map around Crack on Section 10 of SH 288.

APPENDIX E

COLOR CODED MAPS FOR SEISMIC MODULUS ON SECTIONS OF SH 288

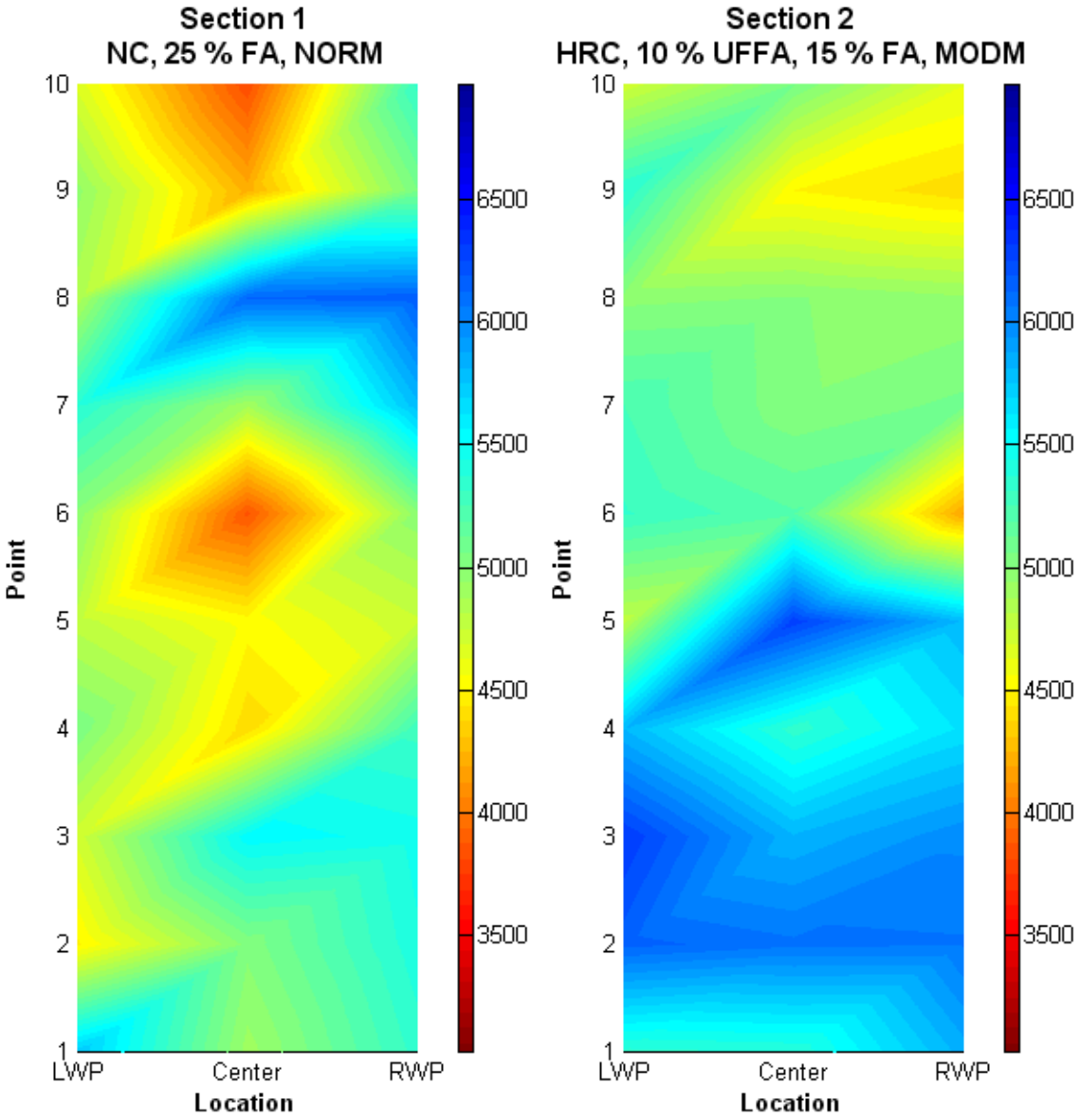
Section 1
NC, 25 % FA, NORM
Section 2
HRC, 10 % UFFA, 15 % FA, MODM
Point
Location
LWP
Center
RWP
10
9
8
7
6
5
4
3
2
1
6500
6000
5500
5000
4500
4000
3500

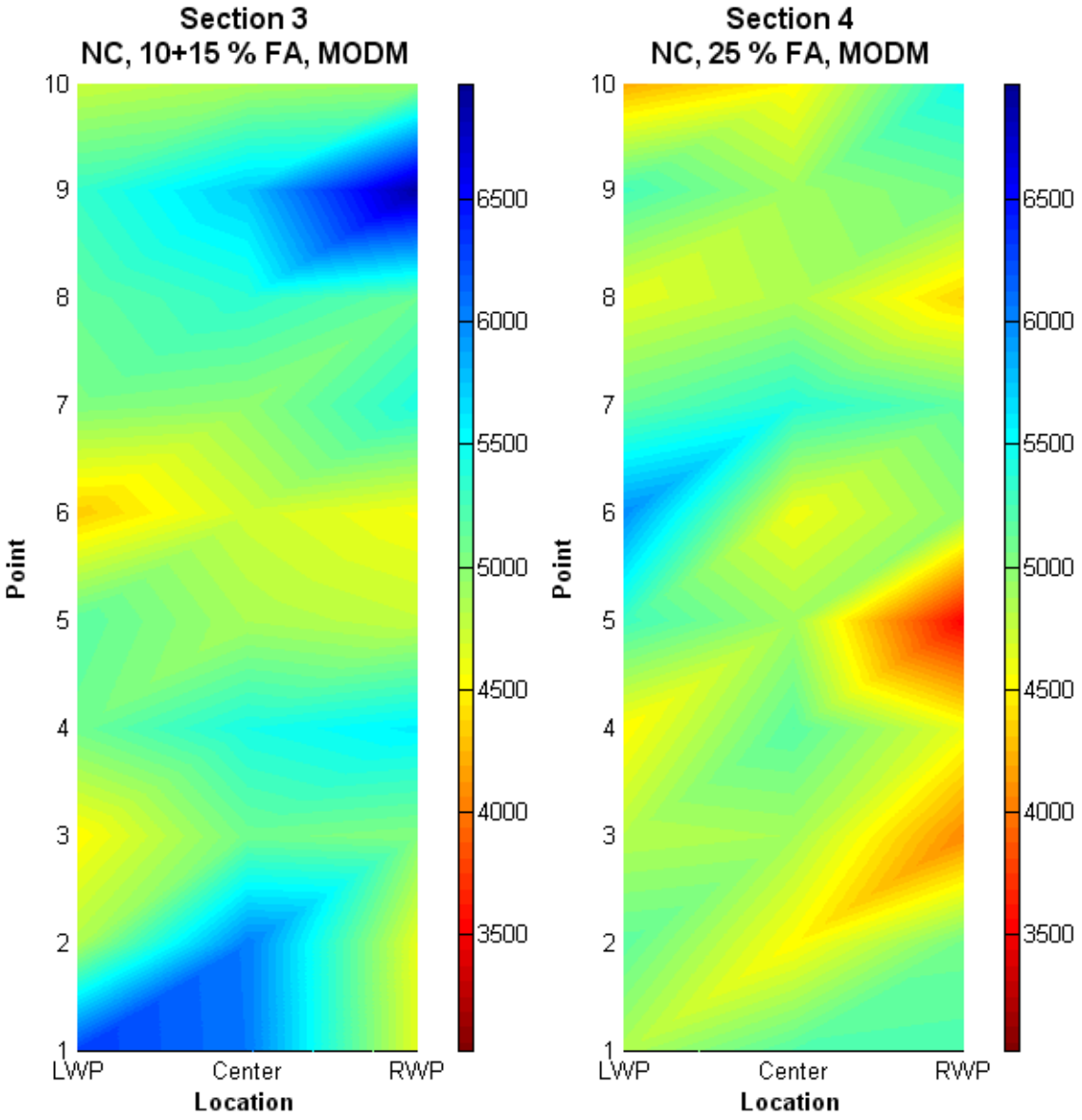
Section 3
NC, 10+15 % FA, MODM
Point
Location
LWP
Center
RWP
10
9
8
7
6
5
4
3
2
1
6500
6000
5500
5000
4500
4000
3500
Section 4
NC, 25 % FA, MODM
Point
Location
LWP
Center
RWP
10
9
8
7
6
5
4
3
2
1
6500
6000
5500
5000
4500
4000
3500

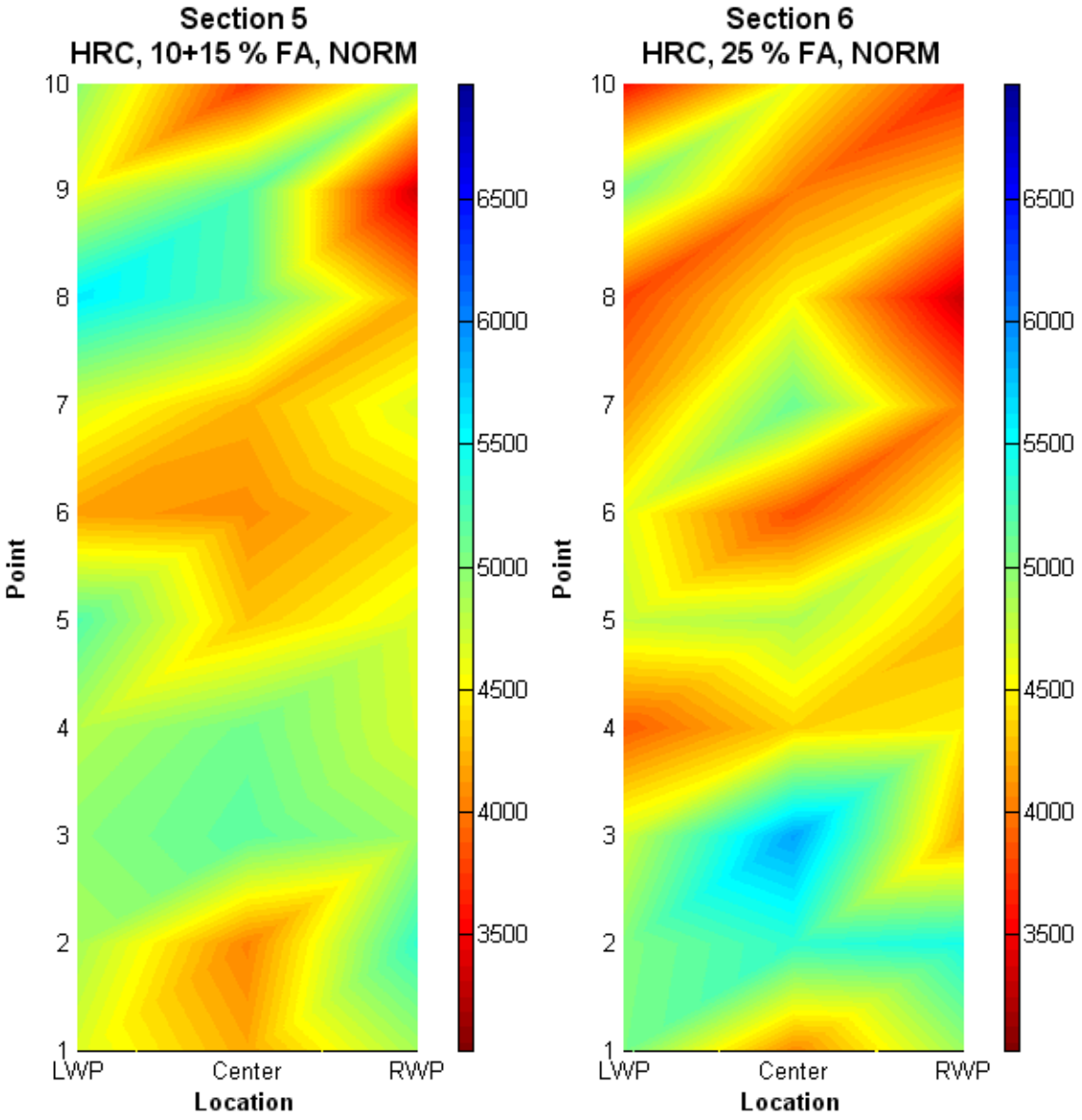
Section 5
HRC, 10+15 % FA, NORM
Point
Location
LWP
Center
RWP
10
9
8
7
6
5
4
3
2
1
6500
6000
5500
5000
4500
4000
3500
Section 6
HRC, 25 % FA, NORM
Point
Location
LWP
Center
RWP
10
9
8
7
6
5
4
3
2
1
6500
6000
5500
5000
4500
4000
3500

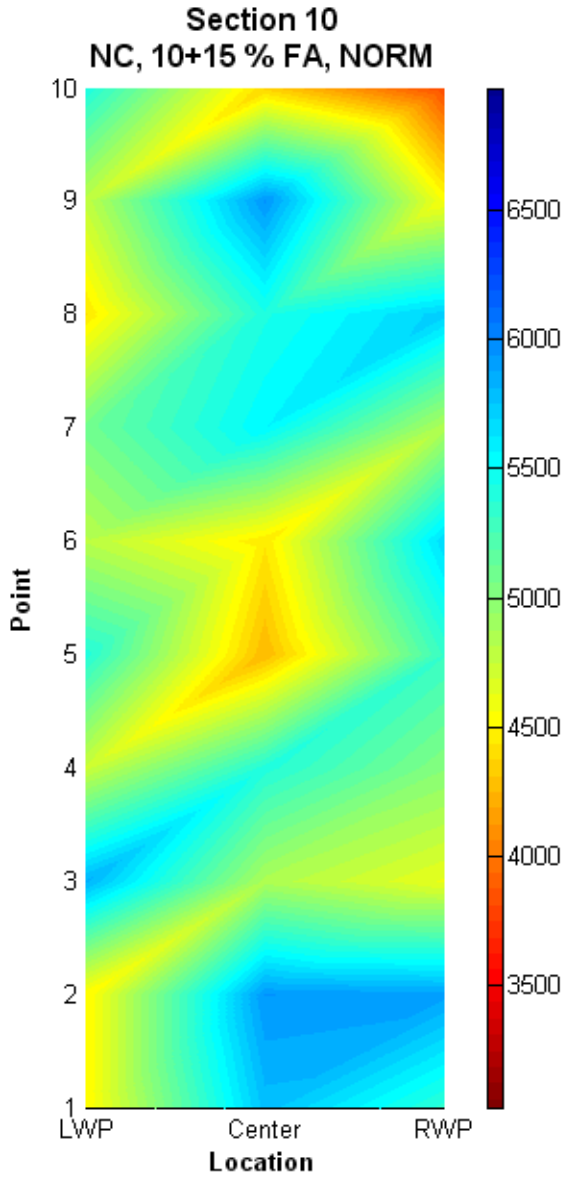
Section 10
NC, 10+15 % FA, NORM
Point
10
9
8
7
6
5
4
3
2
1
LWP
Center
RWP
Location
6500
6000
5500
5000
4500
4000
3500

APPENDIX F

DATA DETAILS OF FIELD TESTS AT SH 35

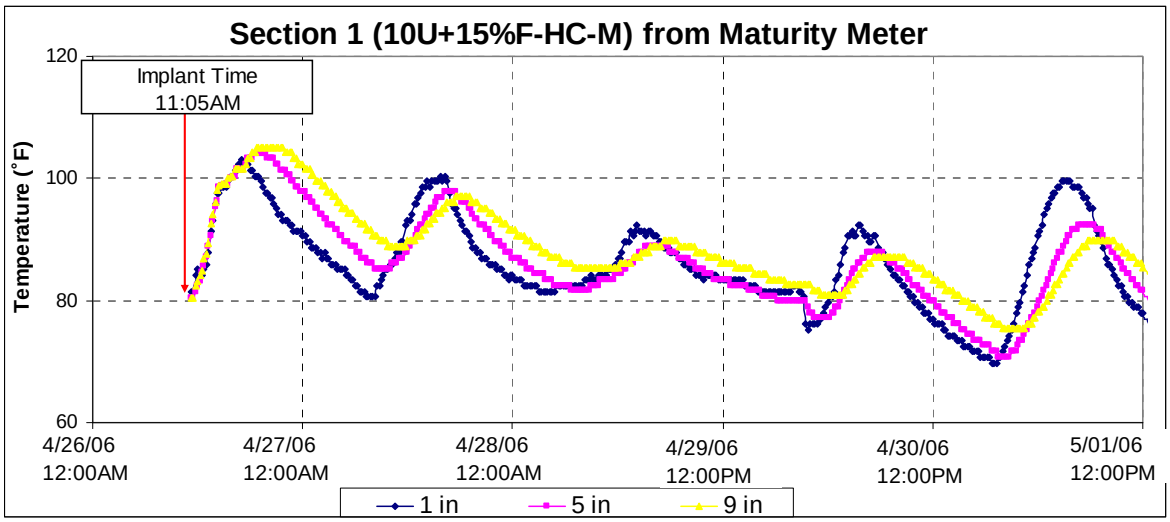

Figure F.1. Temperature Profile of Test Section 1.

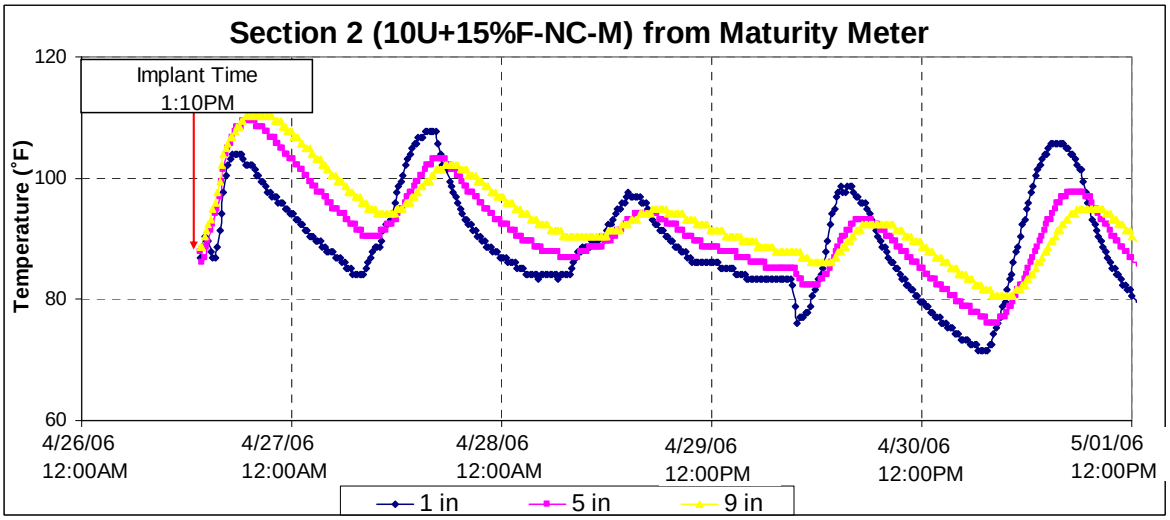

Figure F.2. Temperature Profile of Test Section 2.

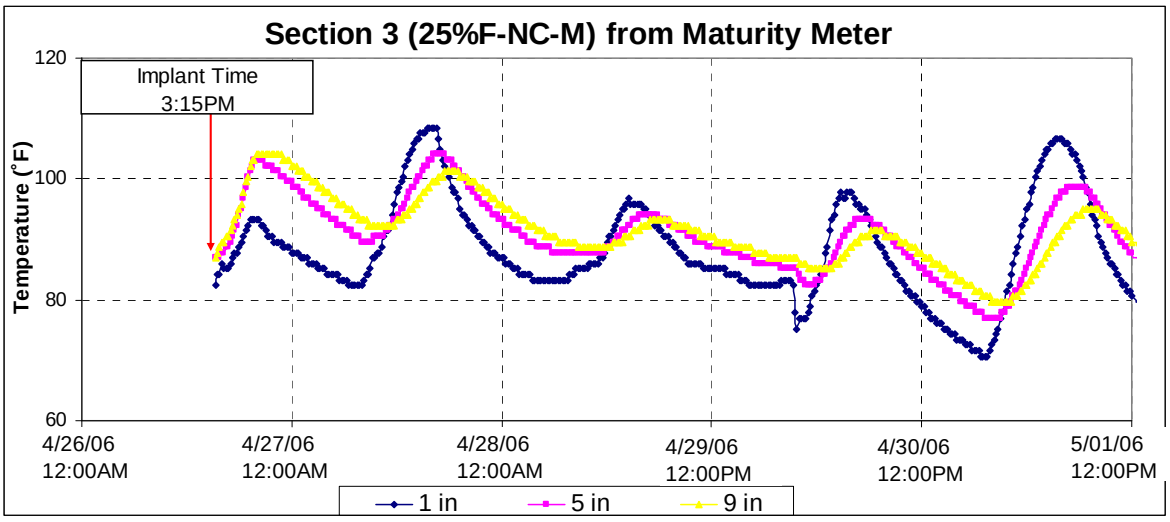

Figure F.3. Temperature Profile of Test Section 3.

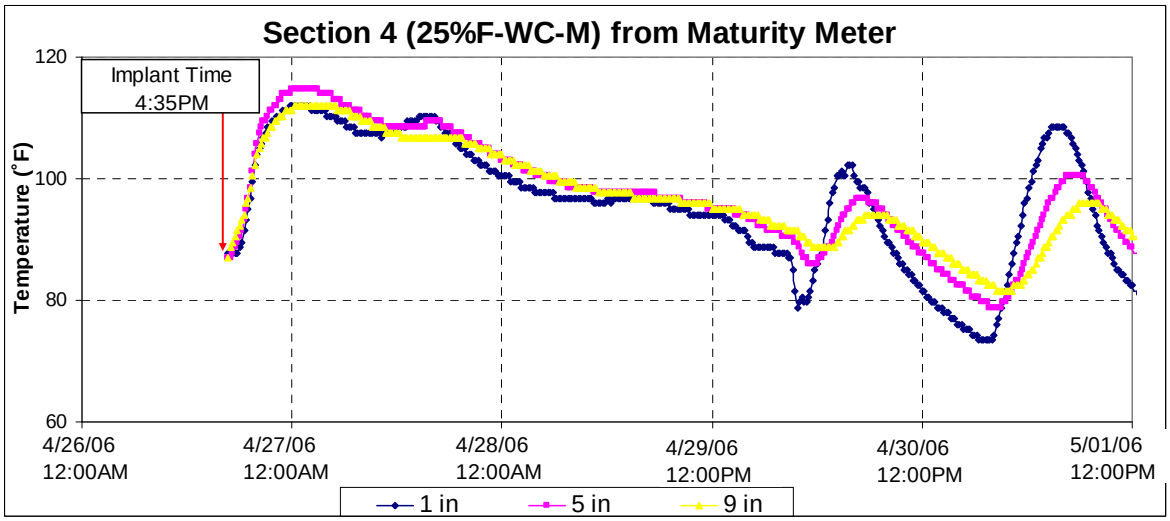

Figure F.4. Temperature Profile of Test Section 4.

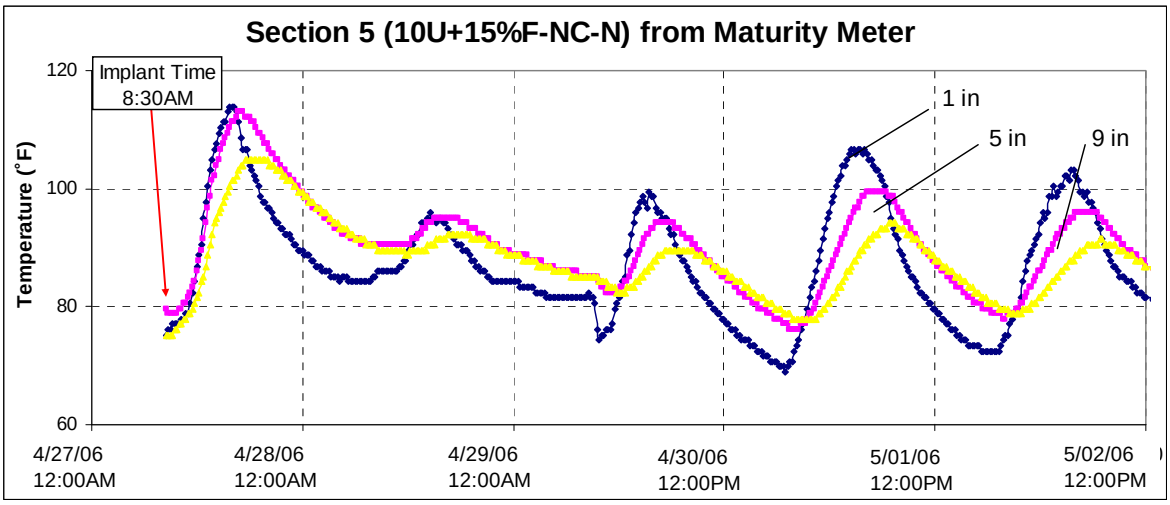

Figure F.5. Temperature Profile of Test Section 5.

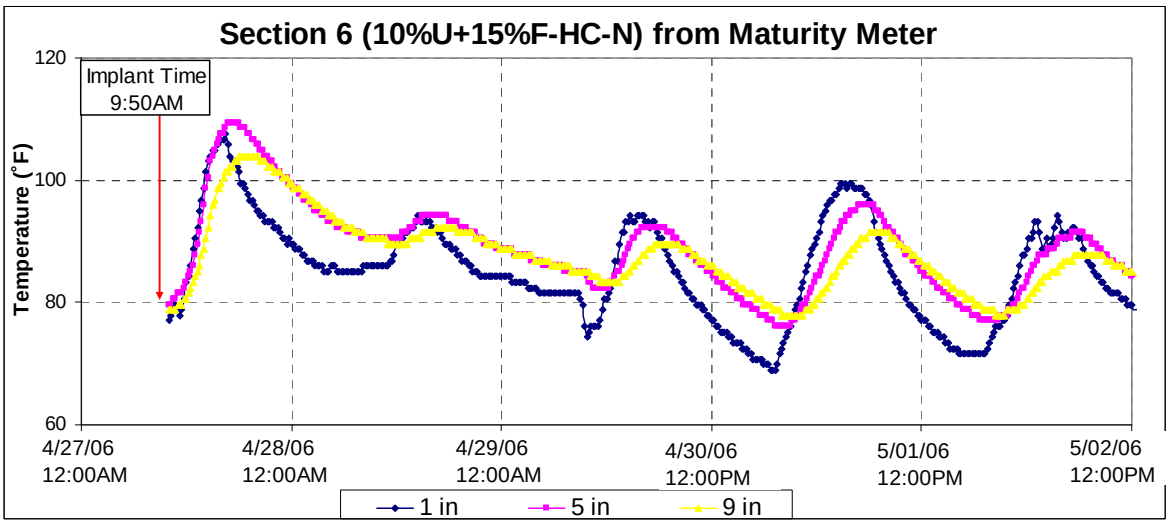

Figure F.6. Temperature Profile of Test Section 6.

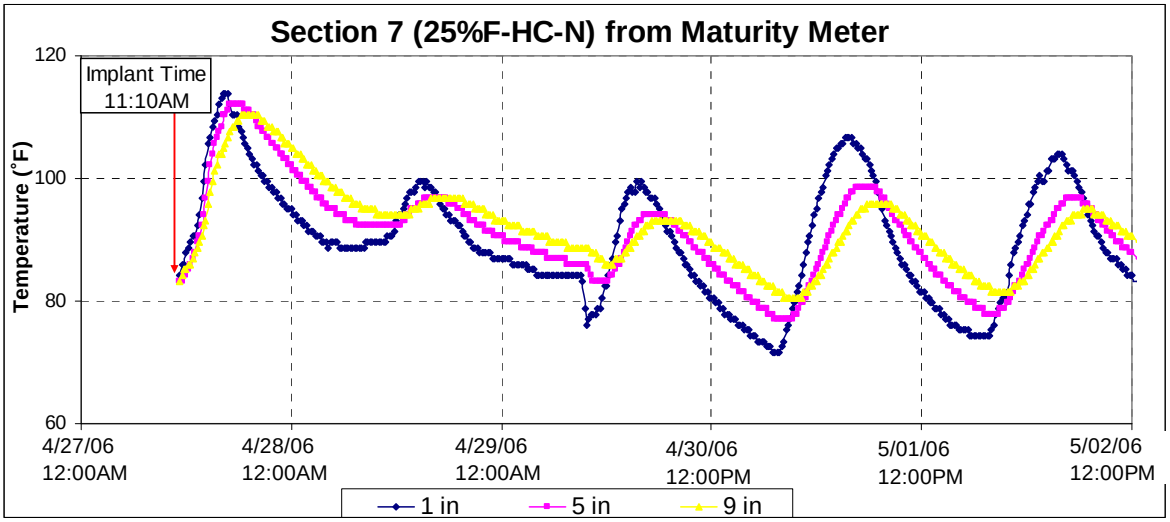

Figure F.7. Temperature Profile of Test Section 7.

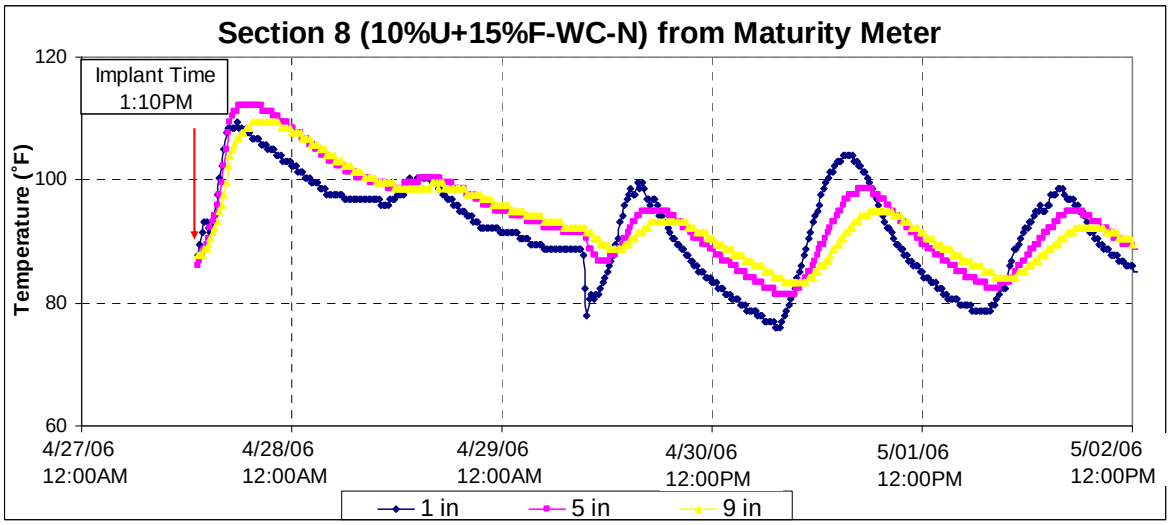

Figure F.8. Temperature Profile of Test Section 8.

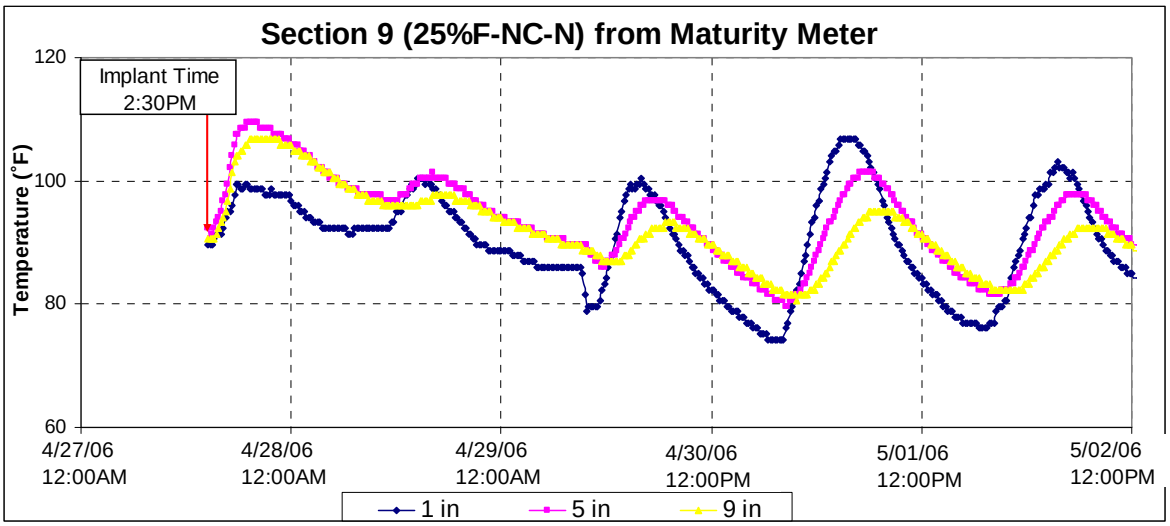

Figure F.9. Temperature Profile of Test Section 9.

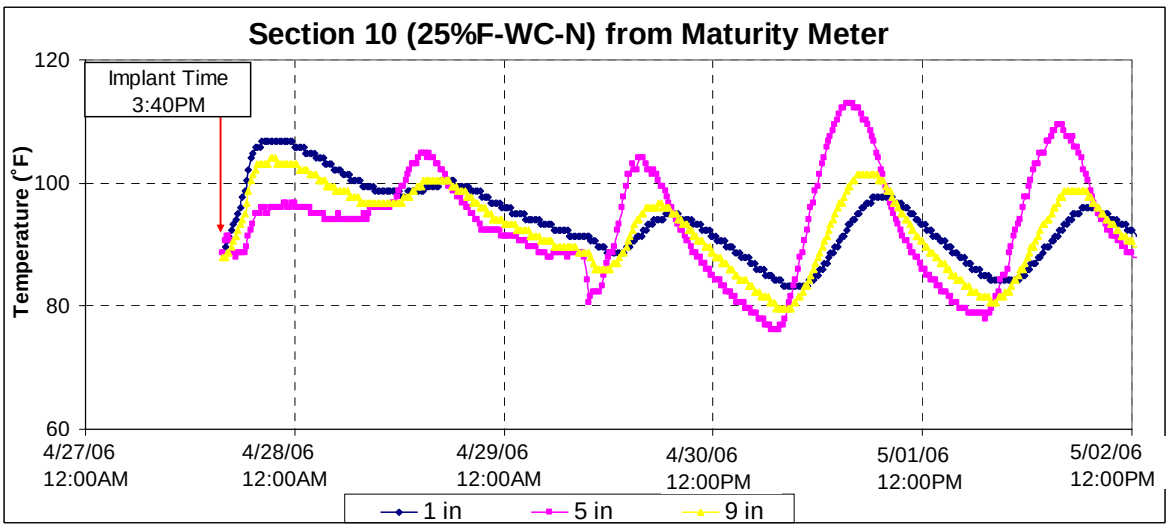

Figure F.10. Temperature Profile of Test Section 10.

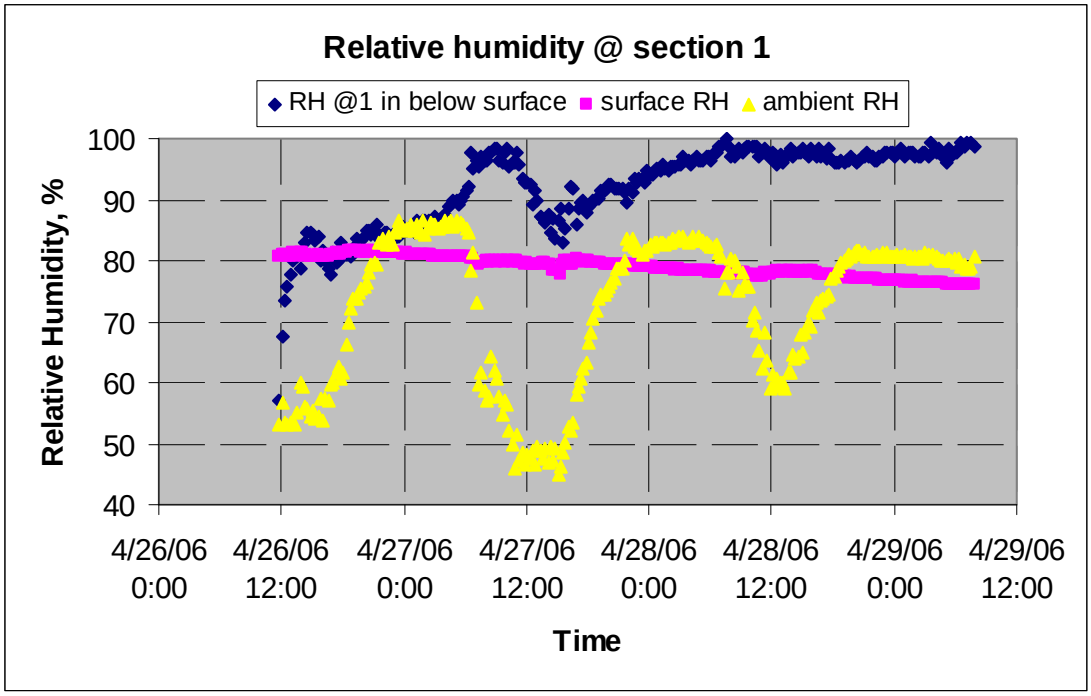

Figure F.11. Moisture Profiles of Test Section 1.

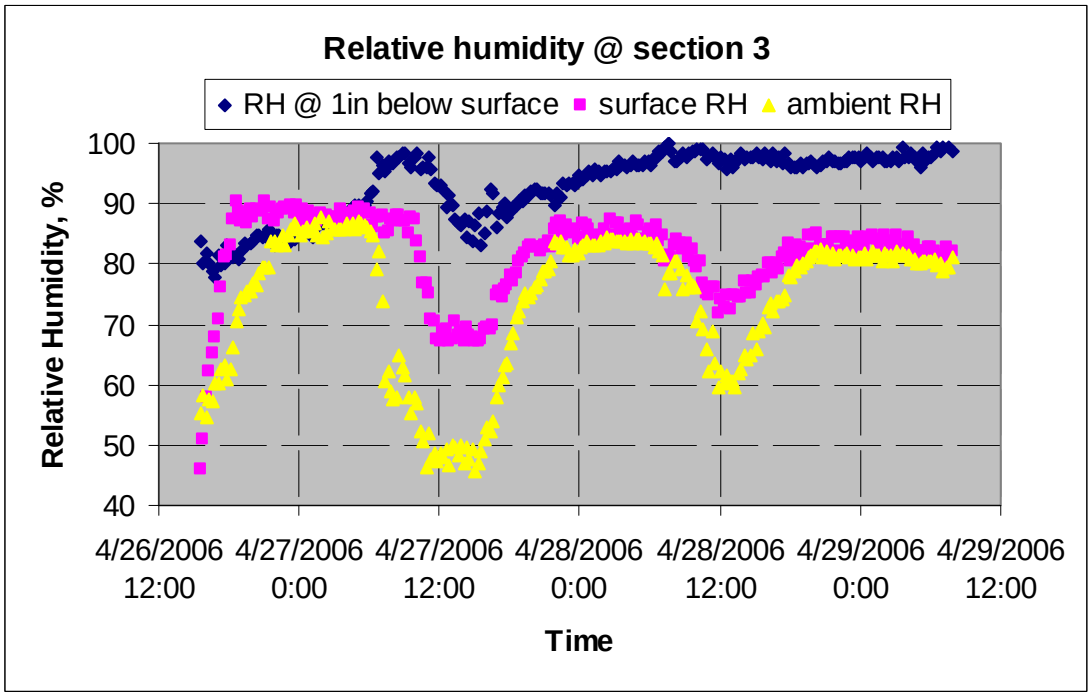

Figure F.12. Moisture Profiles of Test Section 3.

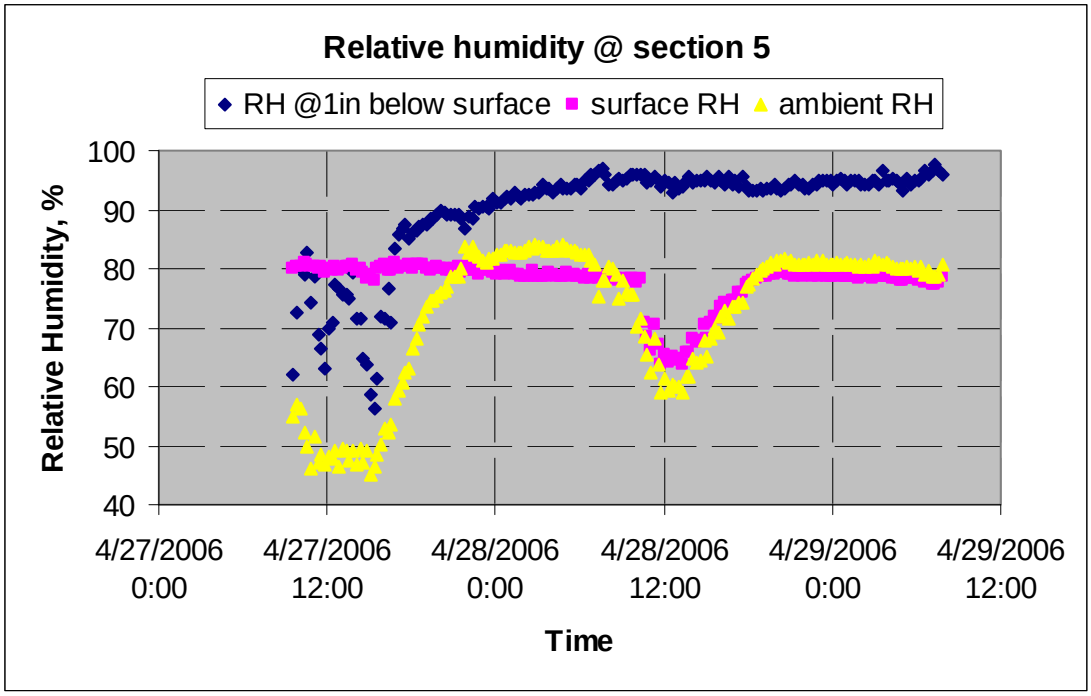

Figure F.13. Moisture Profiles of Test Section 5.

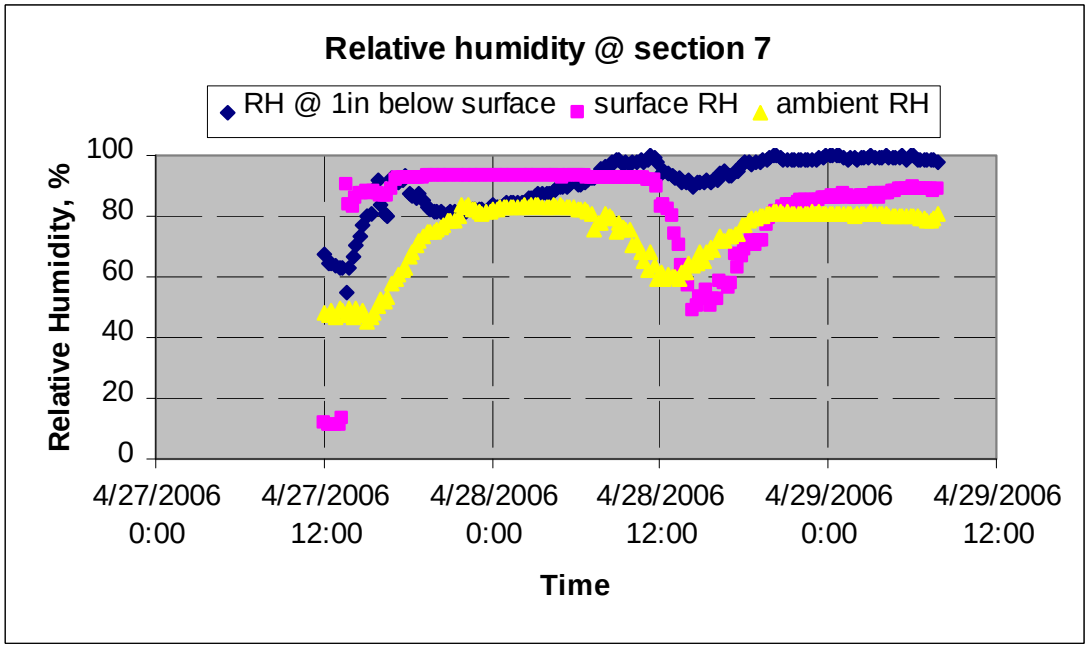

Figure F.14. Moisture Profiles of Test Section 7.

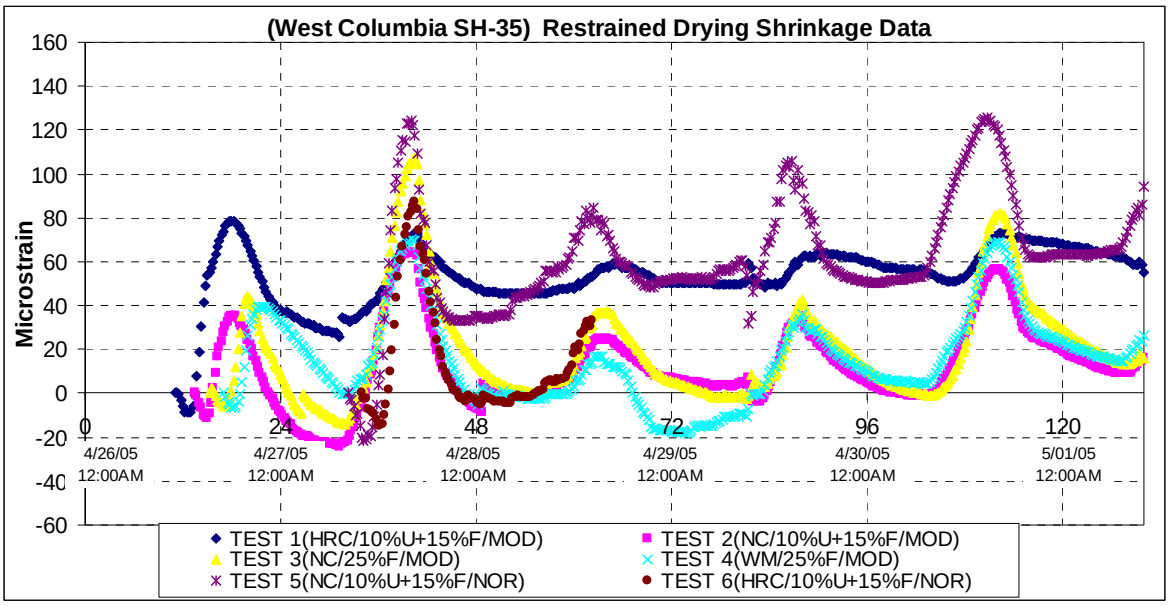

Figure F.15. Gage Shrinkage with Time for Different Sections.

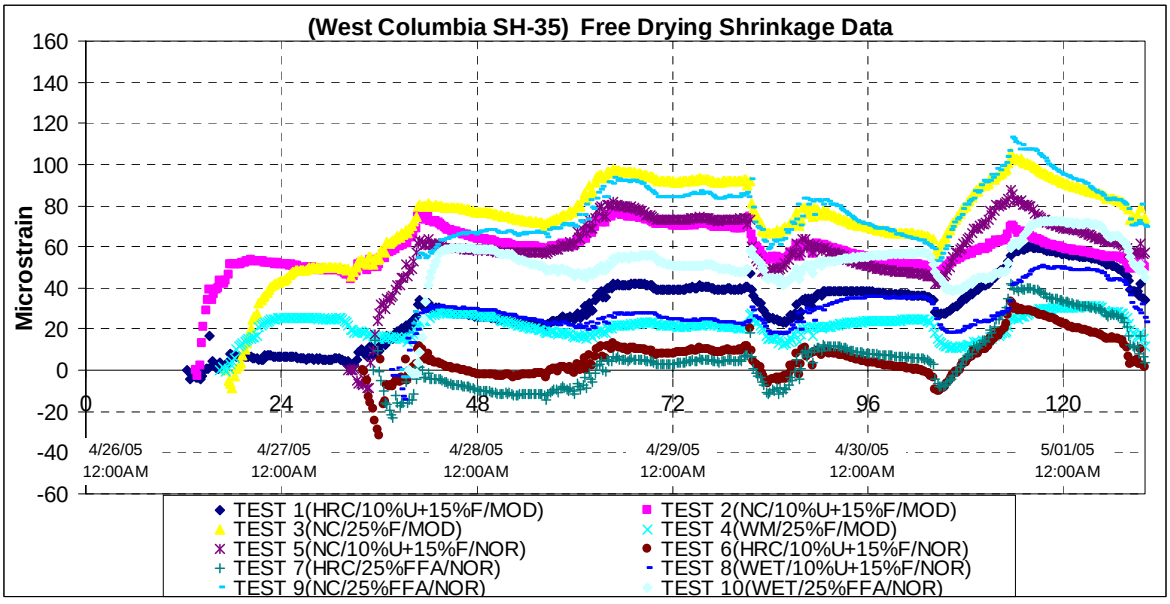

Figure F.16. Free Shrinkage with Time for Different Sections.

APPENDIX G

TxDOT COMPRESSIVE STRENGTH AND FFRC RESULTS OF SH 35

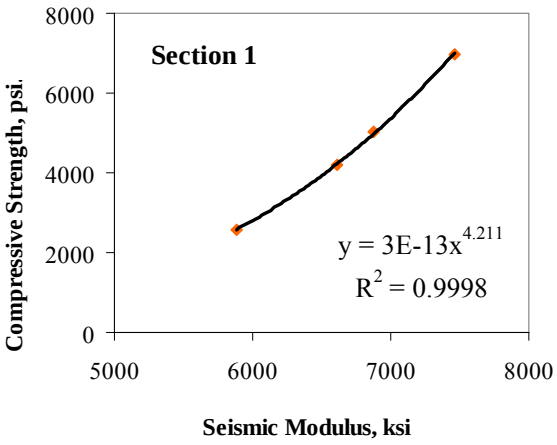
Section 1
Compressive Strength, psi.
Seismic Modulus, ksi
y = 3E-13x^4.211
R^2 = 0.9998
8000
6000
4000
2000
0
5000
6000
7000
8000

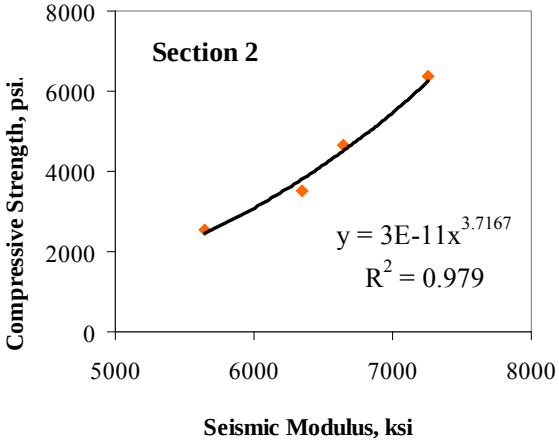
Section 2
Compressive Strength, psi.
Seismic Modulus, ksi
y = 3E-11x^3.7167
R^2 = 0.979
8000
6000
4000
2000
0
5000
6000
7000
8000

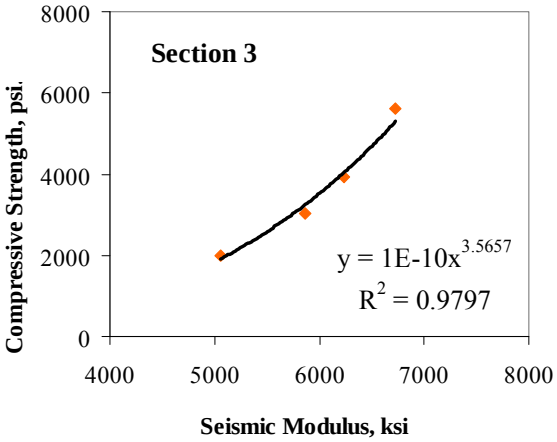
Section 3
Compressive Strength, psi.
Seismic Modulus, ksi
y = 1E-10x^3.5657
R^2 = 0.9797
8000
6000
4000
2000
0
4000
5000
6000
7000
8000

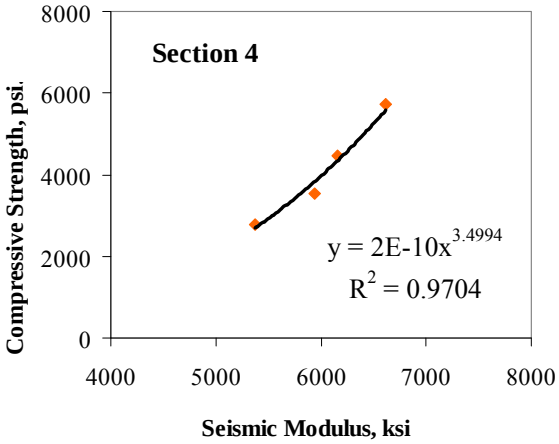
Section 4
Compressive Strength, psi.
Seismic Modulus, ksi
y = 2E-10x^3.4994
R^2 = 0.9704
8000
6000
4000
2000
0
4000
5000
6000
7000
8000

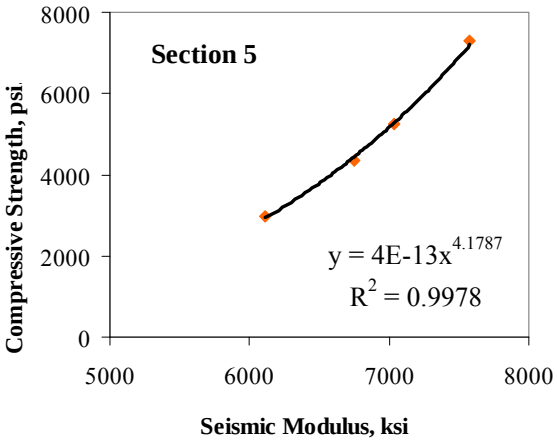
Section 5
Compressive Strength, psi.
Seismic Modulus, ksi
y = 4E-13x^4.1787
R^2 = 0.9978
8000
6000
4000
2000
0
5000
6000
7000
8000

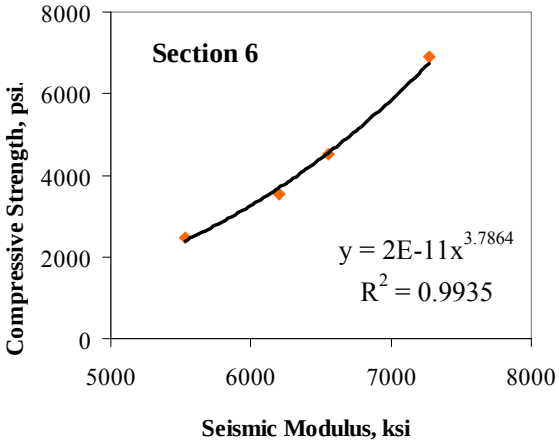
Section 6
Compressive Strength, psi.
Seismic Modulus, ksi
y = 2E-11x^3.7864
R^2 = 0.9935
8000
6000
4000
2000
0
5000
6000
7000
8000

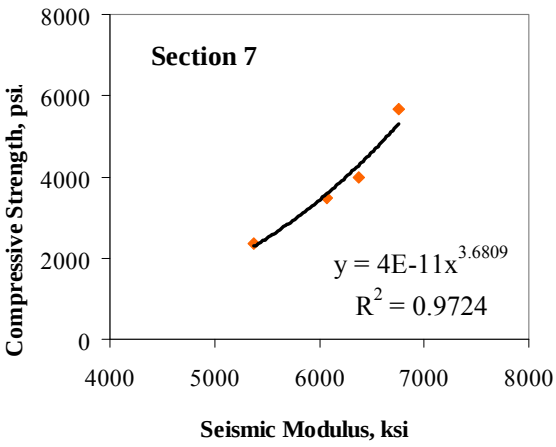
Section 7
Compressive Strength, psi.
Seismic Modulus, ksi
y = 4E-11x^3.6809
R^2 = 0.9724
8000
6000
4000
2000
0
4000
5000
6000
7000
8000

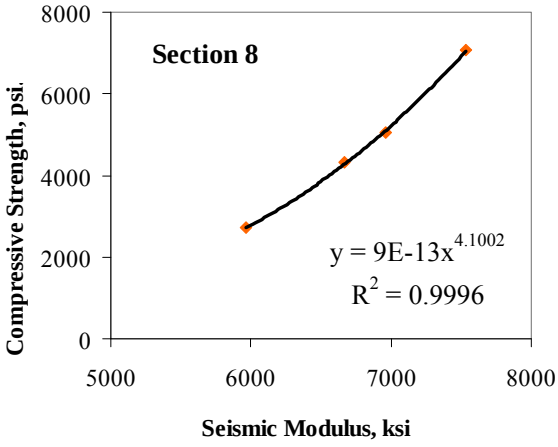
Section 8
Compressive Strength, psi.
Seismic Modulus, ksi
y = 9E-13x^4.1002
R^2 = 0.9996
8000
6000
4000
2000
0
5000
6000
7000
8000

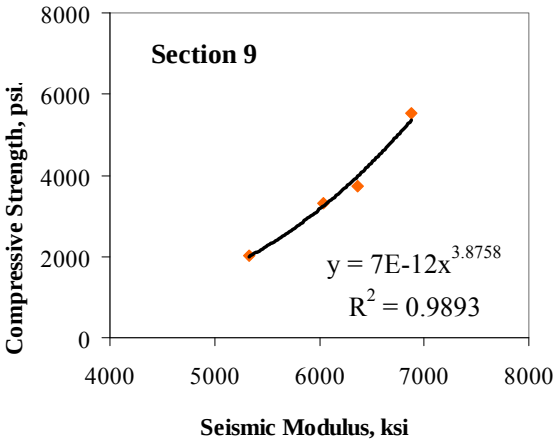
Section 9
Compressive Strength, psi.
Seismic Modulus, ksi
y = 7E-12x^3.8758
R^2 = 0.9893
8000
6000
4000
2000
0
4000
5000
6000
7000
8000

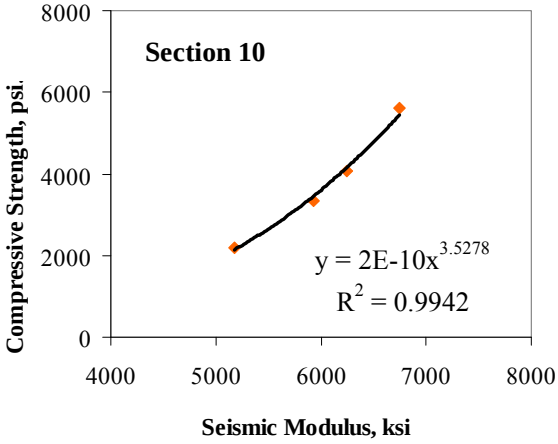
Section 10
Compressive Strength, psi.
Seismic Modulus, ksi
y = 2E-10x^3.5278
R^2 = 0.9942
8000
6000
4000
2000
0
4000
5000
6000
7000
8000

APPENDIX H

CONTOUR MAPS FOR CONCRETE CONDITION ON CRACKS OF SH 35

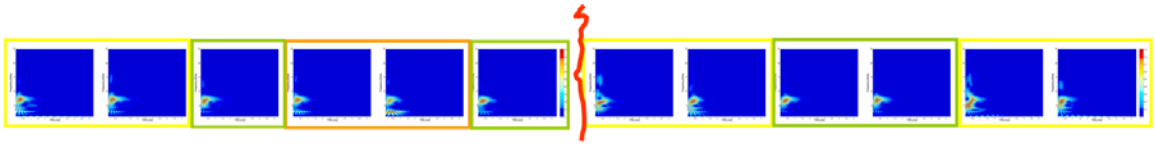

Figure H.1. Results on Core 1 of SH 35.

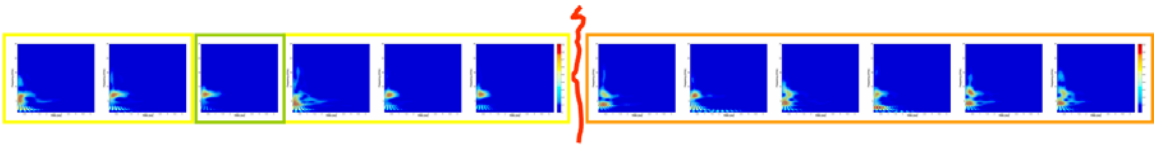

Figure H.2. Results on Core 2 of SH 35.

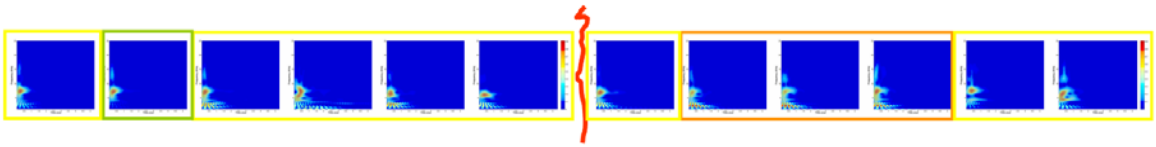

Figure H.3. Results on Core 3 of SH 35.

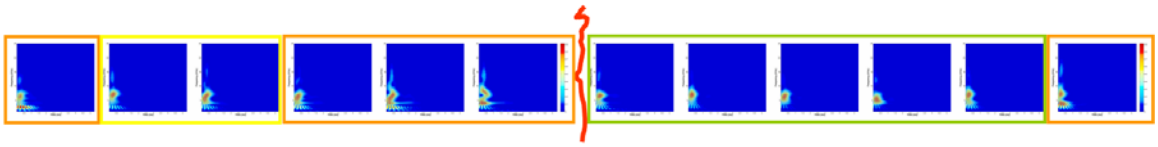

Figure H.4. Results on Core 4 of SH 35 (Sawcut Area).

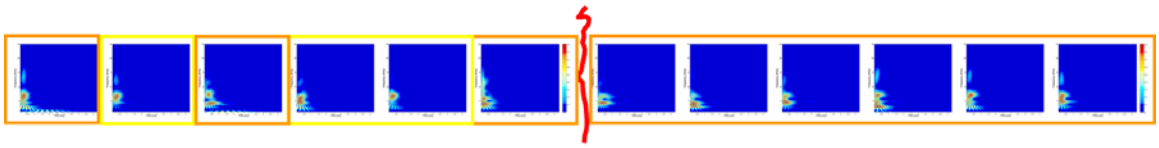

Figure H.5. Results on Core 5 of SH 35 (Sawcut Area).

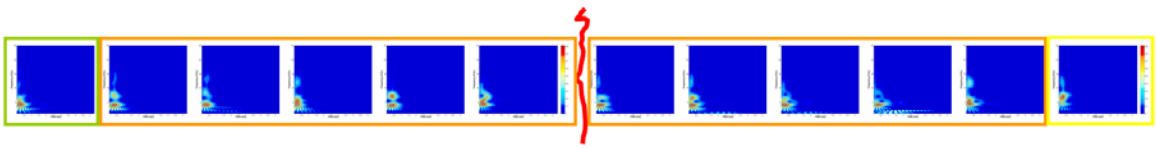

Figure H.6. Results on Core 6 of SH 35 (Sawcut Area).

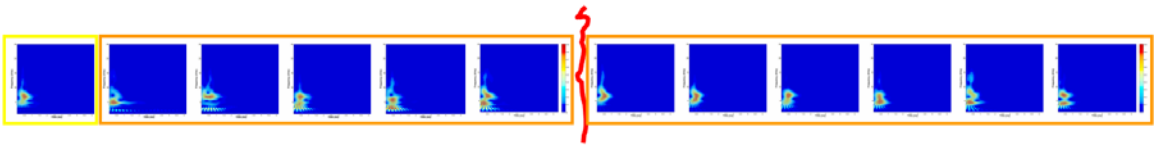

Figure H.7. Results on Core 7 of SH 35 (Sawcut Area).

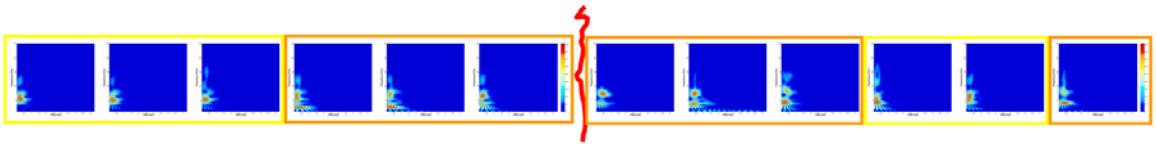

Figure H.8. Results on Core 8 of SH 35.

APPENDIX I

COLOR CODED MAPS FOR SEISMIC MODULUS ON SECTIONS OF SH 35

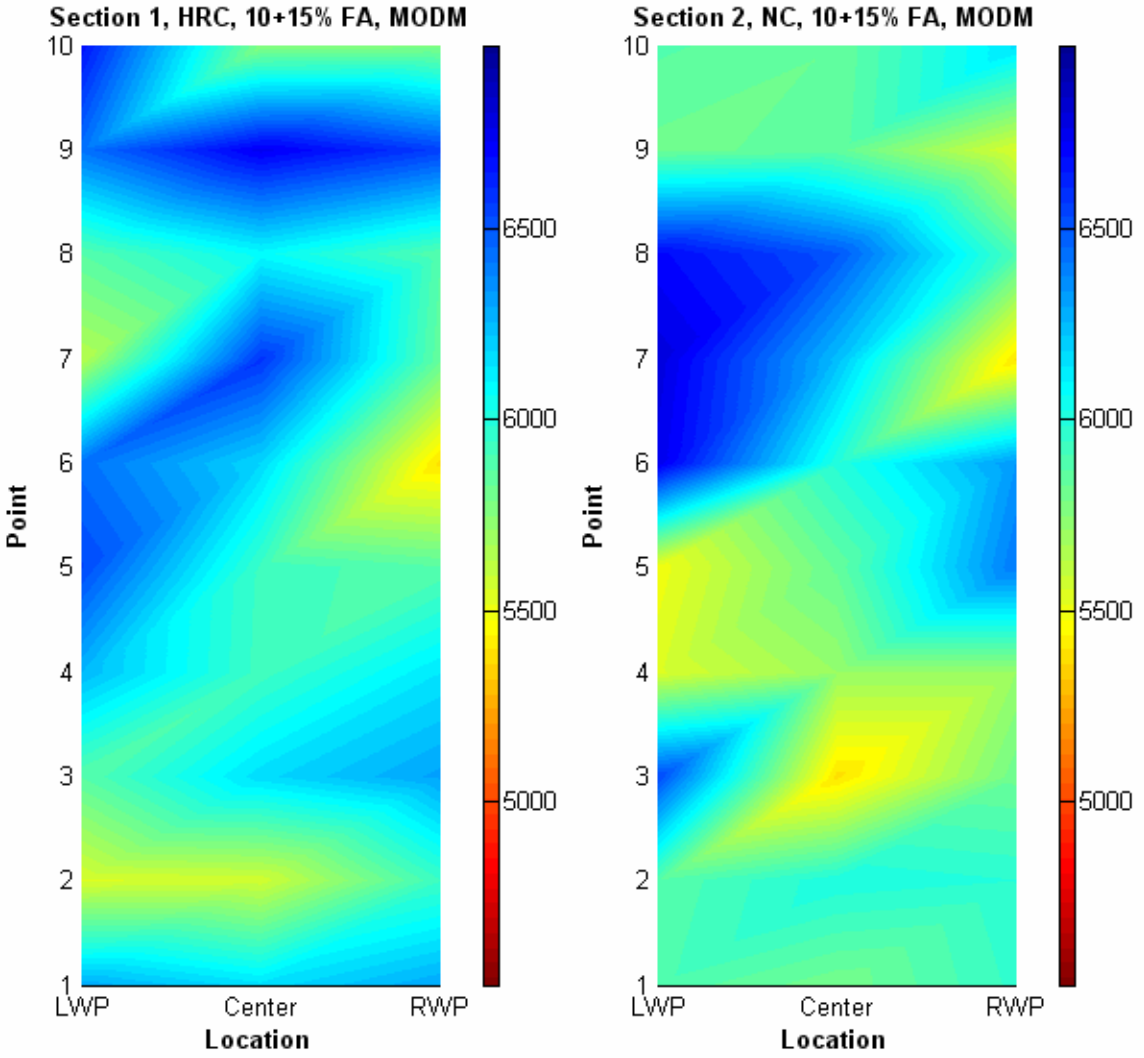
Section 1, HRC, 10+15% FA, MODM
Point
10
9
8
7
6
5
4
3
2
1
LWP
Center
RWP
Location
6500
6000
5500
5000
Section 2, NC, 10+15% FA, MODM
Point
10
9
8
7
6
5
4
3
2
1
LWP
Center
RWP
Location
6500
6000
5500
5000

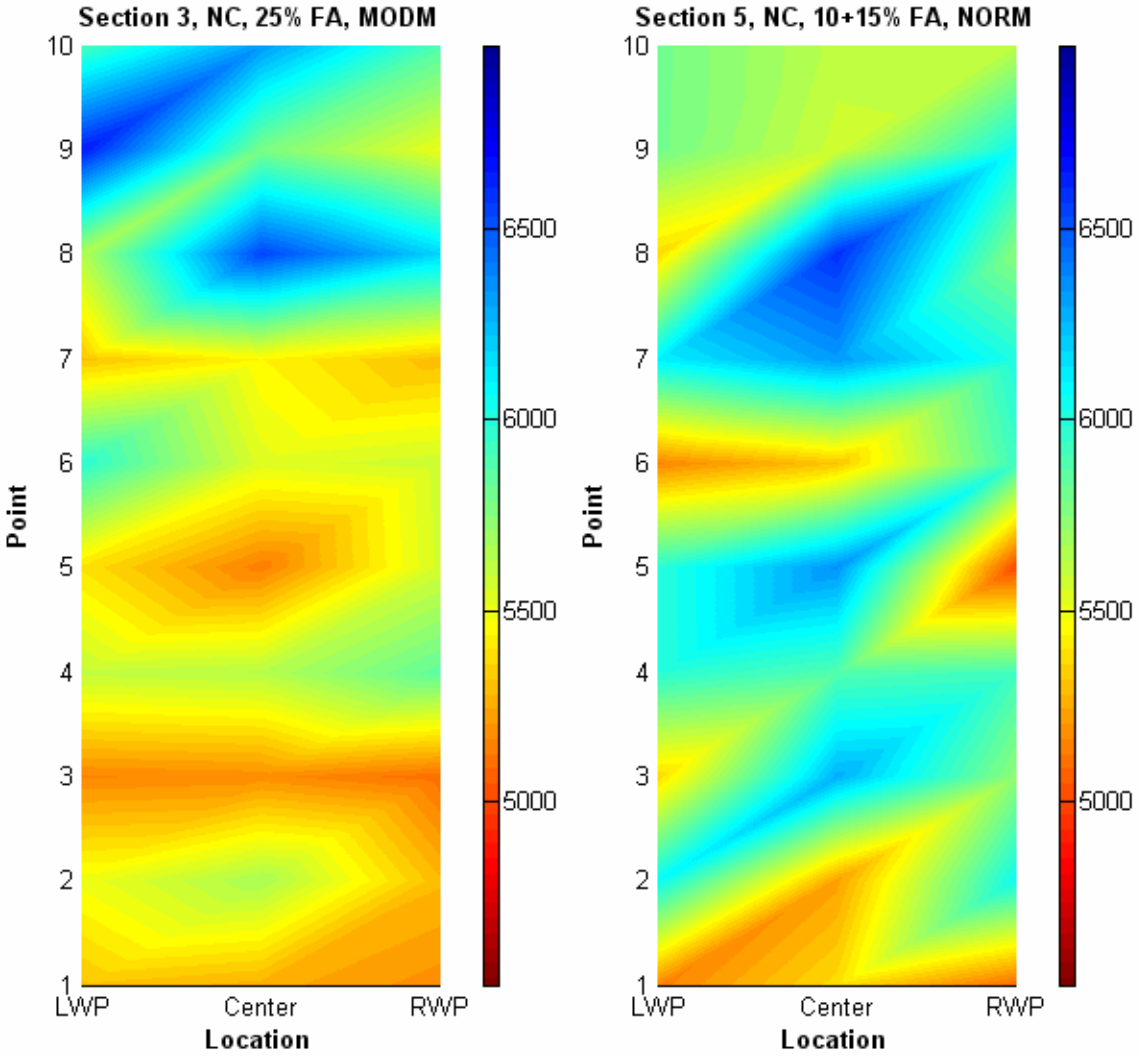
Section 3, NC, 25% FA, MODM
Point
10
9
8
7
6
5
4
3
2
1
LWP
Center
RWP
Location
6500
6000
5500
5000
Section 5, NC, 10+15% FA, NORM
Point
10
9
8
7
6
5
4
3
2
1
LWP
Center
RWP
Location
6500
6000
5500
5000

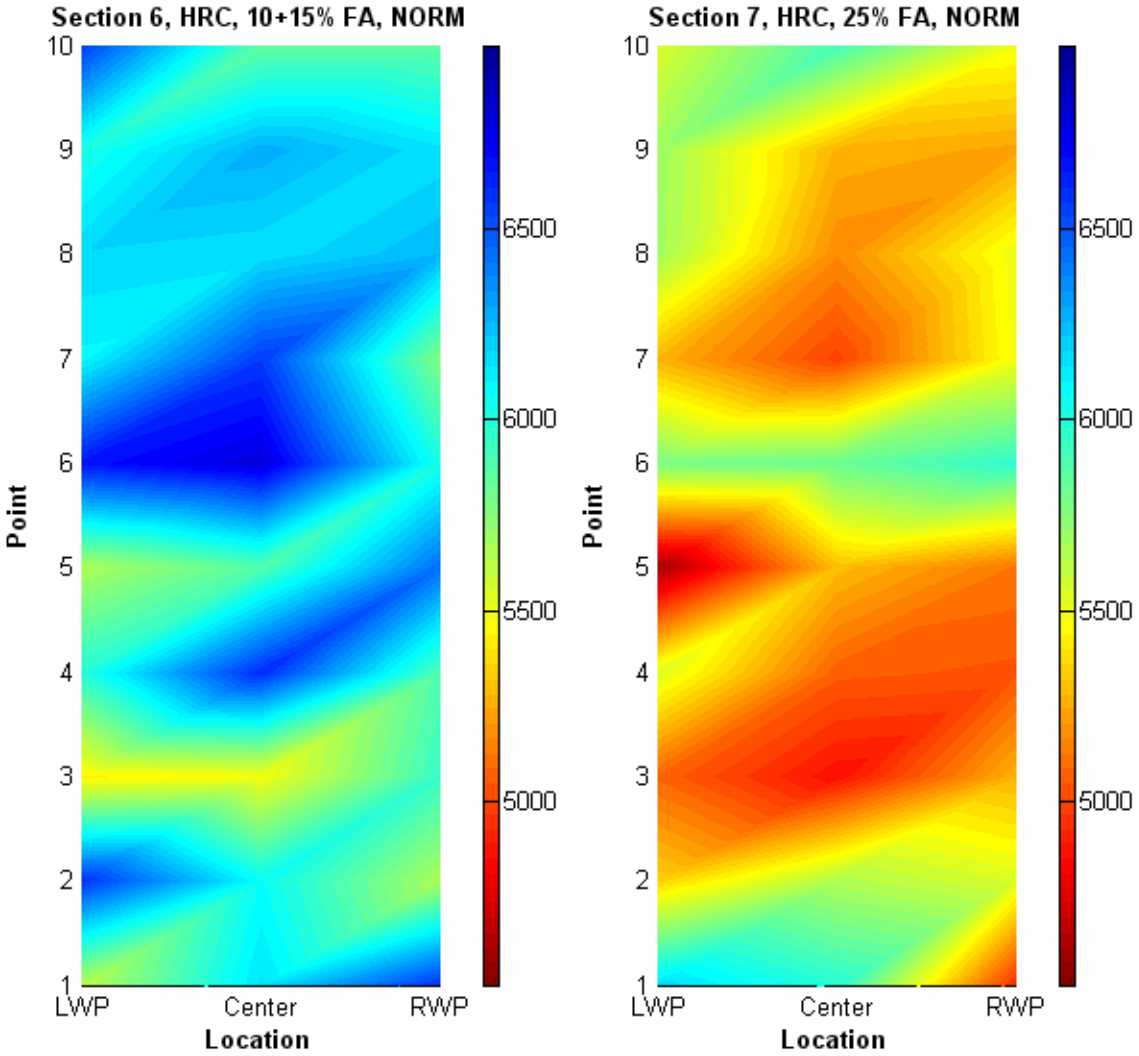
Section 6, HRC, 10+15% FA, NORM
Point
10
9
8
7
6
5
4
3
2
1
LWP
Center
RWP
Location
6500
6000
5500
5000
Section 7, HRC, 25% FA, NORM
Point
10
9
8
7
6
5
4
3
2
1
LWP
Center
RWP
Location
6500
6000
5500
5000

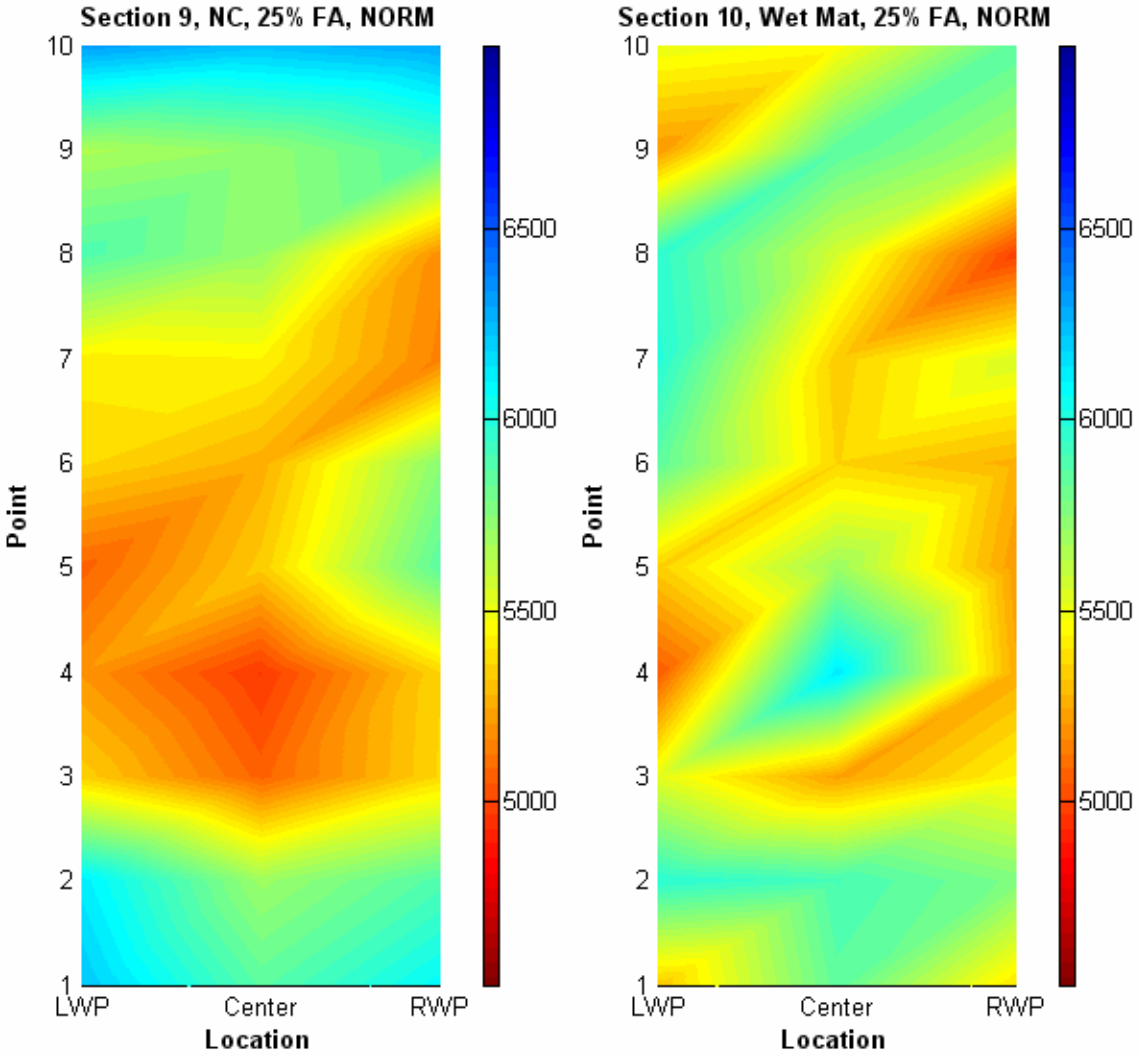
Section 9, NC, 25% FA, NORM
Point
10
9
8
7
6
5
4
3
2
1
LWP
Center
RWP
Location
6500
6000
5500
5000
Section 10, Wet Mat, 25% FA, NORM
Point
10
9
8
7
6
5
4
3
2
1
LWP
Center
RWP
Location
6500
6000
5500
5000